

PLANETARY DYNAMO MODELS: GENERATION MECHANISMS AND THE  
INFLUENCE OF BOUNDARY CONDITIONS

by

Girija Dharmaraj

A thesis submitted in conformity with the requirements  
for the degree of Doctor of Philosophy  
Graduate Department of Physics  
University of Toronto

© Copyright 2013 by Girija Dharmaraj

# Abstract

Planetary Dynamo Models: Generation Mechanisms and the Influence of Boundary  
Conditions

Girija Dharmaraj

Doctor of Philosophy

Graduate Department of Physics

University of Toronto

2013

The Earth's magnetic field is generated in its fluid outer core through dynamo action. In this process, convection and differential rotation of an electrically conducting fluid maintain the magnetic field against its ohmic decay. Using numerical models, we can investigate planetary dynamo processes and the importance of various core properties on the dynamo. In this thesis, I use numerical dynamo models in Earth-like geometry in order to understand the influence of inner core electrical conductivity and the choice of thermal and velocity boundary conditions on the resulting magnetic field. I demonstrate how an electrically conducting inner core can reduce the frequency of reversals and produce axial-dipolar dominated fields in our models. I also demonstrate that a strong planetary magnetic field intensity does not imply that the dynamo operates in the strong field regime as is usually presumed. Through a scaling law analysis, I find that irrespective of the choice of thermal or velocity boundary conditions, the available power determines the magnetic and velocity field characteristics like the field strength, polarity and morphology. Also, whether a dynamo model is in a dipolar, transitional or multipolar regime is dependent on the force balance in the model. I demonstrate that the Lorentz force is balanced by the Coriolis force in the dipolar dynamo regime models resulting in magnetostrophically balanced dynamos whereas the Lorentz force is balanced by the Inertial force (and not the Coriolis force) in the multipolar dynamo regime models.

resulting in a non-magnetostrophically balanced dynamo. The generation mechanism differs between the regimes and depends on the velocity boundary conditions. The zonal flows of the stress-free models are stronger than in the no-slip models, and bistability is more prominent when stress-free boundary conditions are used. A single scaling law may be feasible for all the models, but there does appear to be some variation for models with different thermal and velocity boundary conditions. The results presented in this thesis are not only applicable to the geodynamo, but will also aid in understanding the dynamos of other planets and exoplanets.

## **Dedication**

To my loving husband

**Dr. Ankur Saxena**

and family

**Mr. S. Dharmaraj, Mrs. Jothi Dharmaraj and Mr. Anand Dharmaraj**

## Acknowledgements

First and foremost I would like to express my sincere gratitude to my advisor Dr. Sabine Stanley for her immense support, consistent encouragement, motivation, enthusiasm, patience, and a wealth of knowledge. I am most grateful to her for allowing me the flexibility in research and for providing some of the best computational and storage facilities available.

I extend my sincere thanks to my committee members, Dr. Stephen Morris and Dr. Qinya Liu for their stimulating discussion, guidance and encouragement throughout the course of my research. I would also like to thank Dr. Mathieu Dumberry for fruitful discussion on my manuscript.

I would like to thank all my friends for the interesting discussions I had with them. Special thanks are due to my friends, Snezana Prodan, Ryan Vilim, Bob Tian, Ramin Saleh, Reza Mir, Philip Joseph Heron, Keely O'Farrell and Ken Nurse for also creating a healthy fun filled office environment.

Most of all, my deepest gratitude goes to my husband, parents and my brother for their love, unquestioned support and encouragement. I owe it all to them.

I gratefully acknowledge financial support from Ontario Graduate Scholarship in Science and Technology. The numerical simulations used in this thesis were made possible by the General Purpose Cluster (GPC) at the SciNet High Performance Computing (HPC) consortium.

# Contents

<b>List of Tables</b>	<b>xii</b>
<b>List of Figures</b>	<b>xv</b>
<b>Nomenclature</b>	<b>xvi</b>
<b>1 Introduction</b>	<b>1</b>
1.1 Planetary Magnetic Fields . . . . .	1
1.2 Fundamentals of Fluid Dynamics . . . . .	8
1.3 Fundamentals of Electromagnetism . . . . .	9
1.4 Magnetohydrodynamic Approximation . . . . .	11
1.5 Governing Equations . . . . .	13
1.5.1 Fluid Flow . . . . .	13
1.5.2 Magnetic Field . . . . .	14
1.5.3 Temperature . . . . .	15
1.6 Non-Dimensional Governing equations . . . . .	16
1.7 Boundary Conditions . . . . .	18
1.7.1 Temperature Boundary Conditions . . . . .	18
1.7.2 Velocity Boundary Conditions . . . . .	18
1.7.3 Magnetic Field Boundary Conditions . . . . .	19
1.8 Thesis Overview . . . . .	19

<b>2 Numerical Model</b>	<b>21</b>
2.1 Numerical Method . . . . .	21
2.2 High Performance Computing . . . . .	24
2.3 Effect of Hyperdiffusivity . . . . .	25
2.3.1 Results . . . . .	27
Surface Magnetic Power Spectra . . . . .	27
Magnetic Energy . . . . .	28
Magnetic Field . . . . .	30
Kinetic Energy . . . . .	34
Velocity Field . . . . .	37
Nusselt number . . . . .	37
2.3.2 Conclusion . . . . .	37
2.4 Benchmarking . . . . .	40
<b>3 Effect of Inner Core Conductivity</b>	<b>47</b>
3.1 Introduction . . . . .	47
3.2 Numerical Model . . . . .	52
3.3 Results . . . . .	55
3.3.1 Dipole Tilt . . . . .	55
3.3.2 Surface Magnetic Power Spectra . . . . .	56
3.3.3 Magnetic Energy . . . . .	56
3.3.4 Magnetic Field . . . . .	58
3.3.5 Kinetic Energy . . . . .	60
3.3.6 Velocity Field . . . . .	62
3.3.7 Force Balance . . . . .	64
3.3.8 Magnetic Braking . . . . .	68
3.4 Discrepancy Between Studies . . . . .	70
3.5 Conclusions . . . . .	73

<b>4 Scaling Laws and Effect of Boundary Conditions</b>	<b>75</b>
4.1 Introduction . . . . .	75
4.1.1 Dynamo scaling laws . . . . .	76
4.1.2 The influence of boundary conditions . . . . .	77
Thermal boundary conditions . . . . .	77
Velocity Boundary Conditions . . . . .	78
4.1.3 Dynamo generation mechanisms . . . . .	79
4.2 Numerical Model . . . . .	81
4.3 Results . . . . .	81
4.3.1 Dynamo Regimes and Scaling Laws . . . . .	82
Dynamo Regimes . . . . .	82
Heat Transport . . . . .	85
Fluid Dynamic Regimes . . . . .	93
4.3.2 Field Morphology, Force Balance and Generation Mechanisms . . . . .	94
Characteristic Models . . . . .	95
Surface Magnetic Power Spectra . . . . .	95
Magnetic Field . . . . .	96
Velocity Field . . . . .	100
Force Balance . . . . .	104
Match Coefficient . . . . .	104
Power Budget . . . . .	105
Dynamo Generation Mechanism . . . . .	112
Boundary Layer Dynamics Controlled by Force Balances . . . . .	121
4.3.3 Anomalous Dynamo . . . . .	123
4.4 Conclusion . . . . .	126
<b>5 Conclusions and Future Work</b>	<b>130</b>
5.1 Influence of Inner Core Conductivity . . . . .	130

5.2	Influence of Boundary Conditions on Planetary Dynamos and Scaling Laws	131
5.3	Future Research Projects . . . . .	132
5.3.1	Understanding and Predicting Planetary Magnetic Field Reversals	132
5.3.2	Anelastic Dynamo Model . . . . .	133
<b>A</b>	<b>Control Parameters</b>	<b>136</b>
A.1	Input Control Parameters . . . . .	136
A.2	Output Control Parameters . . . . .	137
A.2.1	Nusselt number calculation for fixed heat flux and fixed temperature boundary conditions . . . . .	138
	Relationship between $Ra_{flux}$ and $Ra_{tem}$ . . . . .	144
	Computing $\overline{\Delta\Theta}$ . . . . .	144
<b>B</b>	<b>Spherical Harmonic Expansions of Magnetic and Velocity Fields</b>	<b>146</b>
B.1	Magnetic Field Expansion . . . . .	146
B.1.1	First Derivatives of Fields . . . . .	150
B.1.2	Second Derivatives of Fields . . . . .	152
B.1.3	Current . . . . .	159
	Current Derivatives . . . . .	161
B.2	Velocity Field Expansion . . . . .	164
<b>C</b>	<b>Force</b>	<b>165</b>
C.1	Lorentz Force . . . . .	165
C.1.1	Curl of Lorentz Force . . . . .	166
C.2	Coriolis Force . . . . .	166
C.2.1	Curl of the Coriolis Force ( $\mathbf{F}_C$ ) in Spherical Coordinates . . . . .	167
C.3	Inertial Force . . . . .	169
C.4	Viscous Force . . . . .	170
C.5	Dynamo Generation Term . . . . .	172

C.6	Dynamo Creation Term	174
<b>D</b>	<b>Benchmark</b>	<b>176</b>
D.1	Non-dimensionalization and Conversion of Control Parameters	177
D.2	Computing Energy Density in the Kuang-Bloxham Model	177
D.3	Conversion of Christensen's Initial Magnetic & Temperature Field to Kuang-Bloxham	180
D.3.1	Initial Magnetic Field	180
	Axisymmetric Poloidal Magnetic Field	183
	Axisymmetric Toroidal Magnetic Field	184
D.3.2	Initial Velocity Field	185
D.3.3	Initial Temperature Field	185
	Conductive State	185
	Conductive state and 4 <sup>th</sup> order and 4 <sup>th</sup> degree temperature perturbation	185
<b>E</b>	<b>Coordinate Transformation</b>	<b>188</b>
E.1	Spherical to Cartesian	188
E.2	Derivative of unit vectors in spherical coordinates	192
<b>F</b>	<b>Tables</b>	<b>194</b>
<b>G</b>	<b>Power-Law Implications</b>	<b>204</b>
	<b>Bibliography</b>	<b>229</b>

# List of Tables

2.1	Hyperdiffusivity Results of Dynamo Models . . . . .	26
2.2	Benchmark Results . . . . .	41
3.1	Results of CIC and IIC Models . . . . .	55
4.1	Scaling Laws for dynamo and non-magnetic convection models. The subscript C denotes convection models. $\Delta a$ and $\Delta b$ are standard errors in the the offset or Y-intercept ( $a$ ) and slope ( $b$ ) respectively. These power laws are obtained for models with $Nu > 2$ and $E < 3e - 4$ . Dipolar dynamo models have $f_{Dip} > 0.35$ and multipolar dynamo models have $f_{Dip} < 0.35$ . Ignore the polarity for convection models. . . . .	88
D.1	Non-Dimensionalization . . . . .	177
D.2	Input Control Parameters Conversion . . . . .	178
D.3	Output Control Parameters Conversion . . . . .	179
F.1	Results of Dynamo Models for Hyperdiffusivity . . . . .	195
F.2	Results of Dynamo Models for Scaling Laws and Influence of Boundary Conditions . . . . .	196
F.3	Results of Convection Models for Scaling Laws and Influence of Boundary Conditions . . . . .	201
G.1	Known physical properties . . . . .	204

G.2	Thermodynamic and transport properties . . . . .	205
G.3	Scaling Laws Implications. The multipolar values are mentioned for reference and does not apply to Earth. . . . .	208
G.4	Scaling Laws Implications. The multipolar values are mentioned for reference and does not apply to Earth. . . . .	218

# List of Figures

1.1	Illustration of Earth's interior	5
1.2	Schematic view of the core geometry	6
2.1	Illustration of canonical poloidal and toroidal magnetic field	23
2.2	Surface magnetic power spectra for fixed flux and no-slip models with different hyperdiffusivities	29
2.3	Magnetic Energy vs Hyperdiffusivity	31
2.4	Magnetic energy for fixed flux and no-slip models with different hyperdiffusivities	32
2.5	Axisymmetric magnetic fields for fixed flux and no-slip models with different hyperdiffusivities	33
2.6	Kinetic Energy vs Hyperdiffusivity	35
2.7	Kinetic energy for fixed flux and no-slip models with different hyperdiffusivities	36
2.8	Axisymmetric velocity fields for fixed flux and no-slip models with different hyperdiffusivities	38
2.9	Nusselt number vs Hyperdiffusivity	39
2.10	Initial magnetic field for benchmarking	42
2.11	Benchmarking Non-magnetic Convection Model	43
2.12	Benchmarking Conducting Inner Core Dynamo Model	44
2.13	Benchmark Illustrative Solution for Comparison	45

3.1	Anchoring Effect: Illustration of the Frozen-in-field Theorem . . . . .	50
3.2	Dipole Tilt versus Time for CIC and IIC models . . . . .	56
3.3	Surface Magnetic Power Spectra for CIC and IIC models . . . . .	57
3.4	Magnetic Energy versus Time for CIC and IIC models . . . . .	59
3.5	Radial Magnetic Field at the CMB for CIC and IIC models . . . . .	60
3.6	Axisymmetric Magnetic Field for CIC and IIC models . . . . .	61
3.7	Kinetic Energy versus Time for CIC and IIC models . . . . .	63
3.8	Axisymmetric Velocity Fields for CIC, IIC and non-magnetic convection models . . . . .	65
3.9	Force Balance for CIC and IIC models . . . . .	69
3.10	Magnetic Braking for CIC and IIC models . . . . .	70
4.1	Relative dipole strength and magnetic energy versus local Rossby number	84
4.2	Nusselt number versus Rayleigh number scaling . . . . .	86
4.3	Rossby # versus modified flux based Rayleigh # scaling . . . . .	94
4.4	Surface magnetic power spectra . . . . .	96
4.5	Radial magnetic field at the CMB . . . . .	98
4.6	Axisymmetric magnetic field . . . . .	99
4.7	Axisymmetric velocity field for dynamo models . . . . .	102
4.8	Axisymmetric velocity field for non-magnetic convection models . . . . .	103
4.9	Force balance . . . . .	106
4.10	Power Budget for dynamo models . . . . .	108
4.11	Power Budget for non-magnetic convection models . . . . .	109
4.12	RMS Force Integrals . . . . .	110
4.13	RMS Force Integrals of the $\phi$ component . . . . .	111
4.14	Illustration of $\alpha$ effect (Parker loop mechanism) . . . . .	114
4.15	Illustration of $\omega$ effect . . . . .	115
4.16	Illustration of $\vec{B}_P$ generation from $\vec{B}_T$ through columnar convection . . .	116

4.17	$\omega$ Effect . . . . .	117
4.18	Match coefficient of $\alpha$ and $\omega$ effects versus local Rossby # . . . . .	118
4.19	Dynamo generation mechanism . . . . .	119
4.20	Boundary Layer Thickness versus Nusselt Number . . . . .	123
4.21	Temperature profile for estimating boundary layer thickness . . . . .	124
4.22	Velocity profile for estimating boundary layer thickness . . . . .	125
4.23	Anomalous dynamo results . . . . .	127
E.1	Spherical Polar Coordinates . . . . .	189
E.2	Spherical to Cartesian Coordinates . . . . .	190
G.1	Our estimates for Earth: Ohmic Dissipation ( $D_\eta$ ) = 0.4 - 1 TW and Magnetic Dissipation Time ( $\tau_\eta$ ) = 20.3 yrs. (top) $Lo/f_{ohm}^{1/2}$ vs $Ra_Q^*$ . (bottom) $\tau_{diss}^*$ vs $Rm$ . . . . .	216

# Nomenclature

## List of Abbreviation

CIC	Conducting inner core
CMB	Core mantle boundary
FFNS	Fixed flux and no-slip
$\text{FFNS}_C$	Fixed flux and no-slip of non-magnetic convection models
FFSF	Fixed flux and stress-free
$\text{FFSF}_C$	Fixed flux and stress-free of non-magnetic convection models
FTNS	Fixed temperature and no-slip
$\text{FTNS}_C$	Fixed temperature and no-slip of non-magnetic convection models
FTSF	Fixed temperature and stress-free
$\text{FTSF}_C$	Fixed temperature and stress-free of non-magnetic convection models
ICB	Inner core boundary
IIC	Insulating inner core

## List of Symbols

$\alpha_T$	Coefficient of thermal expansion
$\delta_E$	Ekman boundary layer thickness
$\delta_T$	Thermal boundary layer thickness
$\eta$	Magnetic diffusivity
$\eta_{io}$	Ratio of inner to outer core magnetic diffusivity
$\eta_i$	Magnetic diffusivity at inner core
$\eta_o$	Magnetic diffusivity at outer core
$\kappa$	Thermal diffusivity
$\kappa_0, \eta_0, \nu_0$	Constant values that depend on the choice of control parameters
$\hat{\phi}$	Unit vector in the $\phi$ direction
$\hat{\theta}$	Unit vector in the $\theta$ direction
$\hat{\mathbf{r}}$	Unit vector in the radial direction
$\hat{\mathbf{z}}$	Unit vector in the direction of the rotation axis
$\mu_0$	Magnetic permeability of free space
$\nu$	Kinematic viscosity
$\Omega$	Rotation rate
$\Phi$	Scalar potential
$\rho$	Density
$\sigma$	Electrical conductivity

$\tau$	Magnetic diffusion time
$\Theta$	Temperature perturbation field
$\Delta T$	Temperature difference between the inner and outer core boundaries
$\vec{B}$	Magnetic field
$\vec{B}_P$	Poloidal magnetic field
$\vec{B}_P^{Axi}$	Axisymmetric poloidal magnetic field
$\vec{B}_P^{NAxi}$	Non-axisymmetric poloidal magnetic field
$\vec{B}_r$	Radial component of the magnetic field
$\vec{B}_T$	Toroidal magnetic field
$\vec{B}_T^{Axi}$	Axisymmetric toroidal magnetic field
$\vec{B}_T^{NAxi}$	Non-axisymmetric toroidal magnetic field
$\vec{B}_\phi$	Longitudinal component of the magnetic field
$\vec{B}_\theta$	Latitudinal component of the magnetic field
$\vec{v}$	Velocity field
$\vec{v}_P$	Poloidal velocity field
$\vec{v}_P^{Axi}$	Axisymmetric poloidal velocity field
$\vec{v}_P^{NAxi}$	Non-axisymmetric poloidal velocity field
$\vec{v}_r$	Radial component of the velocity field
$\vec{v}_T$	Toroidal velocity field
$\vec{v}_T^{Axi}$	Axisymmetric toroidal velocity field

$\vec{v}_T^{N\ Axi}$	Non-axisymmetric toroidal velocity field
$\vec{v}_\phi$	Longitudinal component of the velocity field
$\vec{v}_\theta$	Latitudinal component of the velocity field
$a$	Radius of the planet
$D = r_o - r_i$	Shell thickness
$E$	Ekman number
$E_B$	Magnetic energy
$E_k$	Kinetic energy
$E_{B_P^{Axi}}$	Axisymmetric poloidal magnetic energy
$E_{B_P^{N\ Axi}}$	Non-axisymmetric poloidal magnetic energy
$E_{B_P}$	Poloidal magnetic energy
$E_{B_T^{Axi}}$	Axisymmetric toroidal magnetic energy
$E_{B_T^{N\ Axi}}$	Non-axisymmetric toroidal magnetic energy
$E_{B_T}$	Toroidal magnetic energy
$E_{v_P^{Axi}}$	Axisymmetric poloidal kinetic energy
$E_{v_P^{N\ Axi}}$	Non-axisymmetric poloidal kinetic energy
$E_{v_P}$	Poloidal kinetic energy
$E_{v_T^{Axi}}$	Axisymmetric toroidal kinetic energy
$E_{v_T^{N\ Axi}}$	Non-axisymmetric toroidal kinetic energy
$E_{v_T}$	Toroidal kinetic energy

$g_l^m, h_l^m$	Gauss coefficients for each spherical harmonic degree and order
$g_o$	Gravitational acceleration at $r_o$
$h_T$	Incoming heat flux at the inner core boundary
$l$	Spherical harmonic degree
$l_0$	Constant value that lies between (1 to $L_{max}$ )
$l_B$	Length scale of magnetic field
$l_v$	Length scale of velocity field
$L_{max}$	Maximum value of spherical harmonic degree
$m$	Spherical harmonic order
$M_\alpha$	Match coefficient of $\alpha$ effect that creates $\vec{B}_T$ and total creation term of $\vec{B}_T$
$M_\omega$	Match coefficient of $\omega$ effect that creates $\vec{B}_T$ and total creation term of $\vec{B}_T$
$M_{LC}$	Match coefficient of Lorentz force and Coriolis force
$M_{max}$	Maximum value of spherical harmonic order
$Nu$	Nusselt number
$Nu^*$	Modified Nusselt number
$p(l, m, r)$	Power in each spherical harmonic degree and order
$P_l^m$	Schmidt normalized associated Legendre polynomial
$q_k$	Roberts number
$r, \theta, \phi$	Radial distance, latitude and longitude in spherical coordinate system
$r_{io}$	Ratio of inner to outer core radius

$r_i$	Inner core radius
$r_o$	Outer core radius
$Ra_C$	Critical Rayleigh number
$Ra_Q^*$	Modified flux based Rayleigh number
$Ra_{FF}$	Modified Rayleigh number (fixed heat flux)
$Ra_{FT}$	Modified Rayleigh number (fixed temperature)
$Ro$	Rossby number
$Ro_l$	Local Rossby number
$Ro_M$	Magnetic Rossby number
$T$	Temperature field
$T_0(r)$	Background state temperature solution
$V$	Non-dimensional volume of the outer core

# <sup>1</sup> Chapter 1

## <sup>2</sup> Introduction

### <sup>3</sup> 1.1 Planetary Magnetic Fields

<sup>4</sup> It is important to study the Earth's magnetic field as it shields us from cosmic radiation,  
<sup>5</sup> solar winds and magnetic storms. It is a crucial component in our understanding of  
<sup>6</sup> how adverse solar wind interaction with Earth's magnetosphere can cause disruption of  
<sup>7</sup> satellite operations and electric power grids causing socioeconomic losses [Kerr, 2009].  
<sup>8</sup> It can be used for orientation and navigation, not just by humans, but also by birds,  
<sup>9</sup> animals and bacteria that use their inbuilt compass capability for migration [Johnsen  
<sup>10</sup> and Lohmann, 2005]. Earth science applications also make use of Earth's magnetic field  
<sup>11</sup> history, like a geophysical correlation technique called magneto-stratigraphy, used to date  
<sup>12</sup> sedimentary and volcanic sequences. Studying the Earth's magnetic field strength, mor-  
<sup>13</sup> phology, generation mechanism and evolution can provide vital information about its  
<sup>14</sup> interior structure and thermal evolution that is not observable from spacecraft.

<sup>15</sup>

<sup>16</sup> Over the past 40 years, a series of spacecraft missions have significantly enhanced our  
<sup>17</sup> knowledge of planetary magnetic fields in the solar system, including some moons. Mer-  
<sup>18</sup> cury, Earth, Jupiter, Saturn, Uranus, Neptune and Ganymede have actively-generated,

<sup>19</sup> global-scale magnetic fields, while Mars, Earth and Earth's moon have crustal magnetic  
<sup>20</sup> fields most likely due to magnetic field generation in their pasts.

<sup>21</sup>

<sup>22</sup> The observed global magnetic fields in planets cannot be due to permanent magnetism  
<sup>23</sup> since the temperatures in planetary cores are well above the Curie temperature. In  
<sup>24</sup> the absence of a self-sustained magnetic field generation mechanism, the field strength  
<sup>25</sup> would decay by a factor of  $e$  every magnetic diffusion time (for Earth it is approximately  
<sup>26</sup> 20,000 years). These global magnetic fields are generated by dynamo action, an idea  
<sup>27</sup> conceived by Larmor [1919]. The necessary components needed for planetary magnetic  
<sup>28</sup> field generation through a self sustained dynamo are as follows:

- <sup>29</sup> • an electrically conducting fluid layer in the planet's interior, like an iron core  
<sup>30</sup> • an energy supply to churn the fluid against loss due to Ohmic dissipation, like  
<sup>31</sup> thermal or compositional convection, precession or tidal interaction etc.  
<sup>32</sup> • planetary rotation, even though not a necessity for convective dynamos helps to  
<sup>33</sup> organize the fluid motion to provide a large scale field. On the other hand, rotation  
<sup>34</sup> is the ultimate energy source for dynamos driven by precession or tidal interaction  
<sup>35</sup> [Tilgner, 2007].

<sup>36</sup> Other possible explanations for the global fields, such as the thermoelectric effect, mag-  
<sup>37</sup> netic monopoles etc. have been proposed as potential mechanisms but they are either  
<sup>38</sup> not physically valid or produce weak fields that have not been observed yet [Stevenson,  
<sup>39</sup> 2007]. In this thesis we will focus on thermal convection driven dynamos.

<sup>40</sup>

<sup>41</sup> The planets in our solar system can be divide into three subgroups (adopted from [Steven-  
<sup>42</sup> son, 2003]):

- <sup>43</sup> 1. **Terrestrial planets** (and moons) with rocky interiors: Mercury, Venus, Earth,  
<sup>44</sup> Earth's moon, Mars and Jupiter's largest moon Ganymede etc.

45      2. **Gas giants:** Jupiter and Saturn that are mainly composed of hydrogen and helium,  
46                    and

47     3. **Ice giants:** Uranus and Neptune that have deep gaseous atmospheres that are  
48                 mainly composed of water ( $H_2O$ ), ammonia ( $NH_3$ ) and methane ( $CH_4$ ).

<sup>49</sup> The magnetic field morphologies of planets and moons in our solar system can be divided  
<sup>50</sup> into five subgroups (adopted from [Stanley \[2004\]](#)):

## 51 1. Strong axially dipolar dominated fields: Earth, Jupiter and Saturn

## 52 2. Weak axially dipolar dominated fields: Mercury

### 3. Strong non-dipolar, non-axisymmetric fields: Uranus and Neptune

## 5. Local crustal magnetic fields: Mars, Earth and Earth's moon.

57 From current observations, we know that Ganymede has an internally generated mag-  
58 netic field but we don't know enough to categorize it, i.e. it could have a large multipolar  
59 component that has not been observed yet, so it could fit in category 1 or 3. Mars' strong  
60 remanent magnetism was discovered by the Mars Global Surveyor Mission [Acuña et al.,  
61 1999]. So, it most likely had a dynamo between 4.5 to 3.9 Ga but ceased to exist [Stanley  
62 and Glatzmaier, 2009]. Earth's moon has patches of crustal magnetization (rock samples  
63 brought back by the Apollo missions bear evidence). The moon has a solid inner core  
64 and a fluid outer core but does not have a dynamo at present as the fluid outer core may  
65 be subadiabatic and stably stratified [Weber et al., 2011]. Venus may or may not have  
66 had a dynamo in its history. So far we have not been able to measure any presence of its  
67 internal magnetic field.

<sup>69</sup> The reason why planets in our solar system have different magnetic field morphologies is  
<sup>70</sup> because they have different convective region geometries and are either in different stages  
<sup>71</sup> of evolution or have evolved differently [Stanley and Bloxham, 2004, Stanley, 2004].

<sup>72</sup>

<sup>73</sup> We know most about the Earth as we live on it and have easy access to it, and thus  
<sup>74</sup> have accumulated a wealth of information about its past. We will begin by examining  
<sup>75</sup> the Earth's magnetic field to understand its characteristics. The Earth's magnetic field,  
<sup>76</sup> also known as the geomagnetic field, is mainly dipolar with a strong symmetry about  
<sup>77</sup> its rotation axis. The magnetic north pole, i.e, where magnetic field lines exit Earth is  
<sup>78</sup> in the southern hemisphere and the magnetic south pole, i.e. where the field lines enter  
<sup>79</sup> Earth is in the northern hemisphere. The magnetic poles are not perfectly aligned with  
<sup>80</sup> the geographic poles, but instead, the magnetic dipole axis is tilted at an angle of 11.5  
<sup>81</sup> degrees with respect to the rotation axis. The strength of the field ranges from 25,000 nT  
<sup>82</sup> to 65,000 nT (0.25 G to 0.65 G) on Earth's surface. It is 4.2 to 4.4 billion years old [Tar-  
<sup>83</sup> duno et al., 2012] and has maintained its intensity to the same order of magnitude as the  
<sup>84</sup> present field, as known through aircraft and satellite surveys, surface and oceanographic  
<sup>85</sup> observatories, ship logs, and paleomagnetic records [Merrill et al., 1996]. The observed  
<sup>86</sup> field varies on timescales ranging from milliseconds to millions of years. Variations over  
<sup>87</sup> timescales that range between a year to hundreds of years (e.g. westward drifting flux  
<sup>88</sup> spots) are called geomagnetic secular variation and are caused by internal dynamics of  
<sup>89</sup> the fluid outer core. The shorter timescale variations occur due to external sources such  
<sup>90</sup> as currents flowing in the ionosphere and magnetosphere giving rise to magnetic storms.  
<sup>91</sup> The geomagnetic field also chaotically reverses its polarity in time which takes a few  
<sup>92</sup> thousand years to complete and the rate of reversals change over time [Merrill et al.,  
<sup>93</sup> 1996]. Using this information we can attempt to determine what these characteristic  
<sup>94</sup> properties tell us about Earth's interior.

<sup>95</sup>

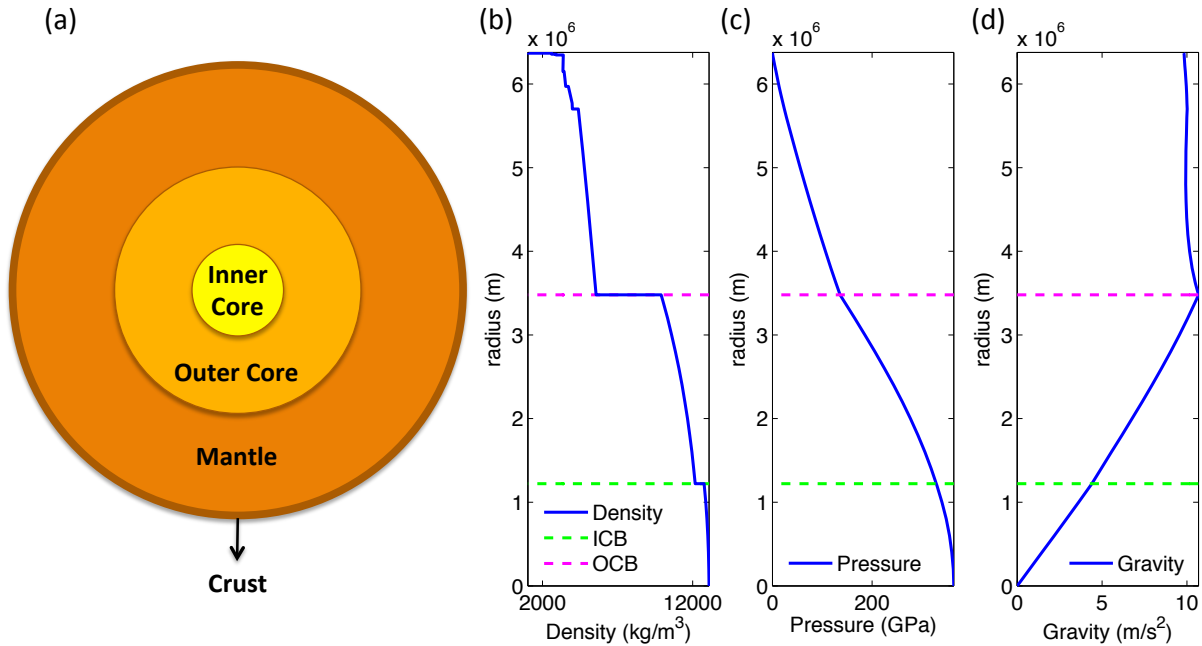


Figure 1.1: **Earth’s interior:** (a) Illustration, Radius versus (b) density, (c) pressure and (d) gravity plotted using the 1D Preliminary Reference Earth Model (PREM) from Dziewonski and Anderson [1981]. ICB and OCB are inner and outer core boundary respectively.

96 In order to understand where the Earth’s magnetic field originates from, we will examine  
 97 its interior structure. Figure 1.1 shows an illustration of the interior structure of Earth.  
 98 It is layered in spherical shells. The outermost layer is a solid silicate crust, then comes  
 99 the thickest layer of Earth, the highly viscous mantle (silicate rocks that are rich in iron  
 100 and magnesium), then the liquid outer core and the solid inner core, both of which are  
 101 mainly composed of iron, some nickel and other impurities like sulphur and oxygen.

102

103 For the Earth, the electrically conducting region for dynamo generation corresponds to  
 104 the fluid outer core that surrounds the solid inner core. Although the Earth’s inner core  
 105 occupies only about 4 % of the total core volume, it has significant influences on core  
 106 dynamics. The solid inner core acts as a barrier to fluid flow since the flow structure  
 107 must take into account the presence of the inner core boundary. In addition, due to  
 108 the Taylor-Proudman constraint [Proudman, 1916, Taylor, 1917, Proudman, 1956] fluid

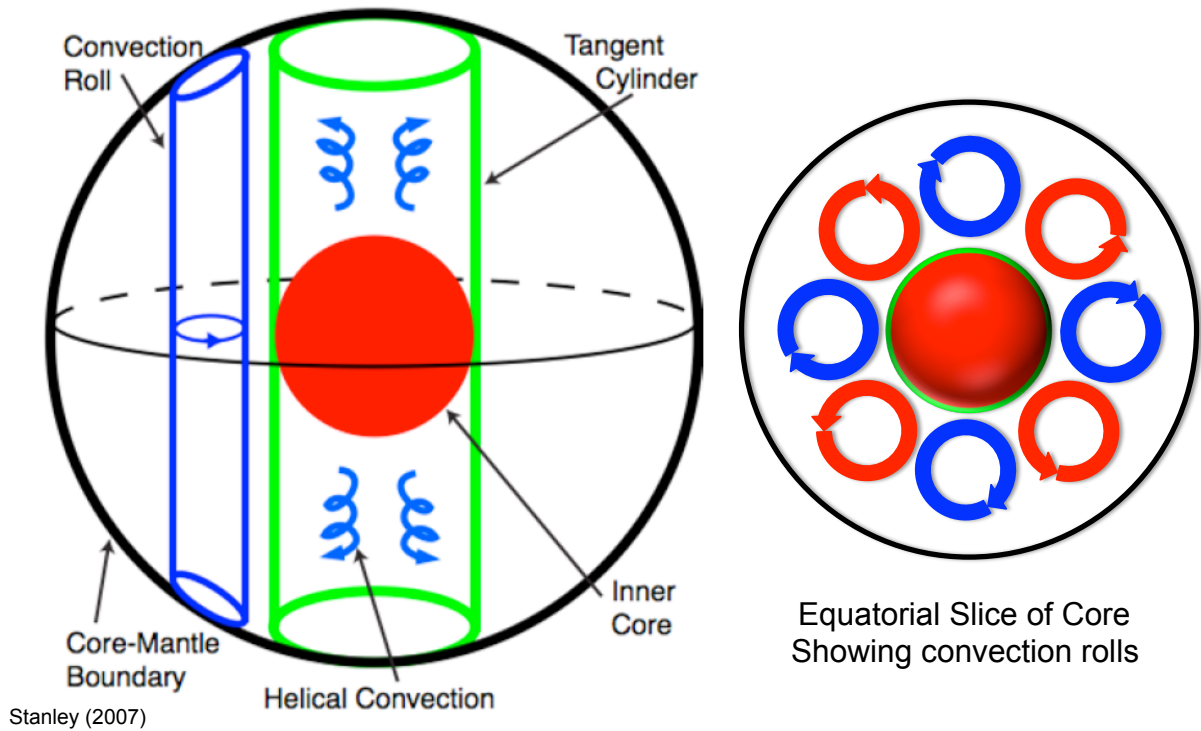


Figure 1.2: Schematic view of the core geometry: In both plots the solid inner core is shown in red, the core mantle boundary (CMB) is the solid black circle and the tangent cylinder is shown in green. In the left plot, the different convection modes are shown in blue inside and outside the tangent cylinder. The right plot shows an equatorial slice of the core showing pairs of convection rolls.

flows are largely confined to regions inside or outside the tangent cylinder (an imaginary cylinder that is co-axial with the rotation axis and tangent to the inner core boundary) as shown in figure 1.2. The fluid inside the tangent cylinder includes both small and large scale convective motions. The small scale convective motions consist of helical plumes, whereas the large scale flows consists of a rising motion close to the poles and a descending motion close to the tangent cylinder in the meridional direction. Computational and laboratory experiments have investigated the influence of the tangent cylinder on core dynamics e.g. [Hollerbach, 1994, Olson and Aurnou, 1999, Aurnou et al., 2003, Sreenivasan and Jones, 2005, 2006a]. When simulating the geodynamo, it is necessary to model a spherical shell rather than a full sphere in order to capture the effects of the inner core on the fluid dynamics of a rapidly rotating spherical shell.

120

The inner core can also influence the dynamo generation through its finite electrical conductivity. Magnetic field lines that diffuse from the fluid outer core into the solid inner core are governed by the slower magnetic diffusion time scale in the inner core rather than the advective time scale of the outer core. This suggests that the inner core may have a stabilizing influence on magnetic field variability and could affect reversals and excursions in planetary cores.

127

Studying core dynamics and dynamo processes is aided through numerical models and laboratory experiments. Most of the control parameters used in numerical dynamo models are far from realistic. Thus, their usefulness may be restricted to understanding the generation mechanism of the geomagnetic field at a larger scale. Laboratory dynamo experiments are capable of reaching some realistic parameter values and thus aid in understanding turbulence locally. In the past few decades, three-dimensional numerical geodynamo models driven by convection in rotating spherical shells have been successful in generating some of the basic properties of the observed geomagnetic field, such as, the

<sup>136</sup> field's dipole dominance, approximate strength and reversal statistics, for a range of pa-  
<sup>137</sup> rameters, and irrespective of the choice of boundary conditions and inner core electrical  
<sup>138</sup> conductivity. However, it is known that dynamo simulations with different parameter  
<sup>139</sup> values and boundary conditions result in different force balances and energetics.

## <sup>140</sup> 1.2 Fundamentals of Fluid Dynamics

<sup>141</sup> The theory of fluid dynamics was descriptive until Newton published his *Philosophiae*  
<sup>142</sup> *Naturalis Principia Mathematica* in 1687. We begin with his second law of dynamics  
<sup>143</sup> that relates acceleration of a particle to the force exerted on it:

$$\vec{F} = m\vec{a} \quad (1.1)$$

<sup>144</sup> where,  $\vec{F}$  is force,  $m$  is mass and  $\vec{a}$  is acceleration.

<sup>145</sup>

<sup>146</sup> In 1757, Euler generalized Newton's second law to a continuous medium with no internal  
<sup>147</sup> shear stress, published in his *Mémoires de l'académie des sciences de Berlin*:

$$\rho \frac{\partial}{\partial t} \vec{v} + \rho(\vec{v} \cdot \nabla) \vec{v} = -\nabla p \quad (1.2)$$

<sup>148</sup> by taking into account his discovery of the continuity equation:

$$\frac{\partial}{\partial t} \rho + \nabla \cdot (\rho \vec{v}) = 0 \quad (1.3)$$

<sup>149</sup> where,  $\rho$  is fluid density,  $t$  is time,  $\vec{v}$  is fluid velocity and  $p$  is pressure.

<sup>150</sup>

<sup>151</sup> In 1821, Navier accounted for dissipation and modified Euler's equation as follows:

$$\rho \frac{\partial}{\partial t} \vec{v} + \rho(\vec{v} \cdot \nabla) \vec{v} = -\nabla p + \mu \nabla^2 \vec{v} \quad (1.4)$$

<sup>152</sup> where,  $\mu$  is dynamic viscosity.

<sup>153</sup>

<sup>154</sup> In 1845, Stokes introduced the concept of internal shear stress and developed the mathematical tools needed to explain it in the Navier-Stokes equation (equation 1.4), as published in his *On the theories of the internal friction of fluids in motion*.

### <sup>157</sup> 1.3 Fundamentals of Electromagnetism

<sup>158</sup> Research in electricity was made possible by the invention of the “voltaic pile” or the  
<sup>159</sup> battery in the 1800’s by Volta. In 1820, Ampère made the link between electricity and  
<sup>160</sup> magnetism by showing how electric currents could produce magnetic fields. In 1827, Ohm  
<sup>161</sup> discovered the law of electrical conduction and published it in his book, *Die galvanische*  
<sup>162</sup> *Kette, mathematisch bearbeitet*:

$$\vec{J} = \sigma \vec{E} \quad (1.5)$$

<sup>163</sup> where  $\vec{J}$  is current density,  $\sigma$  is electrical conductivity and  $\vec{E}$  is electric field.

<sup>164</sup>

<sup>165</sup> If an external magnetic field is present and the conductor is moving then we have to  
<sup>166</sup> account for the current induced by the Lorentz force (combined electric and magnetic  
<sup>167</sup> force applied to a charge) on the charge carriers:

$$\vec{f}_L = \vec{f}_E + \vec{f}_B = Q(\vec{E} + \vec{v} \times \vec{B}) \quad (1.6)$$

<sup>168</sup> Where,  $\vec{f}_L$ ,  $\vec{f}_E$  and  $\vec{f}_B$  are the Lorentz, electric and magnetic forces,  $Q$  is charge, and  $\vec{v}$   
<sup>169</sup> and  $\vec{B}$  are velocity and magnetic fields.

<sup>170</sup>

<sup>171</sup> In this thesis we will be using Lorentz force per unit volume,  $\vec{F}_L = \vec{f}_L/V$  (where V is the  
<sup>172</sup> volume) , which can be obtained by using charge density,  $\rho_e = Q/V$  and  $\vec{J} = \rho_e \vec{v}$ :

$$\vec{F}_L = \rho_e \vec{E} + \vec{J} \times \vec{B} \quad (1.7)$$

<sup>173</sup> In most materials,  $\vec{J}$  is proportional to force per unit charge ( $\vec{f}_L/Q$ ), so

$$\text{Ohm's Law : } \vec{J} = \sigma(\vec{E} + \vec{v} \times \vec{B}) \quad (1.8)$$

<sup>174</sup> In 1831, Faraday discovered the law of induction and showed that varying magnetic flux  
<sup>175</sup> across a loop could produce difference in electric potential. In 1855 and 1856, Maxwell  
<sup>176</sup> extended Faraday's work and put together a set of partial differential equations that form  
<sup>177</sup> the foundation of classical electrodynamics:

$$\text{Gauss's Law : } \nabla \cdot \vec{E} = \frac{\rho_e}{\epsilon_0} \quad (1.9)$$

i.e. charged particles create an electric field

$$\text{Gauss's Magnetism Law : } \nabla \cdot \vec{B} = 0 \quad (1.10)$$

i.e. there are no magnetic monopoles

$$\text{Faraday's Law : } \nabla \times \vec{E} = -\frac{\partial}{\partial t} \vec{B} \quad (1.11)$$

i.e. a changing magnetic field creates an electric field

$$\text{Ampère-Maxwell Law : } \nabla \times \vec{B} = \mu_0 \vec{J} + \frac{1}{c^2} \frac{\partial}{\partial t} \vec{E} \quad (1.12)$$

i.e. currents and changing electric fields create magnetic fields

<sub>178</sub> where,  $\epsilon_0$  is free space permittivity  $\approx 8.85 \times 10^{-12}$  Farads/m,  $\mu_0$  is free space permeability  
<sub>179</sub>  $= 4\pi \times 10^{-7}$  Henry/m, and  $c$  is the speed of light  $= \frac{1}{\sqrt{\mu_0\epsilon_0}}$ .

## <sub>180</sub> 1.4 Magnetohydrodynamic Approximation

<sub>181</sub> In this section, using the magnetohydrodynamic (MHD) approximation, we will neglect  
<sub>182</sub> terms in Maxwell's equations that are insignificant to our study of planetary dynamos.  
<sub>183</sub> We define the characteristic scales as follows:

<sub>184</sub>

<sub>185</sub>  $B$ : Magnetic field scale

<sub>186</sub>  $E$ : electric field scale

<sub>187</sub>  $U$ : velocity field scale

<sub>188</sub>  $L$ : Length scale

<sub>189</sub>  $\tau$ : Time scale

<sub>190</sub>

<sub>191</sub> Using these characteristic scales in Faraday's law (equation 1.11) gives:

$$\frac{E}{L} \approx \frac{B}{\tau} \implies E \approx \frac{BL}{\tau} \quad (1.13)$$

<sub>192</sub> Using characteristic scales and the expression for  $E$  as given in equation 1.13, the dis-  
<sub>193</sub> placement current term in Ampère-Maxwell's law can be approximated as:

$$\frac{1}{c^2} \frac{E}{\tau} \approx \frac{1}{c^2} \frac{BL}{\tau^2} \quad (1.14)$$

<sub>194</sub> Comparing the size of the left-hand-side and the last term on the right-hand-side of the  
<sub>195</sub> Ampère-Maxwell's law (equation 1.12) we get:

$$\frac{\frac{1}{c^2} \frac{BL}{\tau^2}}{\frac{B}{L}} \approx \frac{\left(\frac{L}{\tau}\right)^2}{c^2} \quad (1.15)$$

<sup>196</sup> So, the displacement current can be neglected if:

$$\frac{L}{\tau} = U \ll c \quad (1.16)$$

<sup>197</sup> i.e. if the velocities in the core are smaller than the speed of light then we can neglect the  
<sup>198</sup> displacement current term in Ampère-Maxwell's law. The velocities in planetary cores  
<sup>199</sup> are of the order of mm/s (e.g. for Earth the characteristic large scale velocity in the core  
<sup>200</sup> is  $\approx 0.5$  mm/s [Roberts and Glatzmaier, 2000]), so we can neglect these terms and use  
<sup>201</sup> the pre-Maxwell version of Ampère's law:

$$\nabla \times \vec{B} = \mu_0 \vec{J} \quad (1.17)$$

<sup>202</sup> We can also neglect terms in the Lorentz force by using this approximation. Gauss's law  
<sup>203</sup> (equation 1.9) and the pre-Maxwell version of Ampère's law can be estimated as:

$$\frac{E}{L} \approx \frac{\rho_e}{\epsilon_0} \implies \rho_e = \frac{\epsilon_0 E}{L} \quad (1.18)$$

$$\frac{B}{\mu_0 L} \approx \vec{J} \quad (1.19)$$

<sup>204</sup> Comparing the size of the terms on the right-hand-side of the Lorentz force (equation  
<sup>205</sup> 1.7), and using equations 1.13, 1.18 and 1.19 we get:

$$\frac{\frac{\epsilon_0 E^2}{L}}{\frac{B^2}{\mu_0 L}} \approx \frac{\epsilon_0 \mu_0 (\frac{BL}{\tau})^2}{B^2} \approx \frac{U^2}{c^2} \quad (1.20)$$

<sup>206</sup> As mentioned above, in planetary dynamos since  $U^2/c^2 \ll 1$ , we can neglect the electric  
<sup>207</sup> force relative to the magnetic force in the expression for the Lorentz force (equation 1.7):

$$\therefore \vec{F}_L = \vec{J} \times \vec{B} \quad (1.21)$$

## 208 1.5 Governing Equations

### 209 1.5.1 Fluid Flow

210 Using the Navier-Stokes equation and Maxwell's equations we can obtain the magnetohy-  
 211 drodynamics (MHD) governing equations. In order to have a mutual interaction between  
 212 fluid flows and electromagnetism, we will add the Lorentz force (equation 1.21) to the  
 213 Navier-Stokes equation. Using the Navier-Stokes equation with the Lorentz force in a  
 214 gravity field, the compressible fluid flow is governed by the following two equations:

215

216 Conservation of Mass as given in equation 1.3

217 Momentum Equation:

$$\rho \left( \frac{\partial}{\partial t} + \vec{v} \cdot \nabla \right) \vec{v} + 2\rho \vec{\Omega} \times \vec{v} = -\nabla p + \rho \vec{g} + \rho \nu \nabla^2 \vec{v} + \frac{1}{3} \rho \nu \nabla (\nabla \cdot \vec{v}) + \vec{J} \times \vec{B} \quad (1.22)$$

218 where,  $\vec{\Omega}$  is the planetary rotation rate,  $p$  is the modified pressure that includes centrifu-  
 219 gal force,  $\vec{g}$  is the gravitational acceleration, and  $\nu$  is the kinematic viscosity.

220

221 When studying planetary dynamos, it is common to consider perturbations about the  
 222 hydrostatic state and to use the Boussinesq approximation to simplify the equations (1.3  
 223 and 1.22) which assumes that the fluid is incompressible except for its effects on thermal  
 224 buoyancy. This results in the following equations:

$$\nabla \cdot \vec{v} = 0 \quad (1.23)$$

$$\underbrace{\rho_0 \left( \frac{\partial}{\partial t} + \vec{v} \cdot \nabla \right) \vec{v}}_{Inertia} + \underbrace{2\rho_0 \vec{\Omega} \times \vec{v}}_{Coriolis} = \underbrace{-\nabla \tilde{p}}_{Pressure} + \underbrace{\Delta \rho \vec{g}}_{Buoyancy} + \underbrace{\rho_0 \nu \nabla^2 \vec{v}}_{Viscous} + \underbrace{\vec{J} \times \vec{B}}_{Lorentz} \quad (1.24)$$

225 where,  $\tilde{p}$  is the modified non-hydrostatic pressure,  $\rho_0$  is constant average fluid density,  
 226 and  $\Delta \rho$  is density variation in terms of temperature perturbation.

$$\Delta\rho = -\rho_0\alpha_T\Theta \quad (1.25)$$

227 where,  $\alpha_T$  is coefficient of thermal expansion and  $\Theta$  is temperature perturbation about  
228 the background state (as shown in equation 1.33).

229

230 Compositional buoyancy is modelled identically to thermal buoyancy and so the tem-  
231 perature in the above equations could be interpreted as a compositional variable if one  
232 is interested in compositional convection. Here we will refer to our buoyancy source as  
233 thermal in nature, but this is for simplicity and could instead be compositional in nature.

### 234 1.5.2 Magnetic Field

235 Magnetic field is governed by the magnetic induction equation, which is obtained by  
236 using Maxwell's equations (equations 1.9 to 1.12) and Ohm's law (equation 1.8). As  
237 presented earlier, using the magnetohydrodynamic (MHD) approximation i.e. assuming  
238 that fluid flows in planetary cores are much slower than the speed of light, we can reduce  
239 the Ampère-Maxwell Law to (by neglecting the displacement current term) equation 1.17.

240 By taking the curl of Ohm's law, we get:

$$\nabla \times \vec{J} = \sigma(\nabla \times \vec{E} + \nabla \times (\vec{v} \times \vec{B})) \quad (1.26)$$

241 Using Ampère's law to substitute for  $\vec{J}$  on the left-hand-side and using Faraday's law to  
242 substitute for  $\vec{E}$  on the right-hand-side of equation 1.26, we get:

$$\nabla \times (\nabla \times \vec{B}) = -\mu_0\sigma \frac{\partial}{\partial t} \vec{B} + \mu_0\sigma \nabla \times (\vec{v} \times \vec{B}) \quad (1.27)$$

<sup>243</sup> Using the vector identity:

$$\nabla \times (\nabla \times \vec{B}) = \nabla(\nabla \cdot \vec{B}) - \nabla^2 \vec{B} \quad (1.28)$$

<sup>244</sup> and using Gauss's law (equation 1.9), we obtain the magnetic induction equation:

$$\left( \frac{\partial}{\partial t} - \eta \nabla^2 \right) \vec{B} = \nabla \times (\vec{v} \times \vec{B}) \quad (1.29)$$

<sup>245</sup> where the magnetic diffusivity:

$$\eta = \frac{1}{\sigma \mu_0} \quad (1.30)$$

### <sup>246</sup> 1.5.3 Temperature

<sup>247</sup> The buoyancy force in the momentum equation (equation 1.24) includes the temperature  
<sup>248</sup> perturbation  $\Theta$ , which is governed by the heat equation as follows:

$$\left( \frac{\partial}{\partial t} - \kappa \nabla^2 \right) \Theta = -\vec{v} \cdot \nabla [T_0(r) + \Theta] + Q \quad (1.31)$$

<sup>249</sup> where,  $\kappa$  is thermal diffusivity. Internal heating ( $Q$ ) is assumed to be of the form:

$$Q = \frac{\epsilon h_T \kappa}{r_o} \quad (1.32)$$

<sup>250</sup> where,  $h_T$  is incoming heat flux at the inner core boundary,  $\epsilon$  is the magnitude of heat  
<sup>251</sup> sources, and  $r_o$  is outer core radius. The background conductive temperature solution is:

$$T_0(r) = \tilde{T}_0 + r_o h_T \left[ \frac{r_{io}^2}{r/r_o} \left( 1 - \frac{\epsilon}{3} r_{io} \right) - \frac{\epsilon}{3} \left( \frac{r}{r_o} \right)^2 \right] \quad (1.33)$$

<sup>252</sup> In this study, we assume no internal heating sources ( $\epsilon = 0$ ), so:

$$T_0(r) = \tilde{T}_0 + h_T \frac{r_i^2}{r} \quad (1.34)$$

## <sup>253</sup> 1.6 Non-Dimensional Governing equations

<sup>254</sup> We non-dimensionalize the governing equations (1.24, 1.29 and 1.31) by using the following characteristic scales:

Length Scale : Radius of the outer core ( $r_o$ )

Time Scale : Magnetic diffusion time  $\left(\tau = \frac{r_o^2}{\eta}\right)$

Magnetic Field Scale : Magnetostrophic balance estimate ( $B = \sqrt{2\Omega\rho\mu_0\eta}$ )

Temperature Scale :  $(h_T r_o)$

(Fixed Flux)

Temperature Scale :  $\left(\frac{\Delta T}{(r_{io}(1 - r_{io}))}\right)$

(Fixed Temperature)

<sup>256</sup> and obtain the following non-dimensional equations:

<sup>257</sup> The Continuity equation:

$$\nabla \cdot \vec{v} = 0 \quad (1.35)$$

<sup>258</sup> The Momentum equation:

$$\underbrace{Ro_M \left( \frac{\partial}{\partial t} + \vec{v} \cdot \nabla \right) \vec{v}}_{Inertia} + \underbrace{\hat{\mathbf{z}} \times \vec{v}}_{Coriolis} = \underbrace{-\nabla p}_{Pressure Gradient} + \underbrace{Ra\Theta \vec{r}}_{Buoyancy} + \underbrace{E\nabla^2 \vec{v}}_{Viscous} + \underbrace{\vec{J} \times \vec{B}}_{Lorentz} \quad (1.36)$$

<sup>259</sup> The Magnetic Induction equation:

$$\left( \frac{\partial}{\partial t} - \nabla^2 \right) \vec{B} = \underbrace{\nabla \times (\vec{v} \times \vec{B})}_{Advection} \quad (1.37)$$

*Diffusion*

<sup>260</sup> The Thermal equation:

$$\left( \frac{\partial}{\partial t} - q_k \nabla^2 \right) \Theta = \underbrace{-\vec{v} \cdot \nabla [T_0(r) + \Theta]}_{Advection} \quad (1.38)$$

*Diffusion*

<sup>261</sup> where,  $\hat{\mathbf{z}}$  is the unit vector in the direction of the rotation axis.

<sup>262</sup>

<sup>263</sup> The definition of the nondimensional numbers used in the above equations are as follows:

$$\text{Magnetic Rossby number : } Ro_M = \frac{\eta}{2\Omega r_o^2} \quad (1.39)$$

$$\text{Ekman number : } E = \frac{\nu}{2\Omega r_o^2} \quad (1.40)$$

$$\text{Modified Rayleigh number: } Ra_{FF} = \frac{\alpha_T g_o h_T r_o^2}{2\Omega \eta} \quad (1.41)$$

(for fixed heat flux models)

$$\text{Modified Rayleigh number: } Ra_{FT} = \frac{\alpha_T g_o \Delta T r_o}{2\Omega \eta r_{io} (1 - r_{io})} \quad (1.42)$$

(for fixed temperature models)

$$\text{Roberts number : } q_k = \frac{\kappa}{\eta} \quad (1.43)$$

<sup>264</sup> Derivations of the non-dimensional numbers can be found in appendix A.

## **1.7 Boundary Conditions**

<sup>265</sup> The above non-dimensional equations require boundary conditions. Typical choices made  
<sup>266</sup> in the studies of planetary dynamos are:

### **268 1.7.1 Temperature Boundary Conditions**

<sup>269</sup> Fixed heat flux at the boundaries:

$$\frac{\partial}{\partial r} \Theta = 0, \quad \text{at} \quad r = r_{io}, 1 \quad (1.44)$$

<sup>270</sup> Fixed temperature at the boundaries:

$$\Theta = 0, \quad \text{at} \quad r = r_{io}, 1 \quad (1.45)$$

<sup>271</sup> Note that the non-dimensional inner core radius is the inner to outer core radius and the  
<sup>272</sup> non-dimensional outer core radius is equal to 1.

### **273 1.7.2 Velocity Boundary Conditions**

<sup>274</sup> No-slip boundaries:

$$[\vec{v}] = 0, \quad \text{at} \quad r = r_{io}, 1 \quad (1.46)$$

<sup>275</sup> where, [ ] is the difference across the boundaries.

<sup>276</sup>

<sup>277</sup> Impenetrable and viscous stress-free boundaries:

$$\hat{n} \cdot \vec{v} = \hat{n} \times (\sigma_\nu \cdot \hat{n}) = 0, \quad \text{at} \quad r = r_{io}, 1 \quad (1.47)$$

<sup>278</sup> where,  $\hat{n}$  is the normal of the boundaries,  $\sigma_\nu$  is the viscous stress tensor (an expression

<sup>279</sup> for  $\sigma_\nu$  in spherical coordinates can be found in [Landau and Lifshitz, 1981]). By viscous  
<sup>280</sup> stress-free boundaries, we mean that there are no shear stress on the boundaries.

### <sup>281</sup> 1.7.3 Magnetic Field Boundary Conditions

<sup>282</sup> Perfectly electrically conducting boundaries:

$$\hat{n} \cdot \vec{B} = \hat{n} \times \vec{J} = 0, \quad \text{at } r = r_{io}, 1 \quad (1.48)$$

<sup>283</sup> Perfectly electrically insulating boundaries:

$$[\vec{B}] = \hat{n} \cdot \vec{J} = 0, \quad \text{at } r = r_{io}, 1 \quad (1.49)$$

<sup>284</sup> Finitely electrically conducting boundaries:

$$[\vec{B}] = [\hat{n} \cdot \vec{J}] = [\hat{n} \times \vec{E}] = 0, \quad \text{at } r = r_{io}, 1 \quad (1.50)$$

## <sup>285</sup> 1.8 Thesis Overview

<sup>286</sup> The objective of my thesis involves carrying out a comprehensive and systematic study  
<sup>287</sup> of:

- <sup>288</sup> • The influence of inner core conductivity on planetary dynamo models,
- <sup>289</sup> • The influence of thermal and velocity boundary conditions on planetary dynamo  
<sup>290</sup> models, and
- <sup>291</sup> • Scaling laws and dynamo generation mechanisms of planetary dynamo models.

<sup>292</sup> In this thesis we include numerical simulation results of planetary dynamo models and  
<sup>293</sup> non-magnetic convection models. In Chapter 2, we describe our numerical dynamo model.

<sup>294</sup> Since we use hyperdiffusivities to work at highly super-critical Rayleigh numbers, we

295 include a study of the influence of hyperdiffusivities on dynamo models. In this chapter,  
296 we also include a benchmark study of our dynamo model. In Chapter 3, we present  
297 the results of the influence of inner core conductivity on planetary dynamo models.  
298 In Chapter 4, we present the results of the influence of different thermal and velocity  
299 boundary conditions on planetary dynamo models along with studies on scaling laws,  
300 dynamo generation mechanisms and boundary layer analysis. In Chapter 5, we present  
301 our conclusions and future work. The spherical harmonic expansions of the magnetic,  
302 velocity and temperature fields and their derivatives along with non-dimensionalization  
303 and derivatives of forces are presented in the appendices.

# <sup>304</sup> Chapter 2

## <sup>305</sup> Numerical Model

### <sup>306</sup> 2.1 Numerical Method

<sup>307</sup> In our numerical dynamo simulations, we use the [Kuang and Bloxham \[1999\]](#) three-  
<sup>308</sup> dimensional numerical dynamo model to study the magnetic field generation in a spher-  
<sup>309</sup> ical, rotating, electrically conducting fluid shell surrounding a solid inner core using the  
<sup>310</sup> Boussinesq approximation which solves the system described in section [1.6](#). In our mod-  
<sup>311</sup> els, the inner core is free to oscillate in response to magnetic and viscous torques. Here  
<sup>312</sup> we introduce the basics of the numerical model.

<sup>313</sup>

<sup>314</sup> The magnetic and velocity fields have three components in spherical geometry but since  
<sup>315</sup> they are both divergence free in the Boussinesq approximation, only two independent  
<sup>316</sup> scalar fields are needed to specify each of them. We use the poloidal-toroidal decompo-

317 sition as follows:

$$\vec{B} = \vec{B}_T + \vec{B}_P \quad (2.1)$$

$$= \nabla \times T_b \hat{\mathbf{r}} + \nabla \times \nabla \times P_b \hat{\mathbf{r}} \quad (2.2)$$

$$\vec{v} = \vec{v}_P + \vec{v}_T \quad (2.3)$$

$$= \nabla \times T_v \hat{\mathbf{r}} + \nabla \times \nabla \times P_v \hat{\mathbf{r}} \quad (2.4)$$

318 where,  $\hat{\mathbf{r}}$  is the radial unit vector,  $\vec{B}_T$  and  $\vec{B}_P$  are the toroidal and poloidal magnetic field  
319 respectively,  $\vec{v}_T$  and  $\vec{v}_P$  are the toroidal and poloidal velocity field respectively,  $T_b$  and  $P_b$   
320 are the toroidal and poloidal scalars for magnetic field respectively, and  $T_v$  and  $P_v$  are  
321 the toroidal and poloidal scalars for velocity field respectively.

322

323 An illustration of poloidal and toroidal magnetic fields are shown in Figure 2.1. Toroidal  
324 magnetic fields live on surfaces of spheres in the core and hence are not observable by  
325 spacecraft which fly outside the dynamo generation region. However, since the poloidal  
326 field has a radial component it can be observed by spacecraft. This poses a challenge  
327 to the dynamo community as it is believed that the toroidal component is the dominant  
328 component and is not measurable.

329

330 For a given radius  $r$ , we expand the variables in spherical harmonics as described in Ap-  
331 pendix B. Similarly, temperature perturbation is also expanded in spherical harmonics.  
332 From a computational point of view, since infinite series of spherical harmonics cannot  
333 be used to represent the fields, we truncate them at maximum spherical harmonic de-  
334 gree,  $L_{max}$  and maximum spherical harmonic order,  $M_{max}$ . We also choose rhomboidal  
335 truncation, i.e.,  $L_{max} > M_{max}$  in our models. So, the azimuthal truncation is lower than  
336 the meridional truncation.

337

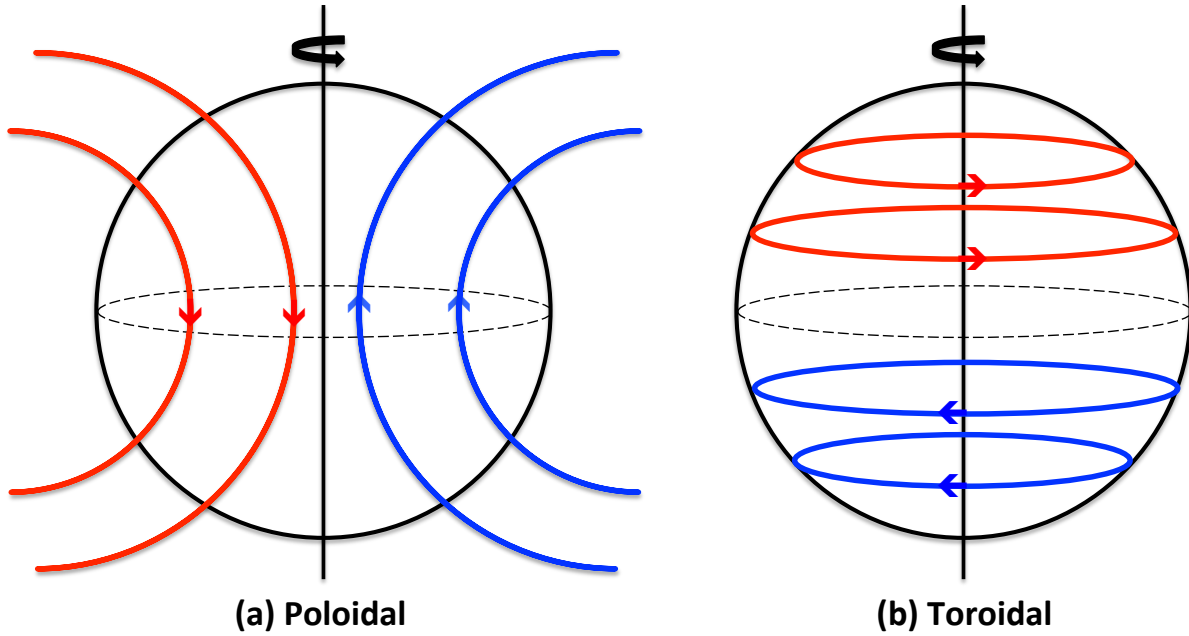


Figure 2.1: **Illustration of canonical poloidal (left) and toroidal (right) magnetic field.** Red and blue curves are field lines in different direction. The vertical line is the rotation axis, black solid circle is the outer core boundary and the dotted circle represents the equator (adopted from [Stanley, 2004])

<sup>338</sup> The partial differential equations for spectral coefficients can be obtained by using the  
<sup>339</sup> spherical harmonic expansions in the non-dimensional governing equations as follows:

$$A_1 \frac{\partial}{\partial t} \hat{s}_1 + A_2 \hat{s}_1 = \hat{N}_1 \quad (2.5)$$

<sup>340</sup> where,  $\hat{s}_1$  is a vector of variables in spectral space,  $A_1$  and  $A_2$  are the matrices of linear  
<sup>341</sup> radial differential operators, and  $\hat{N}_1$  is the non-linear interaction term solved by collocation  
<sup>342</sup> point method via spherical transforms. Most ( $\approx 80\%$ ) of our numerical simulation  
<sup>343</sup> time is spent on spherical transforms.

<sup>344</sup>

<sup>345</sup> We evaluate spherical transforms separately at each radii, and between each radii we use  
<sup>346</sup> a fourth order finite difference scheme on non-uniform grid points. To resolve boundary  
<sup>347</sup> layers, we use collocation points of Chebyshev polynomials as the radial grid points. So,

348 equation 2.5 reduces to the following ordinary differential equation:

$$B_1 \frac{\partial}{\partial t} \hat{s}_2 + B_2 \hat{s}_2 = \hat{N} \quad (2.6)$$

349 where,  $B_1$  and  $B_2$  are the linear time dependent matrices and  $\hat{s}_2$  is a vector of variables  
350 in spectral space.

351

352 To solve the linear terms in equation 2.6, we use the second order Crank-Nicolson implicit  
353 scheme, and to solve the non-linear terms we use the Adams family (Bashforth-Moulton)  
354 third order predictor-corrector method. The Courant Friedrichs Lewy (CFL) condition  
355 is tested at each time step for the stability of the algorithm that is determined by the  
356 non-linear terms that are solved explicitly.

## 357 2.2 High Performance Computing

358 The computationally intensive numerical simulations were run on SciNet's General Pur-  
359 pose Cluster (GPC). SciNet is one of 7 regional high performance computing (HPC)  
360 consortia across Canada. It is the most powerful university HPC system outside of the  
361 United States. The GPC was ranked 16th in the world at its inception and is the fastest  
362 in Canada. It has 3,780 nodes of IBM iDataPlex DX360M2 with 30,912 cores (proces-  
363 sors) of an Intel Nehalem-based (Xeon E5540) at 2.53GHz, with 16GB RAM per node  
364 (2GB per core), with theoretical peak of 306 TFlops and 60 TiB of RAM. The compute  
365 nodes are accessed through a queuing system that allows a maximum wall time of 48  
366 hours. The time required to run the simulations ranged from a few weeks to a few years  
367 depending on the input parameters like the Ekman number and the Rayleigh number.  
368 For example, as the Rayleigh number (ratio of buoyancy to Coriolis force) is increased,  
369 turbulence increases in the system and a higher resolution is needed to resolve the small  
370 scaled features, which takes longer to run. The Fortran based OpenMP code is run

<sup>371</sup> simultaneously on one node with 8 cores using hyperthreading.

### <sup>372</sup> 2.3 Effect of Hyperdiffusivity

<sup>373</sup> The [Kuang and Bloxham \[1999\]](#) numerical model allows for the implementation of hy-  
<sup>374</sup> perdiffusivities to work at highly supercritical Rayleigh numbers. The hyperdiffusivity  
<sup>375</sup> is applied in such a way that the thermal and magnetic diffusivity, and the kinematic  
<sup>376</sup> viscosity are scale-dependent:

$$\kappa(l) = \kappa_0[1 + 0.06(l - l_0)^2] \quad (2.7)$$

$$\eta(l) = \eta_0[1 + 0.06(l - l_0)^2] \quad (2.8)$$

$$\nu(l) = \nu_0[1 + 0.05(l - l_0)^2] \quad (2.9)$$

<sup>377</sup> where,  $\kappa_0$ ,  $\eta_0$  and  $\nu_0$  are constant values, and  $l_0$  is a constant value that lies in the range  
<sup>378</sup> 0 to  $L_{max}$  and determines the minimum spherical harmonic degree at which hyperdiffu-  
<sup>379</sup> sivity onsets.

<sup>380</sup>

<sup>381</sup> Previous work suggests that great care should be taken while using hyperdiffusivities in  
<sup>382</sup> dynamo models [[Grote et al., 2000](#), [Zhang and Jones, 1997](#), [Zhang et al., 1998](#)]. For  
<sup>383</sup> example, models that used hyperdiffusivity of the form:

$$\nu = \nu_0[1 + \epsilon(l - l_0)^n] \quad (2.10)$$

<sup>384</sup> with a constant  $\epsilon$ ,  $n = 3$  and  $l_0 = 0$  had characteristics significantly different from models  
<sup>385</sup> at the same parameter values but no hyperdiffusivity, such as larger length scales and an  
<sup>386</sup> increases in the critical Rayleigh number [[Zhang et al., 1998](#)].

<sup>387</sup>

388 Here we test the effects of the form of hyperdiffusivity we use in our models to ensure  
 389 they don't affect our results in future chapters. In equations 2.7 to 2.9, we varied  $l_0$  in  
 390 the range 0 to 50 and examined the resulting magnetic and velocity fields. The control  
 391 parameters, boundary conditions and results are summarized in Table 2.1 for dynamo  
 392 models. Since we use models with different thermal and velocity boundary conditions,  
 393 for convenience, we will use the abbreviation, **FFSF** for fixed heat flux and stress-free  
 394 models, **FFNS** for fixed heat flux and no-slip models, **FTSF** for fixed temperature and  
 395 stress-free models and **FTNS** for fixed temperature and no-slip models. The simulations  
 396 were run for many magnetic dipole diffusion times and the results presented were analyzed  
 397 after the initial transients decayed.

**Table 2.1: Hyperdiffusivity Results of Dynamo Models.** The boundary conditions are applied at both the inner and outer core boundaries. For definition of the symbols please refer to the nomenclature.

Model	$l_0$	$Ra$	$\frac{Ra}{Ra_C}$	$E_B$	$E_k$	$\frac{E_{BP}}{E_{BT}}$	$\frac{E_{BP}^{N\text{Axi}}}{E_{BP}}$	$\frac{E_{BT}^{N\text{Axi}}}{E_{BT}}$	$\frac{E_{kP}^{N\text{Axi}}}{E_{kP}}$	$\frac{E_{kT}^{N\text{Axi}}}{E_{kT}}$	$Nu$
$E = 6.00\text{e-}05$ , $Ro_M = 2.00\text{e-}05$ and $q_k = 1$											
FFSF-01	0	1.00e+04	34.97	1.5e+00	2.4e+05	3.8e-01	2.5e-01	2.8e-01	9.9e-01	4.1e-01	2.55
FFSF-02	10	1.00e+04	34.97	1.9e+00	2.2e+05	7.2e-01	4.5e-01	6.1e-01	9.7e-01	5.8e-01	3.24
FFSF-03	20	1.00e+04	34.97	3.5e+00	1.5e+05	8.7e-01	4.1e-01	4.6e-01	9.7e-01	6.6e-01	3.40
FFSF-04	30	1.00e+04	34.97	3.8e+00	1.5e+05	8.0e-01	4.0e-01	4.4e-01	9.7e-01	6.4e-01	3.37
FFSF-05	40	1.00e+04	34.97	3.9e+00	1.5e+05	8.0e-01	4.0e-01	4.3e-01	9.7e-01	6.2e-01	3.38
FFSF-06	50	1.00e+04	34.97	3.7e+00	1.2e+05	1.2e+00	3.3e-01	4.6e-01	9.7e-01	6.6e-01	3.47
FFNS-01	0	7.50e+03	31.12	1.1e-02	8.7e+04	4.8e-01	3.0e-01	2.9e-01	9.8e-01	5.7e-01	2.67
FFNS-02	10	7.50e+03	31.12	3.3e+00	8.8e+04	8.4e-01	3.1e-01	4.0e-01	9.6e-01	5.4e-01	3.21
FFNS-03	20	7.50e+03	31.12	4.0e+00	6.5e+04	7.3e-01	3.7e-01	4.1e-01	9.6e-01	7.2e-01	3.41
FFNS-04	30	7.50e+03	31.12	2.9e+00	6.6e+04	9.1e-01	3.8e-01	5.0e-01	9.7e-01	8.1e-01	3.54
FFNS-05	40	7.50e+03	31.12	2.5e+00	7.2e+04	8.0e-01	3.9e-01	4.6e-01	9.7e-01	7.3e-01	3.43
FFNS-06	50	7.50e+03	31.12	2.9e+00	6.6e+04	9.0e-01	3.6e-01	5.0e-01	9.7e-01	7.6e-01	3.54
FTSF-01	0	3.00e+03	8.70	1.1e+00	7.3e+04	3.7e-01	1.3e-01	2.0e-01	1.0e+00	7.4e-01	2.13
FTSF-02	10	3.00e+03	8.70	2.1e+00	1.4e+05	9.0e-01	3.8e-01	5.9e-01	9.8e-01	7.9e-01	3.21
FTSF-03	20	3.00e+03	8.70	2.4e+00	1.4e+05	1.3e+00	3.5e-01	6.1e-01	9.9e-01	8.7e-01	3.56
FTSF-04	30	3.00e+03	8.70	2.5e+00	1.3e+05	1.5e+00	3.4e-01	6.2e-01	9.9e-01	8.4e-01	3.57
FTSF-05	40	3.00e+03	8.70	2.6e+00	1.2e+05	1.5e+00	3.2e-01	6.4e-01	9.9e-01	8.3e-01	3.60
FTSF-06	50	3.00e+03	8.70	2.9e+00	1.1e+05	1.5e+00	3.0e-01	5.9e-01	9.9e-01	8.0e-01	3.51
FTNS-01	0	3.00e+03	10.83	2.3e+00	5.3e+04	9.6e-01	1.1e-01	1.6e-01	9.9e-01	6.9e-01	2.45
FTNS-02	10	3.00e+03	10.83	3.7e+00	1.0e+05	1.3e+00	2.5e-01	4.8e-01	9.7e-01	6.6e-01	3.44
FTNS-03	20	3.00e+03	10.83	4.8e+00	8.0e+04	1.6e+00	2.8e-01	5.9e-01	9.7e-01	7.8e-01	3.76
FTNS-04	30	3.00e+03	10.83	4.9e+00	7.7e+04	1.5e+00	2.9e-01	5.6e-01	9.7e-01	8.0e-01	3.70

*Continued on next page*

Table 2.1 -- Continued from previous page

Model	$l_0$	$Ra$	$\frac{Ra}{Ra_C}$	$E_B$	$E_k$	$\frac{E_{B_P}}{E_{B_T}}$	$\frac{E_{B_P}^{N\text{Axi}}}{E_{B_P}}$	$\frac{E_{B_T}^{N\text{Axi}}}{E_{B_T}}$	$\frac{E_{k_P}^{N\text{Axi}}}{E_{k_P}}$	$\frac{E_{k_T}^{N\text{Axi}}}{E_{k_T}}$	$Nu$
FTNS-05	40	3.00e+03	10.83	4.7e+00	7.9e+04	1.5e+00	3.0e-01	5.5e-01	9.6e-01	7.5e-01	3.71
FTNS-06	50	3.00e+03	10.83	4.2e+00	8.4e+04	1.6e+00	3.3e-01	6.0e-01	9.7e-01	7.7e-01	3.87

398

### 2.3.1 Results

We compare the typical output parameters of models with FFSF, FFNS, FTSF and FTNS boundary conditions. For convenience and in order to focus on the effect of using hyperdiffusivity, we examine and plot characteristic figures for models with FFNS boundary conditions with identical parameters and different  $l_0$ . We start by examining the observable features of the magnetic fields such as the surface magnetic power spectra. We then examine the characteristics of the magnetic and velocity fields inside the dynamo generation region.

#### 407 Surface Magnetic Power Spectra

The difference in the observed magnetic field between the dynamo models with different hyperdiffusivities can be demonstrated through their surface magnetic power spectra. In a current-free region (which we assume outside the Earth's core), the magnetic field can be represented as the gradient of a scalar potential ( $\vec{B} = -\nabla\Phi$ ). The scalar potential can be expanded in spherical harmonics as follows:

$$\Phi = a \sum_{l=1}^{\infty} \left(\frac{a}{r}\right)^{l+1} P_l^m(\cos\theta) \left[ g_l^m \cos(m\phi) + h_l^m \sin(m\phi) \right] \quad (2.11)$$

where,  $a$  is the radius of the planet,  $(r, \theta, \phi)$  are spherical coordinates,  $P_l^m$  are Schmidt-normalized associated Legendre polynomials,  $g_l^m$  and  $h_l^m$  are Gauss coefficients for each spherical harmonic degree  $l$  and order  $m$  and  $p$  is the power in each degree and order.

416

417 The power can be defined in terms of the mean square field intensity as follows:

$$p(l, m, r) = (l + 1) \left( \frac{a}{r} \right)^{2l+4} \left[ (g_l^m)^2 + (h_l^m)^2 \right] \quad (2.12)$$

418 In Figure 2.2 we show the resulting average surface magnetic power spectra over a mag-  
 419 netic dipole diffusion time for all the FFNS models shown in table 2.1. This figure shows  
 420 that our form of hyperdiffusion does not significantly affect the power spectrum of the  
 421 surface magnetic field, although models with  $l_0 < 20$  have spectra that taper off much  
 422 earlier than the models with  $l_0 > 20$  as expected.

### 423 Magnetic Energy

424 In this section, we examine the characteristics of dynamo models inside the dynamo  
 425 generation region in order to understand to what extent the dynamics that generate  
 426 the potential fields that are observed outside the core are affected by hyperdiffusivities.  
 427 Magnetic energy is defined as the non-dimensional mean square field intensity as follows:

$$E_B = \int_V |\vec{B}|^2 dV \quad (2.13)$$

428 where,  $V$  is the non-dimensional volume of the outer core.

429

430 Because the magnetic field is solenoidal, it can be partitioned into toroidal ( $\vec{B}_T$ ) and  
 431 poloidal ( $\vec{B}_P$ ) fields and hence, magnetic energy can be decomposed into toroidal and  
 432 poloidal components. We can further decompose the toroidal and poloidal energies into  
 433 axisymmetric ( $m = 0$ ) and non-axisymmetric ( $m > 0$ ) components.

434

435 Table 2.1 shows the magnetic energies and ratios of the non-axisymmetric to axisym-

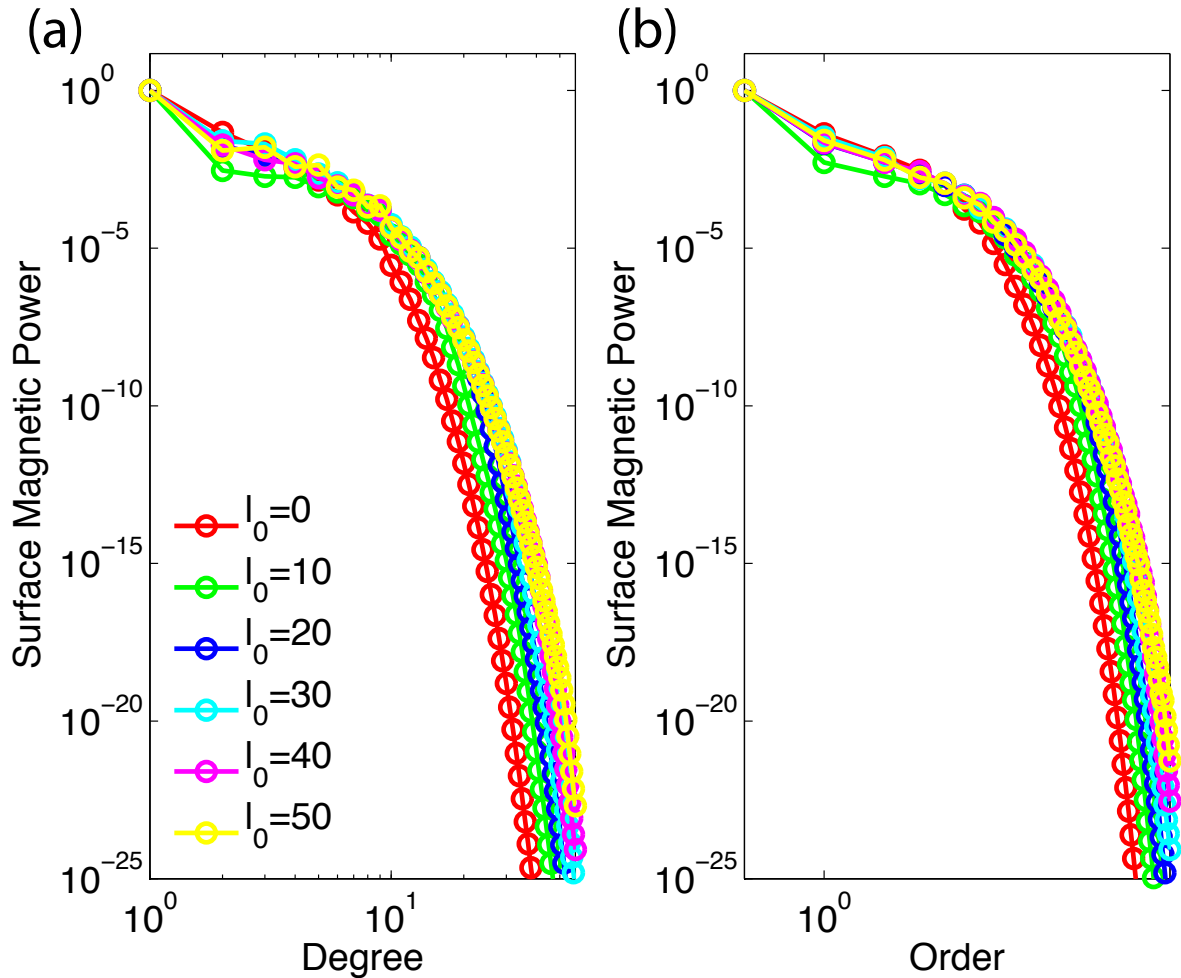


Figure 2.2: **Surface magnetic power spectra** for FFNS models with different  $l_0$ . Left plot shows power vs degree normalized to the dipole ( $l=1$ ) power and the right plot shows power vs order normalized to axisymmetric ( $m=0$ ) power.

metric components of the toroidal and poloidal magnetic energies. Model FFNS-01 is  
 unable to generate a self sustained dynamo when hyperdiffusivities are started at  $l_0 = 0$ .  
 All the other models with  $l_0 \geq 10$  are able to generate a self sustained dynamo. The  
 total magnetic energies of FFSF, FFNS, FTSF and FTNS models are presented in figure  
 2.3. The magnetic energy seems to approximately plateau after  $l_0 \geq 20$ , i.e., for the  
 models with self-sustaining dynamos, the magnetic energy seems to saturate and only  
 varies by approximately 5 % once  $l_0 \geq 20$  (except the FFNS models where the variation  
 is upto 15 %). Table 2.1 demonstrates that the partitioning of energy between toroidal  
 and poloidal components and between axisymmetric and non-axisymmetric components  
 is also not strongly affected by the degree of hyperdiffusivity onset once  $l_0 \geq 20$ .

446

The toroidal and poloidal magnetic energies in every degree and order are plotted in  
 figure 2.4. Starting hyperdiffusivity at  $l_0 \geq 20$ , seems to resolve the energies of the crit-  
 ical modes, i.e., the magnetic energies are saturated at similar lower spherical harmonic  
 orders, and taper off at higher spherical harmonic orders.

## 451 Magnetic Field

Figure 2.5 shows a meridional slice of the axisymmetric toroidal (left) and poloidal (right)  
 magnetic fields of FFNS models to investigate the difference between the magnetic field  
 morphologies inside the dynamo generation region. All the models have strong equa-  
 torially anti-symmetric large scale toroidal fields. The toroidal magnetic field of model  
 FFNS-01 is barely visible and weak since it is not a self sustained dynamo and the field  
 is decaying (dying). For the models with  $l_0 \geq 10$ , the degree of hyperdiffusivity onset  
 has little effect on the magnetic field morphologies or lengthscales.

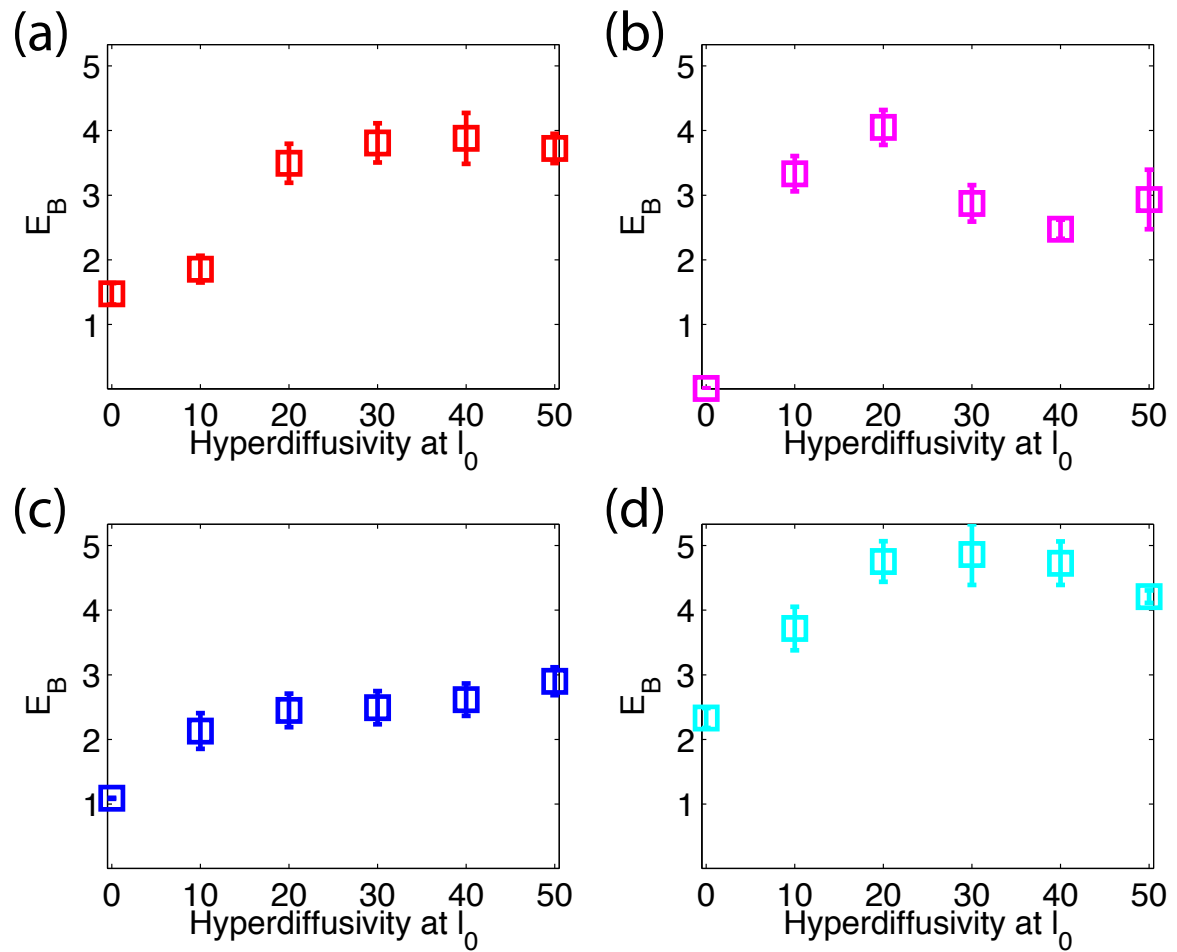


Figure 2.3: **Mean magnetic energy vs hyperdiffusivity** for dynamo models presented in Table 2.1. (a) FFSF, (b) FFNS, (c) FTSF and (d) FTNS. The error bars represent standard deviation in one magnetic dipole diffusion time.

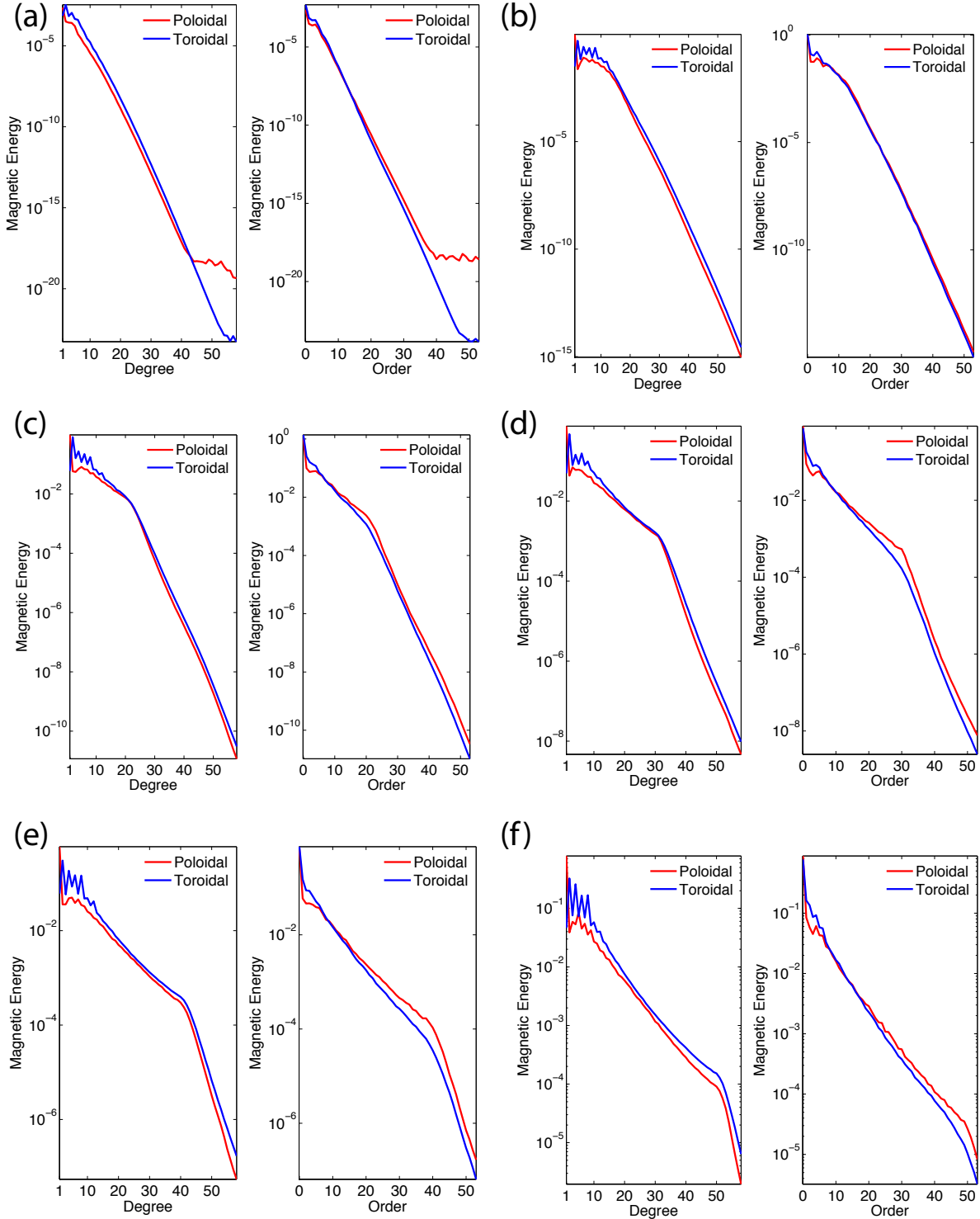


Figure 2.4: **Magnetic energy** for (a) FFNS-01, (b) FFNS-02, (c) FFNS-03, (d) FFNS-04, (e) FFNS-05 and (f) FFNS-06 dynamo models. Left plot shows toroidal and poloidal magnetic energy vs degree and the right plot shows toroidal and poloidal magnetic energy vs order. The units are non-dimensional.

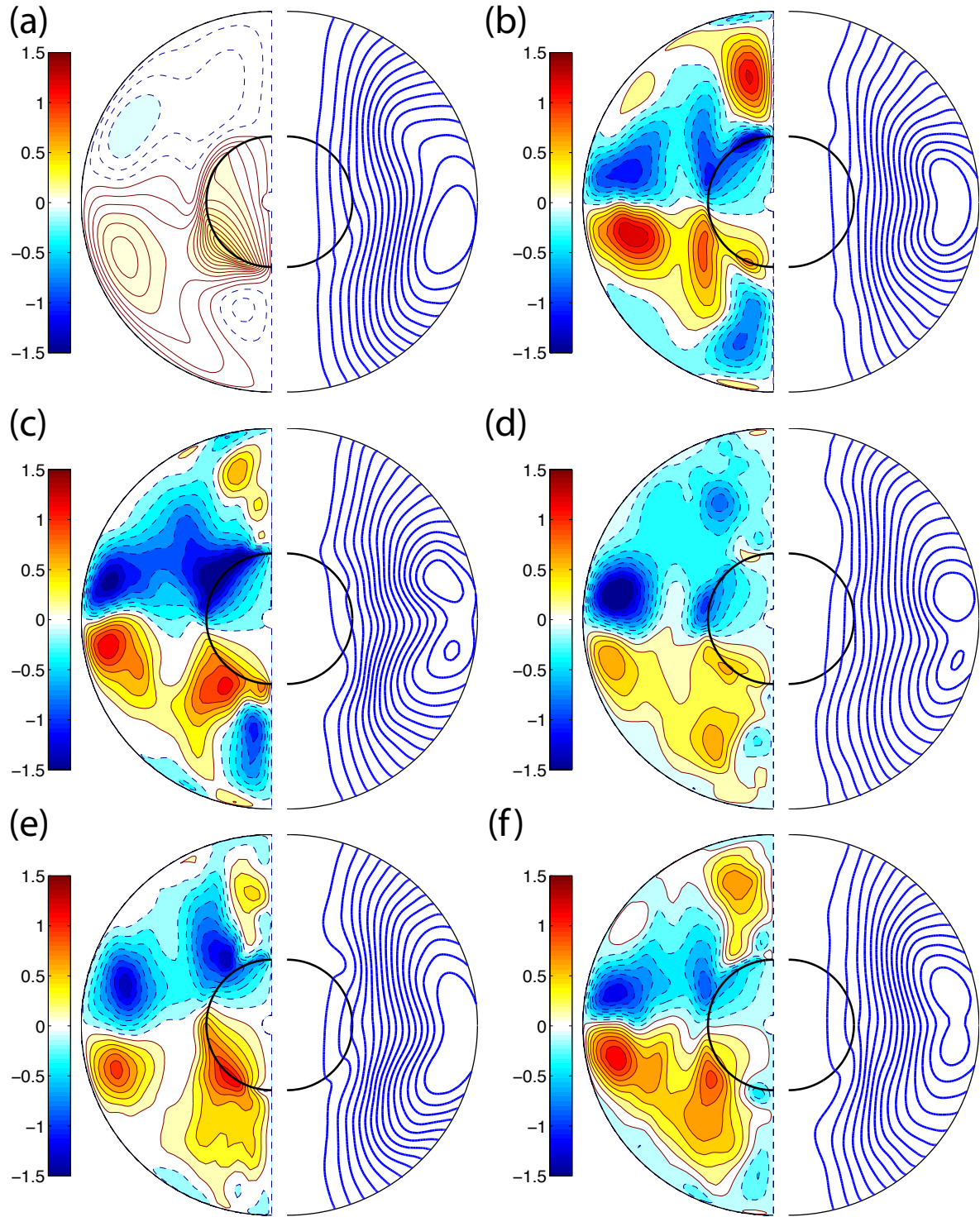


Figure 2.5: **Axisymmetric magnetic field** for (a) FFNS-01, (b) FFNS-02, (c) FFNS-03, (d) FFNS-04, (e) FFNS-05 and (f) FFNS-06 dynamo models. The toroidal magnetic fields are shown on the left where red (blue) denotes prograde (retrograde) direction and streamlines of poloidal magnetic fields are shown on the right where red (blue) denotes clockwise (anti-clockwise) direction.

<sup>459</sup> **Kinetic Energy**

<sup>460</sup> Similar to the magnetic energy, the kinetic energy can also be defined as the non-  
<sup>461</sup> dimensional mean square field intensity as follows:

$$E_k = \int_V |\vec{v}|^2 dV \quad (2.14)$$

<sup>462</sup> Because we use the Boussinesq approximation, the kinetic energy can be partitioned into  
<sup>463</sup> toroidal ( $\vec{v}_T$ ) and poloidal ( $\vec{v}_P$ ) components; and they can be further decomposed into  
<sup>464</sup> axisymmetric and non-axisymmetric components. Table 2.1 shows the kinetic energies and  
<sup>465</sup> ratios of the non-axisymmetric to axisymmetric components of the toroidal and poloidal  
<sup>466</sup> kinetic energies. The total kinetic energies of FFSF, FFNS, FTSF and FTNS models  
<sup>467</sup> are presented in figure 2.6. The kinetic energy seems to approximately plateau after  
<sup>468</sup>  $l_0 \geq 20$ , i.e. it saturates and only varies by approximately 6 % once  $l_0 \geq 20$ . Table  
<sup>469</sup> 2.1 demonstrates that the partitioning of kinetic energy between axisymmetric and non-  
<sup>470</sup> axisymmetric components is also not strongly affected by the degree of hyperdiffusivity  
<sup>471</sup> onset once  $l_0 \geq 20$ . The poloidal and toroidal kinetic energies of all the models are  
<sup>472</sup> dominated by their non-axisymmetric components.

<sup>473</sup>

<sup>474</sup> The toroidal and poloidal kinetic energies in every degree and order are plotted in figure  
<sup>475</sup> 2.7. Starting hyperdiffusivity at  $l_0 \geq 20$ , seems to resolve the energies of the critical  
<sup>476</sup> modes, i.e., the kinetic energies are saturated at similar lower spherical harmonic orders,  
<sup>477</sup> and taper off at higher spherical harmonic orders.

<sup>478</sup>

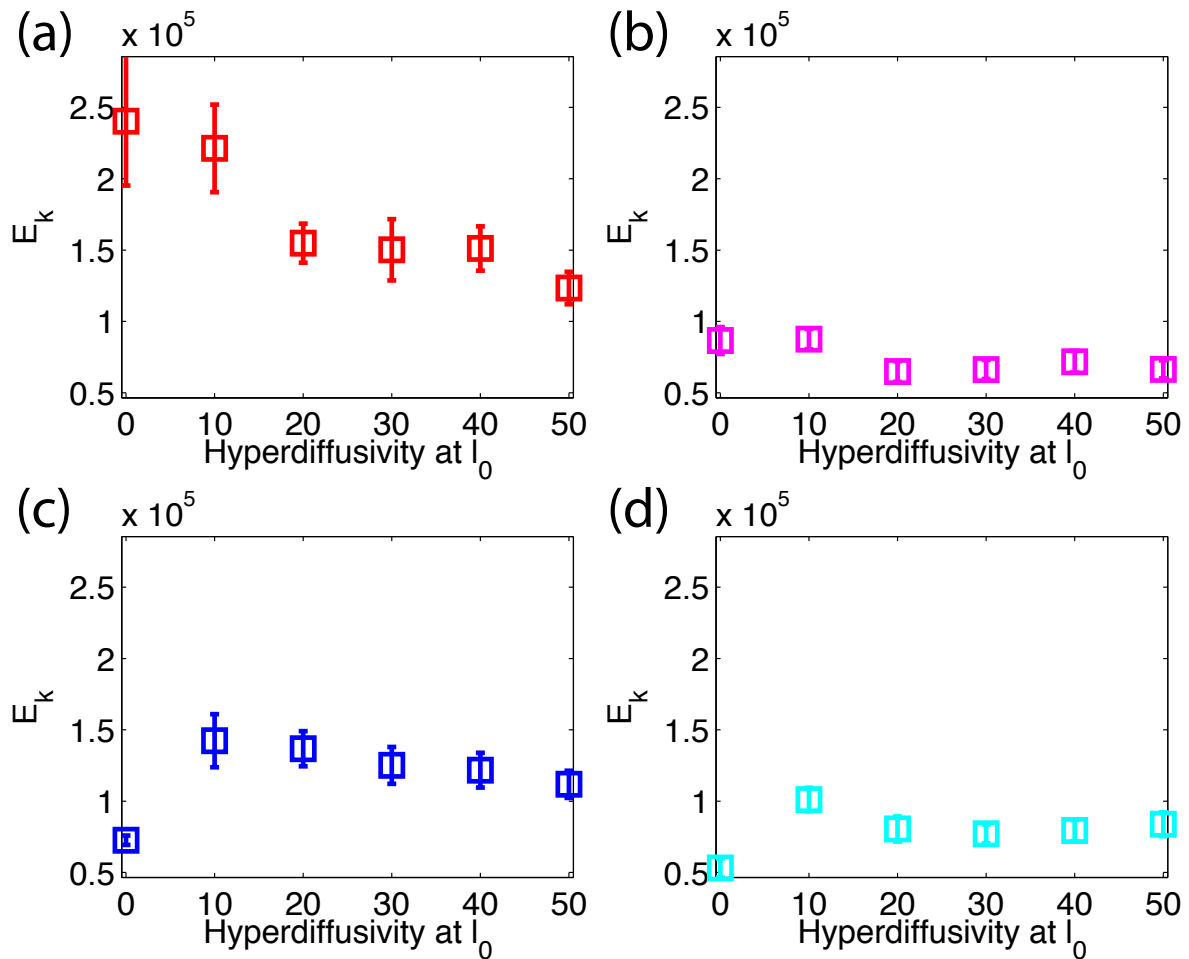


Figure 2.6: **Mean kinetic energy vs hyperdiffusivity** for dynamo models presented in Table 2.1. (a) FFSF, (b) FFNS, (c) FTSF and (d) FTNS. The error bars represent standard deviation in one magnetic dipole diffusion time

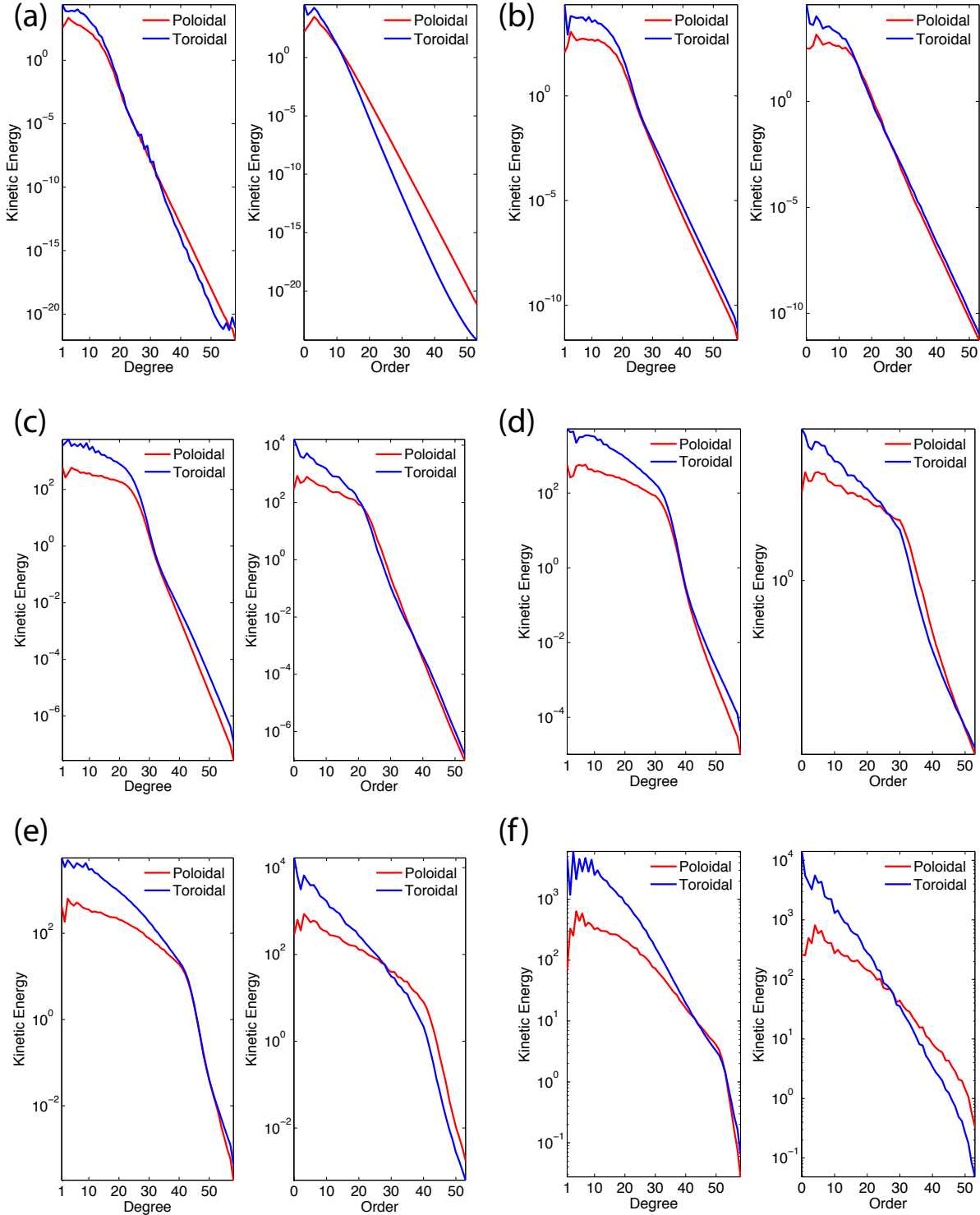


Figure 2.7: **Kinetic energy** for (a) FFNS-01, (b) FFNS-02, (c) FFNS-03, (d) FFNS-04, (e) FFNS-05 and (f) FFNS-06 dynamo models. Left plot shows toroidal and poloidal kinetic energy vs degree and the right plot shows toroidal and poloidal kinetic energy vs order. The units are non-dimensional.

**Velocity Field**

Figure 2.8 shows a meridional slice of the axisymmetric toroidal (left) and poloidal (right) velocity fields of FFNS models to investigate the difference between the velocity field morphologies inside the dynamo generation region. For  $l_0 \geq 20$ , the morphology and length-scale of the velocity fields is not strongly affected by the degree of onset of the hyperdiffusivity.

**Nusselt number**

Nusselt number is the ratio of total (superadiabatic) heat transfer to conductive (diffusive) heat transfer. To obtain a measure of convective heat transport, Nusselt number versus Rayleigh number is conventionally plotted for scaling law analysis in dynamo studies. In Figure 2.9, we plot the Nusselt number versus the hyperdiffusivity (at the same Rayleigh number) for models with FFSF, FFNS, FTSF and FTNS boundary conditions, which demonstrates that for  $l_0 \geq 20$ , the Nusselt number is not affected by the degree of onset of hyperdiffusion in the models.

**2.3.2 Conclusion**

As shown above, taking into account the output parameters like the magnetic and kinetic energy and the Nusselt number versus the hyperdiffusivity, we find that hyperdiffusivity starting at  $l_0 \geq 20$  is sufficient to resolve the critical modes of magnetic and velocity fields. The magnetic and velocity field morphologies also appear to be similar at  $l_0 \geq 20$ . Therefore, as long as  $l_0 > 20$  there is little difference in the resulting solutions and so we feel justified in using hyperdiffusivity in our models onsetting at  $l_0 \geq 20$  in the following chapters.

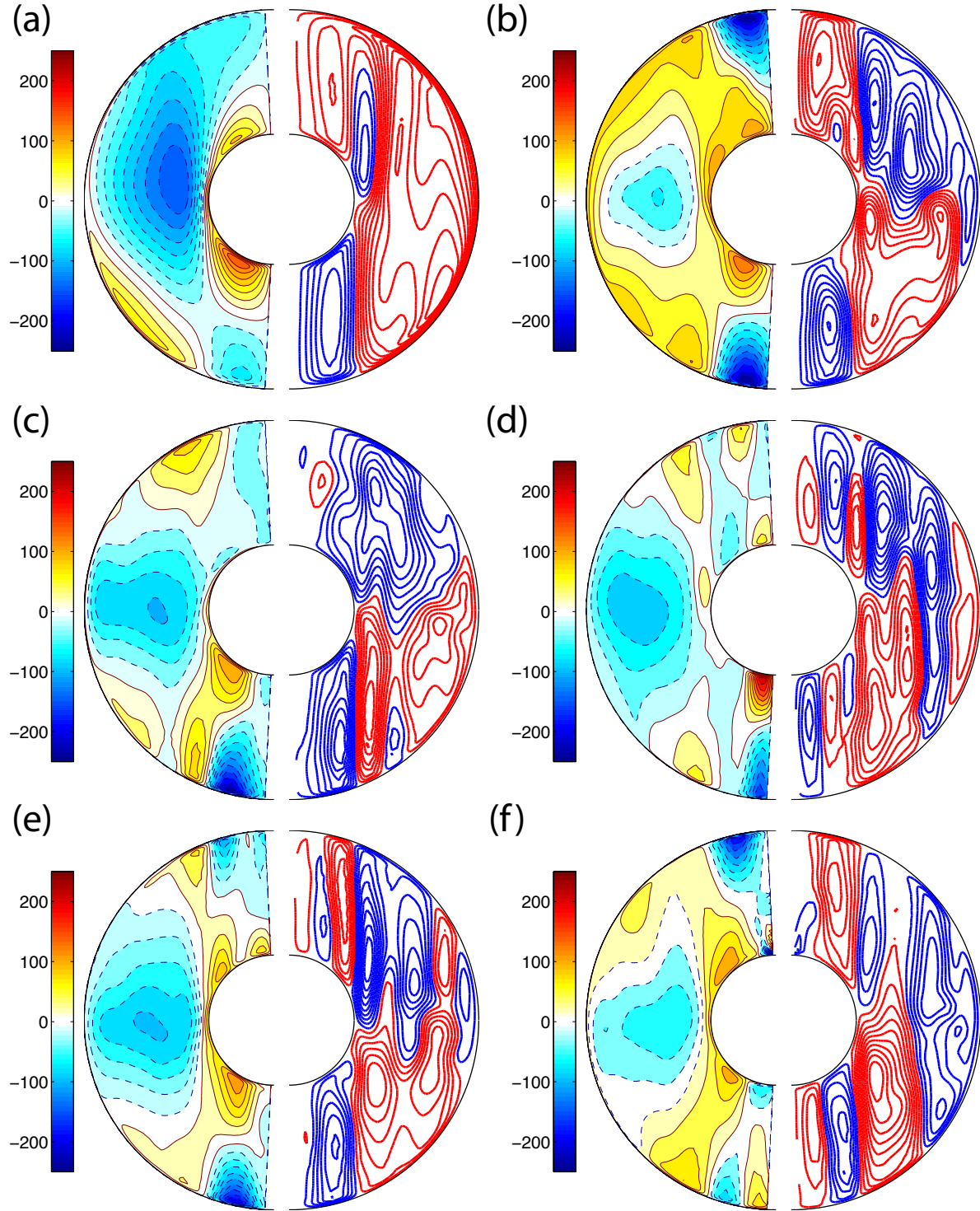


Figure 2.8: **Axisymmetric velocity field** for (a) FFNS-01, (b) FFNS-02, (c) FFNS-03, (d) FFNS-04, (e) FFNS-05 and (f) FFNS-06 dynamo models. The toroidal velocity fields are shown on the left where red (blue) denotes prograde (retrograde) circulation, and streamlines of poloidal velocity fields are shown on the right where red (blue) denotes clockwise (anti-clockwise) circulation.

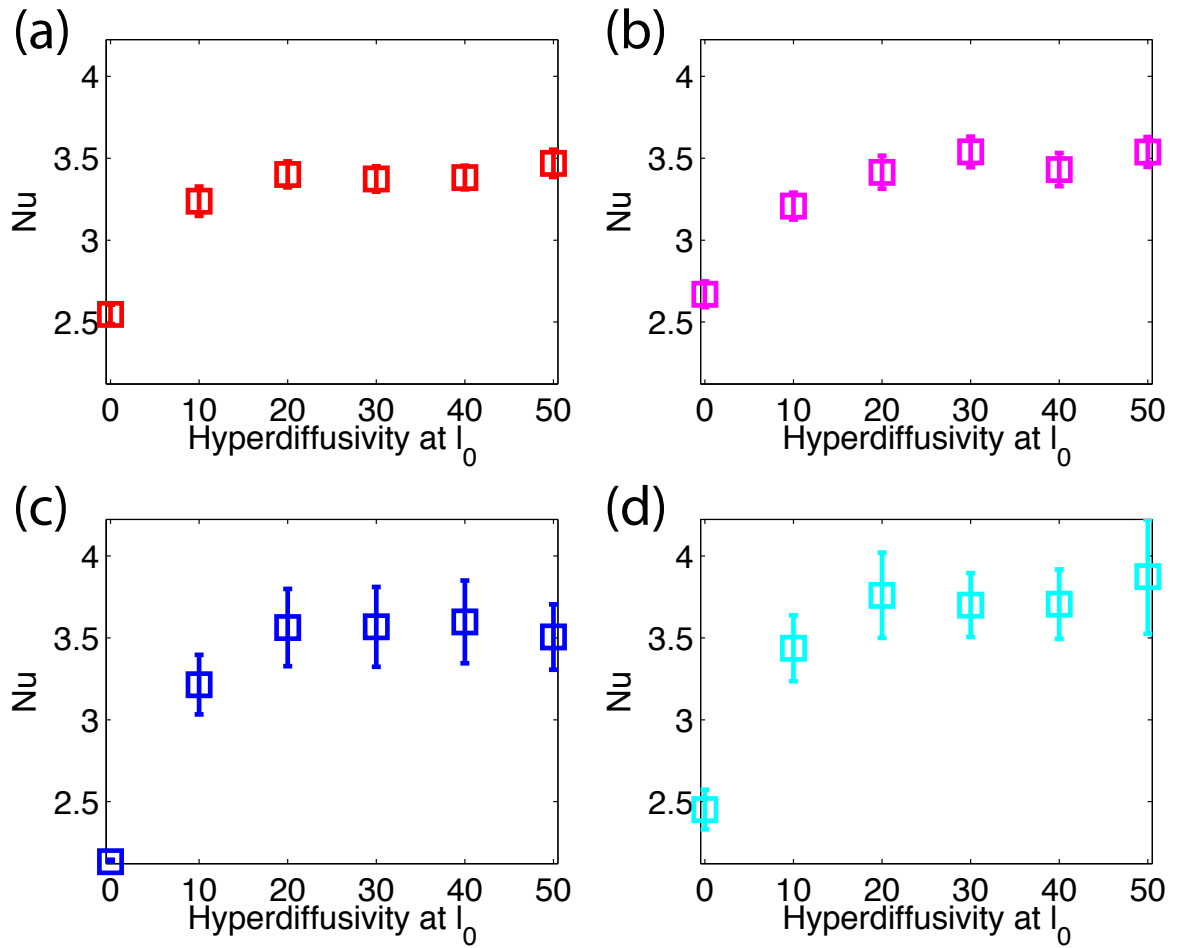


Figure 2.9: **Mean nusselt number vs hyperdiffusivity** for dynamo models presented in Table 2.1. (a) FFSF, (b) FFNS, (c) FTSF and (d) FTNS. The error bars represent standard deviation in one magnetic dipole diffusion time.

## 501 2.4 Benchmarking

502 Verification of computer codes for complex nonlinear problems, such as the dynamo  
503 problem, is crucial. But, verification by comparison of results with snapshots of other  
504 published work is difficult since the solutions are chaotic in time. Many numerical models  
505 have been developed independently by research groups around the world using similar  
506 principles. For example, the magnetic and velocity fields are represented by their poloidal  
507 and toroidal scalar potentials and are expanded in spherical harmonics. The diffusive  
508 terms are treated implicitly and the nonlinear terms are evaluated on grid points using  
509 spectral transform methods. The main difference between the models is the way in which  
510 the radial dependence is treated. Some use collocation method using Chebyshev polyno-  
511 mials while others use finite differencing. Some of these models have been benchmarked  
512 in the community study [Christensen et al., 2001].

513

514 The version of the dynamo code that we have used in this thesis has been benchmarked  
515 against well known studies in thermal instabilities and kinematic dynamos such as the  
516 Kumar-Roberts Kinematic Dynamo Model as presented in Kuang and Bloxham [1999].  
517 However, it has not been previously benchmarked against the Christensen et al. [2001]  
518 study. This is due to the fact that our code version implements an approximation (non-  
519 axisymmetric inertial term is ignored as fast modes associated with the inertial force are  
520 irrelevant to our study) to the momentum equation that is valid for the parameter regime  
521 we work in for our planetary simulations, but is not as good for the parameter regime of  
522 the community benchmark. A newer version of our code (although not implemented in  
523 this thesis) includes the non-axisymmetric inertial term and has been successfully bench-  
524 marked in Jiang and Kuang [2008]. Although we don't expect perfect benchmarking of  
525 our version of the code with the community benchmark (due to the approximation), here  
526 we have run the benchmark case with our code to determine the effect of this approxi-  
527 mation. By doing so, we hope to ease the concerns of the community on the validity of

Parameters	Non-magnetic Convection	Conducting Inner Core Dynamo
Input Parameters:		
$r_{io}$	0.35	0.35
$q_k$	5	5
$E$	$2.1125 e - 4$	$2.1125 e - 4$
$Ro_M$	$4.2250 e - 5$	$4.2250 e - 5$
$Ra_{FT}$	1690.617	1859.679
$l_0$	No hyperdiffusivity	40
Output Parameters:		
$E_B$	NA	782 (845.6)
$T$	0.3386 (0.42812)	0.3292
$v_\phi$	-9.4393 (-10.1571)	-6.8237
$B_\theta$	NA	-5.9783

Table 2.2: Benchmark results. The values in the brackets are expected values from Christensen et al. [2001]. Since the values of  $T$ ,  $v_\phi$  and  $B_\theta$  for conducting inner core dynamo models were not provided by Christensen et al. [2001], we have not presented them here.

528 our model.

529

530 We created the recommended initial conditions and the non-dimensional parameters of  
 531 the benchmark case. Due to a difference in choice of parameter definitions between our  
 532 model and the Christensen et al. [2001] study, we had to convert non-dimensional param-  
 533 eter values accordingly. The conversions are demonstrated in Appendix D. The initial  
 534 magnetic fields created for benchmarking are shown in Figure 2.10. The model parame-  
 535 ters used along with the results are shown in Table 2.2. The resulting values for  $T$ ,  $v_\phi$   
 536 and  $B_\theta$  were obtained by taking a point at mid-depth ( $r = (r_i + r_o)/2$ ) in the equatorial  
 537 plane ( $\theta = \pi/2$ ) at  $\phi$  coordinates where both  $v_r = 0$  and  $\frac{\partial}{\partial \phi} u_r > 0$ , as shown in figures  
 538 2.11 and 2.12.

539

540 The visual aspects of our conducting inner core dynamo solutions and the benchmark

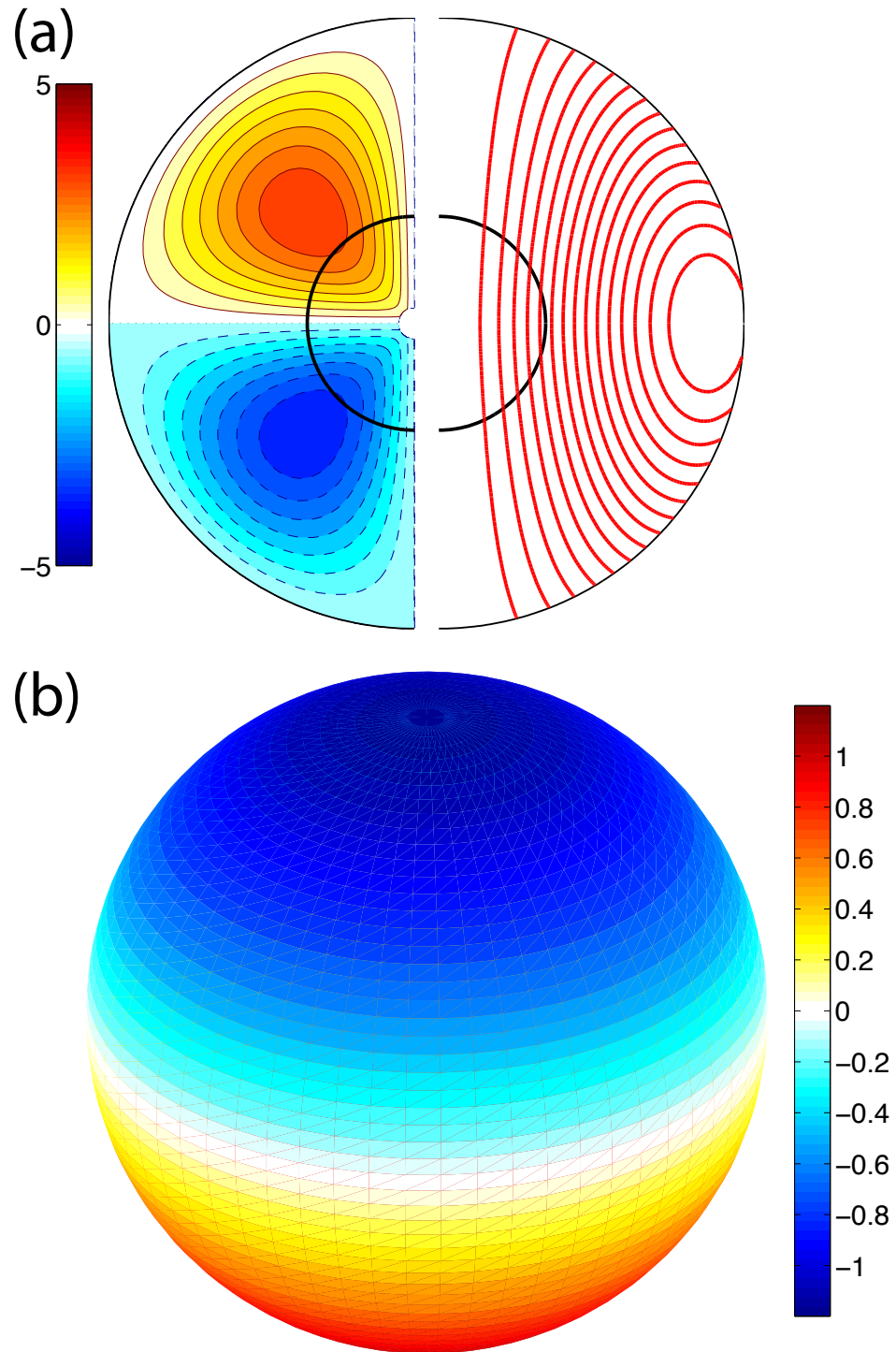


**Figure 2.10: Initial magnetic field for benchmark studies:** (a) Axisymmetric magnetic field. The toroidal magnetic fields are shown on the left where red (blue) denotes prograde (retrograde) direction and streamlines of poloidal magnetic fields are shown on the right where red (blue) denotes clockwise (anti-clockwise) direction, (b) Radial magnetic field at the outer core boundary. Red and blue colours represent different field directions.

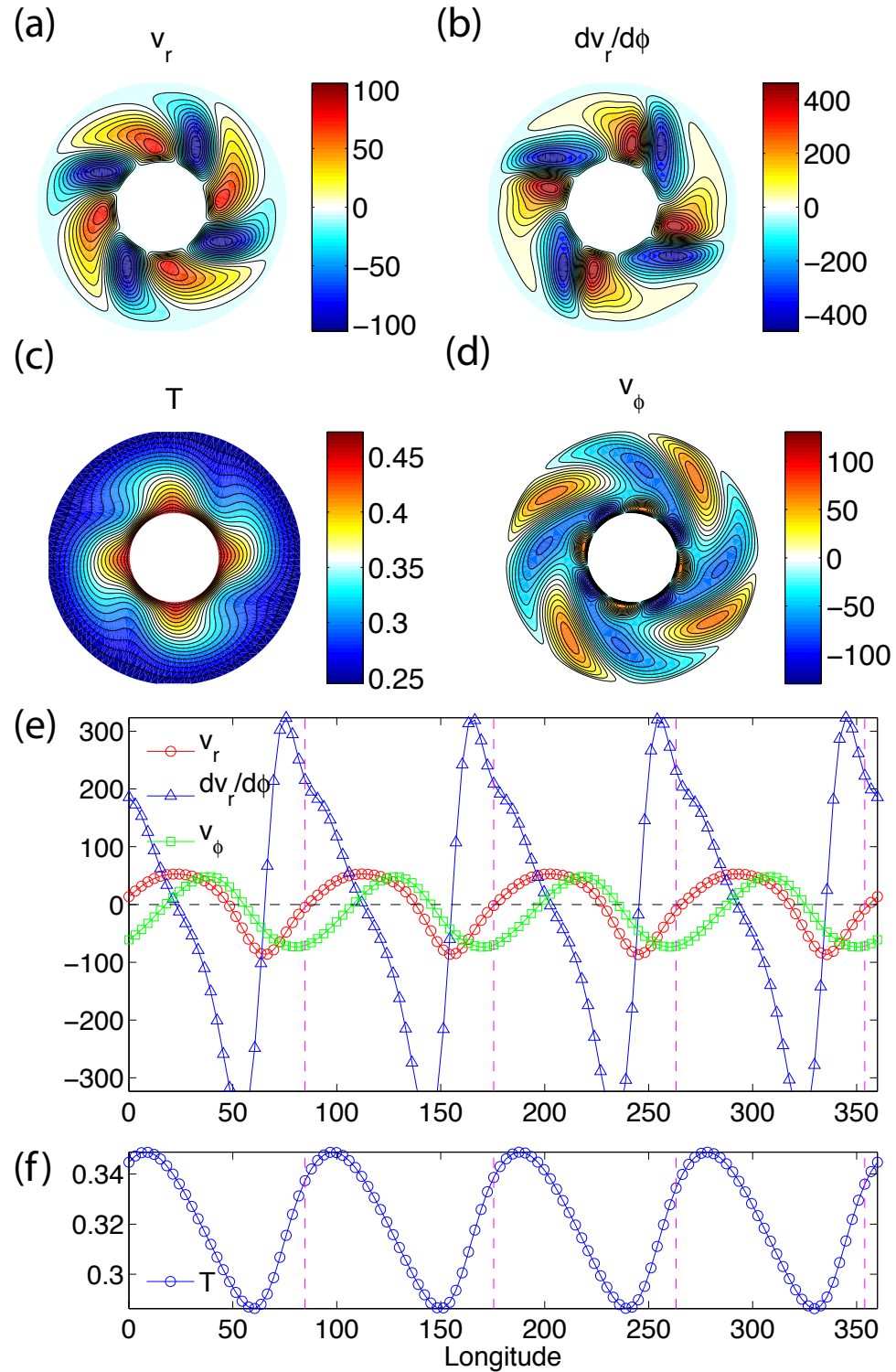


Figure 2.11: **Benchmarking Non-magnetic Convection Models:** Equatorial slice of (a)  $v_r$ , (b)  $\frac{\partial}{\partial\phi}v_r$ , (c)  $T$ , (d)  $v_\phi$ , and profile of (e)  $v_r$ ,  $\frac{\partial}{\partial\phi}v_r$  and  $v_\phi$ , and (f)  $T$  taken at mid depth along the equator.

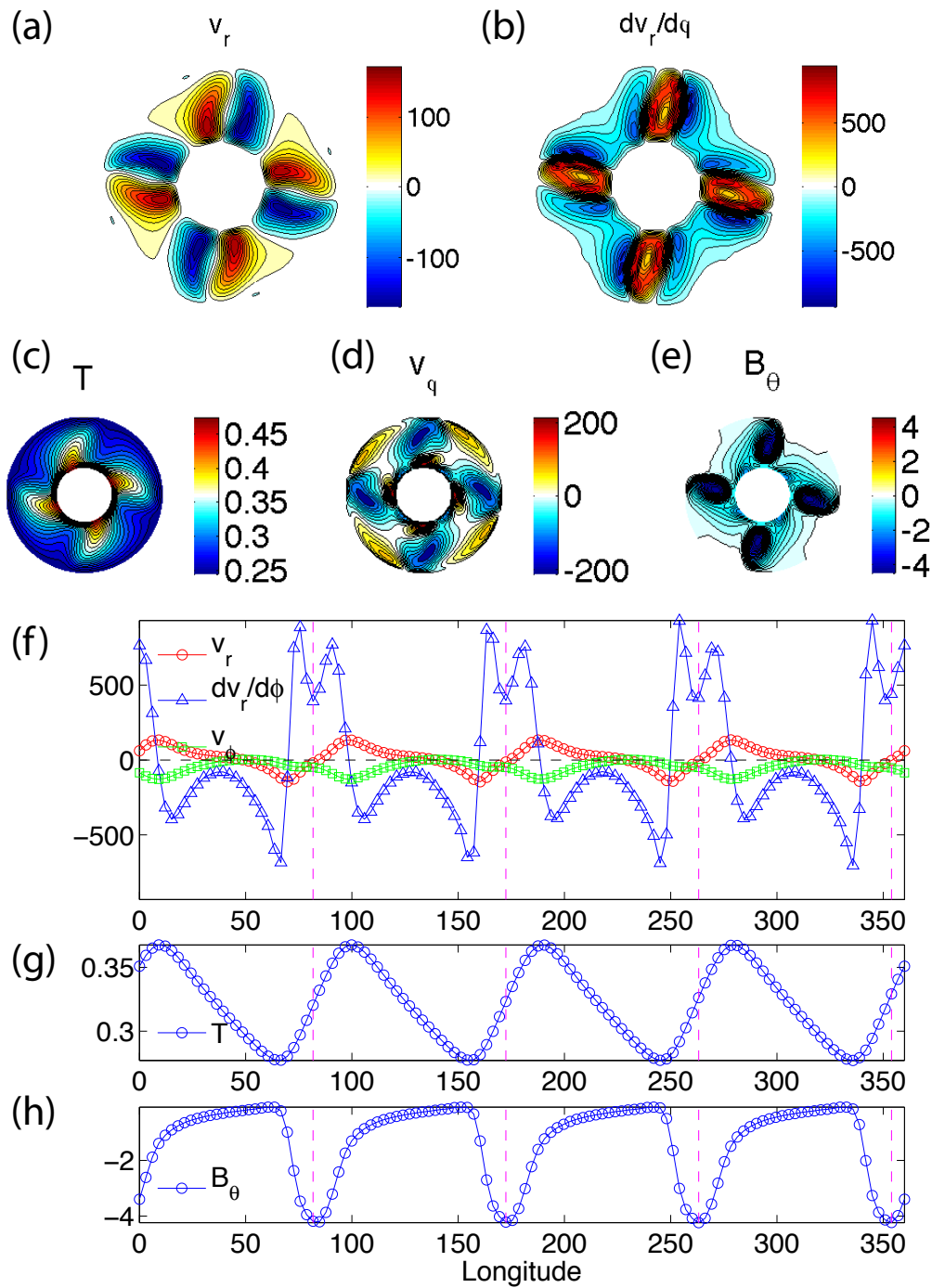
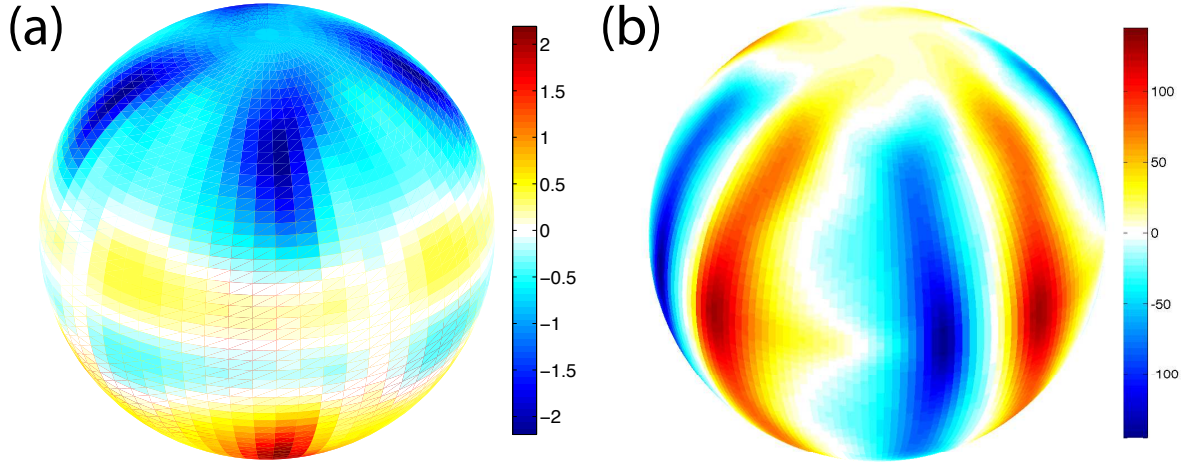


Figure 2.12: **Benchmarking Conducting Inner Core Dynamo Model:** Equatorial slice of (a)  $v_r$ , (b)  $\frac{\partial}{\partial \phi} v_r$ , (c)  $T$ , (d)  $v_\phi$ , (e)  $B_\theta$ , and profile of (f)  $v_r$ ,  $\frac{\partial}{\partial \phi} v_r$  and  $v_\phi$ , (g)  $T$  and (h)  $B_\theta$  at mid depth along the equator.



**Figure 2.13: Benchmark Illustrative Solution for Comparison:** (a) Radial magnetic field at the outer core boundary, (b) Radial velocity field at mid depth in the shell. In both plots, red and blue colours represent different field directions.

study [Christensen et al., 2001] were very similar, i.e. convection was columnar, the magnetic field on the outer core boundary was strongly dipolar, and the dominant convective and magnetic spectral modes were the same as shown in figure 2.13, which should be compared to figure 1 in [Christensen et al., 2001].

545

The magnitude of the temperature, magnetic and velocity fields are 20.9 %, 7.5 % and 7 % smaller in magnitude respectively than the Christensen et al. [2001] benchmark study. This was expected due to the parameter regime of the benchmark case and our neglect of the non-axial inertial term in our model. The parameters used for the benchmark study are far from planetary values and are also not in the asymptotic regime that is computationally possible today or in a parameter regime where dynamo models usually operate. For example, the Magnetic Rossby number ( $Ro_M$ ) of Earth is  $\approx 10^{-9}$  and for the benchmark study we have used  $4.225 \times 10^{-5}$ . The large  $Ro_M$  unrealistically amplifies the effect of the inertial force. Also, the Rayleigh number used is only  $\approx 2Ra_C$  (where,  $Ra_C$  is critical Rayleigh number), which is close to onset of dynamo action and far from the turbulent flow regime.

557

558 It would be interesting if a benchmark was developed closer to the regime where dynamo  
559 models usually operate so we could really test the influence of this approximation. None  
560 of the numerical models developed so far have been able to reach control parameters  
561 (like Ekman number, Magnetic Prandtl number etc.) that are in planetary regimes. The  
562 limiting behaviour of dynamo models at realistic parameters still remain challenging. For  
563 the study presented in this thesis, since we are able to reproduce the critical modes of  
564 magnetic and velocity fields and also able to match the field intensities as mentioned  
565 above, we feel justified to use this model to understand fundamental behaviour like the  
566 influence of inner core conductivity and boundary conditions.

567 **Chapter 3**

568 **Effect of Inner Core Conductivity**

569 The results of this chapter have been published in [Dharmaraj and Stanley \[2012\]](#).

570 **3.1 Introduction**

571 As previously described in Chapter 1, even though the Earth’s inner core occupies only  
572 about 4 % of the total core volume, it has significant influences on core dynamics. The  
573 solid inner core acts as a barrier to fluid flow since the flow structure must take into  
574 account the presence of the inner core boundary, which results in the formation of the  
575 tangent cylinder. The fluid inside the tangent cylinder includes both small and large scale  
576 convective motions. The small scale convective motions consist of helical plumes. The  
577 large scale flows consists of a rising motion close to the poles and a descending motion  
578 close to the tangent cylinder in the meridional direction. Another form of large scale  
579 motion is caused by the thermal winds (azimuthal baroclinic flow) in the prograde direc-  
580 tion close to the inner core boundary and retrograde direction close to the core mantle  
581 boundary [[Hogg and Stommel, 1985](#)]. [Aurnou et al. \[2003\]](#) experimentally found that as  
582 the Rayleigh number is steadily increased, a transition from weak thermal wind that is  
583 solely driven by conduction, to convection along the tangent cylinder, to quasigeostrophic  
584 convection, to 3D turbulent convection occurs. They also show that the thermal wind

585 scale with the ratio of the mean buoyancy flux to the rotation rate.

586

587 Inside the tangent cylinder, the thermal wind produces azimuthal magnetic fields by  
588 shearing radial and meridional magnetic fields [Aurnou et al., 1998]. The converging  
589 meridional flow close to the inner core boundary concentrates the radial and meridional  
590 magnetic field, while the diverging meridional flow close to the core mantle boundary  
591 spreads the radial and meridional magnetic field towards lower latitudes [Glatzmaier and  
592 Roberts, 1995a].

593

594 Olson and Aurnou [1999] examined the Earth's magnetic field along with its secular vari-  
595 ation from 1870 to 1990 and found the existence of an anticyclonic polar vortex along  
596 with a polar upwelling in the northern hemisphere of the core as observed in some nu-  
597 matical models. Sreenivasan and Jones [2005] used a fully 3D model with no longitudinal  
598 symmetry and found that polar vortex is offset from the rotation axis by 10 degrees and  
599 hence is non-axisymmetric and could drift azimuthally even within a magnetic diffusion  
600 time. Sreenivasan and Jones [2006a] found that when the inertial forces are strong, the  
601 thermal winds are cyclonic but in the presence of magnetic field if the Lorentz forces  
602 are strong enough then the thermal winds are anticyclonic as observed in the Earth's  
603 polar region through secular variation. They also found that when convection is strong  
604 in the tangent cylinder, it is controlled by the magnetic field (if its intensity is strong)  
605 and that the vortex plume becomes thinner. In addition, the strong upwelling in the  
606 tangent cylinder could expel magnetic field and created regions of weak or reversed flux  
607 patches that drift westward at a rotation rate slower than the vortex plume. These stud-  
608 ies demonstrate the importance of modelling a spherical shell rather than a full sphere  
609 when simulating the geodynamo in order to capture the effects of the inner core on the  
610 fluid dynamics of a rapidly rotating spherical shell.

611

612 The inner core can also influence the dynamo generation through its finite electrical con-  
613 ductivity. Magnetic field lines that diffuse from the fluid outer core into the solid inner  
614 core are governed by the slower magnetic diffusion time scale in the inner core rather  
615 than the advective time scale of the outer core. This suggests that the inner core may  
616 have a stabilizing influence through its anchoring effect on magnetic field variability and  
617 could affect reversals and excursions in planetary cores. Figure 3.1 shows an illustration  
618 of the anchoring effect that a conducting material provides and an insulating material  
619 does not provide. This can also be considered as an illustration of the frozen-in-field  
620 theorem. In the figure, consider the insulating case where we have placed an insulator  
621 below a finitely conducting box. If these boxes are kept under the influence of magnetic  
622 field then magnetic field can diffuse into the finitely conducting blue box. If we move the  
623 insulating box towards the right, the magnetic field does not change. In the conducting  
624 case, if the lower finitely conducting block is moved to the right, it carries the magnetic  
625 field lines with it as shown in 3.1d. Also, we can see that the field lines are concentrated  
626 in the shear zone at the boundary between the blocks (in planetary cores it would be  
627 analogue to the inner core boundary). Magnetic fields are thus generated at the bound-  
628 aries.

629

630 Numerical dynamo models have been successful in generating the major observable fea-  
631 tures of the geomagnetic field like its dipole dominance, field strength, secular variation  
632 and stochastic dipole reversals (e.g. Kageyama et al. [1994], Glatzmaier and Roberts  
633 [1995b,a], Kuang and Bloxham [1997, 1999], Busse et al. [1998], Christensen and Olson  
634 [1998], Takahashi et al. [2005]). For a recent review of numerical dynamo models and  
635 observations of the geomagnetic field, see Dormy and le Mouël [2008], Wicht and Tilgner  
636 [2010].

637

638 Some numerical models incorporate a conducting inner core (**CIC**) [Glatzmaier and

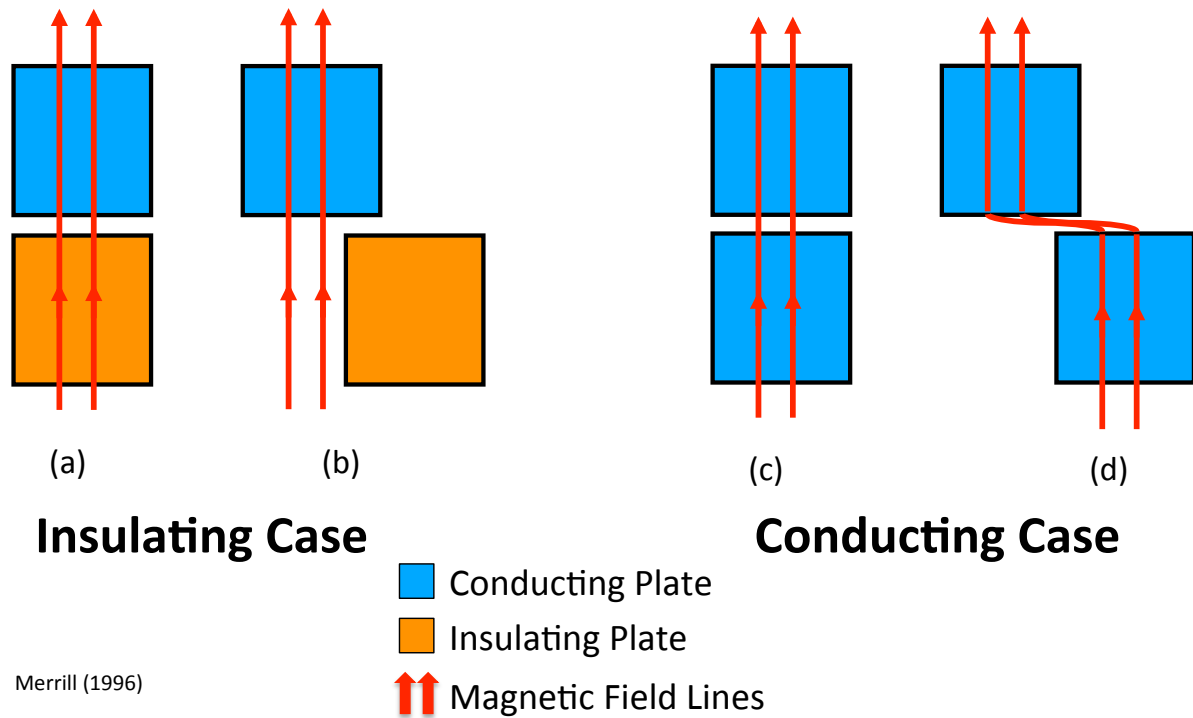


Figure 3.1: Illustration of the anchoring effect that a conducting material provides and an insulating material does not provide. In these figures, the blue boxes are finitely conducting and the orange boxes are insulators. The red lines are the magnetic field lines.

639 Roberts, 1995b, Kuang and Bloxham, 1999, Sakuraba and Kono, 1999] while others in-  
640 corporate an insulating inner core (**IIC**) [Christensen and Olson, 1998, Olson et al., 1999,  
641 Kageyama and Sato, 1997, Kitauchi and Shigeo]. Incorporating an IIC eases numerical  
642 calculations because the inner core magnetic field can be represented as a potential field  
643 rather than solving the magnetic induction equation in the inner core. The choice of  
644 using an IIC is usually justified by the smallness of the inner core and the idea that such  
645 a small CIC might not significantly alter dynamo processes.

646

647 Various studies have investigated the influence of inner core conductivity in modeling  
648 planetary dynamos. Some studies [Hollerbach et al., 1991, Hollerbach and Jones, 1993,  
649 Gubbins, 1999, Stanley and Bloxham, 2006] suggest that the finite conductivity of the  
650 inner core reduces the frequency of reversals and affects magnetic field morphology while  
651 others [Wicht, 2002, Busse and Simitev, 2008] suggest the inner core conductivity does  
652 not have a significant effect on the resulting magnetic fields.

653

654 Hollerbach and Jones [1993] employed an axisymmetric mean field dynamo model with  
655 prescribed buoyancy force. Their results showed that the presence of a conducting inner  
656 core averages out large, rapid fluctuations in the outer core and results in a stable dipolar  
657 field. This idea was confirmed by Glatzmaier and Roberts [1995b] using 3D, convection  
658 driven, self-consistent numerical simulations. They found that IIC models had a ten-  
659 dency to reverse more frequently than CIC models. Stanley and Bloxham [2006] used 3D  
660 dynamo models and demonstrated that thin shell IIC models resulted in frequent rever-  
661 sals and non-axisymmetric, non-dipolar magnetic fields. Their focus was understanding  
662 Uranus' and Neptune's magnetic fields and therefore their core geometry (a thin convect-  
663 ing shell) was not Earth-like. Their results demonstrated that if the inner core is large  
664 enough, then its conductivity does affect the dynamics.

665

666 In contrast, Wicht [2002] showed that in their 3D dynamo simulations with Earth-like  
667 inner core sizes, the influence of inner core conductivity on reversal frequency is insignif-  
668 icant. Busse and Simitev [2008] suggest that reversals and excursions in their models  
669 are independent of the conductivity of the inner core due to its small size, but their  
670 conclusions are based on comparisons of IIC models and perfectly conducting inner core  
671 models. Their CIC models therefore do not allow field to diffuse into the inner core nor  
672 respond to magnetic torques between the fluid outer core and the solid inner core. Other  
673 properties of the inner core such as its relative size (outer core shell thickness) may also  
674 affect reversal rate and field morphology e.g. [Roberts and Glatzmaier, 2001, Stanley  
675 and Bloxham, 2006].

676

677 In this chapter we use numerical dynamo models to study the influence of inner core  
678 conductivity on magnetic field generation and attempt to explain the diverse results of  
679 these previous studies. In section 3.2 we describe our numerical model, and in section 3.3  
680 we present our results. A discussion of the discrepancy between various models is given  
681 in section 3.4 and conclusions are presented in section 3.5.

## 682 3.2 Numerical Model

683 We use the Kuang and Bloxham 3D numerical dynamo model [Kuang and Bloxham, 1997,  
684 1999] to study magnetic field generation in a spherical, rotating, Boussinesq, electrically  
685 conducting fluid shell surrounding a solid inner core as described in detail in Chapter 2.

686

687 The control parameters and boundary conditions that we use to compare the conducting  
688 and insulating inner core models are given in table 3.1. The boundary conditions given  
689 in table 3.1 are applied at both the inner and outer core boundaries. In our models, the  
690 inner core is free to oscillate in response to magnetic and viscous torques. We compare

691 dynamo models with conducting and insulating inner cores.

692

693 In the CIC models, the inner and outer core have the same conductivities. In the IIC  
694 models, the inner core is  $10^4$  times less conducting than the outer core. It was logically  
695 simpler to set the conductivity of the inner core to a very small value rather than to  
696 change the boundary condition to a perfectly insulating inner core. We have run a  
697 few dynamo simulations with perfectly insulating boundaries and found no differences  
698 compared to cases with  $\eta_{io} = 10^4$ . We also include a model of pure thermal convection  
699 (C) in the absence of magnetic fields. This model is not influenced by the conductivity of  
700 the inner core. The simulations were run for many magnetic dipole diffusion times and  
701 the results presented in the next section were analyzed after the initial transients decayed.  
702 For convenience of the reader, we choose a minimalistic approach and first compare a  
703 single pair of models with identical parameters except for inner core conductivity: CIC-7  
704 and IIC-7. These models have fixed heat flux and viscous stress-free boundary conditions  
705 that were run at highly supercritical ( $\approx 50 \times$  critical) Rayleigh number.

Model	Ra	Reversal	$E_B$	$E_k$	$\frac{E_{B_T}}{E_{B_P}}$	$\frac{E_{B_P}^{Ndi}}{E_{B_P}}$	$\frac{E_{B_P}^{Naxi}}{E_{B_P}}$	$\frac{E_{B_T}^{Naxi}}{E_{B_T}}$	$\frac{E_{k_P}^{Naxi}}{E_{k_P}}$	$\frac{E_{k_T}^{Naxi}}{E_{k_T}}$	$\frac{L_v}{L_B}$	Correlation%
Fixed Heat Flux and Viscous Stress-Free												
$E = 2 \times 10^{-5}$ and $R_{o_M} = 2 \times 10^{-5}$												
CIC-1*	2,500	Yes	0.24	$3.3 \times 10^5$	3.0	0.88	0.50	0.49	0.99	0.70	2.8	26
IIC-1*		Yes	0.25	$3.3 \times 10^5$	2.6	0.88	0.44	0.46	0.99	0.70	3.7	24
CIC-2	5,000	No	1.7	$8.6 \times 10^4$	1.2	0.40	0.33	0.48	0.98	0.77	1.0	53
IIC-2*		Yes	0.45	$3.8 \times 10^5$	2.3	0.91	0.80	0.81	0.98	0.14	50	31
CIC-3	7,500	No	2.7	$1.4 \times 10^5$	1.1	0.42	0.36	0.52	0.98	0.76	1.0	60
IIC-3*		Yes	0.84	$4.5 \times 10^5$	1.7	0.90	0.57	0.57	0.95	0.19	45	32
CIC-4	15,000	No	5.8	$2.5 \times 10^5$	1.2	0.47	0.42	0.52	0.97	0.75	1.3	75
IIC-4*		Yes	1.7	$8.0 \times 10^5$	1.9	0.93	0.75	0.63	0.94	0.27	40	34
Fixed Heat Flux and Viscous Stress-Free												
$E = 6 \times 10^{-5}$ and $R_{o_M} = 2 \times 10^{-5}$												
CIC-5	6,000	No	2.2	$8.4 \times 10^4$	1.0	0.43	0.33	0.44	0.98	0.64	1.1	71
IIC-5		Yes	0.29	$1.6 \times 10^5$	2.1	0.93	0.62	0.66	0.98	0.37	150	25
CIC-6	7,500	No	3.1	$1.1 \times 10^5$	1.2	0.41	0.35	0.40	0.98	0.62	1.0	60
IIC-6		Yes	0.31	$2.1 \times 10^5$	2.0	0.95	0.79	0.79	0.97	0.36	260	24
CIC-7	15,000	No	5.8	$2.1 \times 10^5$	1.2	0.50	0.46	0.49	0.97	0.70	1.1	82
IIC-7		Yes	0.81	$6.1 \times 10^5$	2.0	0.96	0.80	0.74	0.91	0.26	50	27
C	15,000			$1.4 \times 10^6$					0.90	0.10		
Fixed Heat Flux and No-Slip												
$E = 6 \times 10^{-5}$ and $R_{o_M} = 2 \times 10^{-5}$												
CIC-8	5,000	No	2.9	$6.3 \times 10^4$	1.3	0.37	0.31	0.40	0.98	0.73	0.80	69
IIC-8		Yes	0.16	$1.2 \times 10^5$	1.8	0.83	0.71	0.78	0.97	0.51	98	13
CIC-9	7,500	No	4.9	$8.3 \times 10^5$	1.2	0.41	0.34	0.43	0.96	0.74	1.5	76
IIC-9		Yes	0.35	$1.9 \times 10^5$	2.0	0.92	0.80	0.80	0.97	0.44	120	17
Fixed Temperature and Viscous Stress-Free												
$E = 2 \times 10^{-4}$ and $R_{o_M} = 1 \times 10^{-4}$												
CIC-10*	2,500	No	4.2	$5.8 \times 10^4$	0.69	0.33	0.27	0.49	0.96	0.73	1.1	61
IIC-10*		No	1.8	$4.3 \times 10^4$	0.90	0.41	0.30	0.41	0.95	0.68	61	43
CIC-11	5,000	Yes	2.6	$8.1 \times 10^5$	2.3	0.95	0.82	0.74	0.89	0.16	3.0	35
IIC-11		Yes	6.1	$1.6 \times 10^6$	2.6	0.96	0.81	0.69	0.83	0.15	140	29
Fixed Temperature and No-Slip												
$E = 2 \times 10^{-4}$ and $R_{o_M} = 1 \times 10^{-4}$												
CIC-12	2,500	No	1.3	$4.7 \times 10^4$	0.93	0.42	0.31	0.45	0.94	0.64	1.2	38
IIC-12*		No	2.0	$4.2 \times 10^4$	0.95	0.39	0.28	0.41	0.93	0.64	69	50
CIC-13*	5,000	Yes	0.28	$1.6 \times 10^5$	1.5	0.94	0.80	0.56	0.90	0.50	2.1	6
IIC-13*		Yes	0.21	$1.6 \times 10^5$	1.6	0.91	0.72	0.59	0.92	0.55	890	8
CIC-14	7,500	Yes	0.62	$3.0 \times 10^5$	1.2	0.95	0.82	0.73	0.88	0.45	2.3	8
IIC-14		Yes	0.37	$2.9 \times 10^5$	1.3	0.96	0.79	0.73	0.89	0.52	190	10

Table 3.1: **Results of CIC and IIC Models.** The column headings from left to right are: model ID, Rayleigh number ( $Ra$ ), reversal frequency, magnetic energy ( $E_B$ ), kinetic energy ( $E_k$ ), ratio of total toroidal ( $E_{B_T}$ ) to total poloidal ( $E_{B_P}$ ) magnetic energy, ratio of non-dipolar ( $E_{B_P}^{Ndi}$ ) to total poloidal magnetic energy, non-axisymmetric ( $E_{B_P}^{Naxi}$ ) to total magnetic poloidal energy, non-axisymmetric ( $E_{B_T}^{Naxi}$ ) to total magnetic toroidal energy, ratio of non-axisymmetric ( $E_{k_P}^{Naxi}$ ) to total ( $E_{k_P}$ ) poloidal velocity, ratio of non-axisymmetric ( $E_{k_T}^{Naxi}$ ) to total ( $E_{k_T}$ ) toroidal velocity, ratio of velocity ( $L_v$ ) to magnetic ( $L_B$ ) length scale and the correlation of the Lorentz to Coriolis force balance in %.  $q_k = 1$  in all the models. Details on implementation of the boundary conditions can be found in [Kuang and Bloxham \[1999\]](#). In all the models, the number of radial grid points used in the inner core is  $N_i = 36$  and the maximum spherical harmonic degree is 58 and order is 53. All models have  $N_o = 64$  radial grid points in the outer core except for those models marked with a \* in the table, which have  $N_o = 93$ . We employ hyper-diffusivity starting at degree 30 or higher to work at more supercritical Rayleigh numbers than feasible without.

### 3.3 Results

We begin by examining the observable features of the magnetic fields such as the dipole tilt and surface magnetic power spectra. We then examine the characteristics of the magnetic and velocity fields inside the dynamo generation region.

#### 3.3.1 Dipole Tilt

Figure 3.2 shows the dipole tilts for the models CIC-7 and IIC-7. Model CIC-7 maintains a strong dipolar field that does not reverse on the time scale we investigate. In contrast, model IIC-7 undergoes many excursions and reversals. It appears that the resulting magnetic fields in our models are strongly dependent on the conductivity of the inner core. Specifically, a conducting inner core can promote the generation of an axially dipolar field and reduce the reversal frequency.

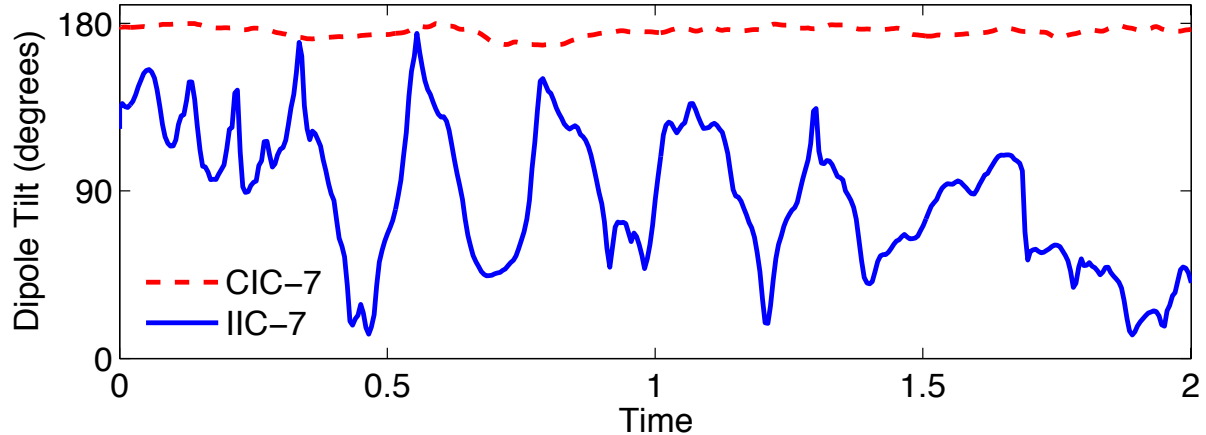


Figure 3.2: **Dipole Tilt versus Time for CIC-7 and IIC-7 models.** Time is non-dimensional in units of magnetic dipole diffusion time.

### 718 3.3.2 Surface Magnetic Power Spectra

719 The difference in the observed magnetic field between the CIC-7 and IIC-7 models can  
 720 be demonstrated through their surface magnetic power spectra. For definition of the  
 721 surface magnetic power spectra please refer to Section 2.3.1 in Chapter 2. In Figure 3.3  
 722 we show the resulting average surface magnetic power spectra over a magnetic dipole  
 723 diffusion time for models CIC-7 and IIC-7. This figure shows that a conducting inner  
 724 core results in axially dipolar dominated fields while an insulating inner core results in  
 725 non-axisymmetric, non-dipolar magnetic fields.

### 726 3.3.3 Magnetic Energy

727 In this section, we examine the characteristics of dynamo models inside the dynamo  
 728 generation region in order to understand the dynamics that generate the potential  
 729 fields that are observed outside the core. For the definition of magnetic energy and the  
 730 toroidal and poloidal partitioning please refer to Section 2.3.1 in Chapter 2. The toroidal  
 731 and poloidal energies can further be partitioned into axisymmetric and non-axisymmetric  
 732 components. Figure 3.4 shows the axisymmetric and non-axisymmetric components of  
 733 the toroidal and poloidal magnetic energies. We can characterize the CIC-7 and IIC-7

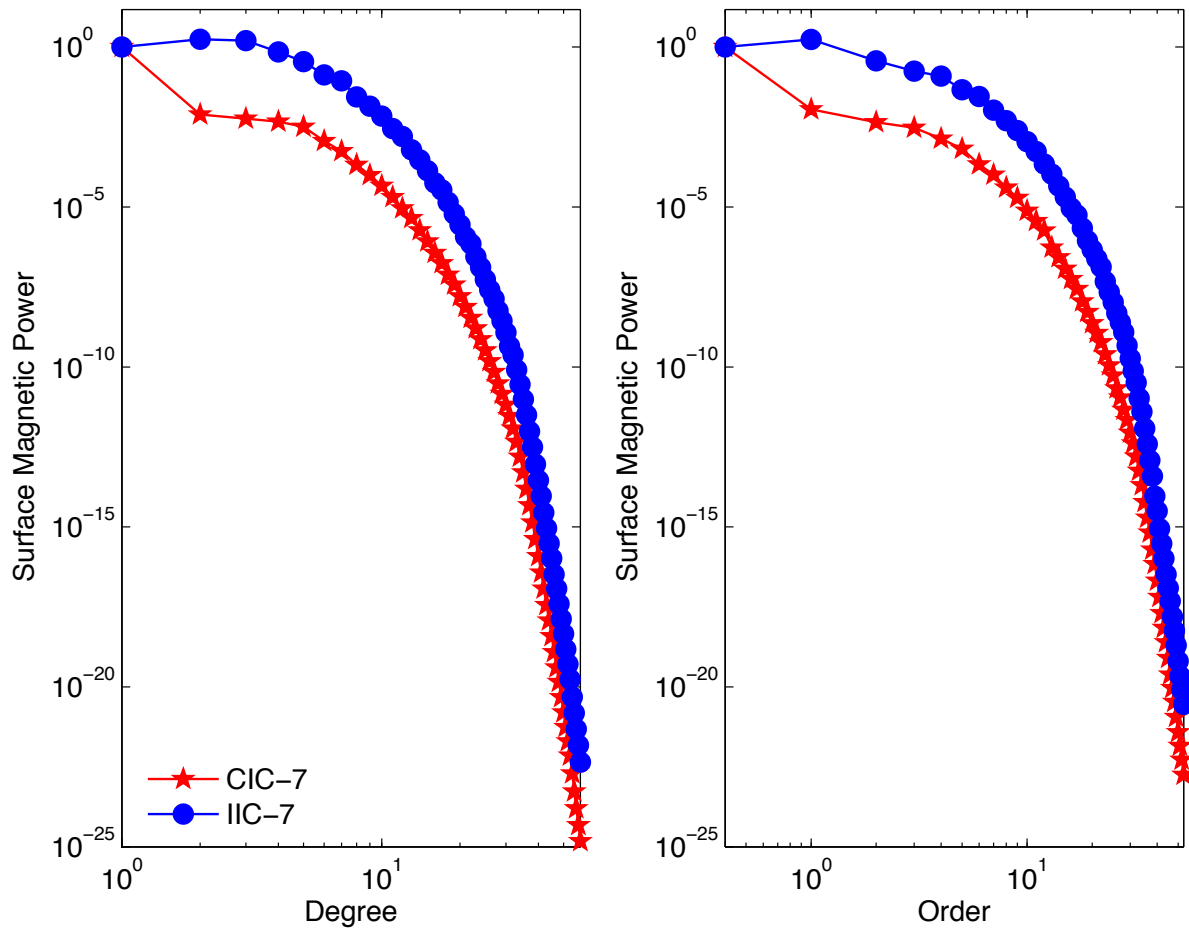


Figure 3.3: **Surface Magnetic Power Spectra for CIC-7 and IIC-7 models.** Left plot shows power vs degree normalized to the dipole ( $l=1$ ) power and the right plot shows power vs order normalized to axisymmetric ( $m=0$ ) power.

734 models as having stronger toroidal energy than poloidal energy but in model CIC-7  
735 (Figure 3.4a) the poloidal energy is dominated by its axisymmetric component and  
736 its toroidal energy has equal contribution from its axisymmetric and non-axisymmetric  
737 components. In contrast, in model IIC-7 (Figure 3.4b), the toroidal and poloidal energies  
738 are both dominated by their non-axisymmetric components.

739

740 We can also decompose the toroidal and poloidal energies into dipole and non-dipole  
741 components. The non-dipolar to total energy ratios of the CIC-7 model is 0.5 and the  
742 IIC-7 model is 0.96. Therefore, the CIC-7 model gets equal contribution of energy from  
743 its dipolar and non-dipolar components whereas the IIC-7 model is dominated by its non-  
744 dipolar components. The potential field that is observed outside the dynamo generation  
745 region is an extension of this poloidal magnetic field.

### 746 3.3.4 Magnetic Field

747 Since the CIC-7 and IIC-7 models result in strong magnetic fields but the CIC-7 model  
748 is dipolar and the IIC-7 model is non-dipolar, we compare the magnetic field morphology  
749 of CIC-7 and IIC-7 models at the core mantle boundary (CMB) and inside the dynamo  
750 generation region. Although Figure 3.5 and Figure 3.6 present snapshots in time of  
751 the resulting magnetic field morphology of models CIC-7 and IIC-7, the characteristics  
752 are similar at other times. Model CIC-7 (Figure 3.5a) produces a magnetic field that  
753 is strong, mainly dipolar with some non-axisymmetry and has westward-drifting flux  
754 patches along the equator (properties that are similar to Earth's field). Model IIC-7  
755 (Figure 3.5b), on the other hand, produces a magnetic field that is weaker than CIC-7,  
756 non-dipolar and non-axisymmetric.

757

758 Figures 3.6a and 3.6b show a meridional slice of the axisymmetric toroidal (left) and  
759 poloidal (right) magnetic fields of models CIC-7 and IIC-7 respectively to demonstrate

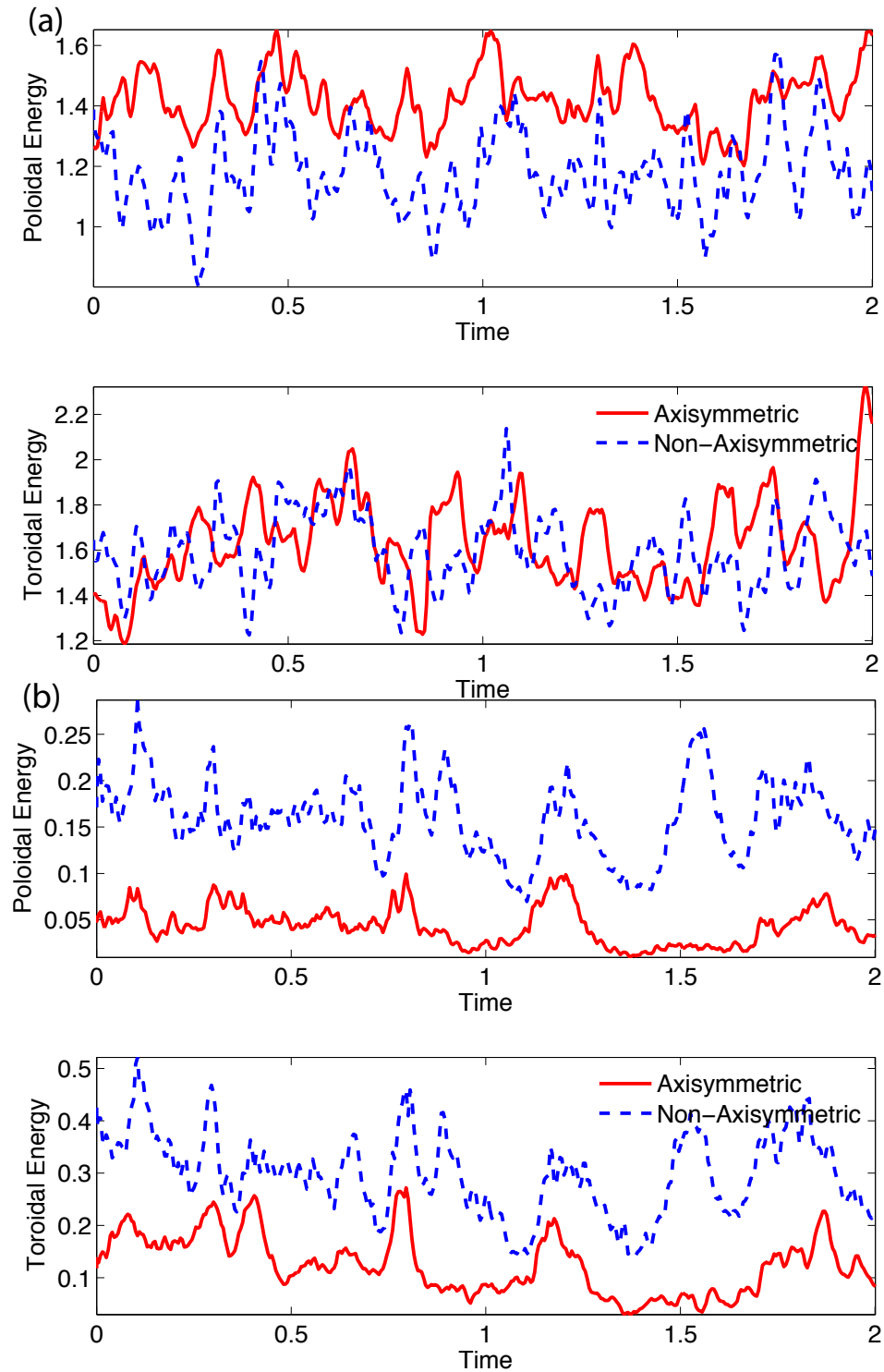


Figure 3.4: **Magnetic Energy versus Time for the CIC-7 (a) and IIC-7 (b) models.** The top (bottom) plot shows the poloidal (toroidal) magnetic energy. The axisymmetric energy is shown in solid red line and the non-axisymmetric energy is shown in dashed blue line. The units are non-dimensional.

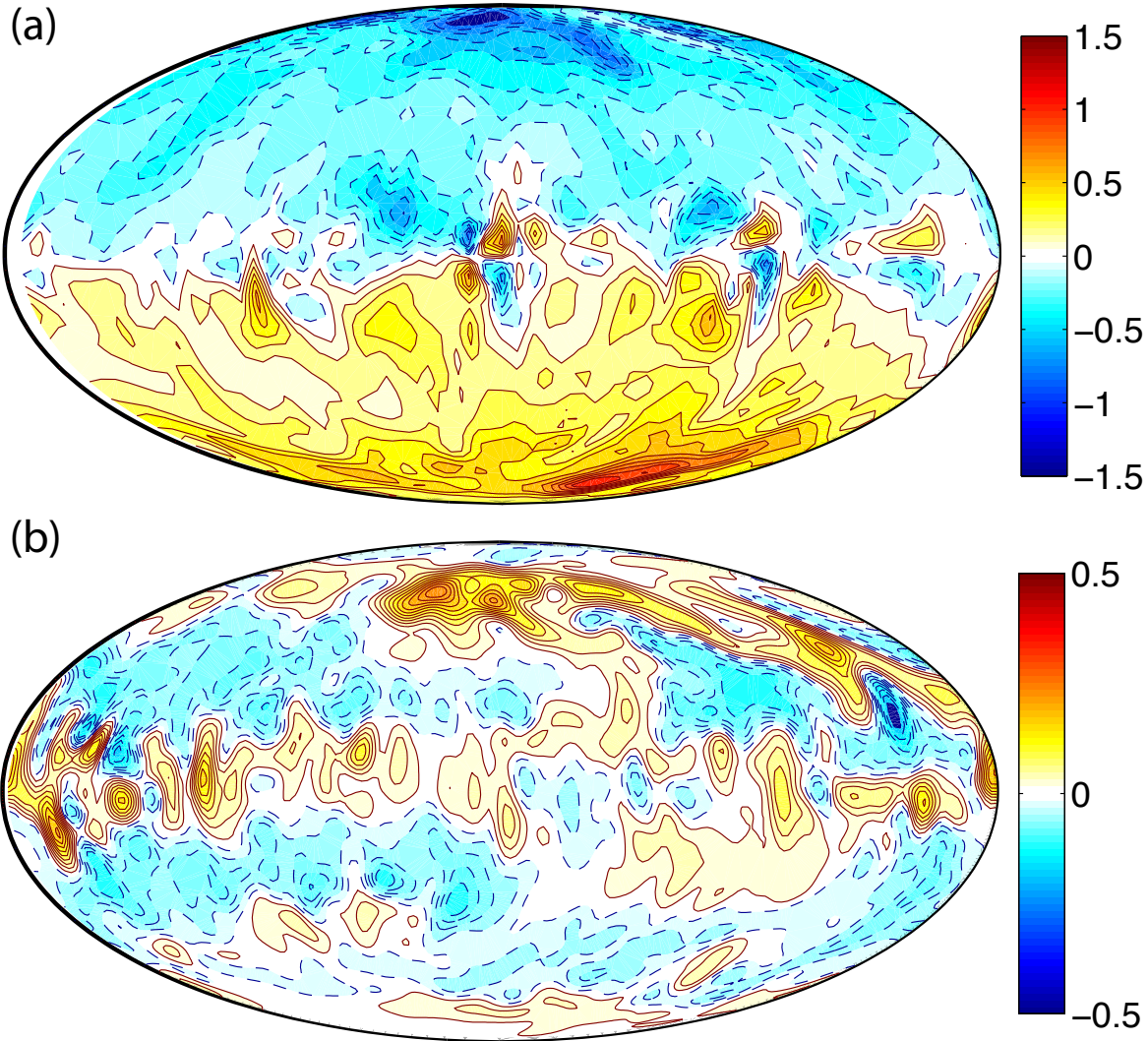
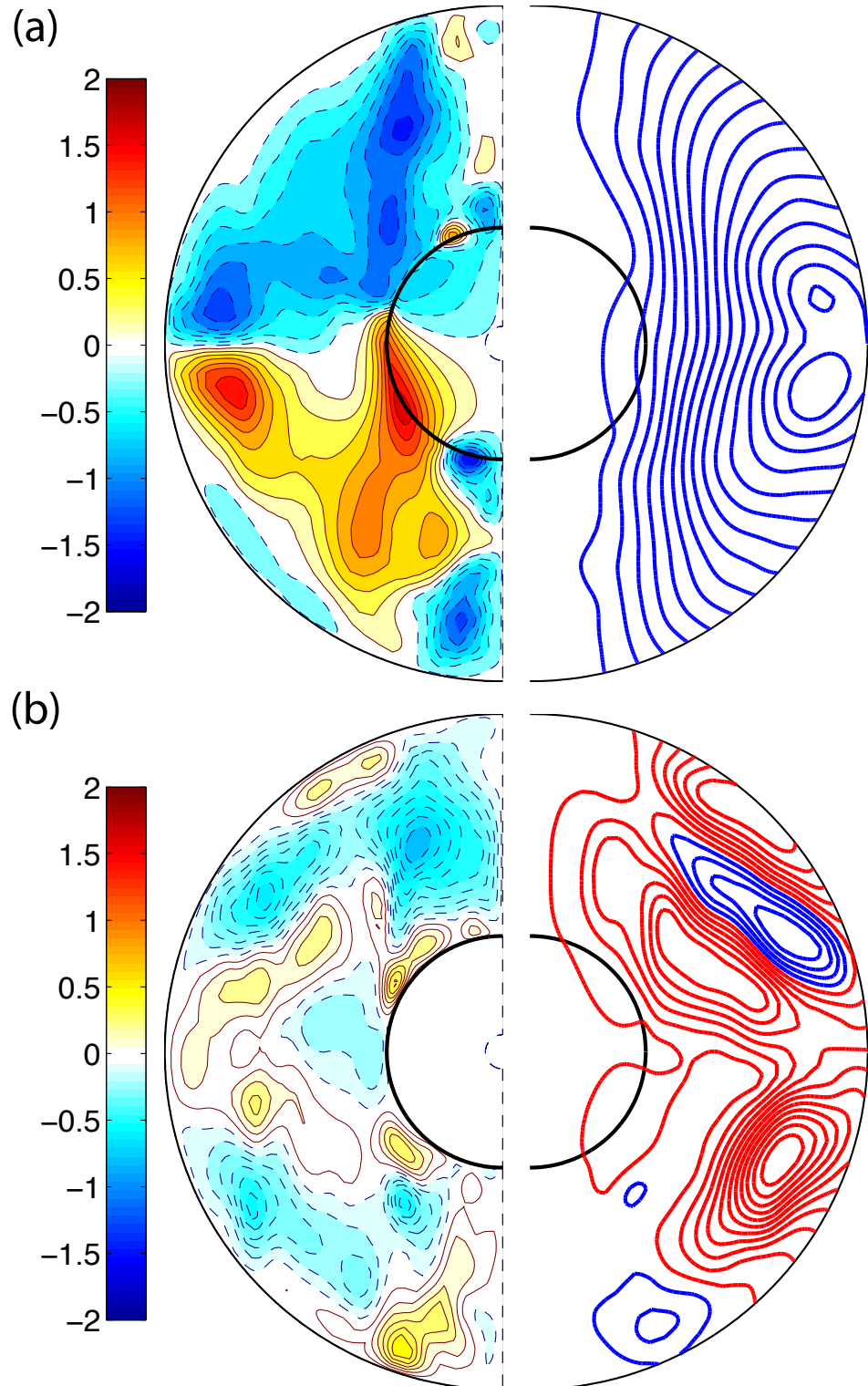


Figure 3.5: **Radial Magnetic Field at the Core Mantle Boundary for CIC-7(a) and IIC-7 (b) models.** The units are non-dimensional.

the difference between the magnetic field morphologies inside the dynamo generation region. The CIC-7 model has strong equatorially anti-symmetric large scale toroidal fields and the IIC-7 model in comparison has weaker, more complex, small scale toroidal fields.

### 3.3.5 Kinetic Energy

Similar to the magnetic energy, the kinetic energy can also be defined as the non-dimensional mean square field intensity. For the definition of kinetic energy and the



**Figure 3.6: Axisymmetric Magnetic Field for the CIC-7 (a) and IIC-7 (b) models.** The left (right) plot shows a meridional slice of the axisymmetric toroidal (streamlines of poloidal) magnetic field. In the toroidal plots, red shades represent prograde direction and blue shades represent retrograde direction. In the poloidal plots, red is clockwise and blue is anti-clockwise. The units are non-dimensional.

767 toroidal and poloidal partitioning please refer to Section 2.3.1 in Chapter 2. The toroidal  
768 and poloidal energies can be further decomposed into axisymmetric and non-axisymmetric  
769 components. Figure 3.7 shows the axisymmetric and non-axisymmetric components of  
770 the toroidal and poloidal kinetic energies. We can characterize the CIC-7 and IIC-7  
771 models as having stronger toroidal energy than poloidal energy. The poloidal energies  
772 of models CIC-7 and IIC-7 are similar in magnitude and are dominated by their non-  
773 axisymmetric components as shown in the top plots of Figures 3.7a and 3.7b. In the CIC-7  
774 model, the toroidal energy is dominated by its non-axisymmetric component whereas in  
775 the IIC-7 model, the toroidal energy is dominated by its axisymmetric components. Also  
776 the non-axisymmetric component of the toroidal energy of models CIC-7 and IIC-7 are  
777 similar in magnitude but the IIC-7 model has larger axisymmetric components. The  
778 IIC-7 model seems to promote strong large scale zonal motions in the core.

### 779 3.3.6 Velocity Field

780 Since models CIC-7 and IIC-7 have different magnetic field morphologies but their  
781 poloidal kinetic energies are similar in magnitude, we examine if they have different  
782 velocity field morphologies.

783

784 Figure 3.8 shows a snapshot of the axisymmetric toroidal (left) and poloidal (right)  
785 velocity field components of the CIC-7 model (Figure 3.8a), IIC-7 model (Figure 3.8b)  
786 and a convection model with no magnetic field (Figure 3.8c). The velocity field of the  
787 CIC-7 model is very different from the IIC-7 and convection models, with a retrograde  
788 equatorial jet outside the tangent cylinder close to the outer core boundary, a sign  
789 that Lorentz forces are strong enough to break the Taylor-Proudman constraint (In  
790 the absence of magnetic field, the main force balance is between the Coriolis force and  
791 the pressure force. Using this force balance along with Boussinesq approximation, it  
792 can be shown that in spherical geometry, fluid motions are constrained to cylinders

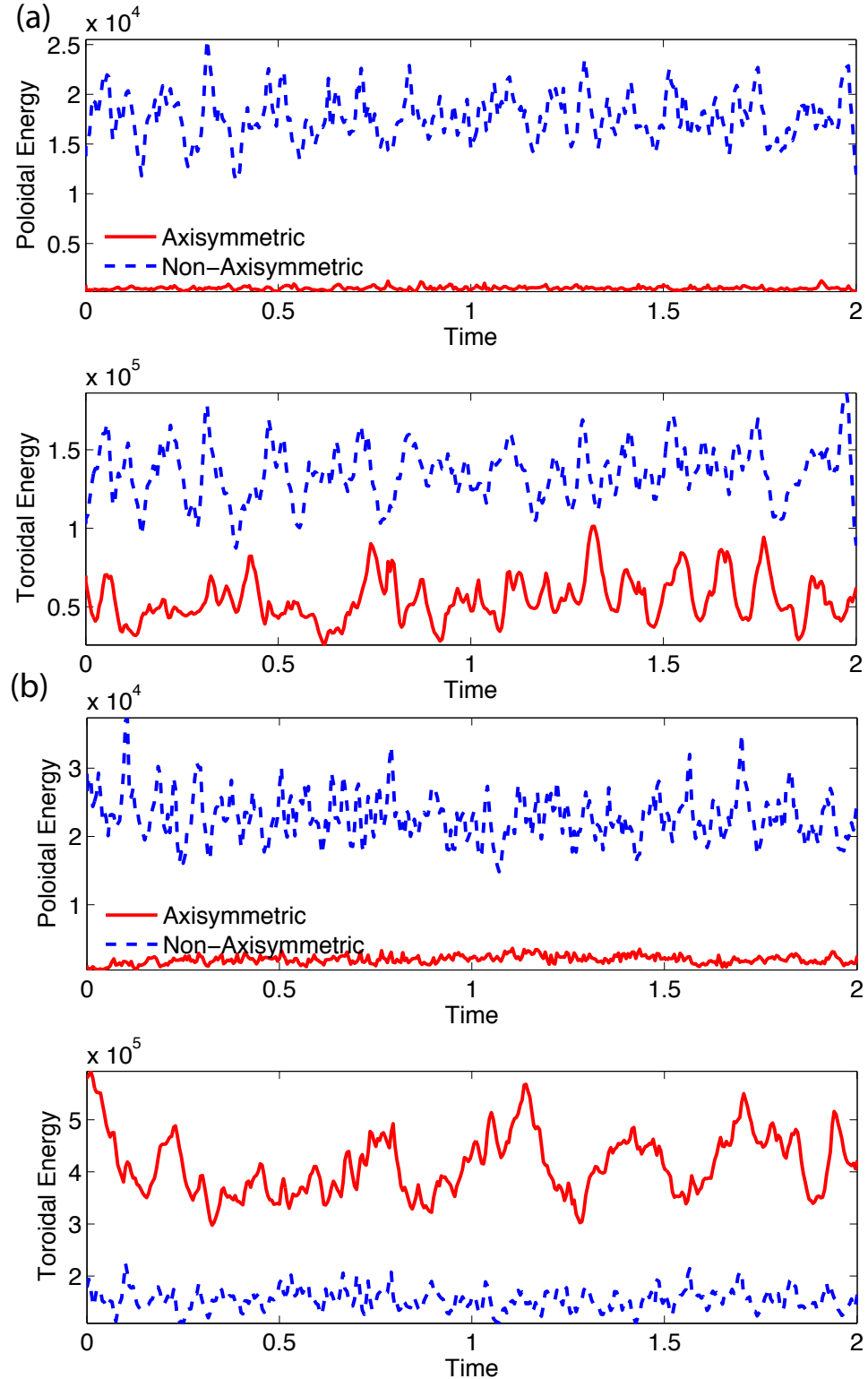


Figure 3.7: Kinetic Energy versus Time for the CIC-7 (a) and IIC-7 (b) models. The top (bottom) plot shows the poloidal (toroidal) kinetic energy. The axisymmetric energy is shown in solid red line and the non-axisymmetric energy is shown in dashed blue line. The units are non-dimensional.

793 co-axial with the rotation axis of constant height in the z-direction, a type of zonal flows  
 794 (axisymmetric  $\phi$  component of the velocity field) in planets [Proudman, 1916, Taylor,  
 795 1917]. The intensity of the zonal flows is also weaker than the IIC-7 and convection  
 796 models due to magnetic braking. The meridional circulation is mostly equatorially  
 797 anti-symmetric and stronger outside the tangent cylinder.

798

799 The toroidal velocity field of the convection model is approximately constant on cylinders  
 800 parallel to the rotation axis, a sign of strong Taylor-Proudman influence. The meridional  
 801 circulation (poloidal velocity) is concentrated inside the tangent cylinder in this case.  
 802 The velocity field morphology of the IIC-7 model is similar to the convection model  
 803 even-though it has a strong magnetic field intensity. In this case, the magnetic fields of  
 804 the IIC-7 models do not influence the velocity field significantly.

### 805 3.3.7 Force Balance

806 In order to understand why models CIC-7 and IIC-7 both produce intense magnetic  
 807 fields but have different magnetic and velocity field morphologies in the core we examine  
 808 the force balance in these models.

809

810 In a numerical planetary dynamo model, the Lorentz force in the momentum equation  
 811 (Eq.1.36) can either dominantly balance the Coriolis force or it can be a secondary term  
 812 that does not participate in the leading order force balance. If the Lorentz force balances  
 813 the Coriolis force then the dynamo is in magnetostrophic balance:

$$\hat{z} \times \vec{v} \approx -\nabla p + \vec{J} \times \vec{B} \quad (3.1)$$

814 The dynamos of Earth, Jupiter, Saturn etc. are considered to be in magnetostrophic  
 815 balance. A dynamo that is in magnetostrophic balance is said to be in the “strong

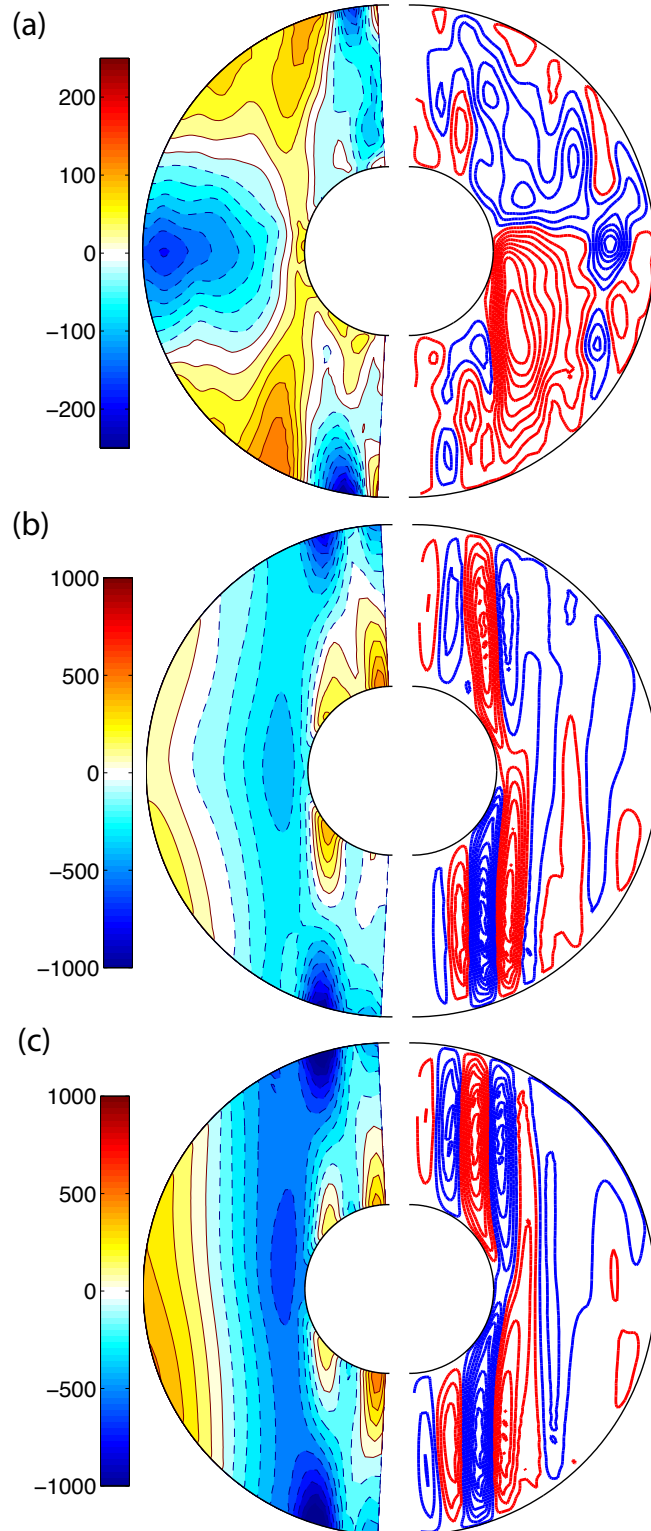


Figure 3.8: **Axisymmetric Velocity Fields for the CIC-7 (a), IIC-7 (b) and no magnetic field convection (c) models.** The toroidal velocity fields are shown on the left where red (blue) denotes prograde (retrograde) circulation and streamlines of poloidal velocity fields are shown on the right where red (blue) denotes clockwise (anti-clockwise) circulation.

816 field regime”. If the Lorentz force is not strong enough to balance the Coriolis force  
 817 then it is assumed that it results in a weak magnetic field. A dynamo that is not in  
 818 magnetostrophic balance is said to be in the “weak field regime”. For the derivation and  
 819 spherical harmonic expansion of the Lorentz and Coriolis force please refer to appendix C.

820

821 The ratio of the Lorentz force to the Coriolis force can be characterized through the  
 822 Elsasser number ( $\Lambda$ ):

$$\Lambda = \frac{|\mathcal{J} \times \mathcal{B}|}{|2\rho\Omega \times \mathcal{V}|} \quad (3.2)$$

$$= \frac{|\mathcal{B}^2|}{|2\rho\Omega \mathcal{V} \mu_0 L_{\mathcal{B}}|} \quad (3.3)$$

823 where the curly alphabets are dimensional quantities and  $L_{\mathcal{B}}$  is the magnetic length  
 824 scale. By this definition a strong field dynamo should have  $\Lambda \approx O(1)$  and a weak field  
 825 dynamo should have  $\Lambda < O(1)$ . Traditionally, the definition of  $\Lambda$  assumes that velocity  
 826 can be scaled in terms of diffusion time [Merrill et al., 1996, Christensen and Wicht,  
 827 2007]. Assuming that the magnetic field is generated in a steady state and using our  
 828 non-dimensionalization:

$$\Lambda \approx |\vec{B}^2| \quad (3.4)$$

829 Using this, the average Elsasser numbers of models CIC-7 and IIC-7 over one diffusion  
 830 time are 5.8 and 0.8 respectively. Therefore, models CIC-7 and IIC-7 appear to both be  
 831 strong field dynamos (the Elsasser numbers are both of  $O(1)$ ). Also, using the observed  
 832 magnetic field strength of Earth in equation 3.4, Earth can be considered to be a strong  
 833 field dynamo, i.e., in magnetostrophic balance.

834

835 However, in Figure 3.9, we have plotted the time-averaged axisymmetric  $\phi$  components  
836 of the Coriolis and Lorentz forces in the core. Model CIC-7 results in  $82 \pm 3\%$   
837 correlation (where the  $\pm 3$  is the standard deviation in one magnetic dipole diffusion  
838 time) in magnitude between the Coriolis force and the Lorentz force which is a good  
839 demonstration that it is in magnetostrophic balance (i.e. in the strong field regime). In  
840 contrast, model IIC-7 results in only  $27 \pm 4\%$  correlation between the Coriolis force and  
841 the Lorentz force and is therefore not in magnetostrophic balance. Since the IIC-7 model  
842 is dominated by the non-axisymmetric component of its magnetic field, we examined the  
843 force balance due to the non-axisymmetric components and found that they were also  
844 weakly correlated. So although both models have strong enough magnetic intensities  
845 to produce Elsasser numbers of  $O(1)$ , only the CIC-7 model is in the magnetostrophic  
846 regime.

847

848 We investigated if the intense magnetic field with small Lorentz force was due to having  
849 a magnetic field that is parallel to the current resulting in  $\vec{J} \times \vec{B} = 0$  but this was not  
850 the case in the IIC-7 model. Instead the small Lorentz force is due to a weak current  
851 magnitude. Since the IIC-7 model has a small magnetic length scale, magnetic intensity  
852  $|\vec{B}|$  can be large while the magnitude of the current density  $|\vec{J}| = |\nabla \times \vec{B}|$  is small  
853 resulting in a weak Lorentz force.

854

855 Our models suggest that the standard definition of the Elsasser number as the mean  
856 square of the non-dimensional magnetic field cannot be used as a measure to distinguish  
857 between dynamos that are in magnetostrophic balance and those that are not. Soderlund  
858 et al. [2012] also find a similar result, that the traditional definition of the Elsasser number  
859 overestimates the Lorentz force and is not a good measure of whether the dynamo is in  
860 the strong or weak field regime. They instead define a dynamic Elsasser number that

better compares the magnitude of the Lorentz and Coriolis force ratios in their models. However, they do not compare the forces in a point by point correlation like we do in Figure 3.9. In the parameter space that they work in they do not see models where the Lorentz and Coriolis forces are solely dominant and balance each other. Therefore they argue that none of their models are in the strong field regime. We look at a point by point correlation of the axisymmetric  $\phi$  component of the Lorentz and Coriolis forces and find that this is a better measure of which of our models are in magnetostrophic balance.

### 3.3.8 Magnetic Braking

In order to understand why the velocity field of the CIC-7 model is different from the IIC-7 model, we examine the rate at which energy is supplied by the Lorentz force to the axisymmetric toroidal velocity field [Buffett and Bloxham, 2002]:

$$\Gamma(\vec{v}_T) = \bar{v}_\phi \overline{(\vec{J} \times \vec{B})}_\phi \quad (3.5)$$

Figure 3.10 shows the rate at which energy is supplied by the Lorentz force to the zonal circulation. Red colour represents areas where the Lorentz force aids in the zonal circulation and blue represents areas where the Lorentz force slows down the zonal flow i.e. regions where magnetic braking happens. The currents associated with the toroidal magnetic field of the CIC-7 model (Figure 3.6a) produce Lorentz forces (Figure 3.9a) that affect its zonal circulation (Figure 3.8a) close to the equator and the tangent cylinder as shown in Figure 3.10a. This is the reason why we see an equatorial jet in the axisymmetric velocity field of the CIC-7 model. In contrast, in the IIC-7 model, the weak Lorentz force generates weak magnetic braking in a region almost parallel to the tangent cylinder in the bulk of the outer core. This is the reason why the axisymmetric toroidal velocity field of the IIC-7 model only slightly differs from the convection model with no magnetic

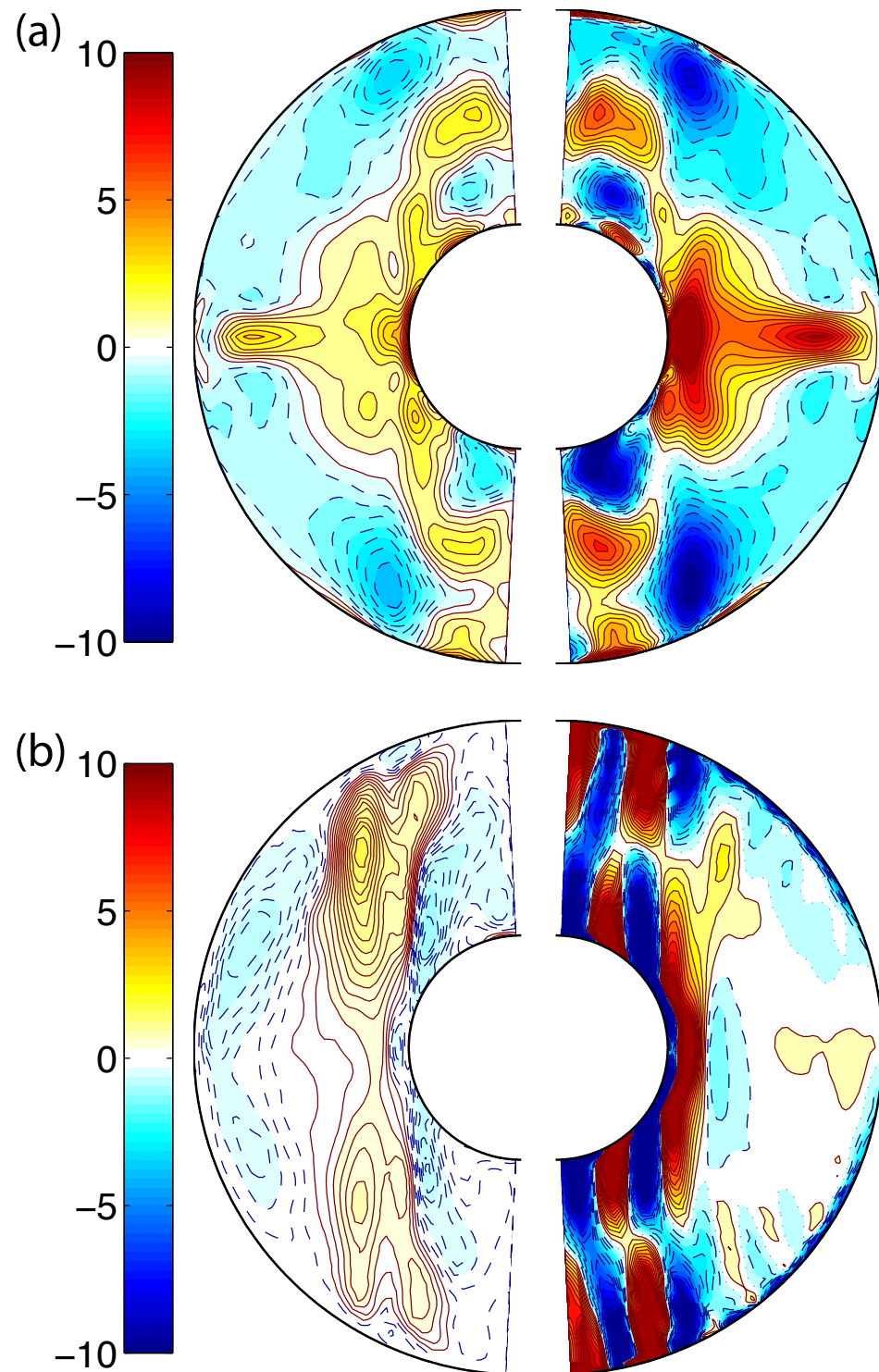


Figure 3.9: **Force Balance for the CIC-7 (a) and IIC-7 (b) models.** Time averaged axisymmetric  $\phi$  components of the Lorentz force (left) and the Coriolis force (right).

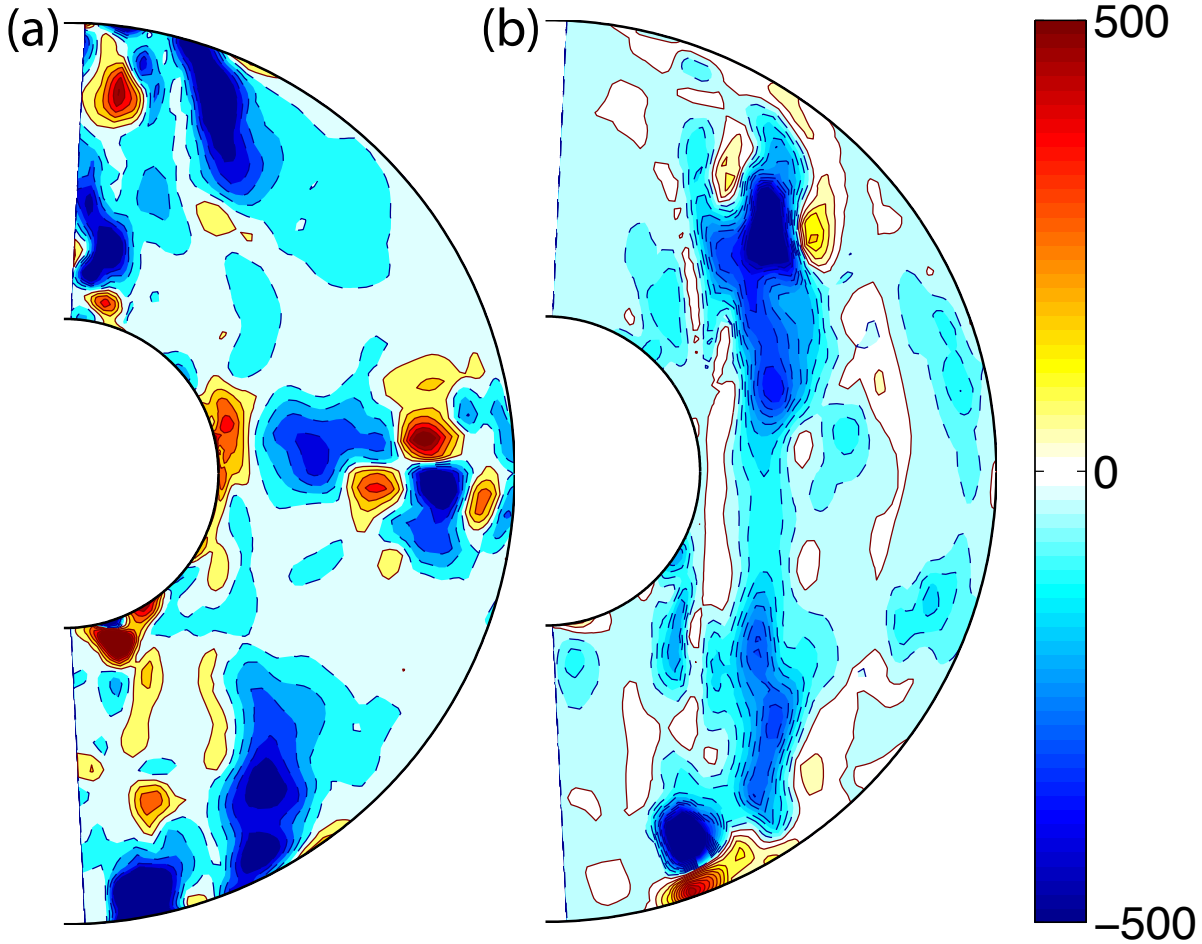


Figure 3.10: **Magnetic Braking for the CIC-7 (a) and IIC-7 (b) models.** Red (blue) denotes the Lorentz force assisting (obstructing) the zonal circulation.

883 field.

### 884 3.4 Discrepancy Between Studies

885 In this chapter we have shown that our dynamo models with a CIC maintain a dipolar  
 886 magnetic field and reverse less frequently than the IIC models. In contrast, Wicht [2002]  
 887 finds that a CIC does not significantly affect the resulting magnetic field. The main dif-  
 888 ference between these studies is the choice of boundary conditions and Rayleigh number.  
 889 Wicht [2002] compared magnetic field morphologies in models with fixed temperature  
 890 and no-slip boundary conditions at lower Rayleigh numbers than our models. The mod-

els we discuss have (physically realistic) fixed heat flux and viscous stress-free boundary conditions and higher Rayleigh numbers. The reason why we choose viscous stress-free boundary conditions instead of the physically realistic no-slip boundary conditions is to eliminate the unrealistic effects due to amplification of the viscous boundary layer thickness. For example, the Ekman number is the ratio of viscous force to the Coriolis force. The Ekman number of the Earth is approximately  $10^{-15}$ . Therefore, for the Earth, the viscous forces are negligible in the bulk of the fluid. However, at the boundaries, since the length scale at which the velocity changes is very small, the velocity gradient is large enough for it to matter. We can find the thickness of the Ekman boundary layer ( $\delta$ ) by setting the Coriolis and viscous forces equal. By doing this we get the following relationship:

$$\delta \approx r_o \sqrt{E} \quad (3.6)$$

The radius of the outer core is approximately 3500 km. Using the values of  $r_o$  and  $E$  for the Earth, we get  $\delta \approx 11\text{ cm}$ . Due to computational constraints, we cannot use  $E = 10^{-15}$  as we would need very high spatial resolution. Hence, in the dynamo community, we use,  $E \approx 10^{-4} - 10^{-7}$ . Using the value of  $E = 2 \times 10^{-5}$ , we get  $\delta \approx 15,650\text{ m}$  which is much thicker than the Ekman boundary layer of the Earth. Hence, we choose stress-free velocity boundary conditions for our model to better approximate the actual size of the boundary layers in planetary cores.

Different boundary conditions may result in different force balances in the models that may influence the dynamo generation mechanism and thus the resulting magnetic fields. Hence, we investigated CIC and IIC models with different thermal and velocity boundary conditions as shown in Table 3.1 to study their influence on the resulting dynamos.

915

916 Irrespective of the velocity boundary conditions, the results of models with fixed heat  
917 flux boundary conditions are different from the fixed temperature models. At moderately  
918 supercritical Rayleigh number (e.g. at  $\text{Ra} = 2,500$ ), the conductivity of the inner core  
919 does not seem to matter in the fixed heat flux models. CIC and IIC models reverse  
920 frequently and produce weak field dynamos. As the Rayleigh number is increased to  
921 higher values ( $\text{Ra} = 5,000$ , 7,500 and 15,000), the difference between CIC and IIC  
922 models emerges as shown in the table 3.1. The CIC models maintain a dipolar magnetic  
923 field and reverse less frequently than the IIC models. The CIC models produce a strong  
924 field dynamo whereas the IIC models produce a weak field dynamo. Also, the length  
925 scales of the velocity and magnetic fields of the CIC models are similar in magnitude  
926 whereas they are different by a factor of  $> 50$  in the IIC cases. This is because the large  
927 scale velocity fields are not dominantly influencing the magnetic fields in the IIC models.

928

929 However, irrespective of the velocity boundary conditions, the results of models with fixed  
930 temperature boundary conditions are the opposite of the fixed heat flux models in terms  
931 of the magnetic field generation. At moderately supercritical Rayleigh number (e.g. at  
932  $\text{Ra} = 2,500$ ), the conductivity of the inner core does not matter in the fixed temperature  
933 models. These results are consistent with those of Wicht [2002]. CIC and IIC models do  
934 not reverse for the observed time and produce strong field dynamos. Similar to Wicht  
935 [2002] we also found that the toroidal flux patches near the equatorial region were stronger  
936 in the CIC model and the toroidal flux patches inside the tangent cylinder were stronger  
937 in the IIC model. In contrast to the fixed heat flux models, as the Rayleigh number is  
938 increased to higher values ( $\text{Ra} = 5,000$  and 7,500), both the CIC and IIC models produce  
939 similar fields, dominantly non-dipolar and frequently reversing. So in fixed temperature  
940 models, it appears that the inner core conductivity does not affect the solutions. Similar  
941 to the fixed heat flux models, the length scales of the velocity and magnetic fields of the

942 CIC models are similar in magnitude whereas they are different by a factor of  $> 50$  in  
943 the IIC cases. Since we use different definitions of Rayleigh numbers for models with  
944 fixed heat flux and fixed temperature boundary conditions, we don't directly compare  
945 a fixed temperature model to a fixed heat flux model with the same Rayleigh number  
946 value. Instead, our comparison demonstrates what happens as we increase the Rayleigh  
947 number from low to moderately high values for a given thermal boundary condition.

### 948 3.5 Conclusions

949 In this chapter we have shown that our fixed heat flux dynamo models, run at relatively  
950 high Rayleigh numbers with a CIC, maintain a dipolar magnetic field and reverse less  
951 frequently than IIC models. We have shown that the dynamo generation mechanism and  
952 reversal frequency are strongly dependent on the inner core conductivity. The magnetic  
953 field morphology inside and outside the core of CIC and IIC models are very different  
954 and will be easily noticeable by an observer who can only measure the outside potential  
955 field.

956

957 To investigate the robustness of our results, we studied a variety of initial conditions for  
958 the magnetic and velocity fields in our models to determine their effects on the resulting  
959 magnetic fields and found that the initial magnetic or velocity fields did not influence  
960 the resulting field morphology or the reversal frequency.

961

962 We investigated the disparities between our model and others that suggest that the  
963 inner core conductivity does not influence the resulting magnetic fields. The main  
964 difference between our models and others is the choice of thermal and velocity boundary  
965 conditions and the super-criticality of Rayleigh numbers used. We ran models at  
966 similar boundary conditions and parameters as other studies and found that the inner

967 core conductivity influences the dynamo generation mechanism and the magnetic and  
968 velocity field morphology in the fixed heat flux models, while it does not significantly  
969 influence the observable field morphology in the fixed temperature models.

970

971 Irrespective of the conductivity of the inner core, we found that dynamo models run at  
972 moderately low supercritical Rayleigh numbers with fixed heat flux boundary conditions  
973 reversed frequently whereas similar models with fixed temperature boundary conditions  
974 did not reverse. Since the characteristics of the dynamo models change as the Rayleigh  
975 number increases, one should use caution in extrapolating results from dynamo models  
976 run at low Rayleigh numbers to interpret and understand dynamo generation mecha-  
977 nisms and reversal mechanisms in the planetary regime. Specifically, we have shown that  
978 at higher Rayleigh numbers than previous studies, for certain thermal boundary condi-  
979 tions, the conductivity of the inner core plays an important role in the generation of the  
980 magnetic field due to different force balances.

981 **Chapter 4**

982 **Scaling Laws and Effects of Thermal  
983 and Velocity Boundary Conditions**

984 This work is submitted for publication to Geophysical Journal International.

985 **4.1 Introduction**

986 As previously described in Chapter 1, dynamo models operate in a parameter regime that  
987 is not representative of planetary interiors due to computational constraints [Glatzmaier  
988 and Roberts, 1996, Kuang and Bloxham, 1997, Takahashi et al., 2005, Miyagoshi et al.,  
989 2010], but these models aid in understanding the basic dynamo mechanisms in planets.

990

991 In the last two decades, three-dimensional numerical geodynamo models driven by con-  
992 vection in rotating spherical shells have been successful in generating some of the basic  
993 properties of the observed geomagnetic field. For example, models with different choices  
994 for governing parameters and boundary conditions are able to produce the geomagnetic  
995 field's dipole dominance, strength and reversal statistics. A question arises as to how  
996 these chosen model parameters and boundary conditions affect the numerical solutions.  
997 Specifically, since we are interested in determining core properties such as the CMB heat

998 flux and ohmic dissipation to understand the Earth's heat budget, are we getting these  
999 right? In order to address this question, a comprehensive and systematic study of the in-  
1000 fluence of model parameters and boundary conditions on dynamo models must be carried  
1001 out.

### 1002 4.1.1 Dynamo scaling laws

1003 As computational capabilities improve, dynamo studies in previously unexplored param-  
1004 eter regimes become feasible. For example, [Sakuraba and Roberts \[2009\]](#) and [Miyagoshi](#)  
1005 [et al. \[2011\]](#) have studied dynamo models at an Ekman number (ratio of viscous to  
1006 Coriolis force) as low as  $10^{-7}$ , and found convective structures shaped in the form of  
1007 narrow plumes with branches similar to those observed in water convection experiments  
1008 at an Ekman number of  $10^{-6}$  [[Sumita and Olson, 2000](#)]. However, the Earth's Ekman  
1009 number is about  $10^{-15}$  and hence this example illustrates the many orders of magnitude  
1010 separating model and planetary parameters. The most practical way to proceed,  
1011 currently, is to run suites of models using numerically-reasonable ranges of parameter  
1012 values to develop scaling laws between the input and output parameters. The scaling  
1013 laws must then be assumed to hold over the many orders of magnitude separating model  
1014 and planetary parameters, and used to infer properties of the geodynamo.

1015

1016 Various studies have developed scaling laws from simulations for dynamo characteristics  
1017 such as magnetic field strength, heat transport and dipolarity (e.g. [Christensen and](#)  
1018 [Tilgner \[2004\]](#), [Aubert \[2005\]](#), [Christensen and Aubert \[2006\]](#), [Olson and Christensen](#)  
1019 [\[2006\]](#), [Takahashi et al. \[2008\]](#), [Aubert et al. \[2009\]](#), [Christensen \[2010\]](#), [Yadav et al.](#)  
1020 [\[2013\]](#), [Selzer and Jackson \[2013\]](#)). Some important results from these scaling law studies  
1021 are that:

- 1022 1. the morphology of the magnetic field depends on the local Rossby number (a proxy  
1023 for the importance of rotation on the convective motions), and

1024     2. diffusivity-free scalings work well for predicting characteristics such as field strength  
1025                 (although a recent analysis calls this into question [Selzer and Jackson, 2013]).

This has lead to the hypothesis that the resulting magnetic field strength depends only on the convective power available to drive the dynamo rather than the balance between Lorentz and Coriolis forces (the so called "magnetostrophic balance" popular in previous literature). The scaling laws developed from these numerical simulations also appear to work well in explaining the field strength for some planets and stars [Christensen et al., 2009].

1032

1033 Most of the models in these simulations use fixed temperature and no-slip boundary  
1034 conditions although a few of the studies do investigate the effects of some other mechanical  
1035 and thermal boundary conditions. Several of the studies also incorporate an insulating  
1036 inner core rather than a conducting inner core, an approximation that can affect force  
1037 balances in the models [Dharmaraj and Stanley, 2012]. A study that investigates scaling  
1038 laws while systematically varying boundary conditions would aid in understanding their  
1039 influence on these scaling laws.

### 4.1.2 The influence of boundary conditions

<sup>1041</sup> Various studies have demonstrated that the choice of thermal and velocity (mechanical)  
<sup>1042</sup> boundary conditions in numerical models can affect the resulting flows and fields as well  
<sup>1043</sup> as the force balances in the models.

1044 Thermal boundary conditions

1045 Kutzner and Christensen [2000, 2002] studied the magnetic field strength and reversal  
1046 frequencies of dynamo models for a range of Rayleigh numbers with no-slip velocity  
1047 boundary conditions and different thermal boundary conditions, with and without  
1048 internal heating. They found that the choice of thermal boundary conditions made little

1049 difference. However, this study utilized a solid inner core that was electrically insulating  
1050 as opposed to the more physically realistic choice of finitely electrically conducting, and  
1051 recent work [Dharmaraj and Stanley, 2012] has demonstrated that this can affect the  
1052 results.

1053

1054 Another study on the influence of different thermal boundary conditions, conducted by  
1055 Sakuraba and Roberts [2009], showed that at lower Ekman numbers, fixed heat flux  
1056 models produce Earth-like, strong dipolar magnetic fields, unlike fixed temperature  
1057 models that produce weak magnetic fields. The difference in the solutions is attributed  
1058 to large scale circulation, i.e., strong differential rotation that is promoted by fixed heat  
1059 flux models, which in turn coherently organizes the magnetic field and enhances the  
1060 dipole component. In the fixed flux models more heat is transported by convection in  
1061 the equatorial region than in the polar regions, whereas the fixed temperature models  
1062 redistribute excess heat more homogeneously at the boundaries.

1063

1064 Hori et al. [2010] studied the influence of thermo-compositional boundary conditions  
1065 on dynamos driven by internal heating. They showed that the impact of the choice of  
1066 thermal boundary conditions at the outer core boundary (OCB) is only large when the  
1067 driving force is dominated by internal buoyancy sources like secular cooling; whereas  
1068 at the inner core boundary (ICB), the impact is only large when the dominant driving  
1069 force is at the ICB, such as the release of light elements and latent heat from a growing  
1070 inner core. This study was also performed using electrically insulating inner cores, and  
1071 as mentioned earlier, this may affect the results.

## 1072 Velocity Boundary Conditions

1073 Studies provide a variety of results for the influence of different velocity boundary  
1074 conditions on the dynamo. For example, Kuang and Bloxham [1997], Kuang [1999]

studied the influence of different velocity boundary conditions for a dynamo model with fixed heat flux thermal boundary conditions. They demonstrated that the velocity boundary condition significantly affects force balances in the models. In contrast, Christensen et al. [1999], using fixed temperature boundary conditions, demonstrated that although the choice of velocity boundary conditions influence the zonal flows that develop in the core, the magnetic field morphology is broadly similar in both cases. Miyagoshi et al. [2010], also using fixed temperature boundaries, demonstrated that at lower Ekman numbers (near the limit of what is numerically achievable currently), the zonal flows are more similar for different mechanical boundary conditions.

1084

Most of the variety in these results is due to the fact that other parameters in these studies are different, for example, different thermal boundary conditions, or control parameter values, or the treatment of the inner core. It would therefore be advantageous for a single study to systematically vary all the boundary conditions to determine the implications.

### 1089 4.1.3 Dynamo generation mechanisms

Dynamo models have also been used to investigate the magnetic field generation mechanism in Earth's core [Christensen and Olson, 1998, Olson et al., 1999, Christensen et al., 1999, Kuang, 1999]. The process by which differential rotation can produce toroidal magnetic field is known as the ' $\omega$  effect'. The process by which convective upwelling produces both toroidal and poloidal magnetic fields is known as the ' $\alpha$  effect'. Using this, planetary dynamos can be characterized into the following three categories:

- 1096 • If the toroidal magnetic field is dominantly produced by the  $\omega$  effect then the  
1097 dynamo is known as the ' $\alpha\omega$  dynamo',
- 1098 • if it is dominantly produced by  $\alpha$  effect then the dynamo is known as the ' $\alpha^2$   
1099 dynamo' and

- 1100 • if  $\alpha$  and  $\omega$  effects are equally important, the dynamo is known as the ‘ $\alpha^2\omega$  dynamo’.

1101 For a schematic illustration of the generation of poloidal from toroidal magnetic field  
1102 and vice versa we refer the reader to [Olson et al. \[1999\]](#).

1103

1104 The generation mechanism of the dynamo depends on the force balance. Non-magnetic  
1105 convection models demonstrate that the flow in a rapidly rotating spherical shell is  
1106 organized by the Coriolis force into axial columns and the main force balance is between  
1107 the Coriolis force and the pressure gradient force. In a dynamo model, the addition of a  
1108 strong magnetic field can influence the fluid motion, breaking the axial column and the  
1109 competition between the Coriolis, viscous and inertial forces has to accommodate the  
1110 Lorentz force. It is often assumed that the influence of magnetic field will be important  
1111 when the Elsasser number (ratio of Coriolis to Lorentz force)  $\geq O(1)$ . However, recent  
1112 studies have shown that the traditional definition of the Elsasser number is not a good  
1113 representation of the Lorentz to Coriolis force balance. [Dharmaraj and Stanley \[2012\]](#)  
1114 demonstrated that a comparison of the axisymmetric  $\phi$  component of the Lorentz  
1115 and Coriolis force gives a better estimate whereas [Soderlund et al. \[2012\]](#) showed that  
1116 calculating volume integrals of the forces can give a better estimate. In this chapter, we  
1117 will examine both methods to understand force balances.

1118

1119 In this chapter we use numerical dynamo models to investigate the influence of different  
1120 thermal and velocity boundary conditions on scaling laws and dynamo generation mech-  
1121 anisms. In section 4.2 we describe our numerical model and in section 4.3 we present our  
1122 results. A discussion of the relationship between boundary layer dynamics and magnetic  
1123 field is presented in section 4.3.2. An anomalous hemispheric dynamo model is presented  
1124 in section 4.3.3. The conclusions are summarized in section 4.4.

## 4.2 Numerical Model

1125 We use the Kuang and Bloxham 3D numerical dynamo model [Kuang and Bloxham,  
1126 1997, 1999] to study magnetic field generation in a spherical, rotating, Boussinesq,  
1127 electrically conducting fluid shell surrounding a solid inner core as described in detail in  
1128 Chapter 2.

1130

1131 The control parameters, boundary conditions and results are summarized in Table F.2 for  
1132 dynamo models and Table F.3 for pure thermal convection models with no magnetic field  
1133 in Appendix F. The boundary conditions given in Tables F.2 and Table F.3 are applied  
1134 at both the inner and outer core boundaries. In all the dynamo models presented in this  
1135 chapter, the inner and outer cores have the same electrical conductivities. In our models,  
1136 the inner core is free to oscillate in response to magnetic and viscous torques. For all the  
1137 models presented in this chapter we use hyperdiffusivities starting at  $l_0 \geq 30$ . Since we  
1138 compare models with different thermal and velocity boundary conditions, for convenience,  
1139 we will use the abbreviation, **FFSF** for fixed heat flux and stress-free models, **FFNS** for  
1140 fixed heat flux and no-slip models, **FTSF** for fixed temperature and stress-free models  
1141 and **FTNS** for fixed temperature and no-slip models. To differentiate between dynamo  
1142 models and pure thermal convection models with no magnetic field, we use a suffix  
1143 “C” for “convection” in the boundary condition abbreviation mentioned above. The  
1144 simulations were run for many magnetic dipole diffusion times and the results presented  
1145 were analyzed after the initial transients decayed.

## 4.3 Results

1146 We have generated 149 dynamo models and 96 non-magnetic convection models with  
1147 different combinations of boundary conditions and control parameters as presented in  
1148 Table F.2 and Table F.3. We begin by examining dynamo models to characterize the  
1149

1150 class of magnetic fields that they produce. We examine the heat transfer and flow ve-  
1151 locity of dipole dominated dynamos by obtaining scaling laws, and compare them to  
1152 non-magnetic convection models while examining if there is a dependence on boundary  
1153 conditions. We investigate if there are any differences between dipolar dynamo models  
1154 with different boundary conditions. Finally, to understand the difference between dipo-  
1155 lar and multipolar dynamos we examine the force balance and generation mechanisms of  
1156 characteristic models.

### 1157 4.3.1 Dynamo Regimes and Scaling Laws

#### 1158 Dynamo Regimes

1159 Dynamo models with different parameters tend to reverse more frequently at high  
1160 Rayleigh numbers. Traditionally it is believed that in dipole dominated dynamos, the  
1161 Lorentz force is balanced by the Coriolis force and in multipole dynamos the inertial  
1162 force starts to play an important role [Sreenivasan and Jones, 2006b, Christensen and  
1163 Aubert, 2006]. Therefore, plotting the relative dipole strength ( $f_{dip}$ ) versus the Rossby  
1164 number (the ratio of inertial forces to Coriolis forces) should be a good measure of  
1165 separating dynamos dominated by dipolar and multipolar dynamos in view of different  
1166 force balances. But, as the Rayleigh number increases, turbulence increases and the  
1167 length scales become smaller. Since the inertial term involves a length scale but the  
1168 Coriolis term does not, the local Rossby number that depends on the characteristic  
1169 length scale of the flow instead of shell thickness would be a better measure as previously  
1170 adopted by Christensen and Aubert [2006].

1171

1172 We investigate whether dynamo di-polarity depends on flow scale for our dynamo models.

<sup>1173</sup> We calculate the relative dipole strength ( $f_{dip}$ ) as:

$$f_{dip} = \left[ \frac{B_r^{l=1}}{B_r^{l=1-12}} \right]_{r_o} \quad (4.1)$$

<sup>1174</sup> where  $B_r$  is the radial magnetic field at the CMB, and plot it versus the local Rossby  
<sup>1175</sup> number ( $Ro_l$ ):

$$Ro_l = Ro_M \sqrt{E_k} \frac{l_v}{\pi} \quad (4.2)$$

<sup>1176</sup> as shown in Figure 4.1a, where  $E_k$  is the kinetic energy:

$$E_k = \int_V |\vec{v}|^2 dV \quad (4.3)$$

<sup>1177</sup> and the characteristic length scale ( $l_v$ ) is:

$$l_v = \frac{\sum l E_k(l)}{\sum E_k} \quad (4.4)$$

<sup>1178</sup> We find a similar dependence of dynamo dipolarity on  $Ro_l$  as Christensen and Aubert  
<sup>1179</sup> [2006]. Irrespective of the control parameters and boundary conditions, most models  
<sup>1180</sup> follow the transition from dipolar ( $f_{dip} > 0.35$ ) to non-dipolar ( $f_{dip} < 0.35$ ) magnetic  
<sup>1181</sup> fields, as  $Ro_l$  increases with a critical value for the transition around  $Ro_l = 10^{-1}$ , except  
<sup>1182</sup> for a couple of anomalous models at low Rayleigh number and low Ekman number.  
<sup>1183</sup> Some of our models were bistable, i.e. for the same set of control parameters and  
<sup>1184</sup> boundary conditions, the field morphology strongly depended on the initial magnetic  
<sup>1185</sup> field. Bistability was especially prominent in fixed flux and stress-free models as also  
<sup>1186</sup> observed by Yadav et al. [2013], Simitev and Busse [2009, 2012], Sasaki et al. [2011],  
<sup>1187</sup> Schrinner et al. [2012] and Gastine et al. [2012]. We applied the model selection criteria  
<sup>1188</sup> suggested by Christensen and Aubert [2006] such as only including models with  $Nu > 2$

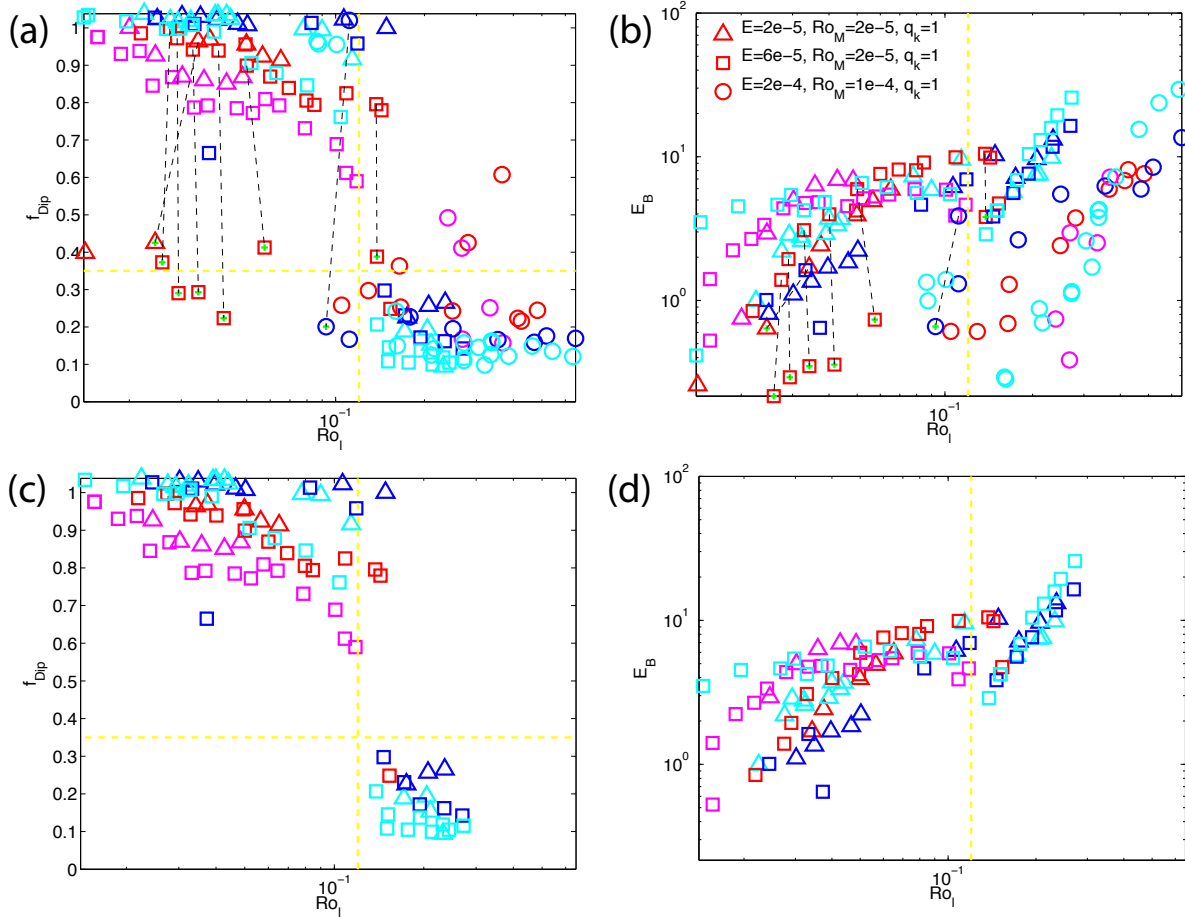


**Figure 4.1: Relative dipole strength and magnetic energy versus local Rossby number:** (a) Relative dipole strength versus local Rossby number, and (b) magnetic energy versus local Rossby number. The bistable models are connected with a dotted line. (c) and (d) are (a) and (b) with the bistable models removed,  $Nu > 2$  and  $E < 3e-4$ . Red denotes fixed flux and stress-free (FFSF) models, magenta denotes fixed flux and no-slip (FFNS) models, blue denotes fixed temperature and stress-free (FTSF) models, cyan denotes fixed temperature and no-slip (FTNS) models, and a green plus sign inside the symbols denotes non-dipolar bistable models.

1189 and  $E < 3e - 4$  and find that our figure 4.1c matches their figure 3, i.e., we observe  
1190 a clear transition from dipolar to non-dipolar regime at  $Ro_l = 0.12$  even though they  
1191 only use fixed temperature and no-slip models and we use different combinations of the  
1192 boundary conditions.

1193

1194 We also plot the time averaged magnetic energy ( $E_B$ ):

$$E_B = \int_V |\vec{B}|^2 dV \quad (4.5)$$

1195 versus the local Rossby number in Figure 4.1b and d to see how magnetic energy depends  
1196 on the dynamo regime. The magnetic energy increases as the local Rossby number  
1197 increases but there is a lot of scatter and  $E_B$  does not simply depend on  $Ro_l$  alone.

## 1198 Heat Transport

1199 In order to examine the influence of boundary conditions on heat transport we begin by  
1200 searching for power-laws. First, we plot the Nusselt number ( $Nu$ ), which is the ratio  
1201 of total heat flux to conductive heat flux, as shown in section A.2.1 in Appendix A,  
1202 vs the Rayleigh number for all our models in Figures 4.2a (dynamo models) and 4.2b  
1203 (non-magnetic convection models). Since the Rayleigh number definition for fixed heat  
1204 flux and fixed temperature boundary conditions are different in our models, we use the  
1205 following relationship to plot all the models using the same horizontal axis (as previously  
1206 done by [Boubnov and Golitsyn \[1990\]](#)):

$$Ra_{FT} = \frac{Ra_{FF}}{Nu} \quad (4.6)$$

1207 In both plots the Nusselt number increases as the Rayleigh number increases as  
1208 expected, but there is a lot of scatter and the results do not fall on a single straight

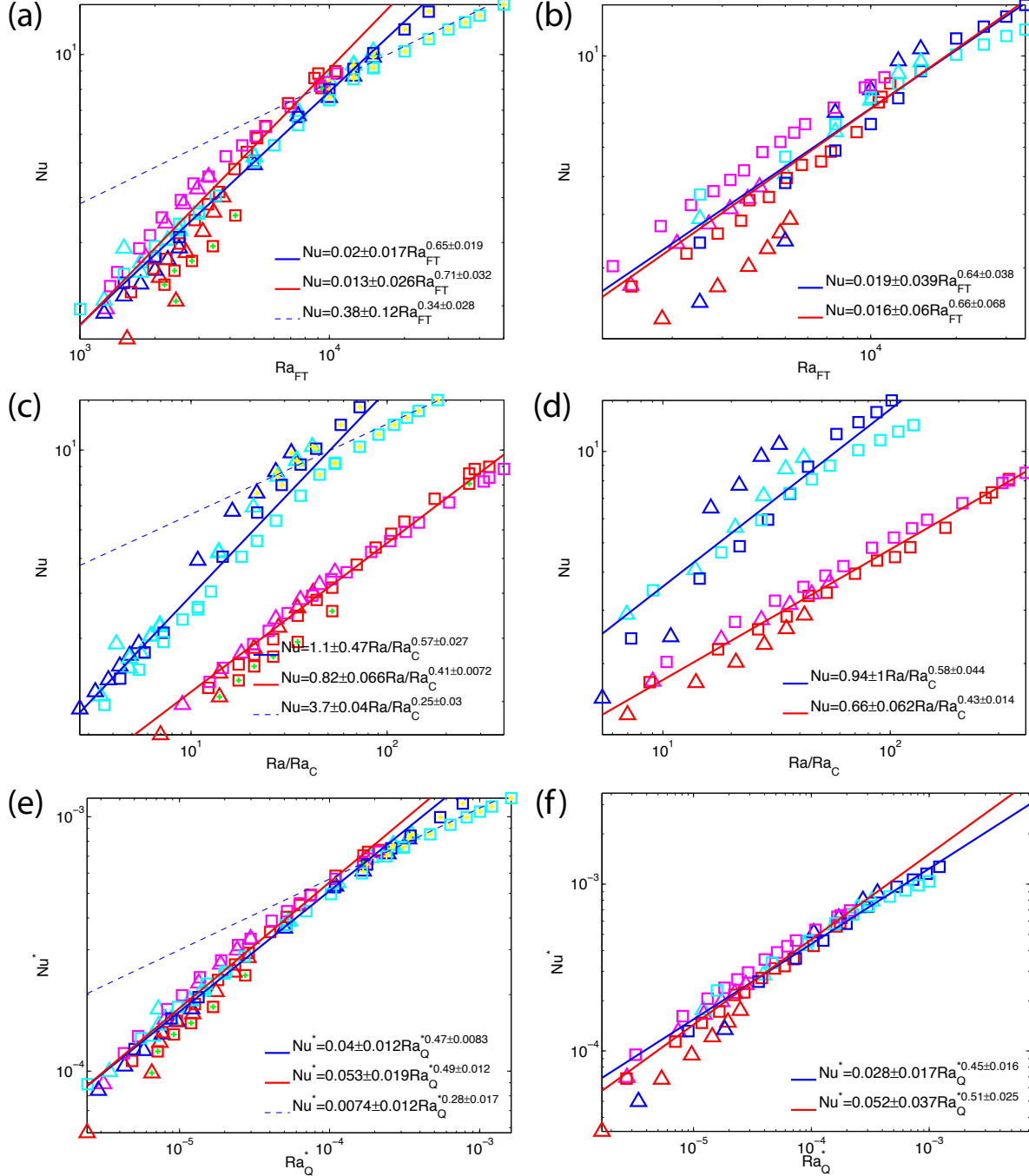


**Figure 4.2: Heat transfer power-laws:** Dynamo models are shown on the left column and convection models with no magnetic field are shown on the right column. The first row plots Nusselt number versus Rayleigh number. The second row plots Nusselt number versus Rayleigh number normalized by its critical value. The third row plots the modified Nusselt number versus modified flux based Rayleigh number. Symbols as in Figure 4.1. The yellow plus sign inside symbols denote multipolar models. The blue and red lines denote power-law fits for fixed temperature and fixed heat flux models respectively. In the dynamo plots (left plots), solid and dotted lines represent power-law fit of dipolar and multipolar models respectively.

line. Dynamo models seem to diverge at high Rayleigh numbers, whereas non-magnetic convection models seem to converge at high Rayleigh numbers. The solid red and blue line represents the best fitting line for dipolar fixed flux and fixed temperature models with  $f_{Dip} > 0.35$  (i.e. dipolar dynamo models for comparison with Christensen and Aubert [2006]), and the dotted blue line represents the best fitting line for multipolar dynamos with fixed temperature boundary conditions. The power-laws are shown in Table 4.1. The offset of the multipolar dynamo models is greater than the dipolar models. Also, the dipolar dynamos have a greater slope than the multipolar dynamos.

1217

Table 4.1: Scaling Laws for dynamo and non-magnetic convection models. The subscript C denotes convection models.  $\Delta a$  and  $\Delta b$  are standard errors in the the offset or Y-intercept ( $a$ ) and slope ( $b$ ) respectively. These power laws are obtained for models with  $Nu > 2$  and  $E < 3e - 4$ . Dipolar dynamo models have  $f_{Dip} > 0.35$  and multipolar dynamo models have  $f_{Dip} < 0.35$ . Ignore the polarity for convection models.

	$a \pm \Delta a$	$b \pm \Delta b$	$a_C \pm \Delta a_C$	$b_C \pm \Delta b_C$
$Nu = (a \pm \Delta a) Ra_{FT}^{(b \pm \Delta b)}$				
All	$0.034 \pm 0.02$	$0.59 \pm 0.01$	$0.017 \pm 0.03$	$0.65 \pm 0.03$
Dipolar Fixed Temperature	$0.02 \pm 0.02$	$0.65 \pm 0.02$	$0.019 \pm 0.04$	$0.64 \pm 0.04$
Dipolar Fixed Flux	$0.013 \pm 0.03$	$0.71 \pm 0.03$	$0.016 \pm 0.06$	$0.66 \pm 0.07$
Multipolar Fixed Temperature	$0.38 \pm 0.1$	$0.34 \pm 0.03$		
Dipolar Stress Free	$0.0055 \pm 0.02$	$0.8 \pm 0.03$	$0.0038 \pm 0.03$	$0.81 \pm 0.04$
Dipolar No Slip	$0.024 \pm 0.02$	$0.64 \pm 0.02$	$0.035 \pm 0.03$	$0.58 \pm 0.02$
Multipolar Stress Free	$0.0064 \pm 0.02$	$0.76 \pm 0.03$		

*Continued on next page*

Table 4.1 – *Continued from previous page*

	$a \pm \Delta a$	$b \pm \Delta b$	$a_C \pm \Delta a_C$	$b_C \pm \Delta b_C$
Multipolar No Slip	$0.53 \pm 0.1$	$0.3 \pm 0.02$		
<hr/>				
$Nu = (a \pm \Delta a) \left( \frac{Ra}{Ra_C} \right)^{(b \pm \Delta b)}$				
<hr/>				
All	$1.6 \pm 0.1$	$0.33 \pm 0.03$	$1.6 \pm 0.2$	$0.3 \pm 0.06$
Dipolar Fixed Temperature	$1.1 \pm 0.5$	$0.57 \pm 0.03$	$0.94 \pm 1$	$0.58 \pm 0.04$
Dipolar Fixed Flux	$0.82 \pm 0.07$	$0.41 \pm 0.007$	$0.66 \pm 0.06$	$0.43 \pm 0.01$
Multipolar Fixed Temperature	$3.7 \pm 0.04$	$0.25 \pm 0.03$		
Dipolar Stress Free	$1.5 \pm 0.1$	$0.28 \pm 0.04$	$1.7 \pm 0.3$	$0.29 \pm 0.1$
Dipolar No Slip	$1.8 \pm 0.07$	$0.25 \pm 0.03$	$1.6 \pm 0.2$	$0.3 \pm 0.07$
Multipolar Stress Free	$2.1 \pm 0.5$	$0.33 \pm 0.2$		
Multipolar No Slip	$3.7 \pm 0.04$	$0.24 \pm 0.03$		

*Continued on next page*

Table 4.1 – *Continued from previous page*

	$a \pm \Delta a$	$b \pm \Delta b$	$a_C \pm \Delta a_C$	$b_C \pm \Delta b_C$
$Nu^* = (a \pm \Delta a) Ra_Q^{*(b \pm \Delta b)}$				
All	$0.027 \pm 0.008$	$0.43 \pm 0.007$	$0.033 \pm 0.02$	$0.47 \pm 0.01$
Dipolar Fixed Temperature	$0.04 \pm 0.01$	$0.47 \pm 0.008$	$0.028 \pm 0.02$	$0.45 \pm 0.02$
Dipolar Fixed Flux	$0.053 \pm 0.02$	$0.49 \pm 0.01$	$0.052 \pm 0.04$	$0.51 \pm 0.02$
Multipolar Fixed Temperature	$0.0074 \pm 0.01$	$0.28 \pm 0.02$		
Dipolar Stress Free	$0.07 \pm 0.02$	$0.53 \pm 0.01$	$0.05 \pm 0.02$	$0.52 \pm 0.02$
Dipolar No Slip	$0.038 \pm 0.01$	$0.46 \pm 0.009$	$0.024 \pm 0.01$	$0.43 \pm 0.01$
Multipolar Stress Free	$0.043 \pm 0.02$	$0.49 \pm 0.01$		
Multipolar No Slip	$0.0059 \pm 0.008$	$0.25 \pm 0.01$		

$$Ro = (a \pm \Delta a) Ra_Q^{*(b \pm \Delta b)}$$

Continued on next page

Table 4.1 – *Continued from previous page*

	$a \pm \Delta a$	$b \pm \Delta b$	$a_C \pm \Delta a_C$	$b_C \pm \Delta b_C$
All	$1.8 \pm 0.1$	$0.47 \pm 0.01$	$9.2 \pm 0.1$	$0.54 \pm 0.06$
Dipolar Fixed Temperature	$0.89 \pm 1$	$0.41 \pm 0.03$	$8 \pm 0.2$	$0.53 \pm 0.09$
Dipolar Fixed Flux	$0.83 \pm 0.6$	$0.4 \pm 0.02$	$20 \pm 0.2$	$0.61 \pm 0.1$
Multipolar Fixed Temperature	$0.33 \pm 0.2$	$0.24 \pm 0.07$		
Dipolar Stress Free	$0.94 \pm 3$	$0.39 \pm 0.03$	$17 \pm 0.08$	$0.54 \pm 0.05$
Dipolar No Slip	$0.93 \pm 0.9$	$0.42 \pm 0.01$	$3.6 \pm 0.08$	$0.5 \pm 0.03$
Multipolar Stress Free	$1.6 \pm 0.2$	$0.42 \pm 0.03$		
Multipolar No Slip	$0.42 \pm 0.2$	$0.28 \pm 0.07$		

1219 The effect of different boundary conditions can be seen by plotting  $Nu$  versus the  
 1220 supercriticality ( $Ra/Ra_C$ ) rather than versus  $Ra$ . In Figures 4.2c and 4.2d, we see a  
 1221 clear difference between the fixed flux and fixed temperature models, even though there  
 1222 is a significant amount of scatter, especially in the fixed temperature models. Also, the  
 1223 power-law exponents (i.e. the line slope) of all the dynamo models are similar to the  
 1224 non-magnetic convection models, and the dipolar dynamo models obey similar scaling  
 1225 laws irrespective of thermal boundary conditions. The power-laws are shown in Table  
 1226 4.1. The offsets of the multipolar models are greater than the dipolar models for the same  
 1227 reason as explained above, and the slope of the dipolar and multipolar models are similar.

1228

1229 Then, for comparison to the power-laws of Christensen and Aubert [2006], we plot the  
 1230 modified Nusselt number (that is independent of thermal diffusivity) vs the modified flux  
 1231 based Rayleigh number (that is independent of diffusivities and based on the advected  
 1232 heat flux) in Figures 4.2e (dynamo models) and 4.2f (non-magnetic convection models),  
 1233 where:

$$\text{Modified Nusselt \#: } Nu^* = (Nu - 1) q_k Ro_M \frac{2}{(1 - r_{io})^2} \quad (4.7)$$

$$\text{Modified Flux-based Rayleigh \#: } Ra_Q^* = 4r_{io} Ra Ro_M Nu^* \quad (4.8)$$

1234 We use the Rayleigh number relationship given above in equation 4.6 to plot all  
 1235 the models with different thermal boundary conditions on the same horizontal axis.  
 1236 The scatter is significantly reduced and we obtain power-laws similar to Christensen  
 1237 and Aubert [2006]. The power-law dependence of models with dipolar dynamos  
 1238 are shown in Table 4.1. The power-law exponent of our fixed temperature dipolar  
 1239 dynamo models with  $Nu > 2$  is similar to Selzer and Jackson [2013] (a more rigorous  
 1240 analysis of Christensen and Aubert [2006] dataset) but our offset is approximately

1241 4 % lower than theirs. This observed difference could have resulted from our use of  
1242 hyperdiffusivities, as the use of hyperdiffusivity promotes large scale motions and a reduc-  
1243 tion in small scale eddies that are efficient in promoting heat transfer through convection.

1244

1245 From heat transfer scaling laws presented in Table 4.1 it is evident that fixed heat flux dy-  
1246 namos obey different power-laws than fixed temperature dynamos, and dipolar dynamos  
1247 also obey different power-laws than multipolar dynamos.

## 1248 Fluid Dynamic Regimes

1249 Since the power-laws of our dipolar dynamo models are different from the multipolar  
1250 dynamo models, we focus on how the magnetic field morphology changes the heat flow  
1251 by affecting the flow dynamics. A measure of flow velocity is the Rossby number ( $Ro$ ):

$$Ro = Ro_M \sqrt{E_k} \quad (4.9)$$

1252 In Figure 4.3a and Figure 4.3b, we plot the Rossby number versus the modified flux based  
1253 Rayleigh number for dynamo models and non-magnetic convection models respectively.  
1254 We choose to use  $Ro$  instead of  $Ro_l$ , as we are also interested in comparing our power-law  
1255 with existing power-law in the literature that only exists for  $Ro$  vs  $Ra_Q^*$ . The power-law  
1256 exponent of our fixed temperature dipolar dynamo models with  $Nu > 2$  is identical  
1257 to Christensen and Aubert [2006]. In both plots, the Rossby number increases with  
1258 modified flux based Rayleigh number. The scatter in the dynamo models is less than in  
1259 non-magnetic convection models. We see a clear difference between the stress-free (yellow  
1260 dotted line) and no-slip models (cyan dotted lines), even though there is a significant  
1261 amount of scatter, especially in the stress-free models. The stress-free models have a  
1262 stronger flow velocity than their respective no-slip models at the same modified flux  
1263 based Rayleigh number. The results depend on the choice of control parameters and

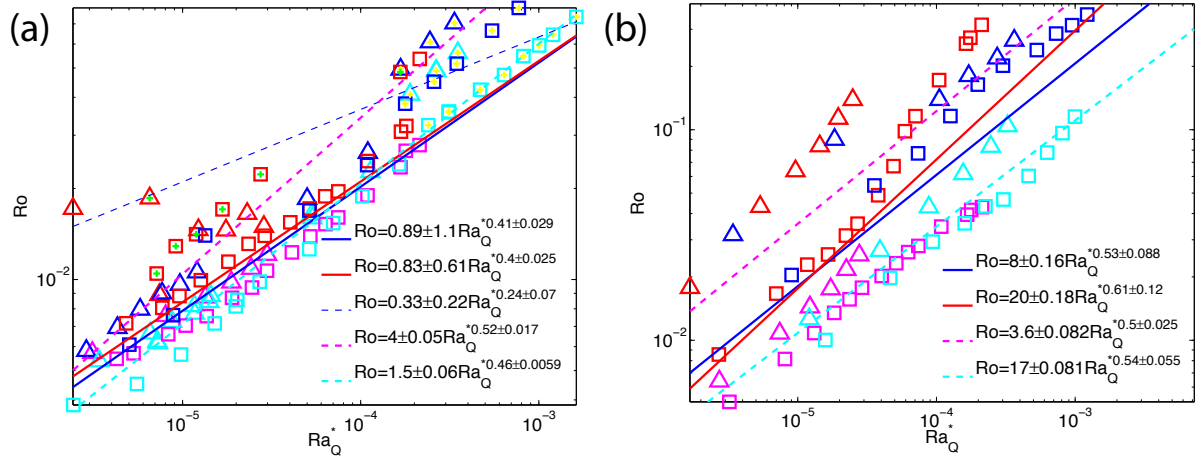


Figure 4.3: **Flow velocity power-laws:** Rossby number versus modified flux based Rayleigh number. Dynamo models are shown on the left column and convection models with no magnetic field are shown on the right column. Symbols as in Figure 4.1. The yellow plus sign inside symbols denote multipolar models. The blue and red lines denote power-law fits for fixed temperature and fixed heat flux models. In the dynamo plots (left plots), solid and dotted lines represent power-law fit of dipolar and multipolar models respectively. The magenta and cyan dotted line represents the power-law fits of stress-free and no-slip models respectively.

1264 velocity boundary conditions.

### 1265 4.3.2 Field Morphology, Force Balance and Generation Mechanisms

1267 Based on the discussion in the above sections, we see that irrespective of the choice of  
 1268 thermal or velocity boundary conditions most of our models follow the transition from  
 1269 dipolar to multipolar dynamos as the local Rossby number increases. The difference  
 1270 between models with different thermal boundary conditions emerges through the Nusselt  
 1271 number versus the supercriticality of the Rayleigh number power-laws; and the difference  
 1272 between different velocity boundary conditions emerges through the Rossby number  
 1273 versus the flux based Rayleigh number power-laws. From the power-laws presented in  
 1274 Table 4.1, it is also clear that dipolar models scale differently than multipolar models  
 1275 unlike [Christensen, 2010] who finds no difference. So, the magnetic field di-polarity is

1276 independent of the choice of thermal or velocity boundary conditions, and only depends  
1277 on the local Rossby number, which depends on the available power to drive the dynamo.  
1278 But, the differences in using different thermal or velocity boundary condition manifests  
1279 through heat transfer scalings and flow velocity analysis.

1280

1281 To investigate the difference in the observable features of the magnetic field such as  
1282 the surface magnetic power spectra, magnetic and velocity field morphology within the  
1283 dynamo generation region, and understanding the force balance that governs the dynamo  
1284 generation mechanism between models with different thermal and velocity boundary  
1285 conditions, we select characteristic dipolar and multipolar models to compare directly.

## 1286 Characteristic Models

1287 In order to focus on the influence of different boundary conditions, we will select models  
1288 with the following identical parameters:  $E = 6e - 5$ ,  $Ro_M = 2e - 5$ ,  $q_k = 1$ . Since the  
1289 Rayleigh number is defined differently for fixed flux and fixed temperature models, we  
1290 choose our characteristic models at similar Nusselt numbers. The characteristic dipolar  
1291 dynamo models at  $Nu \approx 5$  that we choose from Table 4.1 are: FFSF-21, FFNS-15,  
1292 FTSF-15 and FTNS-24, and the characteristic multipolar dynamo models at  $Nu \approx 11.5$   
1293 are: FTSF-20 and FTNS-33. The corresponding non-magnetic convection models at  
1294 similar Nusselt number are: FFSF<sub>C</sub>-16, FFNS<sub>C</sub>-14, FTSF<sub>C</sub>-09, FTNS<sub>C</sub>-08, FTSF<sub>C</sub>-13,  
1295 and FTNS<sub>C</sub>-15. The control parameters and boundary conditions of the dynamo models  
1296 are given in table F.2, and the non-magnetic convection models are given in Table F.3.

## 1297 Surface Magnetic Power Spectra

1298 The difference in the observed magnetic fields can be determined through their surface  
1299 magnetic power spectra. For definition of the surface magnetic power spectra please  
1300 refer to Section 2.3.1 in Chapter 2. In Figure 4.4 we show the resulting average surface

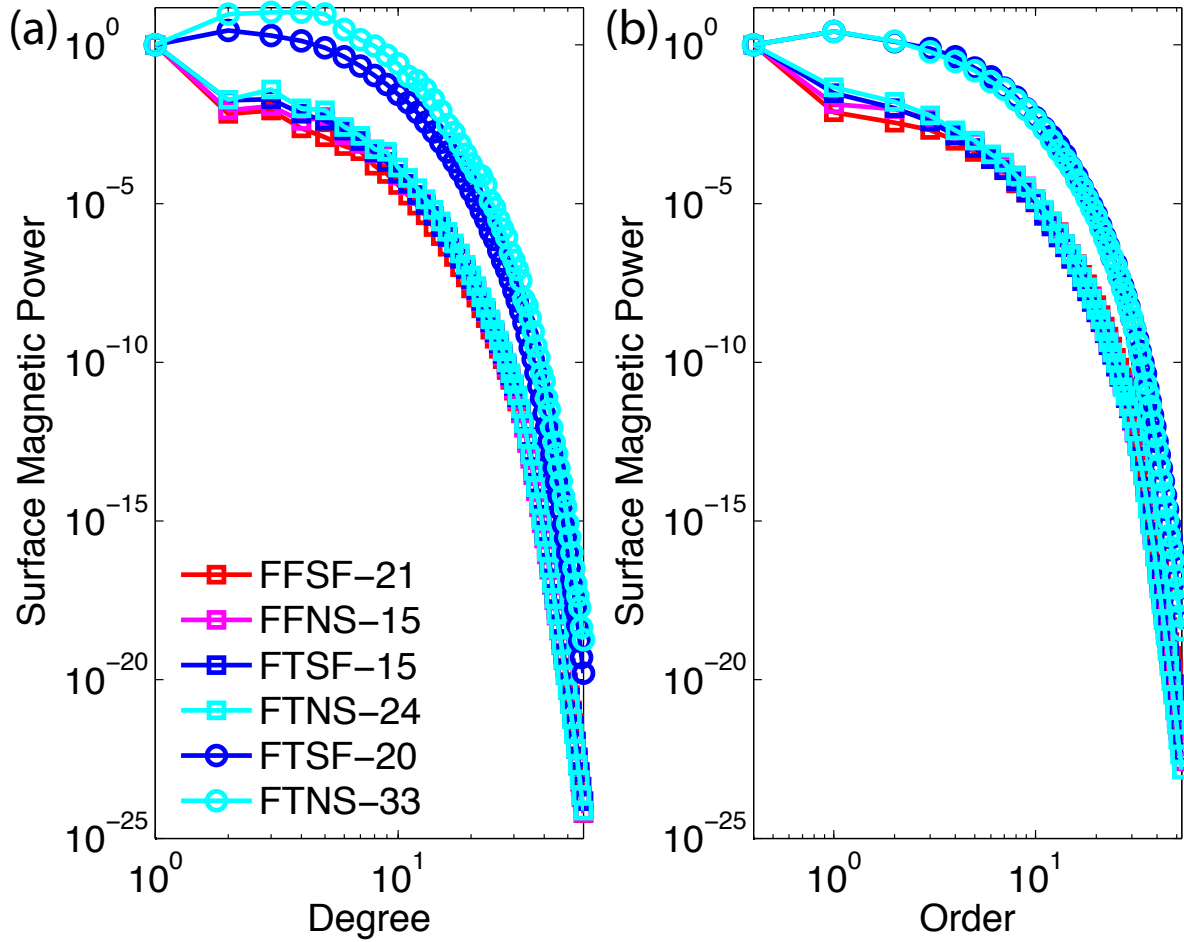


Figure 4.4: **Surface magnetic power spectra:** Left plot shows power vs degree normalized to the dipole ( $l=1$ ) power and the right plot shows power vs order normalized to axisymmetric ( $m=0$ ) power.

1301 magnetic power spectra over a magnetic dipole diffusion time for our characteristic dipolar  
 1302 and multipolar dynamo models. As expected, this figure shows that the dipolar models  
 1303 result in axially dipolar dominated fields while the multipolar models result in non-  
 1304 axisymmetric, non-dipolar magnetic fields. Notably, the spectrum does not strongly  
 1305 depend on the thermal or velocity boundary conditions.

### 1306 Magnetic Field

1307 In this section, we examine the characteristics of the dynamo models inside the dynamo  
 1308 generation region to understand the difference in the potential fields observed outside as

described in the previous section. The magnetic energies of the characteristic dipolar and multipolar models are approximately the same order of magnitude; and the magnetic energies of the characteristic multipolar models (that are found at high  $Ro_l$ ) are twice as strong as their respective characteristic dipolar models with similar boundary conditions. The toroidal magnetic field intensities are approximately equal in magnitude to the poloidal magnetic field intensity in all the characteristic dipolar and multipolar models. The characteristic multipolar dynamo models are dominated by their non-axisymmetric toroidal and poloidal magnetic fields, whereas the characteristic dipolar dynamo models have approximately equal contribution from their axisymmetric and non-axisymmetric components.

Next we examine the magnetic field morphology of dipolar and multipolar dynamos with different boundary conditions at the core mantle boundary (CMB) and inside the dynamo generation region. Although Figures 4.5 and 4.6 present snapshots in time of the resulting magnetic fields of the characteristic dipolar and multipolar models, their characteristics are similar at other times. Figure 4.5 presents the radial magnetic field at the CMB. In the dipolar regime, all the models produce strong magnetic field that is mainly dipolar with some non-axisymmetric features, whereas the models in the multipolar regime produce intense small-scale non-dipolar and non-axisymmetric magnetic fields at the CMB as expected. Even though the fixed flux models produce dipolar dynamos, they produce intense patches at the poles, whereas the fixed temperature models are more homogeneous.

Figure 4.6 presents axisymmetric meridional slices of the toroidal and poloidal magnetic fields. The magnetic field morphologies of the models in the dipolar regime are different from the models in the multipolar regime. The dipolar models produce large scale toroidal flux patches that are anti-symmetric at the equator while the multipolar models produce

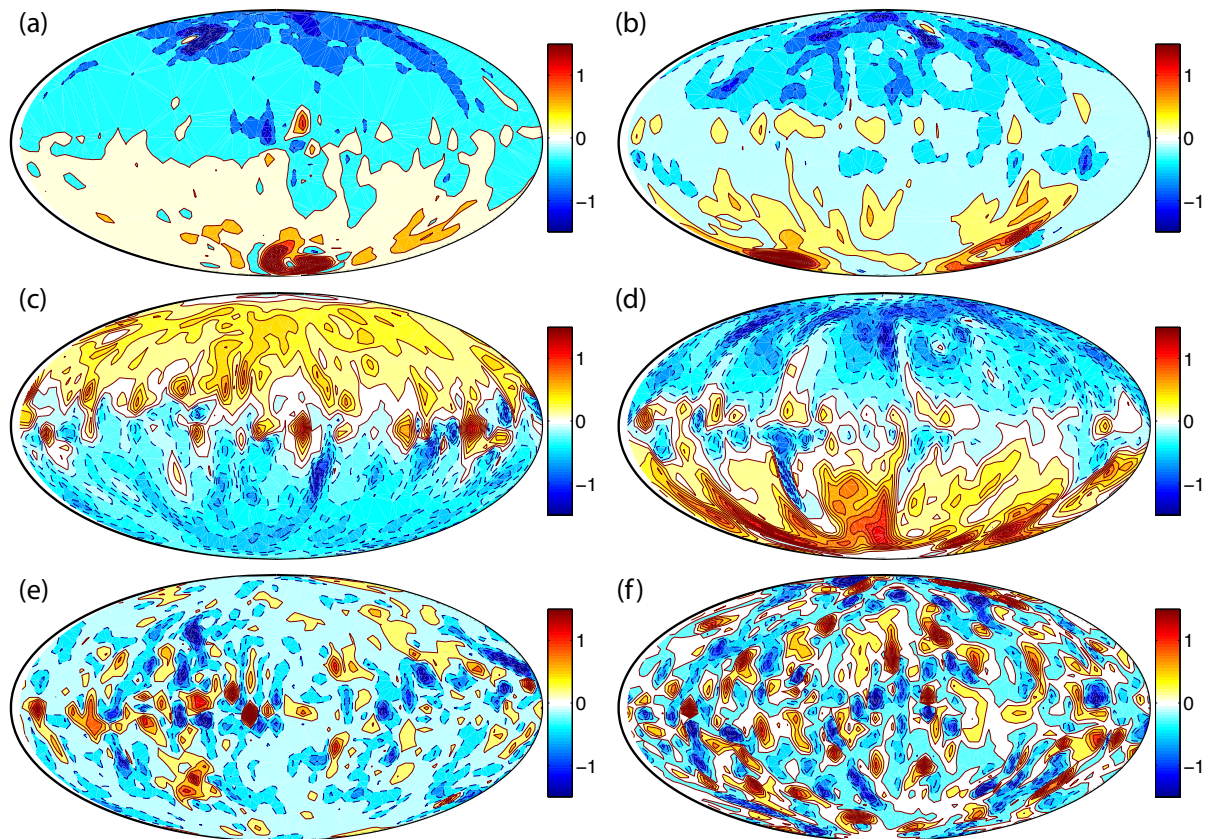
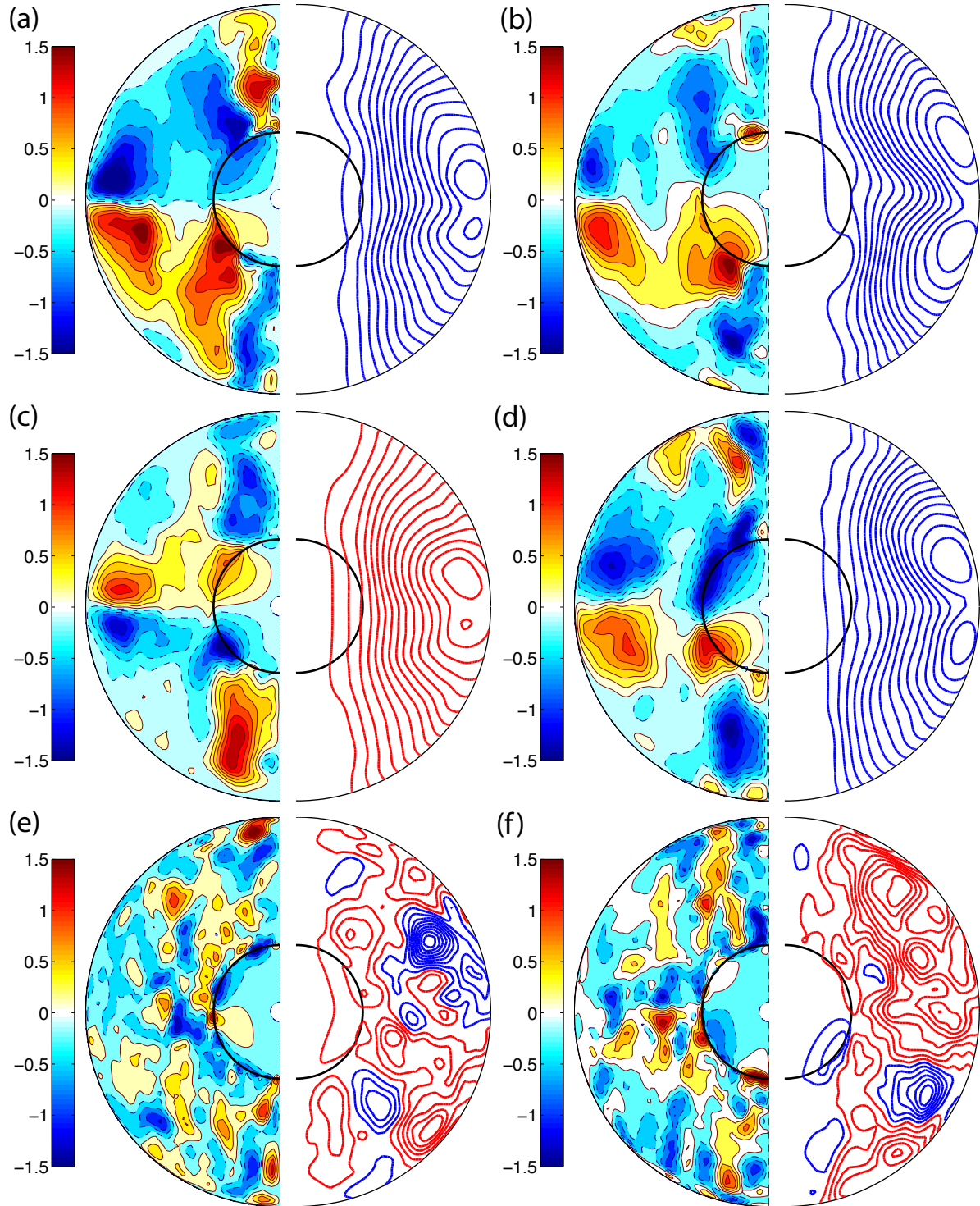


Figure 4.5: **Radial magnetic field at the core mantle boundary:** for (a) FFSF-21, (b) FFNS-15, (c) FTSF-15, (d) FTNS-24, (e) FTSF-20, and (f) FTNS-33 models. Red and blue colours represent different field directions. The units are non-dimensional.



**Figure 4.6: Axisymmetric magnetic field:** for (a) FFSF-21, (b) FFNS-15, (c) FTSF-15, (d) FTNS-24, (e) FTSF-20, and (f) FTNS-33 models. The left (right) plot shows the meridional slice of the axisymmetric toroidal (streamlines of poloidal) magnetic field. In the toroidal plots, red shades represent prograde direction and blue shades represent retrograde direction. In the poloidal plots, red is clockwise and blue is anti-clockwise. The units are non-dimensional.

1336 small scale flux patches that are scattered in the bulk of the outer core. In the dipolar  
1337 regime, the fixed heat flux models seem to promote strong larger scaled toroidal magnetic  
1338 flux patches in the bulk of the outer core, whereas the fixed temperature models produce  
1339 intense flux patches along the equator close to the outer boundary, and inside the tangent  
1340 cylinder. The magnetic field morphology does not strongly depend on the choice of  
1341 thermal or velocity boundary conditions. It only depends on the available power.

## 1342 Velocity Field

1343 In this section, we examine the characteristics of the flow velocities inside the dynamo  
1344 generation region and compare them to non-magnetic convection models at similar pa-  
1345 rameters and boundary conditions. The kinetic energies of the characteristic multipolar  
1346 dynamo models (that are found at high  $Ro_l$ ) are an order of magnitude bigger than the  
1347 dipolar dynamo models. All the characteristic dynamo models are dominated by their  
1348 toroidal kinetic energies. The dominance is more prominent in the stress-free models.  
1349 The characteristic dipolar dynamo models are dominated by the non-axisymmetric  
1350 component of the toroidal kinetic energies, whereas the characteristic multipolar  
1351 dynamo models have equal contribution from the axisymmetric and non-axisymmetric  
1352 components. The characteristic dipolar and multipolar dynamo models are dominated  
1353 by the non-axisymmetric components of the poloidal kinetic energies.

1354

1355 The kinetic energies of the characteristic non-magnetic convection models are an order  
1356 of magnitude bigger than their corresponding characteristic dynamo models. All the  
1357 characteristic non-magnetic convection models are also dominated by their toroidal  
1358 kinetic energies. Again, the dominance is more prominent in the stress-free models.  
1359 Unlike the characteristic dynamo models, the axisymmetric toroidal energy dominates  
1360 the non-axisymmetric component for all non-magnetic convection models. The poloidal  
1361 kinetic energies are dominated by their non-axisymmetric components except for model

1362  $FTSF_C - 13$ , which is dominated by its axisymmetric component.

1363

1364 Next, we examine the velocity field morphology of characteristic dynamo models and  
1365 compare them to the characteristic non-magnetic convection models. Figure 4.7 presents  
1366 a characteristic snapshot of the axisymmetric velocity field of characteristic dynamo  
1367 models for comparison with characteristic non-magnetic convection models as shown in  
1368 figure 4.8. The velocity fields of the models in the dipolar regime are different from the  
1369 models in the multipolar regime and convection models with no magnetic fields. The  
1370 zonal flows of the multipolar models are stronger than the dipolar models. The toroidal  
1371 velocity fields of the convection models with no magnetic field are approximately constant  
1372 on cylinders parallel to the rotation axis, a sign of strong Taylor-Proudman influence.  
1373 The meridional circulation (poloidal velocity) is equatorially symmetric in this case. The  
1374 velocity field morphologies of the multipolar models are similar to the convection models  
1375 even though they produce strong magnetic fields. In this case, the strong magnetic fields  
1376 of multipolar models do not influence the large scale velocity fields. On the other hand,  
1377 the dipolar models have strong differential rotation inside the tangent cylinder and a  
1378 retrograde equatorial jet outside the tangent cylinder close to the outer core boundary;  
1379 a sign that Lorentz forces are strong enough to break the Taylor-Proudman constraint.  
1380 The meridional circulation of the dipolar dynamo models are predominantly equatorially  
1381 anti-symmetric throughout the core. The intensity of the zonal flows of the dynamo  
1382 models are weaker than the convection models without magnetic field due to magnetic  
1383 braking. Notably, the velocity field morphologies do not strongly depend on the choice  
1384 of thermal or velocity boundary conditions. They only depend on the available power,  
1385 and the magnetic field intensity and morphology.

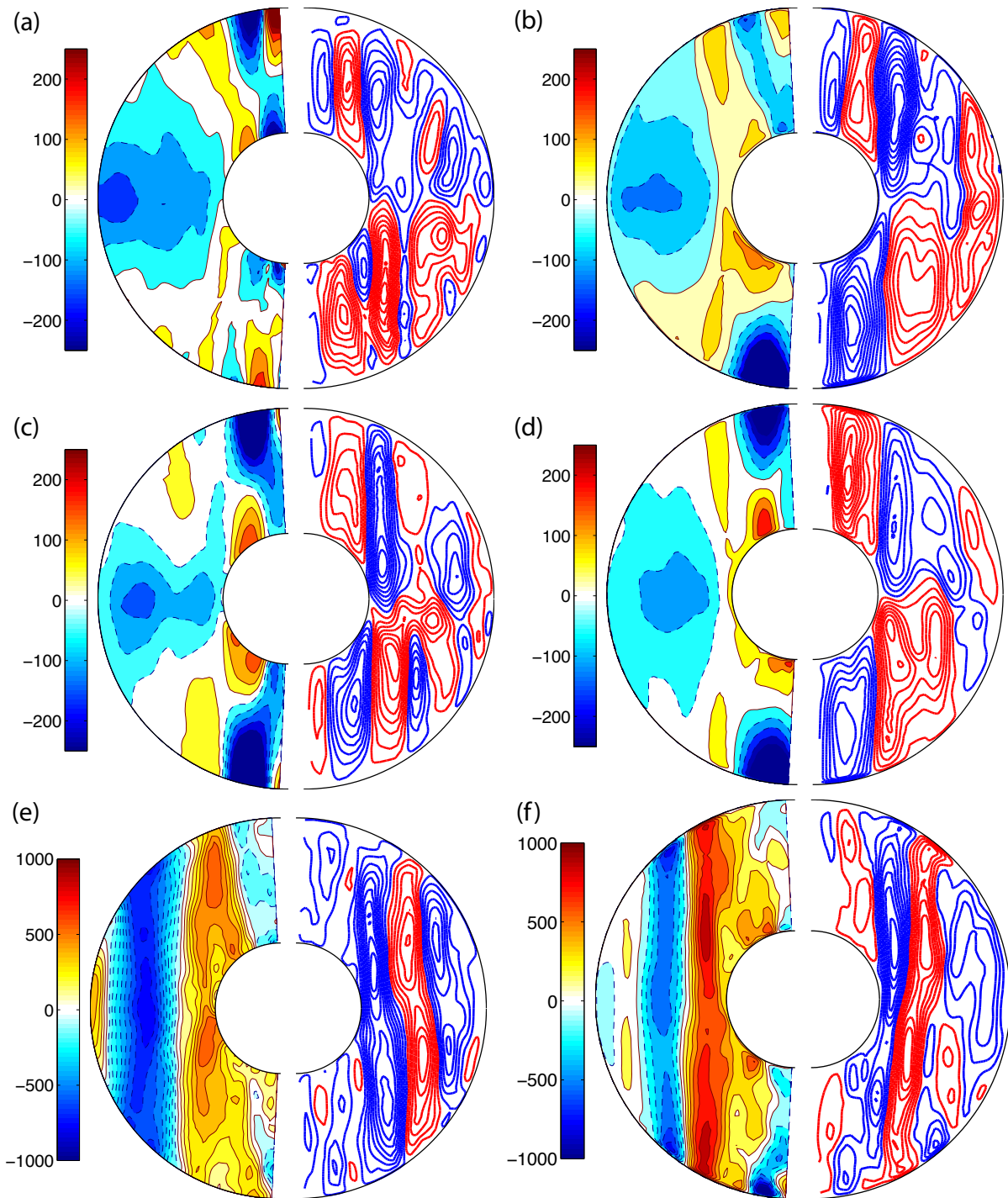


Figure 4.7: **Axisymmetric velocity field:** for (a) FFSF-21, (b) FFNS-15, (c) FTSF-15, (d) FTNS-24, (e) FTSF-20, and (f) FTNS-33 dynamo models. The toroidal velocity fields are shown on the left where red (blue) denotes prograde (retrograde) circulation and streamlines of poloidal velocity fields are shown on the right where red (blue) denotes clockwise (anti-clockwise) circulation.

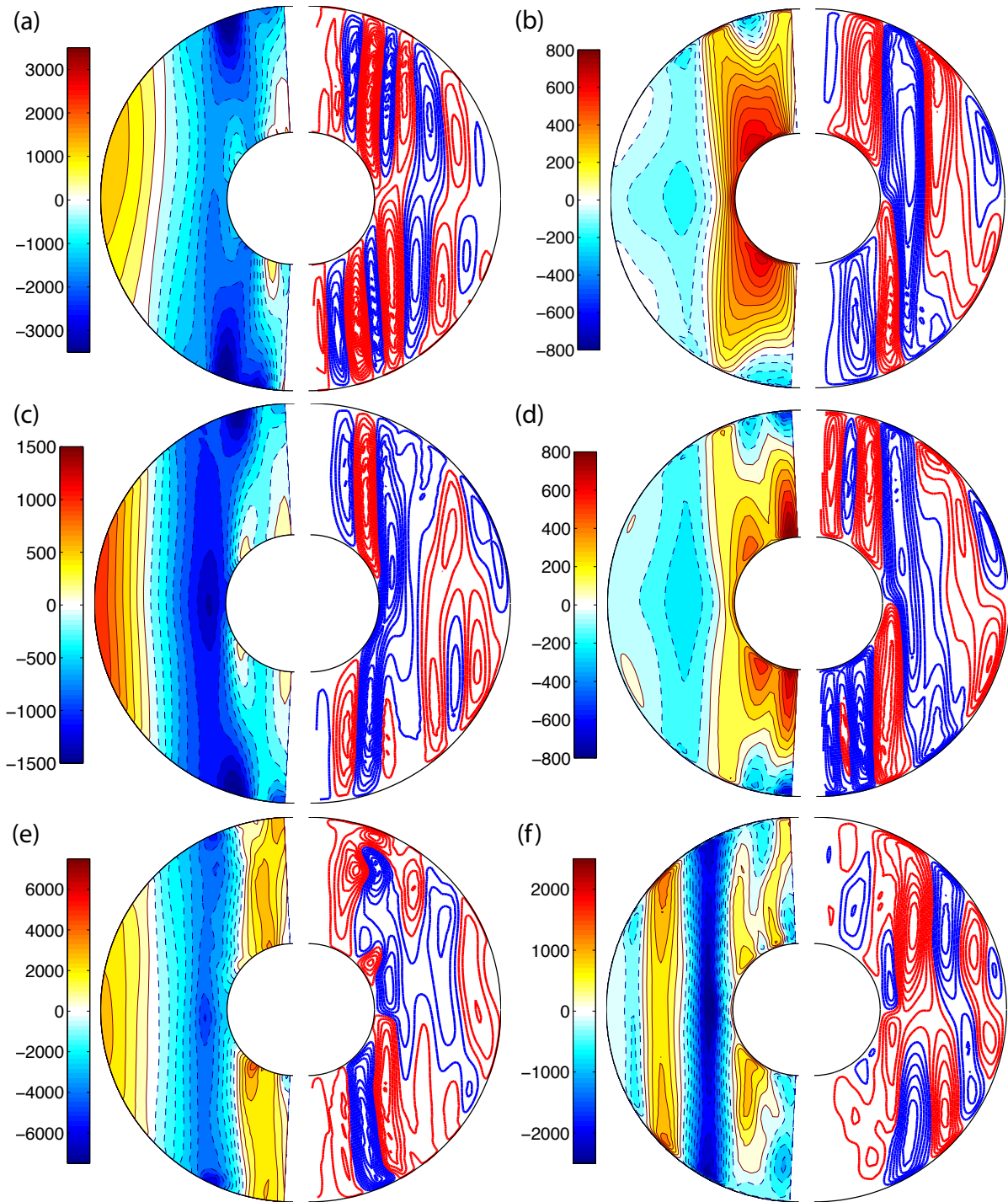


Figure 4.8: **Axisymmetric velocity field:** for (a)  $\text{FFSF}_C\text{-}16$ , (b)  $\text{FFNS}_C\text{-}14$ , (c)  $\text{FTSF}_C\text{-}09$ , (d)  $\text{FTNS}_C\text{-}08$ , (e)  $\text{FTSF}_C\text{-}13$ , and (f)  $\text{FTNS}_C\text{-}15$  convection models with no magnetic field. The toroidal velocity fields are shown on the left where red (blue) denotes prograde (retrograde) circulation and streamlines of poloidal velocity fields are shown on the right where red (blue) denotes clockwise (anti-clockwise) circulation.

1386 **Force Balance**

1387 In this section, we examine the force balances of the characteristic dipolar and multi-  
1388 polar dynamo models. As demonstrated in our previous work [[Dharmaraj and Stanley, 2012](#)], the traditional definition of the Elsasser number to determine the force balance is  
1389 inadequate and we therefore directly plot the axisymmetric  $\phi$  component of the Lorentz  
1390 and Coriolis force to examine if the Lorentz force is balanced by the Coriolis force in all  
1391 our characteristic models as presented in Figure 4.9.

1393 **Match Coefficient**

1394 In order to quantify the force balance we define the “Match Coefficient” ( $M_{LC}$ ) as follows:

$$M_{LC} = \int \frac{F_L * F_C}{(F_L^2 + F_C^2)/2} dV \quad (4.10)$$

1395 where,

1396  $F_L = [\vec{J} \times \vec{B}]_\phi$ :  $\phi$  component of Lorentz force, and

1397  $F_C = [\hat{\mathbf{z}} \times \vec{v}]_\phi$ :  $\phi$  component of Coriolis force.

1398

1399 Match Coefficient is inspired by correlation coefficient. It has the following properties:

1400 1. Match Coefficient  $(F_L, F_C) = \text{Match Coefficient } (F_C, F_L)$

1401 2. Ranges between -1 (forces are equal in magnitude and opposite in direction) and  
1402 +1 (forces are equal in magnitude and direction)

1403 3. 1 is perfect match

1404 4. -1 is perfect opposite match

1405 5. 0 means either  $F_L$  or  $F_C$  is 0

1406 6. If  $F_L$  and  $F_C$  are both zero then the expression for  $M_{LC}$  gives an indefinite number.

1407 If this occurs, we assign  $M_{LC} = 1$ , since it is a perfect match.

1408 The Match Coefficient of the characteristic dipolar and multipolar dynamo models are  
1409 shown in Figure 4.9. The models in the dipolar regime are, to a good degree, in mag-  
1410 netostrophic balance whereas the models in the multipolar regime are not. Since the  
1411 multipolar models are dominated by their non-axisymmetric components we examined  
1412 the force balance due to the non-axisymmetric components and found that they were  
1413 also not in magnetostrophic balance. It is evident that the strong large scale dipolar  
1414 dominated fields of the dipolar models are a result of this magnetostrophic force balance.  
1415 However, the multipolar models also produce intense magnetic fields due to the presence  
1416 of strong Lorentz forces but the Lorentz force is not balanced by the Coriolis force in  
1417 these models. In order to investigate which force balances the Lorentz force, we examine  
1418 the power budget for the zonal flows. We choose to examine the power budget instead  
1419 of just the forces as we have demonstrated in previous sections that irrespective of the  
1420 choice of boundary conditions our dynamo model di-polarities only depend on the avail-  
1421 able power. As an aside, the multipolar dynamos at low  $Ro_l$  that are bistable are not in  
1422 magnetostrophic balance because they have weak magnetic field intensities.

### 1423 Power Budget

1424 Similar to the procedure adapted by [Aubert \[2005\]](#), we multiply the axisymmetric  $\phi$   
1425 component of the momentum equation by the  $\phi$  component of the velocity field to get

$$\frac{1}{2} \frac{\partial}{\partial t} \bar{v}_\phi^2 = -\bar{v}_s \bar{v}_\phi + \overline{[\vec{J} \times \vec{B}]_\phi} \bar{v}_\phi - Ro_M \overline{[(\vec{v} \cdot \nabla) \vec{v}]_\phi} \bar{v}_\phi + E \overline{[\nabla^2 \vec{v}]_\phi} \bar{v}_\phi \quad (4.11)$$

1426 where an over-bar denotes axisymmetric component. For the derivations and spherical  
1427 harmonic expansion of the Lorentz, Coriolis, inertial and viscous forces please refer to

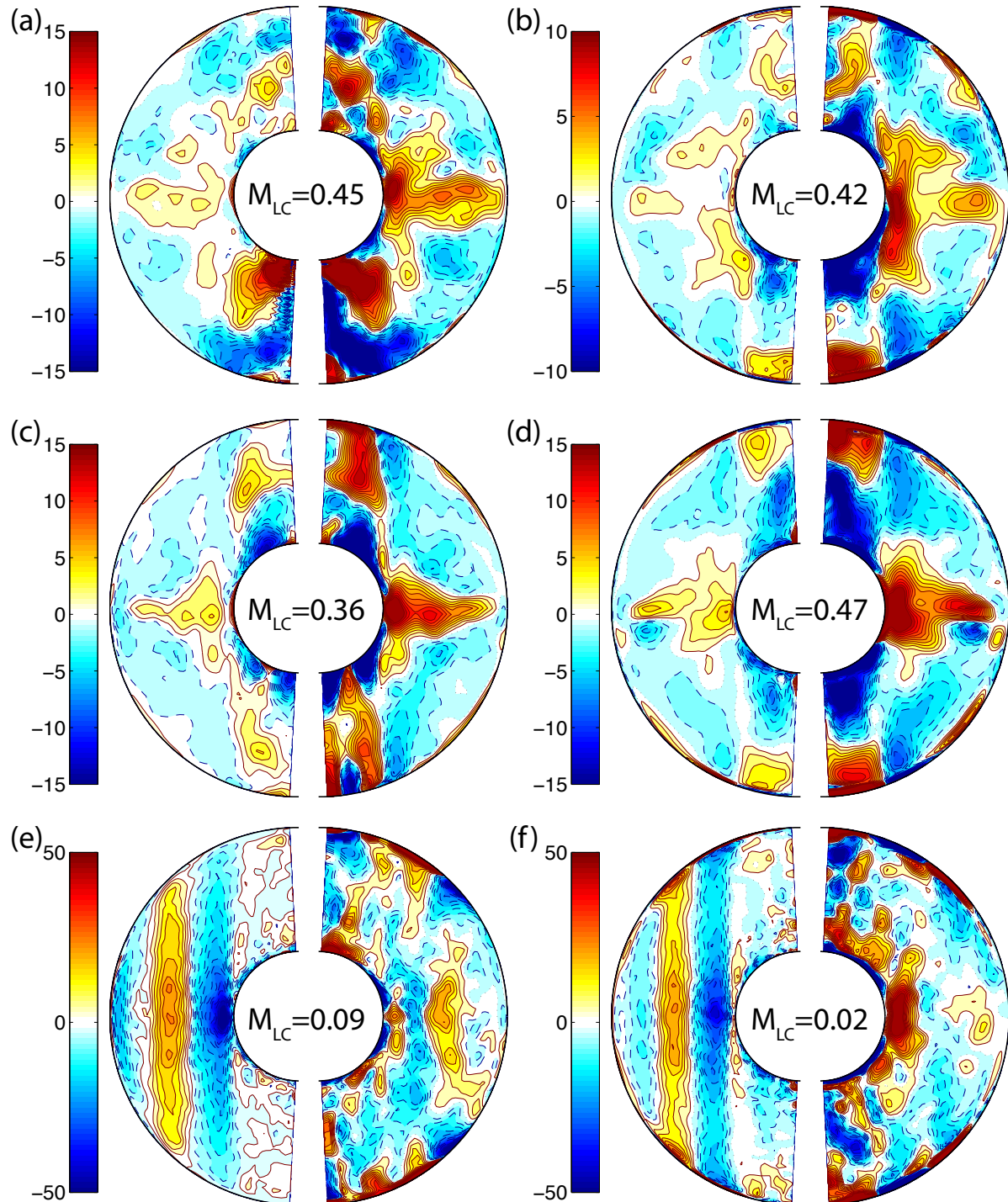
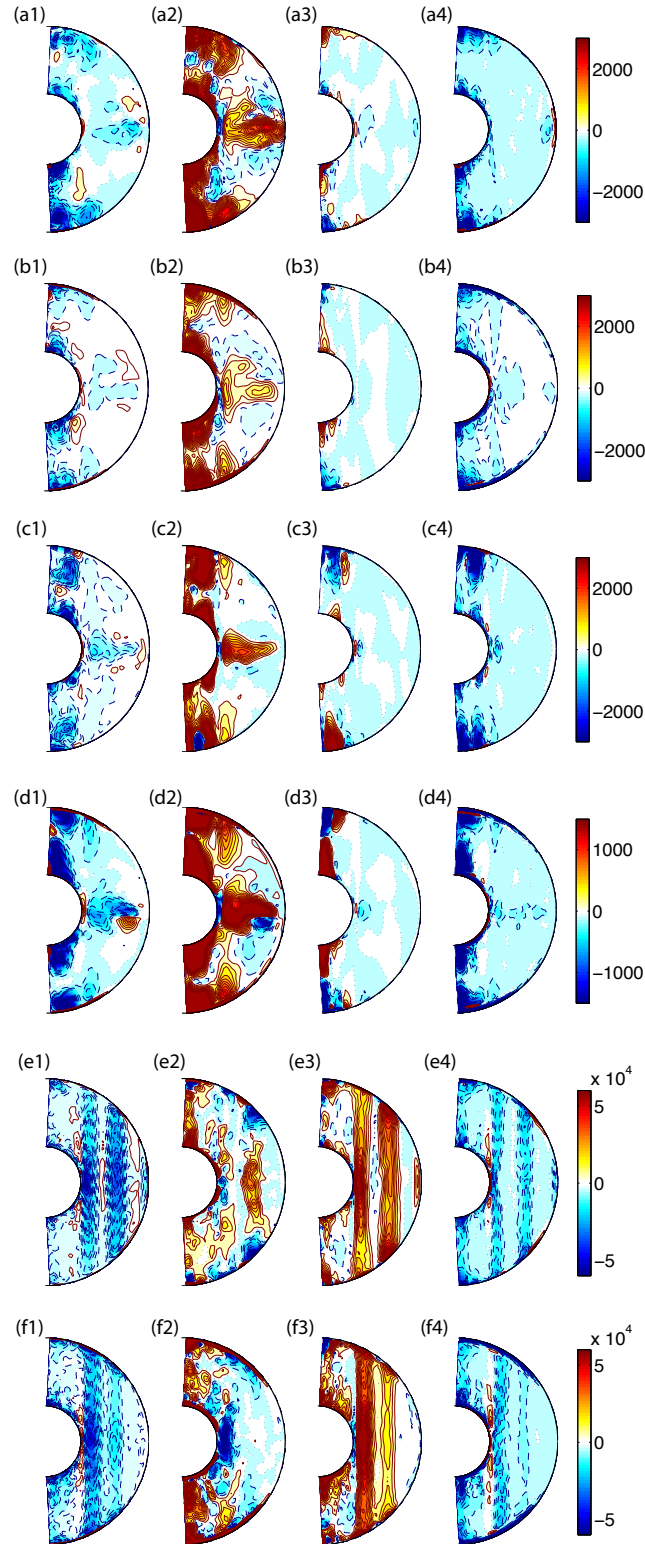


Figure 4.9: **Force Balance:** for (a) FFSF-21, (b) FFNS-15, (c) FTSF-15, (d) FTNS-24, (e) FTSF-20, and (f) FTNS-33 models. The left and right plots show the time averaged axisymmetric  $\phi$  components of the Lorentz and Coriolis forces respectively.

appendix C. Figure 4.10 plots the time average of the 4 terms on the right-hand-side of the equation 4.11, namely, the Coriolis term, Lorentz term, inertial term and the viscous term from left to right respectively. For the models in the dipolar regime, the main power source is the Coriolis term and the Lorentz term acts as a sink (Ohmic dissipation). However, for the models in the multipolar regime, the main power source is the inertial term (Reynolds stress) and the Lorentz and viscous (viscous dissipation) terms act as sinks. In this case the Coriolis term acts as both, a source and a sink in different regions of the outer core. The source is strongest at the location of the equatorial jet and inside the tangent cylinder in the dipolar models. The source is strongest inside the tangent cylinder and at the outer core boundary in the multipolar models. Therefore, it is evident that the Lorentz force is balanced by the Coriolis force in the dipolar dynamo models and the Lorentz force is balanced by the inertial force in the multipolar dynamo models irrespective of the thermal and velocity boundary conditions. For comparison, we plot the Coriolis, inertial and viscous terms of the corresponding non-magnetic convection models in Figure 4.11, and find that in all the models the Coriolis and inertial terms balances the viscous term.

1444

The force balance between the Lorentz, Coriolis, inertial and viscous forces can also be quantified by comparing the total forces over a volume integral in a spherical shell as employed by Soderlund et al. [2012] rather than only the axisymmetric component of the forces as we have done above. Figure 4.12 shows the force integrals and their respective ratios for the different boundary conditions employed. In order to focus on the influence of different boundary conditions, in these plots, we fix the parameters to  $E = 6e - 5$ ,  $Ro_M = 2e - 5$ ,  $q_k = 1$  and vary the  $Ra$ . In the parameter space that we have included here, the Coriolis force dominates all the models. In all the models, irrespective of the choice of thermal or velocity boundary conditions, we observe a similar trend of the Lorentz force being balanced by the Coriolis force at moderately supercritical



**Figure 4.10: Power Budget:** for FFSF-21, FFNS-15, FTSF-15, FTNS-24, FTSF-20, and FTNS-24 dynamo models from the first to last row respectively. The first, second, third and fourth columns show the time averaged axisymmetric  $\phi$  components of the Lorentz, Coriolis, inertial and viscous terms respectively. In these plots, red (blue) denotes sources (sinks) of power.

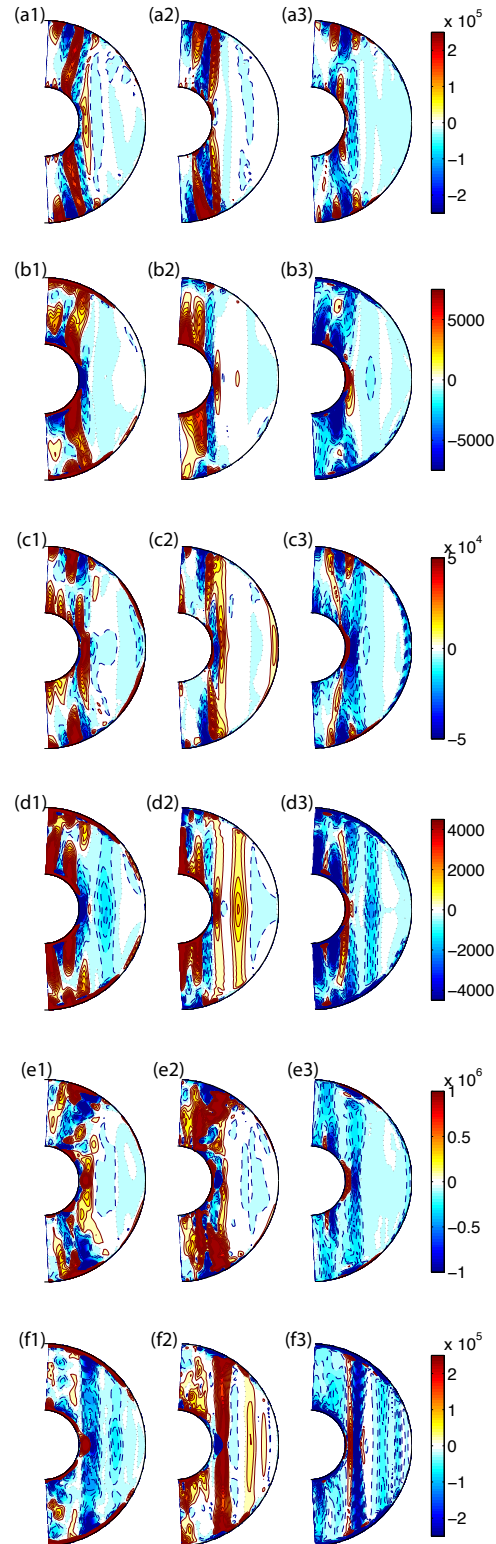


Figure 4.11: **Power Budget:** for the FFSF<sub>C</sub>-16, FFNS<sub>C</sub>-14, FTSF<sub>C</sub>-09, FTNS<sub>C</sub>-08, FTSF<sub>C</sub>-13, and FTNS<sub>C</sub>-15 convection models with no magnetic field from the first to last row respectively. The first, second, and third columns show the time averaged axisymmetric  $\phi$  components of the Coriolis, inertial and viscous terms respectively. In these plots, red (blue) denotes sources (sinks) of power.

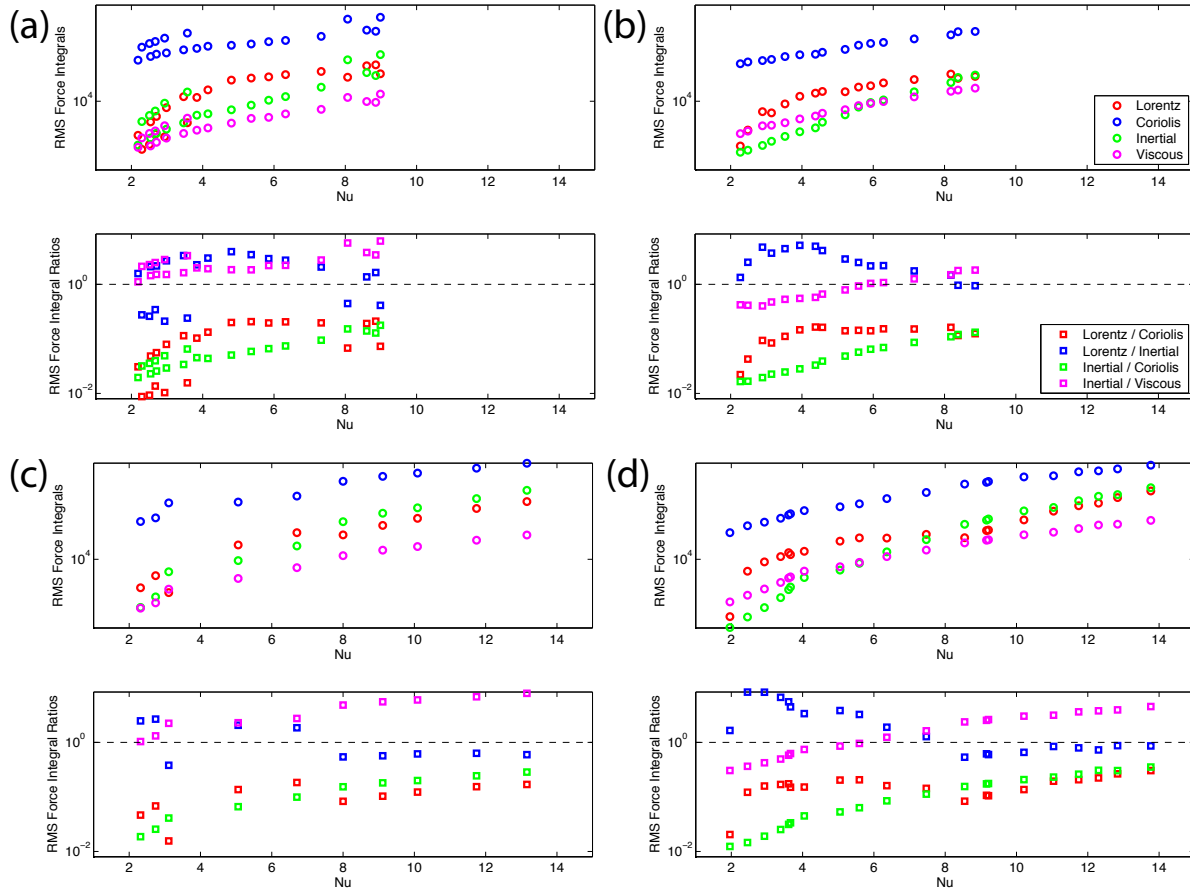


Figure 4.12: **RMS Force Integrals:** for models with  $E = 6e^{-5}$ ,  $Ro_M = 2e^{-5}$  and  $q_k = 1$ . (a) FFSF, (b) FFNS, (c) FTSF and (d) FTNS. The top plots are the time averaged volume integrals of the RMS Lorentz, Coriolis, inertial and viscous forces. The bottom plots are the time averaged ratios of the Lorentz force to the Coriolis and inertial forces, and the ratio of inertial force to Coriolis and viscous forces.

1455 Rayleigh numbers and as the Rayleigh number increases, the Lorentz force is instead  
 1456 balanced by the inertial force.

1457

1458 In order to eliminate the contribution from pressure terms, we only look at the  $\phi$   
 1459 component of these forces as shown in 4.13. Even though the  $\phi$  component provides a  
 1460 better estimate of the force balances, it still does not take into account the sign and  
 1461 location of the forces which can lead us to misinterpret the force balance i.e. just because  
 1462 Coriolis forces are of a similar order of magnitude as the Lorentz forces in a model, it  
 1463 does not mean that they balance each other. We believe that plotting the force balances

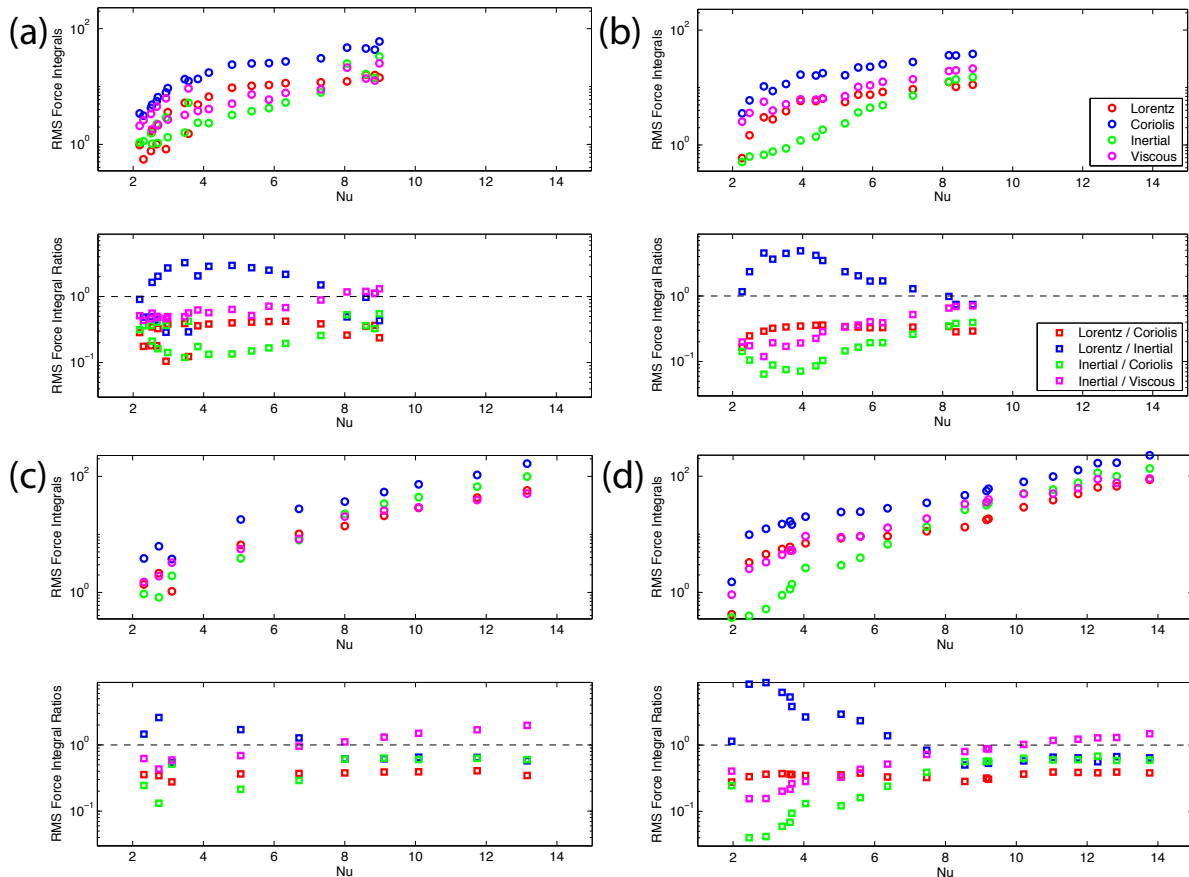


Figure 4.13: **RMS Force Integrals of the  $\phi$  component:** for models with  $E = 6e^{-5}$ ,  $Ro_M = 2e^{-5}$  and  $q_k = 1$ . (a) FFSF, (b) FFNS, (c) FTSF and (d) FTNS. The top plots are the time averaged volume integrals of the  $\phi$  component RMS Lorentz, Coriolis, inertial and viscous forces. The bottom plots are the time averaged ratios of the  $\phi$  component of the Lorentz force to the Coriolis and inertial forces, and the ratio of inertial force to Coriolis and viscous forces.

<sup>1464</sup> and estimating the  $M_{LC}$  gives a better estimate of the dominate force balances.

<sup>1465</sup>

<sup>1466</sup> Since the dipolar and multipolar models have different force balances, we investigate if  
<sup>1467</sup> they have different dynamo generation mechanism.

<sup>1468</sup> **Dynamo Generation Mechanism**

<sup>1469</sup> In dynamo theory, it is important to understand how poloidal magnetic field is generated  
<sup>1470</sup> from toroidal magnetic field and the complementary process of generating toroidal  
<sup>1471</sup> magnetic field from poloidal magnetic field. In some models the poloidal magnetic  
<sup>1472</sup> field is generated by the alpha effect, through shearing and twisting of toroidal mag-  
<sup>1473</sup> netic field lines in a helical flow, whereas the toroidal magnetic field is generated by  
<sup>1474</sup> an omega effect, through shearing of poloidal or toroidal field lines by differential rotation.

<sup>1475</sup>

<sup>1476</sup> Illustrations of magnetic field generation is presented in Figures 4.14, 4.15, 4.16 and  
<sup>1477</sup> 4.17. In Figure 4.14, a rising twisting element of fluid brings up the toroidal magnetic  
<sup>1478</sup> field. A loop of flux is created which is twisted due to helicity and forms the poloidal  
<sup>1479</sup> magnetic field. The loop current is parallel to the original magnetic field. In Figure 4.15,  
<sup>1480</sup> toroidal magnetic loops are generated from poloidal magnetic field through shearing by  
<sup>1481</sup> azimuthal velocity field.

<sup>1482</sup>

<sup>1483</sup> Illustration of Figures 4.16 and 4.17 along with the explanations of magnetic field  
<sup>1484</sup> generation are adopted from Olson et al. [1999]. In Figure 4.16 low latitude  $\vec{B}_T$  is  
<sup>1485</sup> stretched and twisted into  $\vec{B}_P$  by convection columns with negative axial vorticity. The  
<sup>1486</sup> converging and diverging secondary flow at the equator concentrates  $\vec{B}_P$  along negative  
<sup>1487</sup> vortices near the equator, and along positive vortices near the outer core boundary. The  
<sup>1488</sup> induced field has concentrated bundles of twisted magnetic flux that move from one  
<sup>1489</sup> vortex to the other. The superposition of these radial flux patches ( $\vec{B}_P$ ) generate the

1490 axial dipole at the outer core boundary.

1491

1492 Figure 4.17 illustrates how  $\vec{B}_T$  is generated from  $\vec{B}_P$  through columnar convection. In  
1493 Figure 4.17 a, a straight poloidal field line that is in an upwelling between two columnar  
1494 vortices is pushed out towards the outer core while being twisted by the secondary flow.  
1495 While the geostrophic columnar convection advects the field and brings it forward, the  
1496 secondary flow rotates it into an inclined azimuthal direction. This field line converges  
1497 towards the equatorial plane in an upwelling since a material line of fluid that moves  
1498 outwards has to shorten along the vertical axis as shown in the right plot to generate  
1499  $\vec{B}_T$  from  $\vec{B}_P$ .

1500

1501 We estimated helicity and the omega effect as described by Olson et al. [1999] and Chris-  
1502 tensen and Olson [1998] and obtained identical results at identical control parameters  
1503 and boundary conditions, but instead of approximately estimating alpha and omega ef-  
1504 fects like they do, we choose to define our alpha and omega effects by decomposing the  
1505 generation term of the magnetic induction equation (equation 1.37) as follows:

$$\nabla \times (\vec{v} \times \vec{B}) = \underbrace{(\vec{B} \cdot \nabla) \vec{v}}_{\text{Creation}} - \underbrace{(\vec{v} \cdot \nabla) \vec{B}}_{\text{Advection}} \quad (4.12)$$

$$\begin{aligned} (\vec{B} \cdot \nabla) \vec{v} &= \underbrace{(\vec{B}_T \cdot \nabla) \vec{v}_P}_{\text{Creates } \vec{B}_P} + \underbrace{(\vec{B}_P \cdot \nabla) \vec{v}_P + (\vec{B}_P \cdot \nabla) \vec{v}_T^{Naxi} + (\vec{B}_T \cdot \nabla) \vec{v}_T^{Naxi}}_{\alpha \text{ effect}} \\ &\quad + \underbrace{(\vec{B}_P \cdot \nabla) \vec{v}_T^{Axi} + (\vec{B}_T \cdot \nabla) \vec{v}_T^{Axi}}_{\omega \text{ effect}} \end{aligned} \quad (4.13)$$

1506 From equation 4.13 we can see that only  $\alpha$  effect creates  $\vec{B}_P$ . Therefore, if we want

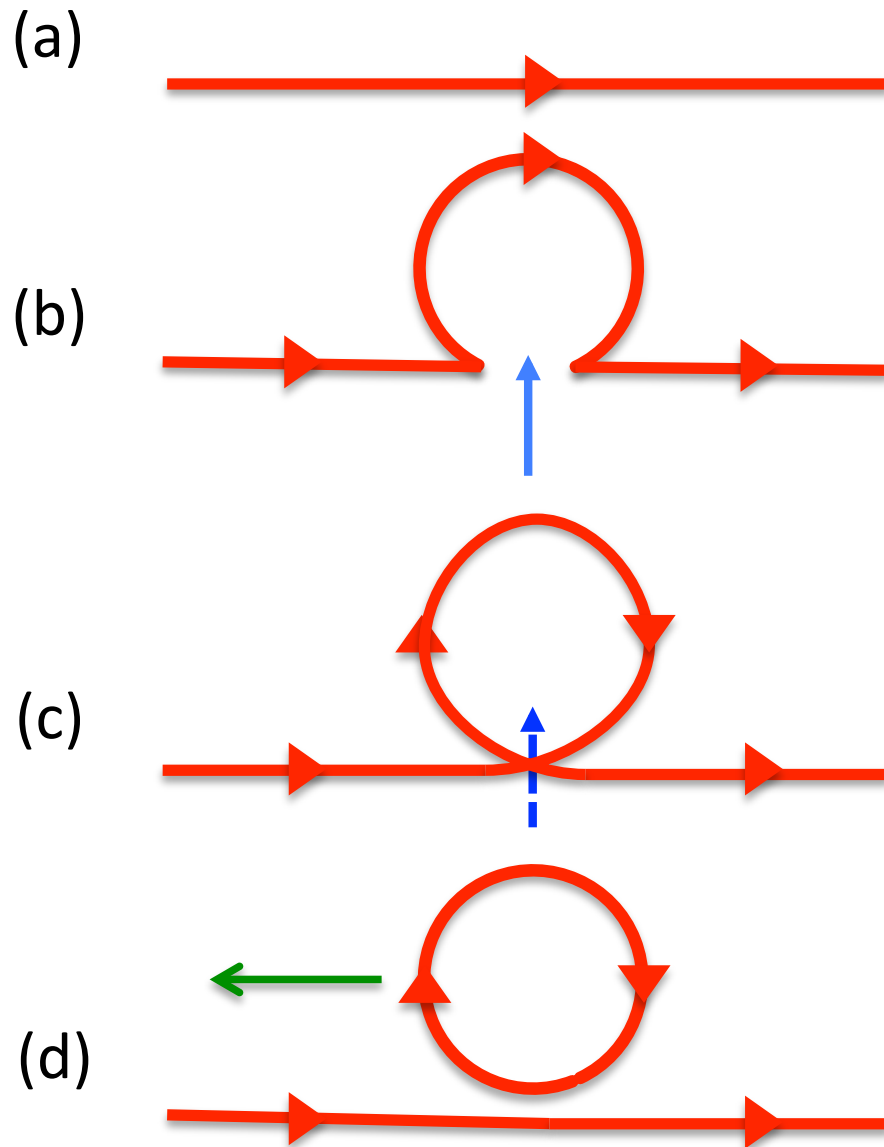


**Figure 4.14: Generation of Poloidal Magnetic Field from Toroidal Magnetic Field through  $\alpha$  effect.** Red lines are magnetic field lines, solid blue line represents rising fluid, blue dotted line represents rising twisting element of fluid, and green line represents the loop current. (a) Toroidal magnetic field line, (b) interaction of the fluid up-welling with  $\vec{B}_T$ , (c) due to the Coriolis force the fluid rotates as it moves upward exhibiting helicity and (d) magnetic field line is carried with the conducting fluid and is twisted to generate  $\vec{B}_P$  loop from  $\vec{B}_T$ .

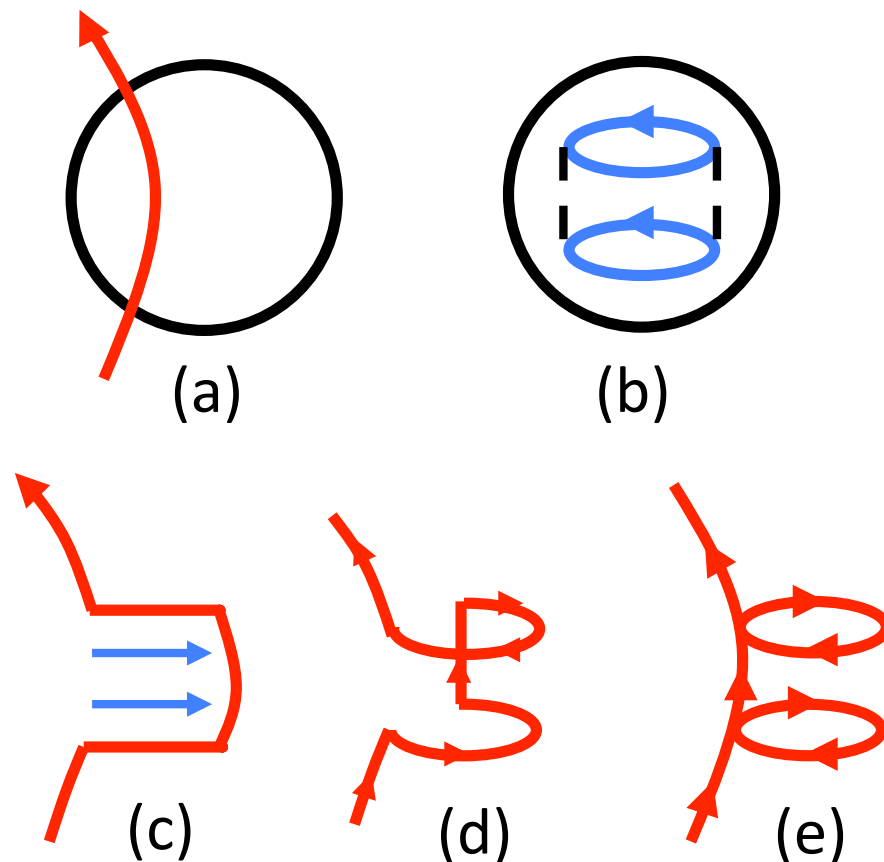
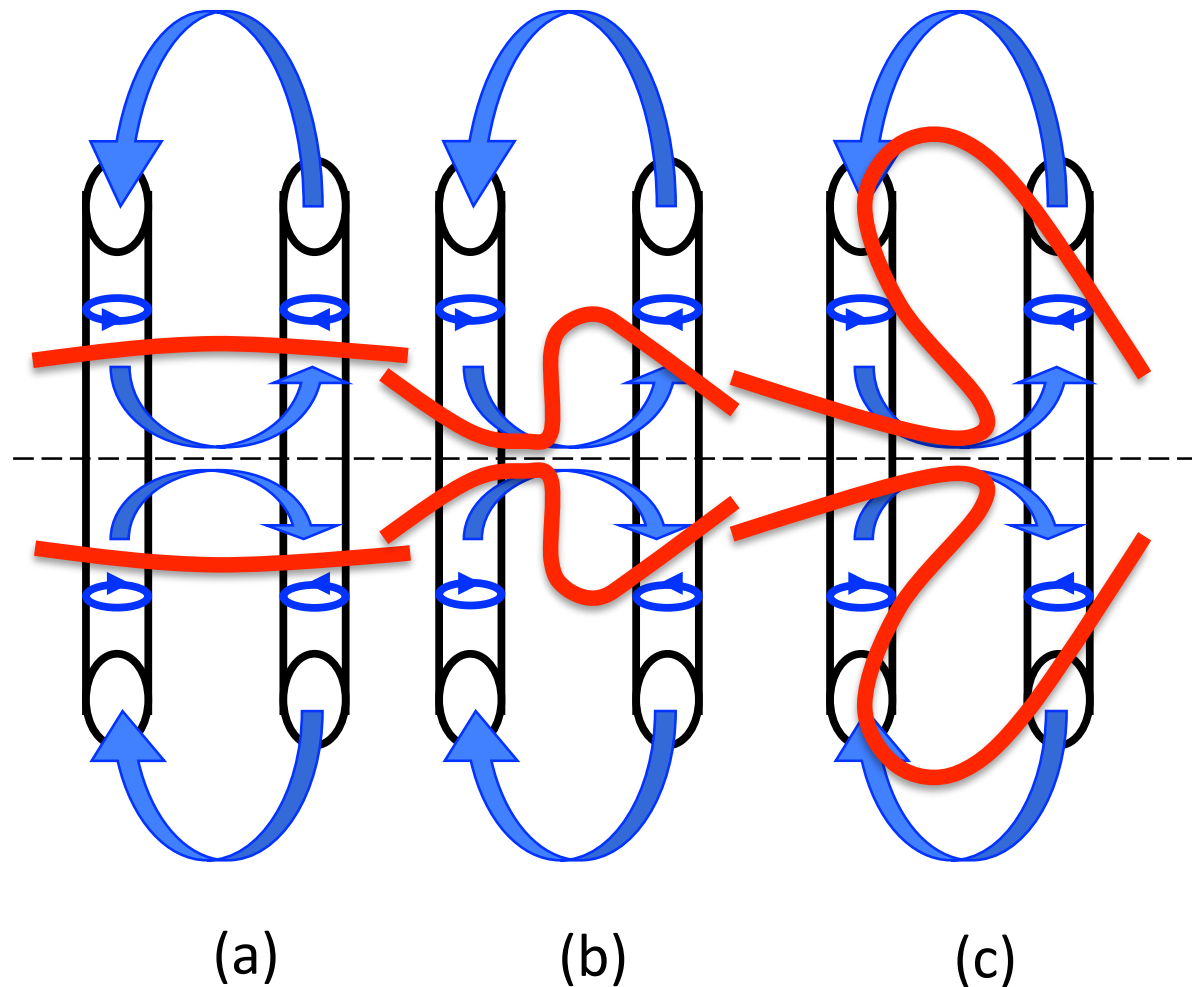
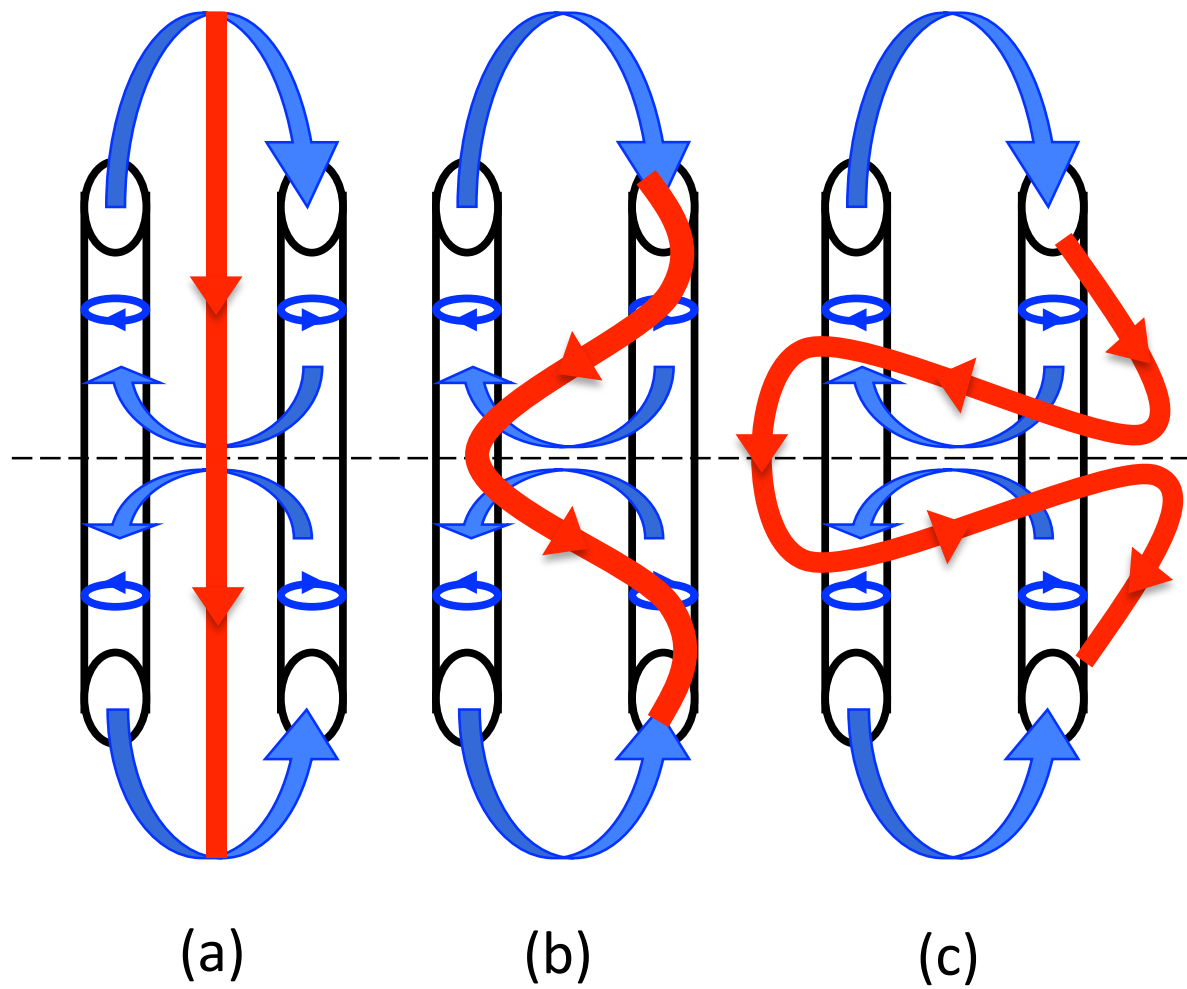


Figure 4.15: **Generation of Toroidal Magnetic Field from Poloidal Magnetic Field through  $\omega$  effect.** Red lines are magnetic field lines and solid blue lines represent azimuthal fluid velocity. (a) Initial  $\vec{B}_P$  passing through the Earth's core, (b) initial cylindrical shear velocity field, (c and d) interaction between the magnetic and the velocity field, and (e) after completing one full circuit two new  $\vec{B}_T$  loops with opposite polarity are produced.



**Figure 4.16: Poloidal magnetic field generation from toroidal magnetic field through columnar convection.** Cylinders are convection columns. The sloping top and bottom of the cylinders indicate the intersection of the columns with the spherical outer core boundary. The dotted line represents the equator. Red lines are magnetic field lines, small blue loops with arrows inside cylinders represent cyclonic and anti-cyclonic rotation of convection columns (geostrophic columnar motion) and large blue arrows between cylinders represents secondary (ageostrophic) flow up and down the convection columns and its recirculation near the equator and core mantle boundary. Motion towards (away from) the equator is caused by columns with positive (negative) vorticity. Near (Away from) the equatorial plane fluid flows from positive (negative) to negative (positive) vortices.



**Figure 4.17: Toroidal magnetic field generation from poloidal magnetic field through  $\omega$  effect.** Cylinders are convection columns. The sloping top and bottom of the cylinders indicate the intersection of the columns with the spherical outer core boundary. The dotted line represents the equator. Red lines are magnetic field lines, small blue loops with arrows inside cylinders represent cyclonic and anti-cyclonic rotation of convection columns (geostrophic columnar motion) and large blue arrows between cylinders represents secondary (ageostrophic) flow up and down the convection columns and its recirculation near the equator and core mantle boundary. Motion towards (away from) the equator is caused by columns with positive (negative) vorticity. Near (Away from) the equatorial plane fluid flows from positive (negative) to negative (positive) vortices.

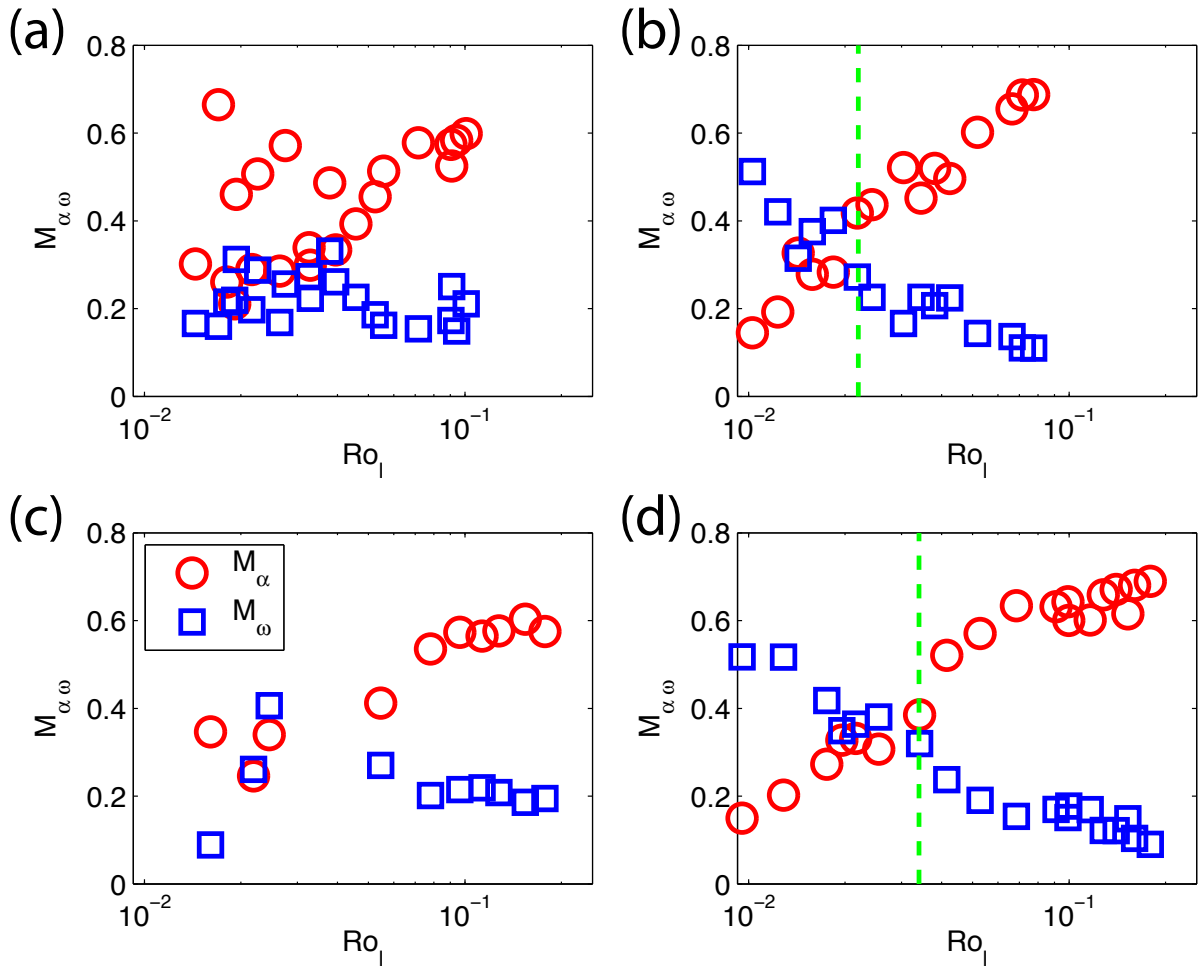


Figure 4.18: **Match coefficient of  $\alpha$  and  $\omega$  effects versus local Rossby number:** for models with  $E = 6e^{-5}$ ,  $Ro_M = 2e^{-5}$  and  $q_k = 1$ . (a) FFSF, (b) FFNS, (c) FTSF and (d) FTNS. The green dotted line marks the transition of  $\alpha$  effect dominance over  $\omega$  effect.

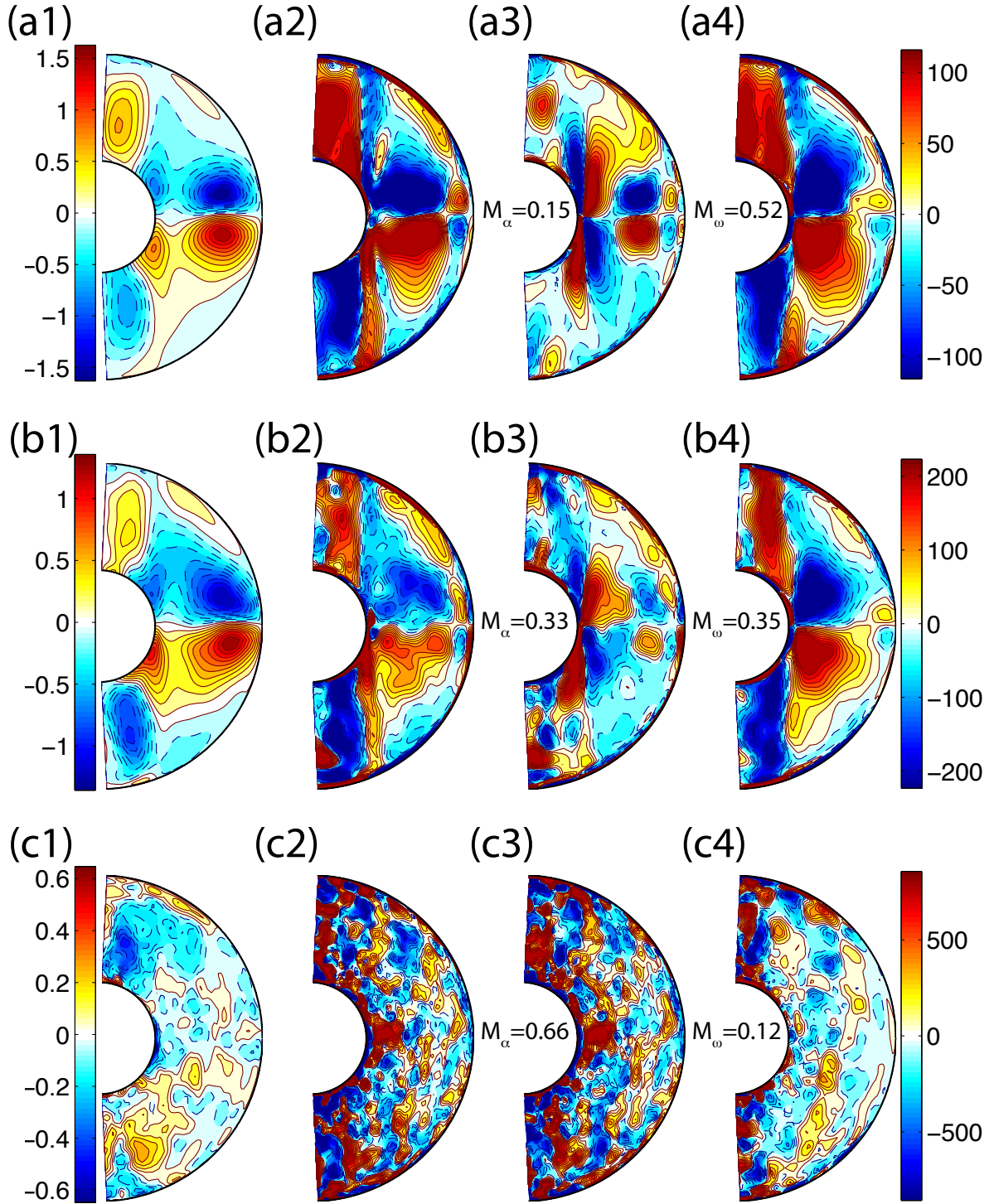


Figure 4.19: **Dynamo creation mechanism:** for models FTNS-18, FTNS-22 and FTNS-32 from first to last row respectively. The first column shows the time averaged axisymmetric toroidal magnetic field. The second, third and fourth column shows the time averaged axisymmetric  $\phi$  component of the total creation term of the toroidal magnetic field, toroidal magnetic field created by  $\alpha$  effect and toroidal magnetic field created by the  $\omega$  effect respectively.

1507 to categorize the type of dynamo it would be sufficient to compare the  $\vec{B}_T$  generation  
 1508 components. For the complete derivation of the generation terms please refer to Section  
 1509 [C.5](#) in Appendix [C](#).

1510

1511 In order to quantify which effect dominates the generation of  $\vec{B}_T$ , we compute the Match  
 1512 Coefficient as follows:

$$M_\alpha = \int \frac{F_\alpha * F_{\vec{B}_T}}{(F_\alpha^2 + F_{\vec{B}_T}^2)/2} dV \quad (4.14)$$

$$M_\omega = \int \frac{F_\omega * F_{\vec{B}_T}}{(F_\omega^2 + F_{\vec{B}_T}^2)/2} dV \quad (4.15)$$

1513 where,  $F_\alpha$  is the  $\alpha$  effect that creates the  $\phi$  component of  $\vec{B}_T$ ,  $F_\omega$  is the  $\omega$  effect that  
 1514 creates the  $\phi$  component of  $\vec{B}_T$ , and  $F_{\vec{B}_T}$  is the sum of  $\alpha$  and  $\omega$  effects that create the  $\phi$   
 1515 component of  $\vec{B}_T$ .

1516

1517 Figure [4.18](#) presents the Match Coefficient of  $\alpha$  and  $\omega$  effects versus local Rossby  
 1518 number. In order to focus on the influence of different boundary conditions, in these  
 1519 plots, we fix the parameters to  $E = 6e - 5$ ,  $Ro_M = 2e - 5$ ,  $q_k = 1$  and vary the  $Ra$ .  
 1520 Irrespective of the thermal boundary conditions, the toroidal magnetic field of all the  
 1521 stress-free models are dominantly created by the  $\alpha$  effect. So, they are all  $\alpha^2$  type  
 1522 dynamos. However, irrespective of the thermal boundary conditions, the toroidal  
 1523 magnetic field of all the no-slip models are dominantly created by  $\omega$  effect at moderately  
 1524 supercritical Rayleigh number, then as the Rayleigh number is increased, the  $\alpha$  and  $\omega$   
 1525 effects become equally important, and then at highly supercritical Rayleigh numbers,  
 1526 the dynamos are dominantly created by  $\alpha$  effect. So, they follow a transition from  
 1527  $\alpha\omega$  type dynamo to  $\alpha^2\omega$  type dynamo to  $\alpha^2$  type dynamo. Therefore, axisymmetric  
 1528 dipolar toroidal magnetic fields are generated by  $\omega$  effect at moderately supercritical  
 1529 Rayleigh numbers through shearing of  $\vec{B}_T$  and  $\vec{B}_P$  by axisymmetric differential rotation.

1530 In this case, the axially dipolar magnetic field influences the velocity field and breaks  
 1531 the Taylor-Proudman columns. As the Rayleigh number is increased, dipolar magnetic  
 1532 fields with some deviations from axisymmetry are generated by  $\alpha$  and  $\omega$  effects through  
 1533 twisting and shearing of  $\vec{B}_T$  and  $\vec{B}_P$ . As Rayleigh number is further increased and  
 1534 the flow becomes turbulent, the resulting magnetic field is dominantly non-dipolar,  
 1535 which is dominantly generated by  $\alpha$  effect through convective motions. In this case,  
 1536 the strongly axisymmetric differential rotation does not contribute substantially in  
 1537 generating  $\vec{B}_T$ , even though the Reynolds stresses strongly influences the large scale  
 1538 flows through inverse cascading of energy. Notably, in the no-slip models, the dominance  
 1539 of  $\alpha$  effect over  $\omega$  effect happens earlier for fixed heat flux models in comparison to fixed  
 1540 temperature models. Also, at high  $Ro_l$ , irrespective of thermal or velocity boundary  
 1541 conditions all the models produce  $\alpha^2$  type dynamo. On the other hand, at low  $Ro_l$ , only  
 1542 no-slip models produce  $\alpha\omega$  type dynamos as they substantially generate more shear at  
 1543 the inner and outer core boundaries.

1544

1545 Figure 4.19 shows the time averaged toroidal magnetic field, creation of  $\vec{B}_T$ , and the  
 1546 creation of  $\vec{B}_T$  due to  $\alpha$  and  $\omega$  effects (terms in equation 4.13) for models FTNS-18,  
 1547 FTNS-22 and FTNS-32. From Figure 4.19 it is evident that model FTNS-18 is an  $\alpha\omega$   
 1548 type dynamo, model FTNS-22 is an  $\alpha^2\omega$  type dynamo and model FTNS-32 is an  $\alpha^2$  type  
 1549 dynamo.

## 1550 Boundary Layer Dynamics Controlled by Force Balances

1551 In planetary dynamos, most of the fluid flows and dynamical processes occur in the  
 1552 bulk of the fluid outer core. Boundary layers are regions where the bulk fluid meets  
 1553 the bounding surfaces i.e. it is a thin region in the fluid adjacent to a surface where  
 1554 velocity, temperature and concentration gradients normal to the surface are significant.  
 1555 The thermal and Ekman boundary layer thickness depends on the thermal forcing, and

1556 the thermal and viscous diffusivities respectively. The sudden change in direction of the  
1557 temperature (Figure 4.21) and RMS velocity (Figure 4.22) profiles close to the inner  
1558 and outer core boundaries represent the thermal and Ekman boundary layers respectively.

1559

1560 King et al. [2009] suggests that when the thermal boundary layer is thicker than the  
1561 Ekman boundary layer, rotational effects control convection and constrain fluid motion.  
1562 On the other hand if the thermal boundary layer is thinner than the Ekman boundary  
1563 layer then convection is turbulent, the upper most part of the Ekman boundary layer is  
1564 mixed with the bulk of the fluid and the influence of rotation on interior fluid dynamics  
1565 is truncated. We examine if this boundary layer dynamics affects the magnetic or  
1566 velocity field morphology or influences the dipolar or multipolar regime in which our  
1567 dynamo models fall in.

1568

1569 Figure 4.20 plots the Thermal and Ekman boundary layer thickness versus Nusselt num-  
1570 ber for models with parameters,  $E = 6e^{-5}$ ,  $Ro_M = 2e^{-5}$  and  $q_k = 1$ , and no-slip velocity  
1571 boundary conditions, for fixed heat flux and fixed temperature boundary conditions for  
1572 dynamo models and corresponding non-magnetic convection models. The boundary layer  
1573 transition for the dynamo and non-magnetic convection models occur at  $Nu \approx 11$  and at  
1574  $Nu \approx 12$  respectively. The transition from dipolar to multipolar dynamo occurs at ap-  
1575 proximately  $Nu = 11$  or  $Ro_l = 10.12$ . The force balance changes at this transition. This  
1576 explains why, velocity field morphology and power budgets of the multipolar dynamos  
1577 are similar to non-magnetic convection models, even though they have strong Lorentz  
1578 forces. At this transition, convection is turbulent, rotational effects become unimportant  
1579 and the inertial and viscous forces become important. The fact that the boundary layer  
1580 transition coincides with the dipolarity transition suggests some correspondence that the  
1581 change in dominant force balances in the bulk affected the boundary layer thicknesses or  
1582 vice versa that we will investigate in future work.

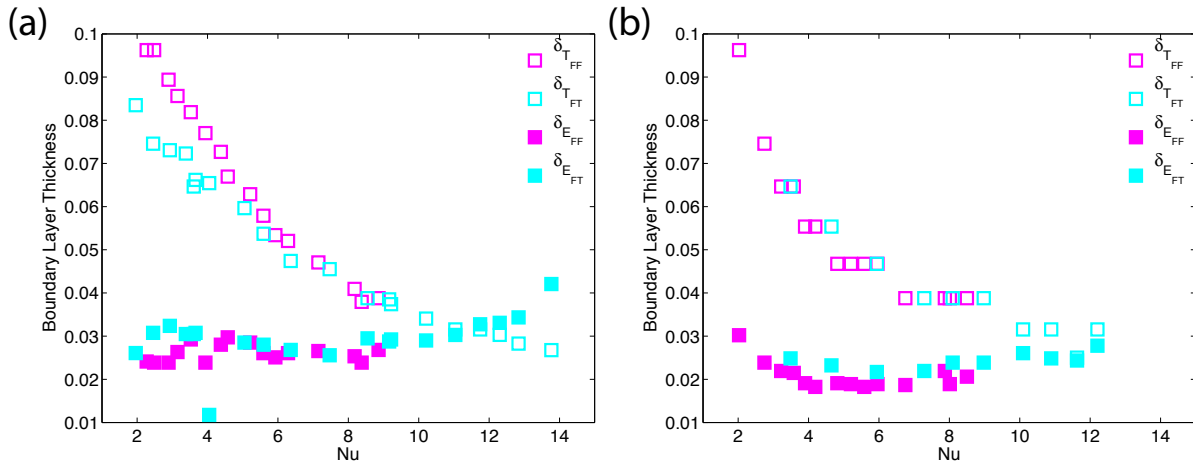


Figure 4.20: Boundary Layer Thickness versus Nusselt number for no-slip models with fixed flux and fixed temperature boundary conditions at  $E = 6e^{-5}$ ,  $\text{Ro}_M = 2e^{-5}$  and  $q_k = 1$ . (a) Dynamo models and (b) Convection models with no magnetic field.

### 4.3.3 Anomalous Dynamo

Model FFSF-1 is the anomalous equilibrated model that stands out in Figure 4.1 and is not a bistable model. Model FFSF-1 uses fixed heat flux and stress-free boundary conditions on both the inner and outer boundaries, and the parameters used can be found in table F.2. This model results in a hemispheric frequently reversing non-dipolar dynamo.

Figure 4.23 shows the magnetic, velocity and temperature fields along with radial magnetic field and temperature perturbation at the CMB, and the force balances. The magnetic field of this model is actively generated only in the northern hemisphere. When the model undergoes a reversal, the toroidal and poloidal fields switch signs in the same hemisphere. The velocity field of this model is similar to a convection model with no magnetic field run at identical control parameters. The temperature gradient from the ICB to CMB in the northern hemisphere, where dynamo action actively occurs is larger than that in the southern hemisphere. We examined if this model is in magnetostrophic balance and found that it is in magnetostrophic balance in the northern hemisphere and

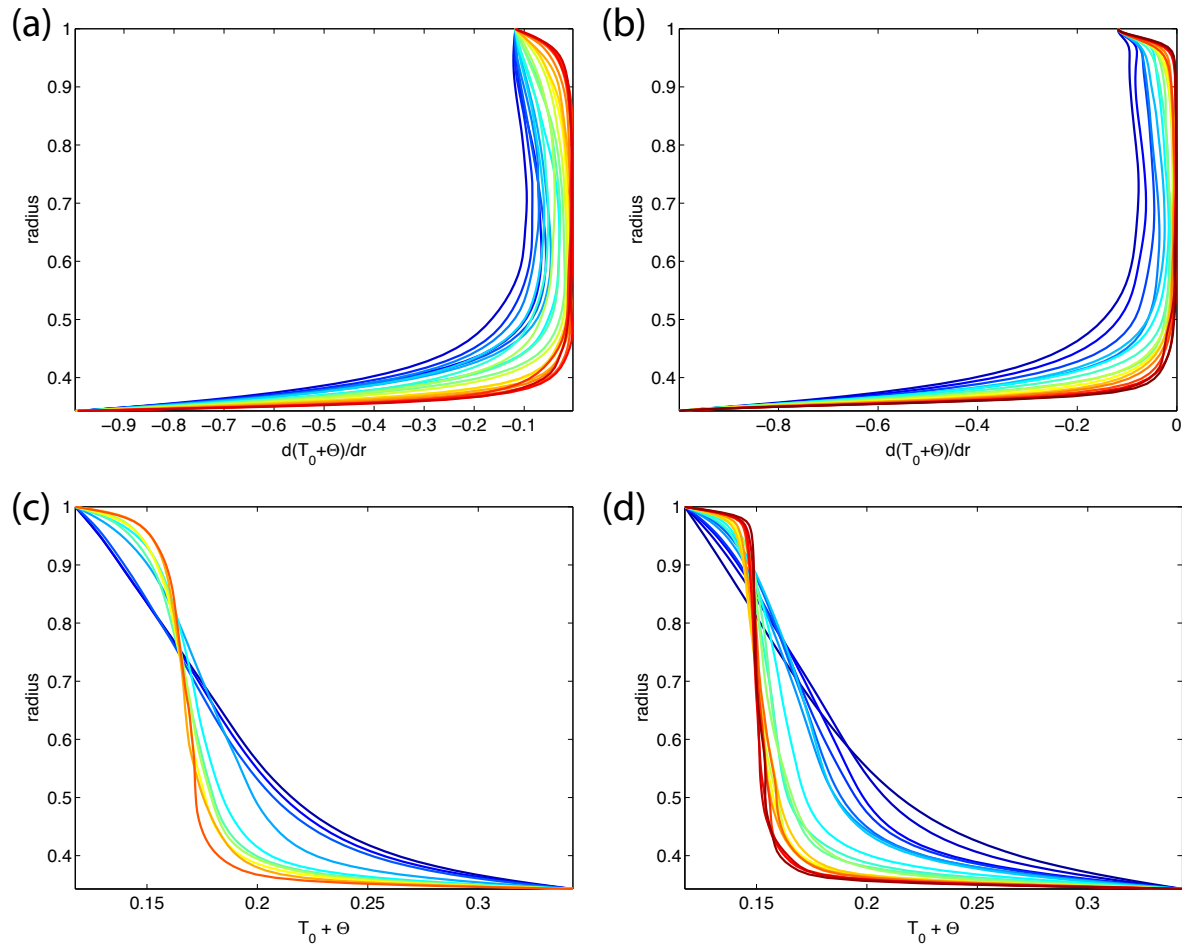


Figure 4.21: Temperature Profile for different boundary conditions for models with  $E = 6e^{-5}$ ,  $Ro_M = 2e^{-5}$  and  $q_k = 1$  for (a) FFSF, (b) FFNS, (c) FTSF and (d) FTNS to estimating boundary layer thickness. (a) and (b) are temperature gradient profiles. Blue represents low Rayleigh numbers and red represents high Rayleigh numbers.

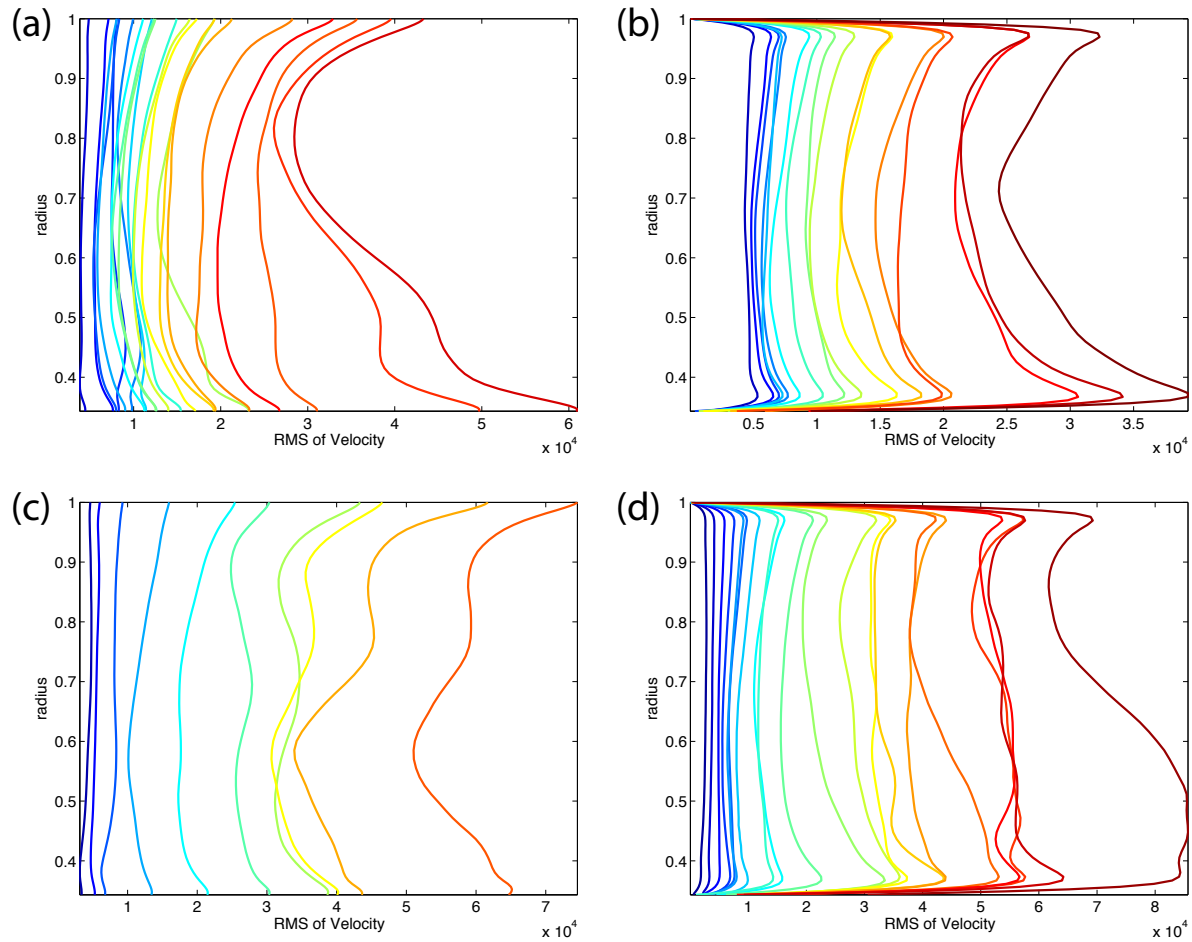


Figure 4.22: Velocity Profile for different boundary conditions for models with  $E = 6e^{-5}$ ,  $Ro_M = 2e^{-5}$  and  $q_k = 1$  for (a) FFSF, (b) FFNS, (c) FTSF and (d) FTNS to estimating boundary layer thickness. Blue represents low Rayleigh numbers and red represents high Rayleigh numbers.

1599 is in geostrophic balance in the southern hemisphere. This was expected as dynamo  
1600 action is mostly occurring in the northern hemisphere. Since, usually in non-dipolar  
1601 dynamos, inertial forces tend to take over the Coriolis force and balances the Lorentz  
1602 force we examined the power budget. We find that this was not the case. The Lorentz  
1603 force is dominantly balanced by the Coriolis force and the inertial force balances the  
1604 viscous force, and does not dominantly contribute in balancing the Lorentz force.

1605

1606 Hemispheric dynamos have been found in earlier studies in some parameter regimes.  
1607 For example, [Stanley et al. \[2008\]](#) find hemispheric dynamo when they impose degree-1  
1608 heat flux outer boundary condition and [Landau and Aubert \[2011\]](#) find them at certain  
1609 parameter values when their fluid flow is driven by equatorially asymmetric convection.  
1610 Their models are driven by internal heating without an inner core.

1611

1612 We tested the robustness of our results by using different initial conditions and found  
1613 that they did not influence our results. Our resulting magnetic field is more similar to  
1614 [Stanley et al. \[2008\]](#), even though we do not use a degree-1 heat flux outer boundary  
1615 condition. The difference is that, unlike them, we find stronger temperature gradient  
1616 across the ICB to CMB in the same hemisphere as the dynamo action. Also, the velocity  
1617 field morphology of our model is not just concentrated in the region where dynamo action  
1618 occurs.

## 1619 4.4 Conclusion

1620 In this chapter we investigated the influence of different thermal and velocity boundary  
1621 conditions on numerical planetary dynamo models and convection models with no  
1622 magnetic fields. In dynamo models, we found that the choice of thermal and velocity  
1623 boundary conditions did not strongly influence the resulting magnetic and velocity

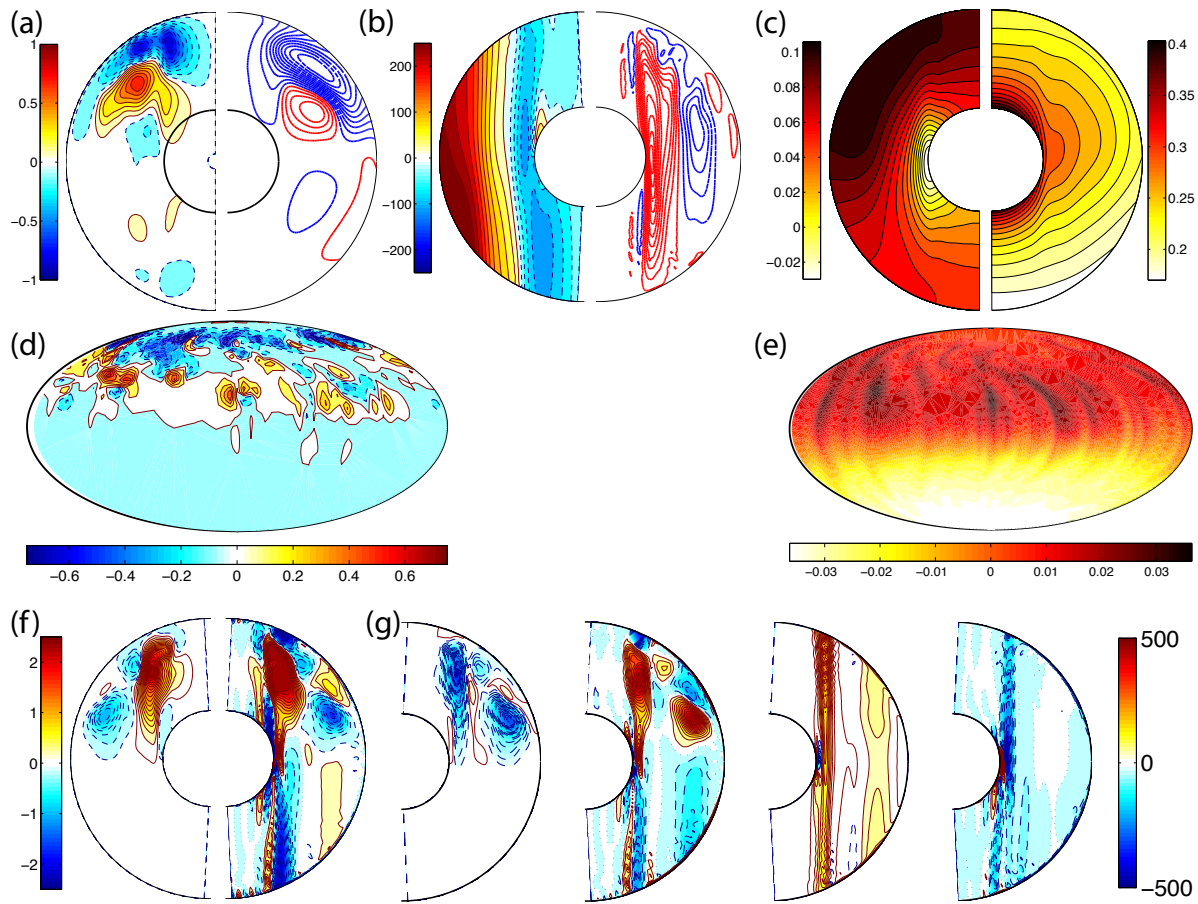


Figure 4.23: Model FFSF-1: (a) Axisymmetric magnetic field, where the left (right) plot shows the meridional slice of the axisymmetric toroidal (streamlines of poloidal) magnetic field, (b) Axisymmetric velocity field, where the toroidal velocity fields are shown on the left where red (blue) denotes prograde (retrograde) circulation and streamlines of poloidal velocity fields are shown on the right where red (blue) denotes clockwise (anti-clockwise) circulation, (c) Axisymmetric temperature, where the left plot shows the temperature perturbation and the right plot shows the total temperature, (d) Radial magnetic field at the CMB, (e) Temperature perturbation at the CMB, (f) Force balance, where the left (right) plot shows the axisymmetric  $\phi$  component of the Lorentz (Coriolis) force and (g) Power budget, where the axisymmetric  $\phi$  components of the Lorentz, Coriolis, inertial and viscous terms are shown from left to right. In these plots, red (blue) denotes sources (sinks) of power. The units are non-dimensional.

field morphologies and intensities at similar Nusselt numbers, although there are some differences. The stress-free models have stronger zonal flows than no-slip models, and are more prone to be bistable. The velocity field morphology of multipolar dynamo models were similar to non-magnetic convection models unlike dipolar dynamo models. The velocity field intensities of dynamo models were weaker than non-magnetic convection models due to magnetic braking. The magnetic field morphology, force balance and generation mechanisms of dipolar models were different from multipolar models. Even though the magnetic energies of the dipolar and multipolar models were of the same order of magnitude, the dipolar dynamo models that were found at moderate Nusselt number, were in magnetostrophic balance where the Lorentz force was balanced by the Coriolis force. In contrast, the multipolar dynamos that were found at high Nusselt number were not in magnetostrophic balance and the Lorentz force was instead balanced by the inertial force. The bistable models that strongly depend on the initial magnetic field fell in both dipolar and multipolar regimes at similar Nusselt numbers. The multipolar bistable models were not in magnetostrophic balance due to their weak field intensities. We showed that plotting the Lorentz and Coriolis forces and estimating the match coefficient is a better way to establish the force balance than just doing volume integrals of the forces and comparing them, or calculating the Elsasser number. We also tested the influence of thermal and Ekman boundary layer thickness in the presence and absence of magnetic fields for different thermal and velocity boundary conditions. We found that they were not affected by the presence of magnetic field and were a product of fluid dynamical flows dependent on the available power.

1646

At high local Rossby numbers, irrespective of thermal or velocity boundary conditions, the dynamo models were generated by  $\alpha^2$  mechanism. On the other hand, at low local Rossby number, no-slip models were generated by  $\alpha\omega$  mechanism due to a substantial amount of toroidal magnetic field generated by  $\omega$  effect through shearing at the

boundaries. At low local Rossby number, even though the velocity field morphology and intensity of the stress-free models were similar to no-slip models, the stress-free dynamos were not generated by  $\alpha\omega$  mechanism since the velocity field was free to flow without shearing at the boundaries. In the stress-free dynamo models, the toroidal magnetic field generated by  $\alpha$  effect was always dominant over  $\omega$  effect. Also, in the no-slip models the transition from  $\alpha\omega$  dynamo to  $\alpha^2$  dynamo happens earlier for fixed flux models in comparison to fixed temperature models.

1658

A single scaling law does seem feasible for all the models but, there does appear to be some variation for models with different boundary conditions when using different thermal and velocity boundary conditions. For example, the power-law obtained between modified Nusselt number and modified flux based Rayleigh number seems to fit all the models, but the power-law of Nusselt number versus supercriticality of Rayleigh number clearly shows the difference between the thermal boundary conditions chosen. Also, the power-law between the Rossby number versus the modified flux based Rayleigh number clearly shows a dependence based on the choice of velocity boundary conditions.

<sup>1667</sup> **Chapter 5**

<sup>1668</sup> **Conclusions and Future Work**

<sup>1669</sup> Along with a series of space missions that has enhanced our knowledge of magnetic  
<sup>1670</sup> fields of planets and moons in our solar system, considerable theoretical progress has  
<sup>1671</sup> also been made in our understanding of convection driven dynamos in spherical shell  
<sup>1672</sup> geometries thanks to remarkable improvements in high performance computing. A crucial  
<sup>1673</sup> component in our understanding of convection in the presence of rotation and magnetic  
<sup>1674</sup> field is through interpretation of results emerging from very complex simulations. The  
<sup>1675</sup> results presented in this thesis crucially contribute to the fundamental understanding of  
<sup>1676</sup> how inner core conductivity and the choice of thermal and velocity boundary conditions  
<sup>1677</sup> can affect the force balance and dynamo generation mechanism which in turn affects the  
<sup>1678</sup> magnetic and velocity field morphology and intensities.

<sup>1679</sup> **5.1 Influence of Inner Core Conductivity**

<sup>1680</sup> I have investigated numerical dynamo models in an Earth-like geometry in order to  
<sup>1681</sup> understand the influence of inner core conductivity on geomagnetic field and showed  
<sup>1682</sup> that a conducting inner core (CIC) can reduce the frequency of reversals and produce  
<sup>1683</sup> axial-dipolar dominated fields in our models. These results are significant because  
<sup>1684</sup> they shed light on existing conflicting results. I further demonstrated that a strong

1685 planetary magnetic field intensity does not imply that the dynamo operates in the  
1686 strong field regime, as is usually presumed in the literature. I also demonstrated that a  
1687 combination of thermal boundary conditions and Rayleigh number plays an important  
1688 role in determining the influence of the inner core's conductivity on planetary dynamos.

1689

1690 In future work, I will investigate if a large conducting inner core can also have a stabilizing  
1691 influence on the magnetic field variability as there are conflicting results in the literature,  
1692 and these results will also be applicable to the dynamos of gas giants and the closest  
1693 terrestrial planet to the Sun, Mercury.

## 1694 **5.2 Influence of Boundary Conditions on Planetary 1695 Dynamos and Scaling Laws**

1696 I have presented a list of different combinations of control parameters and boundary  
1697 conditions that can result in different force balances, which produce strong versus  
1698 weak field dynamos along with polarity reversals. I have explained when thermal and  
1699 velocity boundary conditions influence planetary dynamos in terms of field morphology,  
1700 intensity, generation mechanism and heat transfer. I have also compared scaling laws  
1701 of these models with those in the literature. This work is significant because dynamo  
1702 simulations with different parameter values and boundary conditions are known to result  
1703 in different force balances and energetics. Furthermore, the control parameters used in  
1704 the numerical dynamo models are far from realistic due to computational constraints,  
1705 making it increasingly important to systematically investigate the parameter space with  
1706 different boundary conditions in order to determine the reversal frequency, intensity and  
1707 morphology of the resulting magnetic fields.

1708

1709 In future work, I will investigate the extent to which changing the spherical shell

1710 geometry can influence the obtained scaling laws and the magnetic field generation  
1711 mechanisms; and thus further our understanding of thin shell dynamos that are  
1712 applicable to some gas giants.

1713

## 1714 5.3 Future Research Projects

### 1715 5.3.1 Understanding and Predicting Planetary Magnetic Field 1716 Reversals

1717 The Earth's magnetic field varies on a timescale of months to billions of years. Much of  
1718 the field variation is stochastic, but over long timescales these variability may be related  
1719 to change in heat flow or other mechanisms like change in the intensity and direction  
1720 of inner core oscillations. This mechanism has not been investigated yet, and in my  
1721 previous work, I have observed a correlation between the reversal frequency and change  
1722 in the direction of the inner core rotation. I also showed that the inner core can aid in  
1723 maintaining the dipolarity of the field by providing an anchoring effect and that dif-  
1724 ferent thermal boundary conditions can play a role in determining the reversal frequency.

1725

1726 Core-mantle interactions can vastly affect the dynamics and evolution of both the  
1727 mantle and the core over a timescale of days to Ma. Previous studies that have used  
1728 mantle heterogeneity to mimic local heat flow at the core mantle boundary (CMB)  
1729 have been successful in producing a dipolar magnetic field with persistent non-dipolar  
1730 flux patches. Another work has shown that different patterns of heat flow at the CMB  
1731 can alter the frequency of reversals. Attempts have also been made to investigate the  
1732 influence of varying electrical conductivity at the CMB to determine preferred reversal  
1733 paths, but were unable to distinguish between effects due to electromagnetic core-mantle  
1734 interaction and variations that originate within the core.

1735

1736 I propose to simulate the following scenarios with identical control parameters:

- 1737 1. a reference model for comparison,
- 1738 2. models with a range of inner core angular momentum intensity and direction to  
1739 determine the minimum requirement needed to trigger a reversal,
- 1740 3. models with varying heat flow at the CMB using mantle heterogeneity to determine  
1741 the type of persistent non-dipolar magnetic flux patches,
- 1742 4. models with varying electrical conductivity at the CMB using mantle heterogeneity  
1743 to determine preferred paths of reversals, and
- 1744 5. a model with an inner core angular momentum and intensity that triggers a reversal  
1745 along with varying heat flow and electrical conductivity at the CMB to investigate  
1746 if the reversal frequencies and preferred paths match the paleomagnetic records or  
1747 if it generates a large scale weak flux patch in the northern or southern hemisphere  
1748 before undergoing a reversal.

1749 This research will further our understanding of how reversals occur, what mechanisms  
1750 can trigger them, what happens during a reversal, and how and why does the magnetic  
1751 field either go through an excursion and then returns to the same polarity or reappears  
1752 with the opposite polarity.

1753

1754 The outcomes of this research will not only be an important contribution to the field of  
1755 geodynamics, but also aid in understanding the dynamos of other planets and exoplanets.

### 1756 **5.3.2 Anelastic Dynamo Model**

1757 Most of the dynamo models used currently use the Boussinesq approximation, including  
1758 the research presented in this thesis. The drawback of using this approximation is that

it approximates the fluid flow dynamics in the planetary dynamo generation region. For example, by assuming that the density is constant, as we do by using the Boussinesq approximation, we cause an error in the fluid flow of approximately upto 20% in Earth and 400% in Jupiter. In planetary cores, fluid flow velocities are several orders of magnitude smaller than acoustic velocities. Since dynamo processes occur on much larger timescales than the acoustic time scale, we do not have to resolve acoustic waves using a fully compressible representation. Instead, it might be appropriate to use the anelastic approximation in modelling planetary dynamos.

1767

I propose to modify an existing numerical dynamo model and implement the anelastic approximation. Using this model, I will determine the onset of thermal convection in a rapidly rotating system. Then investigate if the dynamo generation mechanism and the scaling laws are similar in comparison to a Boussinesq model, and apply this model to study planetary dynamos of gas giants.

1773

By generating dynamo models using the Anelastic approximation, we will gain a better understanding of the processes occurring in planetary cores (especially gas giants). This will help us better understand the fluid flow mechanism and magnetic field generation mechanism of planets, which is important in the understanding of their interiors and evolution.

1779

My long term research plan is to use the data obtained through observation and experiment and combine it with theoretical work and numerical modelling to study the evolution of planets in our solar system and beyond. Presently, space missions are dedicated towards finding habitable planets and the possibility of life in such worlds. Among the things they look for by measuring the atmosphere, the existence of water is considered to be vital. It has been hypothesized that terrestrial planets may begin with a

1786 dense degassed atmosphere, which upon cooling results in water oceans; but only those  
1787 rocky worlds that are big enough, at the right distance from their stars and a shielding  
1788 magnetic field may keep them. I plan to examine such topics through interdisciplinary  
1789 interaction.

<sup>1790</sup> **Appendix A**

<sup>1791</sup> **Control Parameters**

<sup>1792</sup> **A.1 Input Control Parameters**

$$\text{Magnetic Rossby \# : } Ro_M = \frac{\text{Inertial}}{\text{Coriolis}} \quad (\text{A.1})$$

$$= \frac{\rho_0 \frac{D}{Dt} \vec{v}}{2\rho_0 \Omega \times \vec{v}} = \frac{\frac{U}{t_\eta}}{2\Omega U} \quad (\text{A.2})$$

$$= \frac{(L^2/\eta)^{-1}}{2\Omega} \quad (\text{A.3})$$

$$= \frac{\eta}{2\Omega L^2} \quad (\text{A.4})$$

$$\text{Ekman \# : } E = \frac{\text{Viscous}}{\text{Coriolis}} \quad (\text{A.5})$$

$$= \frac{\rho_0 \nu \nabla^2 \vec{v}}{2\rho_0 \Omega \times \vec{v}} = \frac{\nu U}{L^2} \frac{1}{2\Omega U} \quad (\text{A.6})$$

$$= \frac{\nu}{2\Omega L^2} \quad (\text{A.7})$$

$$\text{Rayleigh \# : } Ra_{FF} = \frac{\text{Buoyancy}}{\text{Coriolis}} \quad (\text{A.8})$$

$$= \frac{\alpha_T \Theta g_0}{2\rho_0 \Omega \times \vec{v}} = \frac{\alpha_T h_T L^2 g_0}{2\Omega U} \quad (\text{A.9})$$

$$= \frac{\alpha_T g_o h_T L^2}{2\Omega \eta} \quad (\text{A.10})$$

$$\text{Roberts \# : } q_\kappa = \frac{\text{Thermal Diffusion}}{\text{Magnetic Diffusion}} = \frac{\kappa}{\eta} \quad (\text{A.11})$$

1793

$$\text{Prandtl } \# : Pr = \frac{\text{Viscous Diffusion}}{\text{Thermal Diffusion}} = \frac{\nu}{\kappa} \quad (\text{A.12})$$

$$\text{Magnetic Prandtl } \# : Pm = \frac{\text{Viscous Diffusion}}{\text{Magnetic Diffusion}} = \frac{\nu}{\eta} \quad (\text{A.13})$$

$$\text{Aspect Ratio } \# : r_{io} = \frac{\text{Inner Core Radius}}{\text{Outer Core Radius}} = \frac{r_i}{r_o} \quad (\text{A.14})$$

## <sup>1794</sup> A.2 Output Control Parameters

$$\text{Magnetic Reynolds } \# : Re_M = \frac{\text{Advection}}{\text{Diffusion}} \quad (\text{A.15})$$

$$= \frac{\nabla \times (\vec{v} \times \vec{B})}{\eta \nabla^2 \vec{B}} = \frac{\frac{1}{L} UB}{\eta \frac{B}{L^2}} \quad (\text{A.16})$$

$$= \frac{UL}{\eta} \quad (\text{A.17})$$

$$\text{Kinetic Reynolds } \# : Re = \frac{\text{Advection}}{\text{Diffusion}} \quad (\text{A.18})$$

$$= \frac{\nabla \times (\vec{v} \times \vec{B})}{\nu \nabla^2 \vec{B}} = \frac{\frac{1}{L} UB}{\nu \frac{B}{L^2}} \quad (\text{A.19})$$

$$= \frac{UL}{\nu} \quad (\text{A.20})$$

$$\text{Elsasser } \# : \Lambda = \frac{\text{Lorentz}}{\text{Coriolis}} \quad (\text{A.21})$$

$$= \frac{\vec{J} \times \vec{B}}{2\rho_0 \Omega \times \vec{v}} = \frac{(\frac{1}{\mu_0} \nabla \times B) \times B}{2\rho_0 \Omega \times \vec{v}} \\ = \frac{B^2}{2\rho_0 \mu_0 \Omega U L} \quad (\text{A.22})$$

$$= \frac{B^2}{2\Omega \rho \mu_0 \eta} \quad (\text{If } Re_M = 1 \text{ then } \eta = UL) \quad (\text{A.23})$$

$$\text{Rossby } \# : Ro = \frac{\text{Inertia}}{\text{Coriolis}} \quad (\text{A.24})$$

$$= \frac{\rho_0 \frac{D}{Dt} \vec{v}}{2\rho_0 \Omega \times \vec{v}} = \frac{\frac{U}{t}}{2\Omega U} = \frac{\frac{1}{t}}{2\Omega} = \frac{(\frac{L}{U})^{-1}}{2\Omega} \quad (\text{A.25})$$

$$= \frac{U}{2\Omega L} \quad (\text{A.26})$$

1795 **A.2.1 Nusselt number calculation for fixed heat flux and fixed  
1796 temperature boundary conditions**

$$Nu = \frac{Q_{tot}}{Q_{cond}} \quad (A.27)$$

$$Q_{tot} = -4\pi r_o^2 k \left( \frac{dT}{dr} \right)_{r_o} = -k \int_s \nabla T d\vec{s} \quad (A.28)$$

$$Q_{cond} = -4\pi r_o^2 k \left( \frac{dT_c}{dr} \right)_{r_o} \quad (A.29)$$

1797

1798 **Conductive heat flow in spherical shell:**

1799 1 D steady state heat transfer in homogeneous medium:

$$\begin{aligned} \nabla^2 T_c &= 0 \\ \frac{1}{r^2} \frac{\partial}{\partial r} \left( r^2 \frac{\partial T_c}{\partial r} \right) &= 0 \\ \therefore r^2 \frac{\partial T_c}{\partial r} &= C_1 \\ \therefore \frac{\partial T_c}{\partial r} &= \frac{C_1}{r^2} \end{aligned} \quad (A.30)$$

1800 Integrating on both sides,

$$\begin{aligned} \int_{T_{c_i}}^{T_{c_o}} \partial T_c &= C_1 \int_{r_i}^{r_o} \frac{1}{r^2} \partial r \\ \therefore (T_{c_o} - T_{c_i}) &= C_1 \left( -\frac{1}{r_o} + \frac{1}{r_i} \right) \\ \therefore C_1 &= \left( \frac{T_{c_o} - T_{c_i}}{r_o - r_i} \right) r_o r_i \end{aligned} \quad (A.31)$$

<sub>1801</sub> Using the expression for  $C_1$  from equation A.31 in equation A.30 we get,

$$\begin{aligned}\therefore \frac{\partial T_c}{\partial r} &= \left( \frac{T_{co} - T_{ci}}{r_o - r_i} \right) r_o r_i \frac{1}{r^2} \\ \therefore \left( \frac{\partial T_c}{\partial r} \right)_{r_o} &= \left( \frac{T_{co} - T_{ci}}{r_o - r_i} \right) r_o r_i \frac{1}{r_o^2} = \frac{r_i}{r_0} \frac{\Delta T_c}{\Delta r} \\ \therefore \left( \frac{\partial T_c}{\partial r} \right)_{r_o} &= r_{io} \frac{\Delta T_c}{D} \quad \Leftarrow \text{ Dimensional}\end{aligned}\tag{A.32}$$

<sub>1802</sub> Where,

<sub>1803</sub>  $T_c$  : Conductive Temperature

<sub>1804</sub>  $C_1$  : Constant

<sub>1805</sub>  $T_i$  : Temperature at the inner core boundary

<sub>1806</sub>  $T_o$  : Temperature at the outer core boundary

<sub>1807</sub>

$$\therefore Nu = \frac{\left( \frac{dT}{dr} \right)_{r_o}}{\left( \frac{dT_c}{dr} \right)_{r_o}} = \frac{\left( \frac{dT}{dr} \right)_{r_o}}{\frac{\Delta T r_{io}}{D}}\tag{A.33}$$

<sub>1808</sub> In our Kuang and Bloxham [1999] numerical dynamo model,

$$T = T_0 + \Theta = \text{Background} + \text{Perturbation}\tag{A.34}$$

$$\therefore \Delta T = \Delta T_0 + \Delta \Theta\tag{A.35}$$

$$\therefore Nu = \frac{\left( \frac{dT_0}{dr} \right)_{r_o} + \left( \frac{d\Theta}{dr} \right)_{r_o}}{\frac{\Delta T_0 r_{io}}{D} + \frac{\Delta \Theta r_{io}}{D}}\tag{A.36}$$

<sub>1809</sub> When **heat flux** is fixed at the boundary, we fix the numerator of equation A.36

$$\left( \frac{d\Theta}{dr} \right)_{r_o} = 0 \text{ and } \Delta\Theta \neq 0 \quad (\text{A.37})$$

$$\therefore Nu_{flux} = \frac{\left( \frac{dT_0}{dr} \right)_{r_o}}{\frac{\Delta T_0 r_{io}}{D} + \frac{\Delta\Theta r_{io}}{D}} \quad (\text{A.38})$$

<sub>1810</sub> When the **temperature** is fixed (isothermal) at the boundary, we fix the denominator  
<sub>1811</sub> of equation A.36

$$\Delta\Theta = 0 \text{ and } \left( \frac{d\Theta}{dr} \right)_{r_o} \neq 0 \quad (\text{A.39})$$

$$\therefore Nu_{tem} = \frac{\left( \frac{dT_0}{dr} \right)_{r_o} + \left( \frac{d\Theta}{dr} \right)_{r_o}}{\frac{\Delta T_0 r_{io}}{D}} \quad (\text{A.40})$$

<sub>1812</sub> In our Kuang and Bloxham [1999] numerical dynamo model,

$$T_0 = r_o h_T \left[ \frac{r_{io}^2}{r/r_o} \left( 1 - \frac{\epsilon r_i}{3 r_o} \right) - \frac{\epsilon}{6} \left( \frac{r}{r_o} \right)^2 \right] + \tilde{T}_0 \quad (\text{A.41})$$

$$\text{where, } h_T = Ra \frac{2\Omega\eta}{\alpha_T g_o r_o^2} \quad (\text{A.42})$$

<sub>1813</sub> For Earth like case:

$$\begin{aligned} r_{io} &= \frac{12}{35} = 0.35 \\ \Omega &= 7.3 \times 10^{-5} \text{ s}^{-1} \\ \eta &= 2 \text{ m}^2/\text{s} \\ \alpha_T &= 1.8 \times 10^{-5} \text{ K}^{-1} \\ g_o &= 10.68 \text{ m/s}^2 \\ r_o &= 3.5 \times 10^6 \text{ m} \end{aligned}$$

so, if  $Ra = 15,000$  then,  $h_T = 1.86 \times 10^{-9} \text{ K/m}$

and, if  $Ra = 18,000$  then,  $h_T = 2.23 \times 10^{-9} \text{ K/m}$

<sub>1814</sub> Assuming no internal heating ( $\epsilon = 0$ )

$$\begin{aligned} T_0 &= h_T \frac{r_i^2}{r} + \tilde{T}_0 \quad \text{and} \quad \frac{\partial T_0}{\partial r} = -h_T \frac{r_i^2}{r^2} \\ T_{0i} &= h_T \frac{r_i^2}{r_i} + \tilde{T}_0 \\ T_{0o} &= h_T \frac{r_i^2}{r_o} + \tilde{T}_0 \end{aligned} \tag{A.43}$$

$$\text{Note: } D = r_o - r_i = r_o(1 - r_{io}) \tag{A.44}$$

$$\therefore \Delta T_0 = T_{0o} - T_{0i} = -h_T r_i(1 - r_{io}) = -h_T r_{io} D \Leftarrow \text{Dimensional} \tag{A.45}$$

$$\therefore h_T = \frac{\Delta T_0}{r_{io} D} \tag{A.46}$$

$$\therefore \left( \frac{\partial T_0}{\partial r} \right)_{r_o} = -h_T r_{io}^2 \Leftarrow \text{Dimensional} \tag{A.47}$$

<sup>1815</sup> Non-dimensionalization is done using:

$$r = r_o \bar{r} \quad (\text{A.48})$$

$$r_i = r_o \bar{r}_i \quad (\text{A.49})$$

$$r_o = r_o \bar{r}_o = r_o [\because \bar{r}_o = 1] \quad (\text{A.50})$$

$$D = r_o \bar{D} \quad \text{so, } \bar{D} = (1 - r_{io}) \quad (\text{A.51})$$

$$T = h_T r_o \bar{T} \quad (\text{A.52})$$

$$\Theta = h_T r_o \bar{\Theta} \quad (\text{A.53})$$

<sup>1816</sup> Where, the variables with bar are non-dimensional.

$$\begin{aligned} \therefore \overline{T_0} &= \frac{h_T}{h_T r_o} \frac{r_o^2 \bar{r}_i^2}{r_o \bar{r}} + \tilde{T}_1 = \frac{\bar{r}_i^2}{\bar{r}} + \tilde{T}_1 \quad \text{and} \quad \overline{\frac{\partial T_0}{\partial r}} = -\frac{\bar{r}_i^2}{\bar{r}^2} \\ \therefore \overline{\Delta T_0} &= \frac{\bar{r}_i^2}{\bar{r}_o} - \frac{\bar{r}_i^2}{\bar{r}_i} = -\bar{r}_i(1 - r_{io}) = -r_{io}(1 - r_{io}) \quad \Leftarrow \text{Non-Dimensional} \\ \therefore \overline{\left(\frac{\partial T_0}{\partial r}\right)}_{r_o} &= -r_{io}^2 \quad \Leftarrow \text{Non-Dimensional} \end{aligned} \quad (\text{A.55})$$

$$\text{Note: } \frac{\overline{\Delta T_0} r_{io}}{\bar{D}} = \frac{r_{io}(1 - r_{io}) r_{io}}{(1 - r_{io})} = -r_{io}^2 \quad (\text{A.56})$$

$$\therefore \overline{\left(\frac{\partial T_0}{\partial r}\right)}_{r_o} = \frac{\overline{\Delta T_0} r_{io}}{\bar{D}} \quad (\text{A.57})$$

<sup>1817</sup> Fixed heat flux boundary condition (Dimensional Approach)

$$\therefore Nu_{flux} = \frac{\left(\frac{dT_0}{dr}\right)_{r_o}}{\frac{\overline{\Delta T_0} r_{io}}{D} + \frac{\overline{\Delta \Theta} r_{io}}{D}} \quad (\text{A.58})$$

<sub>1818</sub> Fixed heat flux boundary condition (Non-Dimensional Approach)

$$\therefore Nu_{flux} = \frac{\overline{\left( \frac{dT_0}{dr} \right)}_{r_o}}{\frac{\overline{\Delta T_0 r_{io}}}{D} + \frac{\overline{\Delta \Theta r_{io}}}{D}} = \frac{-r_{io}^2}{-r_{io}^2 + \frac{\overline{\Delta \Theta r_{io}}}{(1-r_{io})}} \quad (\text{A.59})$$

$$\text{Also, } Nu_{flux} = \frac{\overline{\Delta T_0}}{\overline{\Delta T_0} + \overline{\Delta \Theta}} = \frac{-r_{io}(1-r_{io})}{-r_{io}(1-r_{io}) + \overline{\Delta \Theta}} \quad (\text{A.60})$$

<sub>1819</sub> Fixed temperature boundary condition (Dimensional Approach)

$$\therefore Nu_{tem} = \frac{\left( \frac{dT_0}{dr} \right)_{r_o} + \left( \frac{d\Theta}{dr} \right)_{r_o}}{\frac{\overline{\Delta T_0 r_{io}}}{D}} \quad (\text{A.61})$$

<sub>1820</sub> Fixed temperature boundary condition (Non-Dimensional Approach)

$$\therefore Nu_{tem} = \frac{\overline{\left( \frac{dT_0}{dr} \right)}_{r_o} + \overline{\left( \frac{d\Theta}{dr} \right)}_{r_o}}{\frac{\overline{\Delta T_0 r_{io}}}{D}} = \frac{-r_{io}^2 + \overline{\left( \frac{d\Theta}{dr} \right)}_{r_o}}{-r_{io}^2} \quad (\text{A.62})$$

<sub>1821</sub> Relationship between  $Ra_{flux}$  and  $Ra_{tem}$

$$Nu = \frac{-k\nabla T}{\frac{-k\Delta T}{D}} = \frac{Ra_{flux}}{Ra_{tem}} \quad (\text{A.63})$$

$$Ra_{flux} = \frac{\alpha_T g_o h_T r_o^2}{2\Omega\eta} \quad (\text{A.64})$$

$$Ra_{tem} = \frac{\alpha_T g_o \Delta T r_o}{2\Omega\eta r_{io}(1 - r_{io})} \quad (\text{A.65})$$

$$\begin{aligned} \therefore Nu &= \frac{\alpha_T g_o h_T r_o^2}{2\Omega\eta} \frac{2\Omega\eta r_{io}(1 - r_{io})}{\alpha_T g_o \Delta T r_o} \\ &= \frac{h_T r_o r_{io}(1 - r_{io})}{\Delta T} \end{aligned} \quad (\text{A.66})$$

$$\therefore \left( \frac{\partial T_0}{\partial r} \right)_{r_o} = -h_T r_{io}^2, \quad \Delta T = \Delta T_0 + \Delta \Theta \quad \text{and } D = r_o(1 - r_{io})$$

$$Nu = \frac{\left( \frac{\partial T_0}{\partial r} \right)_{r_o} r_{io} D}{r_{io}^2 (\Delta T_0 + \Delta \Theta)} = \frac{\left( \frac{\partial T_0}{\partial r} \right)_{r_o}}{\frac{r_{io} \Delta T_0}{D} + \frac{r_{io} \Delta \Theta}{D}} = Nu_{flux} \quad (\text{A.67})$$

$$\therefore Ra_{flux} = Nu_{flux} Ra_{tem} \quad (\text{A.68})$$

$$\therefore Ra_{tem} = \frac{Ra_{flux}}{Nu_{flux}} \quad (\text{A.69})$$

<sub>1822</sub> Computing  $\bar{\Delta\Theta}$

<sub>1823</sub> Temperature perturbation,  $\Theta(\theta, \phi)$  at specific  $r$  values is given by,

$$\tilde{\Theta} = \frac{1}{2\pi} \int_0^{2\pi} \Theta(\theta, \phi) d\phi \quad (\text{A.70})$$

$$\begin{aligned} \tilde{\Theta}_{avg} &= \frac{1}{\Omega} \int_{d\Omega} \Theta(\theta, \phi) d\Omega \\ &= \frac{1}{4\pi} \int_{\phi=0}^{\phi=2\pi} \int_{\theta=0}^{\theta=\pi} \Theta(\theta, \phi) d\phi \sin(\theta) d\theta \end{aligned} \quad (\text{A.71})$$

<sub>1824</sub> Where,  $\tilde{\Theta}$  is axisymmetric temperature perturbation. Using equation A.70 in equation

<sub>1825</sub> [A.71](#) we get,

$$\begin{aligned}\tilde{\Theta}_{avg} &= \frac{1}{2} \int_{\theta=0}^{\theta=\pi} \tilde{\Theta}(\theta) \sin(\theta) d\theta \\ &= \frac{1}{2} \sum_{nth=1}^{N-1} \tilde{\Theta}(\theta_{nth}) \sin(\theta_{nth}) \Delta\theta \\ \text{Now, } \Delta\theta &= \frac{nth \pi}{N-1} - \frac{(nth-1)\pi}{N-1} \\ &= \frac{\pi}{N-1} \\ \therefore \tilde{\Theta}_{avg} &= \frac{\pi}{2(N-1)} \sum_{nth=1}^{N-1} \tilde{\Theta}(\theta_{nth}) \sin(\theta_{nth}) \quad (\text{A.72})\end{aligned}$$

$$\therefore \overline{\Delta\Theta} = \tilde{\Theta}_{avg_{ro}} - \tilde{\Theta}_{avg_{ri}} \iff \text{Non-Dimensional} \quad (\text{A.73})$$

<sub>1826</sub> **Appendix B**

<sub>1827</sub> **Spherical Harmonic Expansions of**  
<sub>1828</sub> **Magnetic and Velocity Fields**

<sub>1829</sub> **B.1 Magnetic Field Expansion**

<sub>1830</sub> Due to the non existence of magnetic monopoles ( $\nabla \cdot \mathbf{B} = 0$ ), we can use toroidal-poloidal  
<sub>1831</sub> expansion as follows:

$$\mathbf{B} = \nabla \times T\hat{\mathbf{r}} + \nabla \times \nabla \times P\hat{\mathbf{r}}$$

<sub>1832</sub> In component form:

$$\begin{pmatrix} B_r \\ B_\theta \\ B_\phi \end{pmatrix} = \begin{pmatrix} -\frac{\hat{L}}{r^2} P \\ \underbrace{\frac{1}{r} \frac{\partial}{\partial r} \frac{\partial}{\partial r} P}_{\text{Poloidal}} + \underbrace{\frac{1}{r \sin \theta} \frac{\partial}{\partial \phi} T}_{\text{Toroidal}} \\ \underbrace{\frac{1}{r \sin \theta} \frac{\partial}{\partial \phi} \frac{\partial}{\partial r} P}_{\text{Poloidal}} - \underbrace{\frac{1}{r} \frac{\partial}{\partial \theta} T}_{\text{Toroidal}} \end{pmatrix} \quad (\text{B.1})$$

<sup>1833</sup> where,

$$\hat{L} = \frac{1}{\sin \theta} \frac{d}{d\theta} \left( \sin \theta \frac{d}{d\theta} \right) + \frac{1}{\sin^2 \theta} \frac{d^2}{d\phi^2} \quad (\text{B.2})$$

<sup>1834</sup> Separated into toroidal and poloidal fields:

$$\begin{aligned} \mathbf{B}_T &= \frac{1}{r \sin \theta} \frac{\partial}{\partial \phi} T \hat{\theta} - \frac{1}{r} \frac{\partial}{\partial \theta} T \hat{\phi} \\ \mathbf{B}_P &= -\frac{\hat{L}}{r^2} P \hat{\mathbf{r}} + \frac{1}{r} \frac{\partial}{\partial \theta} \frac{\partial}{\partial r} P \hat{\theta} + \frac{1}{r \sin \theta} \frac{\partial}{\partial \phi} \frac{\partial}{\partial r} P \hat{\phi} \end{aligned}$$

<sup>1835</sup> In spherical system we can expand toroidal and poloidal scalars in spherical harmonics:

$$\begin{aligned} \begin{pmatrix} P(r, \theta, \phi) \\ T(r, \theta, \phi) \end{pmatrix} &= \sum_{l=0}^{\infty} \left\{ \begin{pmatrix} v_l^0(r) \\ w_l^0(r) \end{pmatrix} Y_l^0(\theta, \phi) \right. \\ &\quad \left. + \sum_{m=1}^l \left[ \begin{pmatrix} v_l^m(r) \\ w_l^m(r) \end{pmatrix} Y_l^m(\theta, \phi) + \begin{pmatrix} v_l^{m*}(r) \\ w_l^{m*}(r) \end{pmatrix} Y_l^{m*}(\theta, \phi) \right] \right\} \quad (\text{B.3}) \end{aligned}$$

<sup>1836</sup> where the  $m = 0$  coefficients have zero imaginary components and,

$$Y_l^m(\theta, \phi) = P_l^m(\theta) e^{im\phi} \quad (\text{B.4})$$

<sup>1837</sup> Let,

$$v_l^m(r) = a_l^m(r) + i b_l^m(r) \Rightarrow a_l^m(r) = \text{Real } (v_l^m(r)) \quad \text{and} \quad b_l^m(r) = \text{Imaginary } (v_l^m(r))$$

$$w_l^m(r) = c_l^m(r) + i d_l^m(r) \Rightarrow c_l^m(r) = \text{Real } (w_l^m(r)) \quad \text{and} \quad d_l^m(r) = \text{Imaginary } (w_l^m(r))$$

<sup>1838</sup> Then equation (B.3) becomes:

$$\begin{pmatrix} P \\ T \end{pmatrix} = \sum_l \left\{ \begin{pmatrix} a_l^0 \\ c_l^0 \end{pmatrix} P_l^0 + \sum_{m=1}^l \begin{pmatrix} [2a_l^m(r) \cos(m\phi) - 2b_l^m(r) \sin(m\phi)] P_l^m(\theta) \\ [2c_l^m(r) \cos(m\phi) - 2d_l^m(r) \sin(m\phi)] P_l^m(\theta) \end{pmatrix} \right\} \quad (\text{B.5})$$

<sup>1839</sup> **Note:** Equations that contain  $a_l^m(r)$  and  $b_l^m(r)$  are the Poloidal part of that equation  
<sup>1840</sup> and equations that contain  $c_l^m(r)$  and  $d_l^m(r)$  are the Toroidal part of that equation (for  
<sup>1841</sup> Magnetic Field and Velocity Field).

<sup>1842</sup> In the rest of the equations I will only consider the  $m > 0$  terms just to save some writing.

<sup>1843</sup> To add in the  $m = 0$  term you merely append the answers by plugging  $m = 0$  into the  
<sup>1844</sup> equation form and dividing by 2 to get the coefficient  $a$  right.

<sup>1845</sup> Now, let us use an important identity:

$$\hat{L}Y_l^m = -l(l+1)Y_l^m \quad (\text{B.6})$$

<sup>1846</sup> Using equation (B.2) and (B.4) in equation (B.6),

$$\begin{aligned} -l(l+1)Y_l^m &= \left( \frac{1}{\sin\theta} \frac{d}{d\theta} \left( \sin\theta \frac{d}{d\theta} \right) + \frac{1}{\sin^2\theta} \frac{d^2}{d\phi^2} \right) Y_l^m \\ -l(l+1)P_l^m(\theta)e^{im\phi} &= \left( \frac{1}{\sin\theta} \frac{d}{d\theta} \left( \sin\theta \frac{d}{d\theta} \right) + \frac{1}{\sin^2\theta} \frac{d^2}{d\phi^2} \right) P_l^m(\theta)e^{im\phi} \\ \left[ -l(l+1)P_l^m(\theta) \right] e^{im\phi} &= \left[ \cot(\theta) \frac{dP_l^m(\theta)}{d\theta} + \frac{d^2P_l^m(\theta)}{d\theta^2} - \frac{m^2}{\sin^2\theta} P_l^m(\theta) \right] e^{im\phi} \\ \therefore \frac{d^2P_l^m(\theta)}{d\theta^2} &= \left( \frac{m^2}{\sin^2\theta} - l(l+1) \right) P_l^m(\theta) - \cot(\theta) \frac{dP_l^m(\theta)}{d\theta} \quad (\text{B.7}) \end{aligned}$$

$$\begin{aligned} \therefore \frac{d^3P_l^m(\theta)}{d\theta^3} &= \left( \frac{m^2}{\sin^2\theta} - l(l+1) \right) \frac{dP_l^m(\theta)}{d\theta} + P_l^m(\theta) \left( \frac{-2\cot\theta}{\sin^2\theta} m^2 - l(l+1) \right) \\ &\quad - \cot(\theta) \frac{d^2P_l^m(\theta)}{d\theta^2} + \frac{dP_l^m(\theta)}{d\theta} \frac{1}{\sin^2\theta} \\ &= P_l^m(\theta) \left( \frac{-2\cot\theta}{\sin^2\theta} m^2 - l(l+1) \right) \\ &\quad + \left( \frac{m^2}{\sin^2\theta} + \frac{1}{\sin^2\theta} - l(l+1) \right) \frac{dP_l^m(\theta)}{d\theta} - \cot(\theta) \frac{d^2P_l^m(\theta)}{d\theta^2} \quad (\text{B.8}) \end{aligned}$$

<sup>1847</sup> The axisymmetric version is:

$$\frac{d^2 P_l^0(\theta)}{d\theta^2} = -l(l+1)P_l^0(\theta) - \cot(\theta) \frac{dP_l^0(\theta)}{d\theta} \quad (\text{B.9})$$

<sup>1848</sup> Plugging equation (B.5) into equation (B.1) gives the total (axisymmetric  $m = 0$  +  
<sup>1849</sup> non-axisymmetric ( $m > 0$ )) Magnetic field:

$$B_r = \frac{2}{r^2} \sum_{l,m} l(l+1) \left[ a_l^m(r) \cos(m\phi) - b_l^m(r) \sin(m\phi) \right] P_l^m(\theta) \quad (\text{B.10})$$

$$\begin{aligned} B_\theta = & \frac{2}{r} \sum_{l,m} \left\{ \left[ \frac{da_l^m(r)}{dr} \cos(m\phi) - \frac{db_l^m(r)}{dr} \sin(m\phi) \right] \frac{dP_l^m(\theta)}{d\theta} \right. \\ & \left. - \frac{m}{\sin \theta} \left[ c_l^m(r) \sin(m\phi) + d_l^m(r) \cos(m\phi) \right] P_l^m(\theta) \right\} \end{aligned} \quad (\text{B.11})$$

$$\begin{aligned} B_\phi = & -\frac{2}{r} \sum_{l,m} \left\{ \frac{m}{\sin \theta} \left[ \frac{da_l^m(r)}{dr} \sin(m\phi) + \frac{db_l^m(r)}{dr} \cos(m\phi) \right] P_l^m(\theta) \right. \\ & \left. + \left[ c_l^m(r) \cos(m\phi) - d_l^m(r) \sin(m\phi) \right] \frac{dP_l^m(\theta)}{d\theta} \right\} \end{aligned} \quad (\text{B.12})$$

<sup>1850</sup> Axisymmetric ( $m = 0$ ) components of the magnetic field:

$$\overline{B_r} = \frac{1}{r^2} \sum_{l,0} l(l+1) \left[ a_l^0(r) \right] P_l^0(\theta) \quad (\text{B.13})$$

$$\overline{B_\theta} = \frac{1}{r} \sum_{l,0} \left[ \frac{da_l^0(r)}{dr} \right] \frac{dP_l^0(\theta)}{d\theta} \quad (\text{B.14})$$

$$\overline{B_\phi} = -\frac{1}{r} \sum_{l,0} \left[ c_l^0(r) \right] \frac{dP_l^0(\theta)}{d\theta} \quad (\text{B.15})$$

<sub>1851</sub> **B.1.1 First Derivatives of Fields**

$$\begin{aligned} \frac{\partial}{\partial r} B_r &= -\frac{4}{r^3} \sum_{l,m} \left\{ l(l+1) \left[ a_l^m(r) \cos(m\phi) - b_l^m(r) \sin(m\phi) \right] P_l^m(\theta) \right\} \\ &\quad + \frac{2}{r^2} \sum_{l,m} \left\{ l(l+1) \left[ \frac{da_l^m(r)}{dr} \cos(m\phi) - \frac{db_l^m(r)}{dr} \sin(m\phi) \right] P_l^m(\theta) \right\} \end{aligned} \quad (\text{B.16})$$

$$\frac{\partial}{\partial \theta} B_r = \frac{2}{r^2} \sum_{l,m} \left\{ l(l+1) \left[ a_l^m(r) \cos(m\phi) - b_l^m(r) \sin(m\phi) \right] \frac{dP_l^m(\theta)}{d\theta} \right\} \quad (\text{B.17})$$

$$\frac{\partial}{\partial \phi} B_r = -\frac{2}{r^2} \sum_{l,m} \left\{ l(l+1)(m) \left[ a_l^m(r) \sin(m\phi) + b_l^m(r) \cos(m\phi) \right] P_l^m(\theta) \right\} \quad (\text{B.18})$$

$$\begin{aligned} \frac{\partial}{\partial r} B_\theta &= -\frac{2}{r^2} \sum_{l,m} \left\{ \left[ \frac{da_l^m(r)}{dr} \cos(m\phi) - \frac{db_l^m(r)}{dr} \sin(m\phi) \right] \frac{dP_l^m(\theta)}{d\theta} \right. \\ &\quad \left. - \frac{m}{\sin \theta} \left[ c_l^m(r) \sin(m\phi) + d_l^m(r) \cos(m\phi) \right] P_l^m(\theta) \right\} \\ &\quad + \frac{2}{r} \sum_{l,m} \left\{ \left[ \frac{d^2 a_l^m(r)}{dr^2} \cos(m\phi) - \frac{d^2 b_l^m(r)}{dr^2} \sin(m\phi) \right] \frac{dP_l^m(\theta)}{d\theta} \right. \\ &\quad \left. - \frac{m}{\sin \theta} \left[ \frac{dc_l^m(r)}{dr} \sin(m\phi) + \frac{dd_l^m(r)}{dr} \cos(m\phi) \right] P_l^m(\theta) \right\} \end{aligned} \quad (\text{B.19})$$

$$\begin{aligned} \frac{\partial}{\partial \theta} B_\theta &= \frac{2}{r} \sum_{l,m} \left\{ \left[ \frac{da_l^m(r)}{dr} \cos(m\phi) - \frac{db_l^m(r)}{dr} \sin(m\phi) \right] \frac{d^2 P_l^m(\theta)}{d\theta^2} \right. \\ &\quad \left. + m \left[ c_l^m(r) \sin(m\phi) + d_l^m(r) \cos(m\phi) \right] \left( \frac{\cos \theta}{\sin^2 \theta} P_l^m(\theta) \right. \right. \\ &\quad \left. \left. - \frac{1}{\sin \theta} \frac{dP_l^m(\theta)}{d\theta} \right) \right\} \end{aligned} \quad (\text{B.20})$$

$$\begin{aligned} \frac{\partial}{\partial \phi} B_\theta &= -\frac{2}{r} \sum_{l,m} \left\{ m \left[ \frac{da_l^m(r)}{dr} \sin(m\phi) + \frac{db_l^m(r)}{dr} \cos(m\phi) \right] \frac{dP_l^m(\theta)}{d\theta} \right. \\ &\quad \left. + \frac{m^2}{\sin \theta} \left[ c_l^m(r) \cos(m\phi) - d_l^m(r) \sin(m\phi) \right] P_l^m(\theta) \right\} \end{aligned} \quad (\text{B.21})$$

$$\begin{aligned} \frac{\partial}{\partial r} B_\phi &= \frac{2}{r^2} \sum_{l,m} \left\{ \frac{m}{\sin \theta} \left[ \frac{da_l^m(r)}{dr} \sin(m\phi) + \frac{db_l^m(r)}{dr} \cos(m\phi) \right] P_l^m(\theta) \right. \\ &\quad \left. + \left[ c_l^m(r) \cos(m\phi) - d_l^m(r) \sin(m\phi) \right] \frac{dP_l^m(\theta)}{d\theta} \right\} \\ &\quad - \frac{2}{r} \sum_{l,m} \left\{ \frac{m}{\sin \theta} \left[ \frac{d^2 a_l^m(r)}{dr^2} \sin(m\phi) + \frac{d^2 b_l^m(r)}{dr^2} \cos(m\phi) \right] P_l^m(\theta) \right. \\ &\quad \left. + \left[ \frac{dc_l^m(r)}{dr} \cos(m\phi) - \frac{dd_l^m(r)}{dr} \sin(m\phi) \right] \frac{dP_l^m(\theta)}{d\theta} \right\} \end{aligned} \quad (\text{B.22})$$

$$\begin{aligned} \frac{\partial}{\partial \theta} B_\phi &= -\frac{2}{r} \sum_{l,m} \left\{ m \left[ \frac{da_l^m(r)}{dr} \sin(m\phi) + \frac{db_l^m(r)}{dr} \cos(m\phi) \right] \left( -\frac{\cos \theta}{\sin^2 \theta} P_l^m(\theta) + \frac{1}{\sin \theta} \frac{dP_l^m(\theta)}{d\theta} \right) \right. \\ &\quad \left. + \left[ c_l^m(r) \cos(m\phi) - d_l^m(r) \sin(m\phi) \right] \frac{d^2 P_l^m(\theta)}{d\theta^2} \right\} \end{aligned} \quad (\text{B.23})$$

$$\begin{aligned} \frac{\partial}{\partial \phi} B_\phi &= -\frac{2}{r} \sum_{l,m} \left\{ \frac{m^2}{\sin \theta} \left[ \frac{da_l^m(r)}{dr} \cos(m\phi) - \frac{db_l^m(r)}{dr} \sin(m\phi) \right] P_l^m(\theta) \right. \\ &\quad \left. - m \left[ c_l^m(r) \sin(m\phi) + d_l^m(r) \cos(m\phi) \right] \frac{dP_l^m(\theta)}{d\theta} \right\} \end{aligned} \quad (\text{B.24})$$

1852 Axisymmetric components ( $m = 0$ ) of first derivatives of the Magnetic Field:

$$\frac{\partial}{\partial r} \overline{B_r} = \sum_{l,0} \frac{l(l+1)}{r^2} \left[ \frac{da_l^0(r)}{dr} - \frac{2}{r} a_l^0(r) \right] P_l^0(\theta) \quad (\text{B.25})$$

$$\frac{\partial}{\partial \theta} \overline{B_r} = \frac{1}{r^2} \sum_{l,0} l(l+1) \left[ a_l^0(r) \right] \frac{dP_l^0(\theta)}{d\theta} \quad (\text{B.26})$$

$$\frac{\partial}{\partial \phi} \overline{B_r} = 0 \quad (\text{B.27})$$

$$\frac{\partial}{\partial r} \overline{B_\theta} = \sum_{l,0} \frac{1}{r} \left[ \frac{d^2 a_l^0(r)}{dr^2} - \frac{1}{r} \frac{da_l^0(r)}{dr} \right] \frac{dP_l^0(\theta)}{d\theta} \quad (\text{B.28})$$

$$\frac{\partial}{\partial \theta} \overline{B_\theta} = \frac{1}{r} \sum_{l,0} \left[ \frac{da_l^0(r)}{dr} \right] \frac{d^2 P_l^0(\theta)}{d\theta^2} \quad (\text{B.29})$$

$$\frac{\partial}{\partial \phi} \overline{B_\theta} = 0 \quad (\text{B.30})$$

$$\frac{\partial}{\partial r} \overline{B_\phi} = \sum_{l,0} \frac{1}{r} \left[ \frac{1}{r} c_l^0(r) - \frac{dc_l^0(r)}{dr} \right] \frac{dP_l^0(\theta)}{d\theta} \quad (\text{B.31})$$

$$\frac{\partial}{\partial \theta} \overline{B_\phi} = -\frac{1}{r} \sum_{l,0} \left[ c_l^0(r) \right] \frac{d^2 P_l^0(\theta)}{d\theta^2} \quad (\text{B.32})$$

$$\frac{\partial}{\partial \phi} \overline{B_\phi} = 0 \quad (\text{B.33})$$

1853 **B.1.2 Second Derivatives of Fields**

$$\begin{aligned} \frac{\partial^2}{\partial r^2} B_r &= \frac{12}{r^4} \sum_{l,m} \left\{ l(l+1) \left[ a_l^m(r) \cos(m\phi) - b_l^m(r) \sin(m\phi) \right] P_l^m(\theta) \right\} \\ &\quad - \frac{8}{r^3} \sum_{l,m} \left\{ l(l+1) \left[ \frac{da_l^m(r)}{dr} \cos(m\phi) - \frac{db_l^m(r)}{dr} \sin(m\phi) \right] P_l^m(\theta) \right\} \\ &\quad + \frac{2}{r^2} \sum_{l,m} \left\{ l(l+1) \left[ \frac{d^2 a_l^m(r)}{dr^2} \cos(m\phi) - \frac{d^2 b_l^m(r)}{dr^2} \sin(m\phi) \right] P_l^m(\theta) \right\} \end{aligned} \quad (\text{B.34})$$

$$\begin{aligned} \frac{\partial}{\partial \theta} \frac{\partial}{\partial r} B_r &= -\frac{4}{r^3} \sum_{l,m} \left\{ l(l+1) \left[ a_l^m(r) \cos(m\phi) - b_l^m(r) \sin(m\phi) \right] \frac{dP_l^m(\theta)}{d\theta} \right\} \\ &\quad + \frac{2}{r^2} \sum_{l,m} \left\{ l(l+1) \left[ \frac{da_l^m(r)}{dr} \cos(m\phi) - \frac{db_l^m(r)}{dr} \sin(m\phi) \right] \frac{dP_l^m(\theta)}{d\theta} \right\} \end{aligned} \quad (\text{B.35})$$

$$\begin{aligned} \frac{\partial}{\partial \phi} \frac{\partial}{\partial r} B_r &= -\frac{4}{r^3} \sum_{l,m} \left\{ l(l+1) \left[ -a_l^m(r) \sin(m\phi) - b_l^m(r) \cos(m\phi) \right] P_l^m(\theta) \right\} \\ &\quad + \frac{2}{r^2} \sum_{l,m} \left\{ l(l+1) \left[ -\frac{da_l^m(r)}{dr} \sin(m\phi) - \frac{db_l^m(r)}{dr} \cos(m\phi) \right] P_l^m(\theta) \right\} \end{aligned} \quad (\text{B.36})$$

$$\begin{aligned} \frac{\partial}{\partial r} \frac{\partial}{\partial \theta} B_r &= -\frac{4}{r^3} \sum_{l,m} \left\{ l(l+1) \left[ a_l^m(r) \cos(m\phi) - b_l^m(r) \sin(m\phi) \right] \frac{dP_l^m(\theta)}{d\theta} \right\} \\ &\quad + \frac{2}{r^2} \sum_{l,m} \left\{ l(l+1) \left[ \frac{da_l^m(r)}{dr} \cos(m\phi) - \frac{db_l^m(r)}{dr} \sin(m\phi) \right] \frac{dP_l^m(\theta)}{d\theta} \right\} \end{aligned} \quad (B.37)$$

$$\frac{\partial^2}{\partial \theta^2} B_r = \frac{2}{r^2} \sum_{l,m} \left\{ l(l+1) \left[ a_l^m(r) \cos(m\phi) - b_l^m(r) \sin(m\phi) \right] \frac{d^2 P_l^m(\theta)}{d\theta^2} \right\} \quad (B.38)$$

$$\frac{\partial}{\partial \phi} \frac{\partial}{\partial \theta} B_r = \frac{2}{r^2} \sum_{l,m} \left\{ l(l+1) \left[ -a_l^m(r) \sin(m\phi) - b_l^m(r) \cos(m\phi) \right] \frac{dP_l^m(\theta)}{d\theta} \right\} \quad (B.39)$$

$$\begin{aligned} \frac{\partial}{\partial r} \frac{\partial}{\partial \phi} B_r &= \frac{4}{r^3} \sum_{l,m} \left\{ l(l+1)(m) \left[ a_l^m(r) \sin(m\phi) + b_l^m(r) \cos(m\phi) \right] P_l^m(\theta) \right\} \\ &\quad - \frac{2}{r^2} \sum_{l,m} \left\{ l(l+1)(m) \left[ \frac{da_l^m(r)}{dr} \sin(m\phi) + \frac{db_l^m(r)}{dr} \cos(m\phi) \right] P_l^m(\theta) \right\} \end{aligned} \quad (B.40)$$

$$\frac{\partial}{\partial \theta} \frac{\partial}{\partial \phi} B_r = -\frac{2}{r^2} \sum_{l,m} \left\{ l(l+1)(m) \left[ a_l^m(r) \sin(m\phi) + b_l^m(r) \cos(m\phi) \right] \frac{dP_l^m(\theta)}{d\theta} \right\} \quad (B.41)$$

$$\frac{\partial^2}{\partial \phi^2} B_r = -\frac{2}{r^2} \sum_{l,m} \left\{ l(l+1)(m) \left[ a_l^m(r) \cos(m\phi) - b_l^m(r) \sin(m\phi) \right] P_l^m(\theta) \right\} \quad (B.42)$$

$$\begin{aligned}
\frac{\partial^2}{\partial r^2} B_\theta &= \frac{4}{r^3} \sum_{l,m} \left\{ \left[ \frac{da_l^m(r)}{dr} \cos(m\phi) - \frac{db_l^m(r)}{dr} \sin(m\phi) \right] \frac{dP_l^m(\theta)}{d\theta} \right. \\
&\quad \left. - \frac{m}{\sin \theta} \left[ c_l^m(r) \sin(m\phi) + d_l^m(r) \cos(m\phi) \right] P_l^m(\theta) \right\} \\
&\quad - \frac{4}{r^2} \sum_{l,m} \left\{ \left[ \frac{d^2 a_l^m(r)}{dr^2} \cos(m\phi) - \frac{d^2 b_l^m(r)}{dr^2} \sin(m\phi) \right] \frac{dP_l^m(\theta)}{d\theta} \right. \\
&\quad \left. - \frac{m}{\sin \theta} \left[ \frac{dc_l^m(r)}{dr} \sin(m\phi) + \frac{dd_l^m(r)}{dr} \cos(m\phi) \right] P_l^m(\theta) \right\} \\
&\quad + \frac{2}{r} \sum_{l,m} \left\{ \left[ \frac{d^3 a_l^m(r)}{dr^3} \cos(m\phi) - \frac{d^3 b_l^m(r)}{dr^3} \sin(m\phi) \right] \frac{dP_l^m(\theta)}{d\theta} \right. \\
&\quad \left. - \frac{m}{\sin \theta} \left[ \frac{d^2 c_l^m(r)}{dr^2} \sin(m\phi) + \frac{d^2 d_l^m(r)}{dr^2} \cos(m\phi) \right] P_l^m(\theta) \right\} \tag{B.43}
\end{aligned}$$

$$\begin{aligned}
\frac{\partial}{\partial \theta} \frac{\partial}{\partial r} B_\theta &= -\frac{2}{r^2} \sum_{l,m} \left\{ \left[ \frac{da_l^m(r)}{dr} \cos(m\phi) - \frac{db_l^m(r)}{dr} \sin(m\phi) \right] \frac{d^2 P_l^m(\theta)}{d\theta^2} \right. \\
&\quad + m \left[ c_l^m(r) \sin(m\phi) + d_l^m(r) \cos(m\phi) \right] \left( \frac{\cos \theta}{\sin^2 \theta} P_l^m(\theta) - \frac{1}{\sin \theta} \frac{dP_l^m(\theta)}{d\theta} \right) \Big\} \\
&\quad + \frac{2}{r} \sum_{l,m} \left\{ \left[ \frac{d^2 a_l^m(r)}{dr^2} \cos(m\phi) - \frac{d^2 b_l^m(r)}{dr^2} \sin(m\phi) \right] \frac{d^2 P_l^m(\theta)}{d\theta^2} \right. \\
&\quad + m \left[ \frac{dc_l^m(r)}{dr} \sin(m\phi) + \frac{dd_l^m(r)}{dr} \cos(m\phi) \right] \\
&\quad \left. \left( \frac{\cos \theta}{\sin^2 \theta} P_l^m(\theta) - \frac{1}{\sin \theta} \frac{dP_l^m(\theta)}{d\theta} \right) \right\} \tag{B.44}
\end{aligned}$$

$$\begin{aligned}
\frac{\partial}{\partial \phi} \frac{\partial}{\partial r} B_\theta &= -\frac{2}{r^2} \sum_{l,m} \left\{ \left[ -\frac{da_l^m(r)}{dr} \sin(m\phi) - \frac{db_l^m(r)}{dr} \cos(m\phi) \right] \frac{dP_l^m(\theta)}{d\theta} \right. \\
&\quad - \frac{m}{\sin \theta} \left[ c_l^m(r) \cos(m\phi) - d_l^m(r) \sin(m\phi) \right] P_l^m(\theta) \Big\} \\
&\quad + \frac{2}{r} \sum_{l,m} \left\{ \left[ -\frac{d^2 a_l^m(r)}{dr^2} \sin(m\phi) - \frac{d^2 b_l^m(r)}{dr^2} \cos(m\phi) \right] \frac{dP_l^m(\theta)}{d\theta} \right. \\
&\quad \left. - \frac{m}{\sin \theta} \left[ \frac{dc_l^m(r)}{dr} \cos(m\phi) - \frac{dd_l^m(r)}{dr} \sin(m\phi) \right] P_l^m(\theta) \right\} \tag{B.45}
\end{aligned}$$

$$\begin{aligned}
\frac{\partial}{\partial r} \frac{\partial}{\partial \theta} B_\theta &= -\frac{2}{r^2} \sum_{l,m} \left\{ \left[ \frac{da_l^m(r)}{dr} \cos(m\phi) - \frac{db_l^m(r)}{dr} \sin(m\phi) \right] \frac{d^2 P_l^m(\theta)}{d\theta^2} \right. \\
&\quad + m \left[ c_l^m(r) \sin(m\phi) + d_l^m(r) \cos(m\phi) \right] \left( \frac{\cos \theta}{\sin^2 \theta} P_l^m(\theta) - \frac{1}{\sin \theta} \frac{dP_l^m(\theta)}{d\theta} \right) \Big\} \\
&\quad + \frac{2}{r} \sum_{l,m} \left\{ \left[ \frac{d^2 a_l^m(r)}{dr^2} \cos(m\phi) - \frac{d^2 b_l^m(r)}{dr^2} \sin(m\phi) \right] \frac{d^2 P_l^m(\theta)}{d\theta^2} \right. \\
&\quad + m \left[ \frac{dc_l^m(r)}{dr} \sin(m\phi) + \frac{dd_l^m(r)}{dr} \cos(m\phi) \right] \\
&\quad \left. \left( \frac{\cos \theta}{\sin^2 \theta} P_l^m(\theta) - \frac{1}{\sin \theta} \frac{dP_l^m(\theta)}{d\theta} \right) \right\} \tag{B.46}
\end{aligned}$$

$$\begin{aligned}
\frac{\partial^2}{\partial \theta^2} B_\theta &= \frac{2}{r} \sum_{l,m} \left\{ \left[ \frac{da_l^m(r)}{dr} \cos(m\phi) - \frac{db_l^m(r)}{dr} \sin(m\phi) \right] \frac{d^3 P_l^m(\theta)}{d\theta^3} \right. \\
&\quad + m \left[ c_l^m(r) \sin(m\phi) + d_l^m(r) \cos(m\phi) \right] \left( \frac{\cos \theta}{\sin^2 \theta} \frac{dP_l^m(\theta)}{d\theta} + P_l^m(\theta) \frac{(1 + \cos^2 \theta)}{\sin^3 \theta} \right. \\
&\quad \left. \left. - \frac{1}{\sin \theta} \frac{d^2 P_l^m(\theta)}{d\theta^2} + \frac{\cos \theta}{\sin^2 \theta} \frac{dP_l^m(\theta)}{d\theta} \right) \right\} \tag{B.47}
\end{aligned}$$

$$\begin{aligned}
\frac{\partial}{\partial \phi} \frac{\partial}{\partial \theta} B_\theta &= \frac{2}{r} \sum_{l,m} \left\{ \left[ - \frac{da_l^m(r)}{dr} \sin(m\phi) - \frac{db_l^m(r)}{dr} \cos(m\phi) \right] \frac{d^2 P_l^m(\theta)}{d\theta^2} \right. \\
&\quad + m \left[ c_l^m(r) \cos(m\phi) - d_l^m(r) \sin(m\phi) \right] \\
&\quad \left. \left( \frac{\cos \theta}{\sin^2 \theta} P_l^m(\theta) - \frac{1}{\sin \theta} \frac{dP_l^m(\theta)}{d\theta} \right) \right\} \tag{B.48}
\end{aligned}$$

$$\begin{aligned}
\frac{\partial}{\partial r} \frac{\partial}{\partial \phi} B_\theta &= \frac{2}{r^2} \sum_{l,m} \left\{ m \left[ \frac{da_l^m(r)}{dr} \sin(m\phi) + \frac{db_l^m(r)}{dr} \cos(m\phi) \right] \frac{dP_l^m(\theta)}{d\theta} \right. \\
&\quad \left. + \frac{m^2}{\sin \theta} \left[ c_l^m(r) \cos(m\phi) - d_l^m(r) \sin(m\phi) \right] P_l^m(\theta) \right\} \\
&\quad - \frac{2}{r} \sum_{l,m} \left\{ m \left[ \frac{d^2 a_l^m(r)}{dr^2} \sin(m\phi) + \frac{d^2 b_l^m(r)}{dr^2} \cos(m\phi) \right] \frac{dP_l^m(\theta)}{d\theta} \right. \\
&\quad \left. + \frac{m^2}{\sin \theta} \left[ \frac{dc_l^m(r)}{dr} \cos(m\phi) - \frac{dd_l^m(r)}{dr} \sin(m\phi) \right] P_l^m(\theta) \right\} \tag{B.49}
\end{aligned}$$

$$\begin{aligned}
\frac{\partial}{\partial \theta} \frac{\partial}{\partial \phi} B_\theta &= -\frac{2}{r} \sum_{l,m} \left\{ m \left[ \frac{da_l^m(r)}{dr} \sin(m\phi) + \frac{db_l^m(r)}{dr} \cos(m\phi) \right] \frac{d^2 P_l^m(\theta)}{d\theta^2} \right. \\
&\quad \left. + m^2 \left[ c_l^m(r) \cos(m\phi) - d_l^m(r) \sin(m\phi) \right] \left( \frac{1}{\sin \theta} \frac{dP_l^m(\theta)}{d\theta} \right. \right. \\
&\quad \left. \left. - \frac{\cos \theta}{\sin^2 \theta} P_l^m(\theta) \right) \right\} \tag{B.50}
\end{aligned}$$

$$\begin{aligned}
\frac{\partial^2}{\partial \phi^2} B_\theta &= -\frac{2}{r} \sum_{l,m} \left\{ m \left[ \frac{da_l^m(r)}{dr} \cos(m\phi) - \frac{db_l^m(r)}{dr} \sin(m\phi) \right] \frac{dP_l^m(\theta)}{d\theta} \right. \\
&\quad \left. + \frac{m^2}{\sin \theta} \left[ -c_l^m(r) \sin(m\phi) - d_l^m(r) \cos(m\phi) \right] P_l^m(\theta) \right\} \tag{B.51}
\end{aligned}$$

$$\begin{aligned}
\frac{\partial^2}{\partial r^2} B_\phi &= -\frac{4}{r^3} \sum_{l,m} \left\{ \frac{m}{\sin \theta} \left[ \frac{da_l^m(r)}{dr} \sin(m\phi) + \frac{db_l^m(r)}{dr} \cos(m\phi) \right] P_l^m(\theta) \right. \\
&\quad \left. + \left[ c_l^m(r) \cos(m\phi) - d_l^m(r) \sin(m\phi) \right] \frac{dP_l^m(\theta)}{d\theta} \right\} \\
&\quad + \frac{4}{r^2} \sum_{l,m} \left\{ \frac{m}{\sin \theta} \left[ \frac{d^2 a_l^m(r)}{dr^2} \sin(m\phi) + \frac{d^2 b_l^m(r)}{dr^2} \cos(m\phi) \right] P_l^m(\theta) \right. \\
&\quad \left. + \left[ \frac{dc_l^m(r)}{dr} \cos(m\phi) - \frac{dd_l^m(r)}{dr} \sin(m\phi) \right] \frac{dP_l^m(\theta)}{d\theta} \right\} \\
&\quad - \frac{2}{r} \sum_{l,m} \left\{ \frac{m}{\sin \theta} \left[ \frac{d^3 a_l^m(r)}{dr^3} \sin(m\phi) + \frac{d^3 b_l^m(r)}{dr^3} \cos(m\phi) \right] P_l^m(\theta) \right. \\
&\quad \left. + \left[ \frac{d^2 c_l^m(r)}{dr^2} \cos(m\phi) - \frac{d^2 d_l^m(r)}{dr^2} \sin(m\phi) \right] \frac{dP_l^m(\theta)}{d\theta} \right\} \tag{B.52}
\end{aligned}$$

$$\begin{aligned}
\frac{\partial}{\partial \theta} \frac{\partial}{\partial r} B_\phi &= \frac{2}{r^2} \sum_{l,m} \left\{ m \left[ \frac{da_l^m(r)}{dr} \sin(m\phi) + \frac{db_l^m(r)}{dr} \cos(m\phi) \right] \left( \frac{1}{\sin \theta} \frac{dP_l^m(\theta)}{d\theta} - \frac{\cos \theta}{\sin^2 \theta} P_l^m(\theta) \right) \right. \\
&\quad \left. + \left[ c_l^m(r) \cos(m\phi) - d_l^m(r) \sin(m\phi) \right] \frac{d^2 P_l^m(\theta)}{d\theta^2} \right\} \\
&\quad - \frac{2}{r} \sum_{l,m} \left\{ m \left[ \frac{d^2 a_l^m(r)}{dr^2} \sin(m\phi) + \frac{d^2 b_l^m(r)}{dr^2} \cos(m\phi) \right] \left( \frac{1}{\sin \theta} \frac{dP_l^m(\theta)}{d\theta} - \frac{\cos \theta}{\sin^2 \theta} P_l^m(\theta) \right) \right. \\
&\quad \left. + \left[ \frac{dc_l^m(r)}{dr} \cos(m\phi) - \frac{dd_l^m(r)}{dr} \sin(m\phi) \right] \frac{d^2 P_l^m(\theta)}{d\theta^2} \right\} \tag{B.53}
\end{aligned}$$

$$\begin{aligned}
\frac{\partial}{\partial \phi} \frac{\partial}{\partial r} B_\phi &= \frac{2}{r^2} \sum_{l,m} \left\{ \frac{m}{\sin \theta} \left[ \frac{da_l^m(r)}{dr} \cos(m\phi) - \frac{db_l^m(r)}{dr} \sin(m\phi) \right] P_l^m(\theta) \right. \\
&\quad \left. + \left[ -c_l^m(r) \sin(m\phi) - d_l^m(r) \cos(m\phi) \right] \frac{dP_l^m(\theta)}{d\theta} \right\} \\
&\quad - \frac{2}{r} \sum_{l,m} \left\{ \frac{m}{\sin \theta} \left[ \frac{d^2 a_l^m(r)}{dr^2} \cos(m\phi) - \frac{d^2 b_l^m(r)}{dr^2} \sin(m\phi) \right] P_l^m(\theta) \right. \\
&\quad \left. + \left[ -\frac{dc_l^m(r)}{dr} \sin(m\phi) - \frac{dd_l^m(r)}{dr} \cos(m\phi) \right] \frac{dP_l^m(\theta)}{d\theta} \right\} \tag{B.54}
\end{aligned}$$

$$\begin{aligned}
\frac{\partial}{\partial r} \frac{\partial}{\partial \theta} B_\phi &= \frac{2}{r^2} \sum_{l,m} \left\{ m \left[ \frac{da_l^m(r)}{dr} \sin(m\phi) + \frac{db_l^m(r)}{dr} \cos(m\phi) \right] \left( -\frac{\cos \theta}{\sin^2 \theta} P_l^m(\theta) + \frac{1}{\sin \theta} \frac{dP_l^m(\theta)}{d\theta} \right) \right. \\
&\quad \left. + \left[ c_l^m(r) \cos(m\phi) - d_l^m(r) \sin(m\phi) \right] \frac{d^2 P_l^m(\theta)}{d\theta^2} \right\} \\
&\quad - \frac{2}{r} \sum_{l,m} \left\{ m \left[ \frac{d^2 a_l^m(r)}{dr^2} \sin(m\phi) + \frac{d^2 b_l^m(r)}{dr^2} \cos(m\phi) \right] \left( -\frac{\cos \theta}{\sin^2 \theta} P_l^m(\theta) + \frac{1}{\sin \theta} \frac{dP_l^m(\theta)}{d\theta} \right) \right. \\
&\quad \left. + \left[ \frac{dc_l^m(r)}{dr} \cos(m\phi) - \frac{dd_l^m(r)}{dr} \sin(m\phi) \right] \frac{d^2 P_l^m(\theta)}{d\theta^2} \right\} \tag{B.55}
\end{aligned}$$

$$\begin{aligned}
\frac{\partial^2}{\partial \theta^2} B_\phi &= -\frac{2}{r} \sum_{l,m} \left\{ m \left[ \frac{da_l^m(r)}{dr} \sin(m\phi) + \frac{db_l^m(r)}{dr} \cos(m\phi) \right] \right. \\
&\quad \left( -2 \frac{\cos \theta}{\sin^2 \theta} \frac{dP_l^m(\theta)}{d\theta} + \frac{\cos^2 \theta + 1}{\sin^3 \theta} P_l^m(\theta) + \frac{1}{\sin \theta} \frac{d^2 P_l^m(\theta)}{d\theta^2} \right) \\
&\quad \left. + \left[ c_l^m(r) \cos(m\phi) - d_l^m(r) \sin(m\phi) \right] \frac{d^3 P_l^m(\theta)}{d\theta^3} \right\} \tag{B.56}
\end{aligned}$$

$$\begin{aligned}
\frac{\partial}{\partial \phi} \frac{\partial}{\partial \theta} B_\phi &= -\frac{2}{r} \sum_{l,m} \left\{ m \left[ \frac{da_l^m(r)}{dr} \cos(m\phi) - \frac{db_l^m(r)}{dr} \sin(m\phi) \right] \left( -\frac{\cos \theta}{\sin^2 \theta} P_l^m(\theta) + \frac{1}{\sin \theta} \frac{dP_l^m(\theta)}{d\theta} \right) \right. \\
&\quad \left. + \left[ -c_l^m(r) \sin(m\phi) - d_l^m(r) \cos(m\phi) \right] \frac{d^2 P_l^m(\theta)}{d\theta^2} \right\} \tag{B.57}
\end{aligned}$$

$$\begin{aligned} \frac{\partial}{\partial r} \frac{\partial}{\partial \phi} B_\phi &= \frac{2}{r^2} \sum_{l,m} \left\{ \frac{m^2}{\sin \theta} \left[ \frac{da_l^m(r)}{dr} \cos(m\phi) - \frac{db_l^m(r)}{dr} \sin(m\phi) \right] P_l^m(\theta) \right. \\ &\quad \left. - m \left[ c_l^m(r) \sin(m\phi) + d_l^m(r) \cos(m\phi) \right] \frac{dP_l^m(\theta)}{d\theta} \right\} \\ &\quad - \frac{2}{r} \sum_{l,m} \left\{ \frac{m^2}{\sin \theta} \left[ \frac{d^2 a_l^m(r)}{dr^2} \cos(m\phi) - \frac{d^2 b_l^m(r)}{dr^2} \sin(m\phi) \right] P_l^m(\theta) \right. \\ &\quad \left. - m \left[ \frac{dc_l^m(r)}{dr} \sin(m\phi) + \frac{dd_l^m(r)}{dr} \cos(m\phi) \right] \frac{dP_l^m(\theta)}{d\theta} \right\} \end{aligned} \quad (\text{B.58})$$

$$\begin{aligned} \frac{\partial}{\partial \theta} \frac{\partial}{\partial \phi} B_\phi &= -\frac{2}{r} \sum_{l,m} \left\{ m^2 \left[ \frac{da_l^m(r)}{dr} \cos(m\phi) - \frac{db_l^m(r)}{dr} \sin(m\phi) \right] \left( \frac{1}{\sin \theta} \frac{dP_l^m(\theta)}{d\theta} - \frac{\cos \theta}{\sin^2 \theta} P_l^m(\theta) \right) \right. \\ &\quad \left. - m \left[ c_l^m(r) \sin(m\phi) + d_l^m(r) \cos(m\phi) \right] \frac{d^2 P_l^m(\theta)}{d\theta^2} \right\} \end{aligned} \quad (\text{B.59})$$

$$\begin{aligned} \frac{\partial^2}{\partial \phi^2} B_\phi &= -\frac{2}{r} \sum_{l,m} \left\{ \frac{m^2}{\sin \theta} \left[ - \frac{da_l^m(r)}{dr} \sin(m\phi) - \frac{db_l^m(r)}{dr} \cos(m\phi) \right] P_l^m(\theta) \right. \\ &\quad \left. - m \left[ c_l^m(r) \cos(m\phi) - d_l^m(r) \sin(m\phi) \right] \frac{dP_l^m(\theta)}{d\theta} \right\} \end{aligned} \quad (\text{B.60})$$

### B.1.3 Current

1854

Electric current expansion is just the curl of the magnetic field as shown below.

$$\vec{J} = \nabla \times \vec{B} = \begin{vmatrix} \frac{1}{r^2 \sin \theta} \hat{r} & \frac{1}{r \sin \theta} \hat{\theta} & \frac{1}{r} \hat{\phi} \\ \frac{\partial}{\partial r} & \frac{\partial}{\partial \theta} & \frac{\partial}{\partial \phi} \\ B_r & r B_\theta & r \sin \theta B_\phi \end{vmatrix}$$

$$J_r = \frac{1}{r \sin \theta} \left( \sin \theta \frac{\partial}{\partial \theta} B_\phi + B_\phi \cos \theta - \frac{\partial}{\partial \phi} B_\theta \right) \quad (\text{B.61})$$

$$J_\theta = -\frac{1}{r} \left( B_\phi + r \frac{\partial}{\partial r} B_\phi - \frac{1}{\sin \theta} \frac{\partial}{\partial \phi} B_r \right) \quad (\text{B.62})$$

$$J_\phi = \frac{1}{r} \left( B_\theta + r \frac{\partial}{\partial r} B_\theta - \frac{\partial}{\partial \theta} B_r \right) \quad (\text{B.63})$$

<sub>1856</sub> Since  $J = \nabla \times B$ ,  $T$  i.e.  $c_l^m(r)$  and  $d_l^m(r)$  becomes Poloidal and  $P$  i.e.  $a_l^m(r)$  and  $b_l^m(r)$  becomes Toroidal as shown below:

$$\begin{pmatrix} J_r \\ J_\theta \\ J_\phi \end{pmatrix} = \begin{pmatrix} -\frac{\hat{L}}{r^2} T \\ \underbrace{\frac{1}{r} \frac{\partial}{\partial \theta} \frac{\partial}{\partial r} T}_{\text{Poloidal}} - \underbrace{\frac{1}{r \sin \theta} \frac{\partial}{\partial \phi} \left( \frac{\partial^2}{\partial r^2} + \frac{\hat{L}}{r^2} \right) P}_{\text{Poloidal}} \\ \underbrace{\frac{1}{r \sin \theta} \frac{\partial}{\partial \phi} \frac{\partial}{\partial r} T}_{\text{Toroidal}} + \underbrace{\frac{1}{r} \frac{\partial}{\partial \theta} \left( \frac{\partial^2}{\partial r^2} + \frac{\hat{L}}{r^2} \right) P}_{\text{Toroidal}} \end{pmatrix} \quad (\text{B.64})$$

<sub>1858</sub> As shown above, separating the above equations into toroidal and poloidal fields and  
<sub>1859</sub> using the expansion of toroidal and poloidal scalars in spherical harmonics by plugging  
<sub>1860</sub> equation (B.5) into equation (B.64) gives:

$$\begin{aligned}
J_r &= \frac{2}{r^2} \sum_{l,m} l(l+1) \left[ c_l^m(r) \cos(m\phi) - d_l^m(r) \sin(m\phi) \right] P_l^m(\theta) \\
J_\theta &= \frac{2}{r} \sum_{l,m} \left\{ \left[ \frac{dc_l^m(r)}{dr} \cos(m\phi) - \frac{dd_l^m(r)}{dr} \sin(m\phi) \right] \frac{dP_l^m(\theta)}{d\theta} \right. \\
&\quad + \frac{m}{\sin \theta} \left[ \frac{d^2 a_l^m(r)}{dr^2} \sin(m\phi) + \frac{d^2 b_l^m(r)}{dr^2} \cos(m\phi) \right] P_l^m(\theta) \\
&\quad \left. - \frac{l(l+1)}{r^2} \frac{m}{\sin \theta} \left[ a_l^m(r) \sin(m\phi) + b_l^m(r) \cos(m\phi) \right] P_l^m(\theta) \right\} \\
J_\phi &= \frac{2}{r} \sum_{l,m} \left\{ - \frac{m}{\sin \theta} \left[ \frac{dc_l^m(r)}{dr} \sin(m\phi) + \frac{dd_l^m(r)}{dr} \cos(m\phi) \right] P_l^m(\theta) \right. \\
&\quad + \left[ \frac{d^2 a_l^m(r)}{dr^2} \cos(m\phi) - \frac{d^2 b_l^m(r)}{dr^2} \sin(m\phi) \right] \frac{dP_l^m(\theta)}{d\theta} \\
&\quad \left. - \frac{l(l+1)}{r^2} \left[ a_l^m(r) \cos(m\phi) - b_l^m(r) \sin(m\phi) \right] \frac{dP_l^m(\theta)}{d\theta} \right\}
\end{aligned}$$

<sup>1861</sup> Axisymmetric ( $m = 0$ ) components of the electric current:

$$\overline{J}_r = \frac{1}{r^2} \sum_l l(l+1) \left[ c_l^0(r) \right] P_l^0(\theta) \quad (\text{B.65})$$

$$\overline{J}_\theta = \frac{1}{r} \sum_l \left[ \frac{dc_l^0(r)}{dr} \right] \frac{dP_l^0(\theta)}{d\theta} \quad (\text{B.66})$$

$$\overline{J}_\phi = \frac{1}{r} \sum_l \left[ \frac{d^2 a_l^0(r)}{dr^2} - \frac{l(l+1)}{r^2} a_l^0(r) \right] \frac{dP_l^0(\theta)}{d\theta} \quad (\text{B.67})$$

<sup>1862</sup> Current Derivatives

$$\begin{aligned}
\frac{\partial}{\partial r} J_r &= \sum_{l,m} \left\{ - \frac{4l(l+1)}{r^3} \left[ c_l^m(r) \cos(m\phi) - d_l^m(r) \sin(m\phi) \right] P_l^m(\theta) \right. \\
&\quad \left. + \frac{2l(l+1)}{r^2} \left[ \frac{dc_l^m(r)}{dr} \cos(m\phi) - \frac{dd_l^m(r)}{dr} \sin(m\phi) \right] P_l^m(\theta) \right\} \quad (\text{B.68})
\end{aligned}$$

$$\frac{\partial}{\partial \theta} J_r = \frac{1}{r^2} \sum_{l,m} \left\{ 2l(l+1) \left[ c_l^m(r) \cos(m\phi) - d_l^m(r) \sin(m\phi) \right] \frac{dP_l^m(\theta)}{d\theta} \right\} \quad (\text{B.69})$$

$$\frac{\partial}{\partial \phi} J_r = -\frac{1}{r^2} \sum_{l,m} \left\{ 2l(l+1)m \left[ c_l^m(r) \sin(m\phi) + d_l^m(r) \cos(m\phi) \right] P_l^m(\theta) \right\} \quad (\text{B.70})$$

$$\begin{aligned}
\frac{\partial}{\partial r} J_\theta &= -\frac{2}{r^2} \sum_{l,m} \left\{ \left[ \frac{dc_l^m(r)}{dr} \cos(m\phi) - \frac{dd_l^m(r)}{dr} \sin(m\phi) \right] \frac{dP_l^m(\theta)}{d\theta} \right. \\
&\quad + \frac{m}{\sin \theta} \left[ \frac{d^2 a_l^m(r)}{dr^2} \sin(m\phi) + \frac{d^2 b_l^m(r)}{dr^2} \cos(m\phi) \right] P_l^m(\theta) \Big\} \\
&\quad + \frac{2}{r} \sum_{l,m} \left\{ \left[ \frac{d^2 c_l^m(r)}{dr^2} \cos(m\phi) - \frac{d^2 d_l^m(r)}{dr^2} \sin(m\phi) \right] \frac{dP_l^m(\theta)}{d\theta} \right. \\
&\quad + \frac{m}{\sin \theta} \left[ \frac{d^3 a_l^m(r)}{dr^3} \sin(m\phi) + \frac{d^3 b_l^m(r)}{dr^3} \cos(m\phi) \right] P_l^m(\theta) \\
&\quad + \frac{3l(l+1)}{r^3} \frac{m}{\sin \theta} \left[ a_l^m(r) \sin(m\phi) + b_l^m(r) \cos(m\phi) \right] P_l^m(\theta) \\
&\quad \left. \left. - \frac{l(l+1)}{r^2} \frac{m}{\sin \theta} \left[ \frac{da_l^m(r)}{dr} \sin(m\phi) + \frac{db_l^m(r)}{dr} \cos(m\phi) \right] P_l^m(\theta) \right\} \quad (\text{B.71}) \right.
\end{aligned}$$

$$\begin{aligned}
\frac{\partial}{\partial \theta} J_\theta &= \frac{2}{r} \sum_{l,m} \left\{ \left[ \frac{dc_l^m(r)}{dr} \cos(m\phi) - \frac{dd_l^m(r)}{dr} \sin(m\phi) \right] \frac{d^2 P_l^m(\theta)}{d\theta^2} \right. \\
&\quad - \frac{m}{\sin^2 \theta} \cos \theta \left[ \frac{d^2 a_l^m(r)}{dr^2} \sin(m\phi) + \frac{d^2 b_l^m(r)}{dr^2} \cos(m\phi) \right] P_l^m(\theta) \\
&\quad + \frac{m}{\sin \theta} \left[ \frac{d^2 a_l^m(r)}{dr^2} \sin(m\phi) + \frac{d^2 b_l^m(r)}{dr^2} \cos(m\phi) \right] \frac{dP_l^m(\theta)}{d\theta} \\
&\quad + \frac{l(l+1)}{r^2} \frac{m}{\sin^2 \theta} \cos \theta \left[ a_l^m(r) \sin(m\phi) + b_l^m(r) \cos(m\phi) \right] P_l^m(\theta) \\
&\quad \left. - \frac{l(l+1)}{r^2} \frac{m}{\sin \theta} \left[ a_l^m(r) \sin(m\phi) + b_l^m(r) \cos(m\phi) \right] \frac{dP_l^m(\theta)}{d\theta} \right\} \quad (\text{B.72}) \right.
\end{aligned}$$

$$\begin{aligned}
\frac{\partial}{\partial \phi} J_\theta &= -\frac{2}{r} \sum_{l,m} \left\{ m \left[ \frac{dc_l^m(r)}{dr} \sin(m\phi) + \frac{dd_l^m(r)}{dr} \cos(m\phi) \right] \frac{dP_l^m(\theta)}{d\theta} \right. \\
&\quad - \frac{m^2}{\sin \theta} \left[ \frac{d^2 a_l^m(r)}{dr^2} \cos(m\phi) - \frac{d^2 b_l^m(r)}{dr^2} \sin(m\phi) \right] P_l^m(\theta) \\
&\quad + \frac{l(l+1)}{r^2} \frac{m^2}{\sin \theta} \left[ a_l^m(r) \cos(m\phi) - b_l^m(r) \sin(m\phi) \right] P_l^m(\theta) \Big\} \quad (\text{B.73}) \right.
\end{aligned}$$

$$\begin{aligned}
\frac{\partial}{\partial r} J_\phi &= \frac{2}{r^2} \sum_{l,m} \left\{ \frac{m}{\sin \theta} \left[ \frac{dc_l^m(r)}{dr} \sin(m\phi) + \frac{dd_l^m(r)}{dr} \cos(m\phi) \right] P_l^m(\theta) \right. \\
&\quad - \left[ \frac{d^2 a_l^m(r)}{dr^2} \cos(m\phi) - \frac{d^2 b_l^m(r)}{dr^2} \sin(m\phi) \right] \frac{dP_l^m(\theta)}{d\theta} \Big\} \\
&\quad - \frac{2}{r} \sum_{l,m} \left\{ \frac{m}{\sin \theta} \left[ \frac{d^2 c_l^m(r)}{dr^2} \sin(m\phi) + \frac{d^2 d_l^m(r)}{dr^2} \cos(m\phi) \right] P_l^m(\theta) \right. \\
&\quad - \left[ \frac{d^3 a_l^m(r)}{dr^3} \cos(m\phi) - \frac{d^3 b_l^m(r)}{dr^3} \sin(m\phi) \right] \frac{dP_l^m(\theta)}{d\theta} \\
&\quad - \frac{3l(l+1)}{r^3} \left[ a_l^m(r) \cos(m\phi) - b_l^m(r) \sin(m\phi) \right] \frac{dP_l^m(\theta)}{d\theta} \\
&\quad \left. + \frac{l(l+1)}{r^2} \left[ \frac{da_l^m(r)}{dr} \cos(m\phi) - \frac{db_l^m(r)}{dr} \sin(m\phi) \right] \frac{dP_l^m(\theta)}{d\theta} \right\} \tag{B.74}
\end{aligned}$$

$$\begin{aligned}
\frac{\partial}{\partial \theta} J_\phi &= \frac{2}{r} \sum_{l,m} \left\{ \frac{m}{\sin^2 \theta} \cos \theta \left[ \frac{dc_l^m(r)}{dr} \sin(m\phi) + \frac{dd_l^m(r)}{dr} \cos(m\phi) \right] P_l^m(\theta) \right. \\
&\quad - \frac{m}{\sin \theta} \left[ \frac{dc_l^m(r)}{dr} \sin(m\phi) + \frac{dd_l^m(r)}{dr} \cos(m\phi) \right] \frac{dP_l^m(\theta)}{d\theta} \\
&\quad + \left[ \frac{d^2 a_l^m(r)}{dr^2} \cos(m\phi) - \frac{d^2 b_l^m(r)}{dr^2} \sin(m\phi) \right] \frac{d^2 P_l^m(\theta)}{d\theta^2} \\
&\quad \left. - \frac{l(l+1)}{r^2} \left[ a_l^m(r) \cos(m\phi) - b_l^m(r) \sin(m\phi) \right] \frac{d^2 P_l^m(\theta)}{d\theta^2} \right\} \tag{B.75}
\end{aligned}$$

$$\begin{aligned}
\frac{\partial}{\partial \phi} J_\phi &= -\frac{2}{r} \sum_{l,m} \left\{ \frac{m^2}{\sin \theta} \left[ \frac{dc_l^m(r)}{dr} \cos(m\phi) - \frac{dd_l^m(r)}{dr} \sin(m\phi) \right] P_l^m(\theta) \right. \\
&\quad + m \left[ \frac{d^2 a_l^m(r)}{dr^2} \sin(m\phi) + \frac{d^2 b_l^m(r)}{dr^2} \cos(m\phi) \right] \frac{dP_l^m(\theta)}{d\theta} \\
&\quad \left. - \frac{l(l+1)m}{r^2} \left[ a_l^m(r) \sin(m\phi) + b_l^m(r) \cos(m\phi) \right] \frac{dP_l^m(\theta)}{d\theta} \right\} \tag{B.76}
\end{aligned}$$

<sup>1863</sup> Axisymmetric components of derivatives of the electric current:

$$\frac{\partial}{\partial r} \overline{J_r} = \sum_{l,0} \frac{l(l+1)}{r^2} \left[ \frac{dc_l^0(r)}{dr} - \frac{2}{r} c_l^0(r) \right] P_l^0(\theta) \quad (\text{B.77})$$

$$\frac{\partial}{\partial \theta} \overline{J_r} = \frac{1}{r^2} \sum_{l,0} l(l+1) \left[ c_l^0(r) \right] \frac{dP_l^0(\theta)}{d\theta} \quad (\text{B.78})$$

$$\frac{\partial}{\partial \phi} \overline{J_r} = 0 \quad (\text{B.79})$$

$$\frac{\partial}{\partial r} \overline{J_\theta} = \sum_{l,0} \frac{1}{r} \left[ \frac{d^2 c_l^0(r)}{dr^2} - \frac{1}{r} \frac{dc_l^0(r)}{dr} \right] \frac{dP_l^0(\theta)}{d\theta} \quad (\text{B.80})$$

$$\frac{\partial}{\partial \theta} \overline{J_\theta} = \frac{1}{r} \sum_{l,0} \left[ \frac{dc_l^0(r)}{dr} \right] \frac{d^2 P_l^0(\theta)}{d\theta^2} \quad (\text{B.81})$$

$$\frac{\partial}{\partial \phi} \overline{J_\theta} = 0 \quad (\text{B.82})$$

$$\frac{\partial}{\partial r} \overline{J_\phi} = \sum_{l,0} \frac{1}{r} \left\{ \frac{d^3 a_l^0(r)}{dr^3} - \frac{1}{r} \frac{d^2 a_l^0(r)}{dr^2} + \frac{l(l+1)}{r^2} \left[ \frac{3}{r} a_l^0(r) - \frac{da_l^0(r)}{dr} \right] \right\} \frac{dP_l^0(\theta)}{d\theta} \quad (\text{B.83})$$

$$\frac{\partial}{\partial \theta} \overline{J_\phi} = \frac{1}{r} \sum_{l,0} \left\{ \left[ \frac{d^2 a_l^0(r)}{dr^2} \right] \frac{d^2 P_l^0(\theta)}{d\theta^2} - \frac{l(l+1)}{r^2} \left[ a_l^0(r) \right] \frac{d^2 P_l^0(\theta)}{d\theta^2} \right\} \quad (\text{B.84})$$

$$\frac{\partial}{\partial \phi} \overline{J_\phi} = 0 \quad (\text{B.85})$$

## <sup>1864</sup> B.2 Velocity Field Expansion

<sup>1865</sup> Velocity field expansion is exactly similar to section B.1 when the magnetic field is re-  
<sup>1866</sup> placed by the velocity field. In this case, the incompressibility of the fluid ( $\nabla \cdot \mathbf{v} = 0$ ) is  
<sup>1867</sup> used for toroidal-poloidal expansion. Also, since vorticity ( $\omega$ ) is just the curl of velocity,  
<sup>1868</sup> the expansion of vorticity is similar to current.

<sup>1869</sup> **Appendix C**

<sup>1870</sup> **Force**

<sup>1871</sup> **C.1 Lorentz Force**

$$\begin{aligned}
 F_L = J \times B &= \begin{vmatrix} \hat{r} & \hat{\theta} & \hat{\phi} \\ J_r & J_\theta & J_\phi \\ B_r & B_\theta & B_\phi \end{vmatrix} \\
 &= (J_\theta B_\phi - J_\phi B_\theta) \hat{r} - (J_r B_\phi - J_\phi B_r) \hat{\theta} + (J_r B_\theta - J_\theta B_r) \hat{\phi} \\
 &= (J_\theta B_\phi - J_\phi B_\theta) \hat{r} + (J_\phi B_r - J_r B_\phi) \hat{\theta} + (J_r B_\theta - J_\theta B_r) \hat{\phi} \quad (\text{C.1})
 \end{aligned}$$

$$(F_L)_r = (J_\theta B_\phi - J_\phi B_\theta) \quad (\text{C.2})$$

$$(F_L)_\theta = (J_\phi B_r - J_r B_\phi) \quad (\text{C.3})$$

$$(F_L)_\phi = (J_r B_\theta - J_\theta B_r) \quad (\text{C.4})$$

$$(F_L)_z = (F_L)_r \cos \theta - (F_L)_\theta \sin \theta \quad (\text{C.5})$$

$$(F_L)_s = (F_L)_r \sin \theta + (F_L)_\theta \cos \theta \quad (\text{C.6})$$

<sup>1872</sup> **C.1.1 Curl of Lorentz Force**

$$(\nabla \times F_L) = \frac{1}{r^2 \sin \theta} \begin{vmatrix} \hat{r} & r\hat{\theta} & r \sin \theta \hat{\phi} \\ \frac{\partial}{\partial r} & \frac{\partial}{\partial \theta} & \frac{\partial}{\partial \phi} \\ (F_L)_r & r(F_L)_\theta & r \sin \theta (F_L)_\phi \end{vmatrix}$$

$$\begin{aligned} (\nabla \times F_L)_r &= \left( B_r \frac{\partial}{\partial r} J_r - J_r \frac{\partial}{\partial r} B_r \right) + \frac{1}{r} \left( B_\theta \frac{\partial}{\partial \theta} J_r - J_\theta \frac{\partial}{\partial \theta} B_r \right) \\ &\quad + \frac{1}{r \sin \theta} \left( B_\phi \frac{\partial}{\partial \phi} J_r - J_\phi \frac{\partial}{\partial \phi} B_r \right) \end{aligned} \quad (C.7)$$

$$\begin{aligned} (\nabla \times F_L)_\theta &= \frac{1}{r \sin \theta} \left( B_\phi \frac{\partial}{\partial \phi} J_\theta - J_\phi \frac{\partial}{\partial \phi} B_\theta \right) \\ &\quad + \frac{1}{r} \left( J_r B_\theta - J_\theta B_r + B_\theta \frac{\partial}{\partial \theta} J_\theta - J_\theta \frac{\partial}{\partial \theta} B_\theta \right) + B_r \frac{\partial}{\partial r} J_\theta - J_r \frac{\partial}{\partial r} B_\theta \end{aligned} \quad (C.8)$$

$$\begin{aligned} (\nabla \times F_L)_\phi &= \frac{1}{r} \left( J_\phi B_r - J_r B_\phi - B_\phi \frac{\partial}{\partial \theta} J_\theta - J_\theta \frac{\partial}{\partial \theta} B_\phi + B_\theta \frac{\partial}{\partial \theta} J_\phi + J_\phi \frac{\partial}{\partial \theta} B_\theta \right) \\ &\quad + B_r \frac{\partial}{\partial r} J_\phi + J_\phi \frac{\partial}{\partial r} B_r - B_\phi \frac{\partial}{\partial r} J_r - J_r \frac{\partial}{\partial r} B_\phi \end{aligned} \quad (C.9)$$

$$(\nabla \times F_L)_z = (\nabla \times F_L)_r \cos \theta - (\nabla \times F_L)_\theta \sin \theta \quad (C.10)$$

$$(\nabla \times F_L)_s = (\nabla \times F_L)_r \sin \theta + (\nabla \times F_L)_\theta \cos \theta \quad (C.11)$$

<sup>1873</sup> **C.2 Coriolis Force**

<sup>1874</sup> Coriolis Force in the non-dimensionalized equations is given by :

$$\mathbf{F}_C = \hat{\mathbf{z}} \times \mathbf{v} \quad (C.12)$$

<sup>1875</sup> Note that  $\hat{\mathbf{z}}$  is in Cylindrical Coordinate and  $\mathbf{v}$  is in Spherical Coordinates. Since we want

<sup>1876</sup> everything in Spherical Coordinates we transform  $\hat{\mathbf{z}}$  into Spherical Coordinates using:

$$\hat{\mathbf{z}} = \cos \theta \hat{\mathbf{r}} - \sin \theta \hat{\theta} \quad (\text{C.13})$$

<sup>1877</sup> Therefore,

$$\begin{aligned} \mathbf{F}_C = \hat{\mathbf{z}} \times \mathbf{v} &= \begin{vmatrix} \hat{r} & \hat{\theta} & \hat{\phi} \\ \cos \theta & -\sin \theta & 0 \\ v_r & v_\theta & v_\phi \end{vmatrix} \\ &= -\sin \theta v_\phi \hat{\mathbf{r}} - \cos \theta v_\phi \hat{\theta} + (\cos \theta v_\theta + \sin \theta v_r) \hat{\phi} \end{aligned} \quad (\text{C.14})$$

<sup>1878</sup> Coriolis Force in spherical coordinates:

$$(F_C)_r = -v_\phi \sin \theta \quad (\text{C.15})$$

$$(F_C)_\theta = -v_\phi \cos \theta \quad (\text{C.16})$$

$$(F_C)_\phi = v_\theta \cos \theta + v_r \sin \theta \quad (\text{C.17})$$

$$(F_C)_z = (F_C)_r \cos \theta - (F_C)_\theta \sin \theta \quad (\text{C.18})$$

$$(F_C)_s = (F_C)_r \sin \theta + (F_C)_\theta \cos \theta \quad (\text{C.19})$$

### <sup>1879</sup> C.2.1 Curl of the Coriolis Force ( $\mathbf{F}_C$ ) in Spherical Coordinates

$$(\nabla \times F_C) = \frac{1}{r^2 \sin \theta} \begin{vmatrix} \hat{r} & r \hat{\theta} & r \sin \theta \hat{\phi} \\ \frac{\partial}{\partial r} & \frac{\partial}{\partial \theta} & \frac{\partial}{\partial \phi} \\ (F_C)_r & r(F_C)_\theta & r \sin \theta (F_C)_\phi \end{vmatrix}$$

$$\begin{aligned} (\nabla \times F_C)_r &= \frac{1}{r \sin \theta} \left[ \sin \theta \left( 2 \cos \theta v_r + \sin \theta \frac{\partial}{\partial \theta} v_r \right) + \left( (\cos^2 \theta - \sin^2 \theta) v_\theta + \sin \theta \cos \theta \frac{\partial}{\partial \theta} v_\theta \right) \right. \\ &\quad \left. + \left( \cos \theta \frac{\partial}{\partial \phi} v_\phi \right) \right] \end{aligned} \quad (\text{C.20})$$

$$(\nabla \times F_C)_\theta = \frac{1}{r} \left[ -v_r \sin \theta - r \sin \theta \frac{\partial}{\partial r} v_r - v_\theta \cos \theta - r \cos \theta \frac{\partial}{\partial r} v_\theta - \frac{\partial}{\partial \phi} v_\phi \right] \quad (\text{C.21})$$

$$(\nabla \times F_C)_\phi = \frac{1}{r} \sin \theta \frac{\partial}{\partial \theta} v_\phi - \cos \theta \frac{\partial}{\partial r} v_\phi \quad (\text{C.22})$$

1880 Since we use the Boussinesq approximation, the fluid is incompressible i.e.

$$\nabla \cdot v = 0 = 2v_r \sin \theta + r \sin \theta \frac{\partial}{\partial r} v_r + v_\theta \cos \theta + \sin \theta \frac{\partial}{\partial \theta} v_\theta + \frac{\partial}{\partial \phi} v_\phi \quad (\text{C.23})$$

1881

$$\therefore 2v_r \sin \theta + v_\theta \cos \theta + \sin \theta \frac{\partial}{\partial \theta} v_\theta + \frac{\partial}{\partial \phi} v_\phi = - \left( r \sin \theta \frac{\partial}{\partial r} v_r \right) \quad (\text{C.24})$$

$$\therefore v_r \sin \theta + r \sin \theta \frac{\partial}{\partial r} v_r + v_\theta \cos \theta + \frac{\partial}{\partial \phi} v_\phi = - \left( v_r \sin \theta + \sin \theta \frac{\partial}{\partial \theta} v_\theta \right) \quad (\text{C.25})$$

1882 Using equations (C.24) and (C.25) in equations (C.20) and (C.21) respectively we get,

$$(\nabla \times F_C)_r = \frac{\sin \theta}{r} \frac{\partial}{\partial \theta} v_r - \frac{\sin \theta}{r} v_\theta - \cos \theta \frac{\partial}{\partial r} v_r \quad (\text{C.26})$$

$$(\nabla \times F_C)_\theta = \frac{\sin \theta}{r} v_r + \frac{\sin \theta}{r} \frac{\partial}{\partial \theta} v_\theta - \cos \theta \frac{\partial}{\partial r} v_\theta \quad (\text{C.27})$$

$$(\nabla \times F_C)_\phi = \frac{\sin \theta}{r} \frac{\partial}{\partial \theta} v_\phi - \cos \theta \frac{\partial}{\partial r} v_\phi \quad (\text{C.28})$$

$$(\nabla \times F_C)_z = (\nabla \times F_C)_r \cos \theta - (\nabla \times F_C)_\theta \sin \theta \quad (\text{C.29})$$

$$(\nabla \times F_C)_s = (\nabla \times F_C)_r \sin \theta + (\nabla \times F_C)_\theta \cos \theta \quad (\text{C.30})$$

### C.3 Inertial Force

$$F_I = (\vec{v} \cdot \nabla) \vec{v} \quad (\text{C.31})$$

$$\vec{v} = v_r \hat{\mathbf{r}} + v_\theta \hat{\theta} + v_\phi \hat{\phi} \quad (\text{C.32})$$

$$(\vec{v} \cdot \nabla) = v_r \frac{\partial}{\partial r} + \frac{v_\theta}{r} \frac{\partial}{\partial \theta} + \frac{v_\phi}{r \sin \theta} \frac{\partial}{\partial \phi} \quad (\text{C.33})$$

$$\begin{aligned} (\vec{v} \cdot \nabla) \vec{v} &= v_r \frac{\partial}{\partial r} v_r \hat{\mathbf{r}} + v_r^2 \frac{\partial}{\partial r} \hat{\mathbf{r}} + \frac{v_\theta}{r} \frac{\partial}{\partial \theta} v_r \hat{\mathbf{r}} + \frac{v_\theta v_r}{r} \frac{\partial}{\partial \theta} \hat{\mathbf{r}} + \frac{v_\phi}{r \sin \theta} \frac{\partial}{\partial \phi} v_r \hat{\mathbf{r}} + \frac{v_\phi v_r}{r \sin \theta} \frac{\partial}{\partial \phi} \hat{\mathbf{r}} \\ &\quad + v_r \frac{\partial}{\partial r} v_\theta \hat{\theta} + v_r v_\theta \frac{\partial}{\partial r} \hat{\theta} + \frac{v_\theta}{r} \frac{\partial}{\partial \theta} v_\theta \hat{\theta} + \frac{v_\theta^2}{r} \frac{\partial}{\partial \theta} \hat{\theta} + \frac{v_\phi}{r \sin \theta} \frac{\partial}{\partial \phi} v_\theta \hat{\theta} + \frac{v_\phi v_\theta}{r \sin \theta} \frac{\partial}{\partial \phi} \hat{\theta} \\ &\quad + v_r \frac{\partial}{\partial r} v_\phi \hat{\phi} + v_r v_\phi \frac{\partial}{\partial r} \hat{\phi} + \frac{v_\theta}{r} \frac{\partial}{\partial \theta} v_\phi \hat{\phi} + \frac{v_\theta v_\phi}{r} \frac{\partial}{\partial \theta} \hat{\phi} + \frac{v_\phi}{r \sin \theta} \frac{\partial}{\partial \phi} v_\phi \hat{\phi} \\ &\quad + \frac{v_\phi^2}{r \sin \theta} \frac{\partial}{\partial \phi} \hat{\phi} \end{aligned} \quad (\text{C.34})$$

1884 Using the derivatives of the unit vectors as shown in appendix E, in the equation C.34,

1885 we get:

$$\begin{aligned}
 (\vec{v} \cdot \nabla) \vec{v} &= \left[ v_r \frac{\partial}{\partial r} v_r + \frac{v_\theta}{r} \frac{\partial}{\partial \theta} v_r + \frac{v_\phi}{r \sin \theta} \frac{\partial}{\partial \phi} v_r - \frac{(v_\theta^2 + v_\phi^2)}{r} \right] \hat{\mathbf{r}} \\
 &+ \left[ v_r \frac{\partial}{\partial r} v_\theta + \frac{v_\theta}{r} \frac{\partial}{\partial \theta} v_\theta + \frac{v_\phi}{r \sin \theta} \frac{\partial}{\partial \phi} v_\theta + \frac{v_\theta v_r}{r} - \frac{v_\phi^2}{r} \cot \theta \right] \hat{\theta} \\
 &+ \left[ v_r \frac{\partial}{\partial r} v_\phi + \frac{v_\theta}{r} \frac{\partial}{\partial \theta} v_\phi + \frac{v_\phi}{r \sin \theta} \frac{\partial}{\partial \phi} v_\phi + \frac{v_\phi v_r}{r} + \frac{v_\phi v_\theta}{r} \cot \theta \right] \hat{\phi} \quad (\text{C.35})
 \end{aligned}$$

1886 Therefore, the total  $\phi$  component of the inertial term is:

$$[(\vec{v} \cdot \nabla) \vec{v}]_\phi = \left[ v_r \frac{\partial}{\partial r} v_\phi + \frac{v_\theta}{r} \frac{\partial}{\partial \theta} v_\phi + \frac{v_\phi}{r \sin \theta} \frac{\partial}{\partial \phi} v_\phi + \frac{v_\phi v_r}{r} + \frac{v_\phi v_\theta}{r} \cot \theta \right] \hat{\phi} \quad (\text{C.36})$$

1887 Since  $\left( \frac{v_\phi}{r \sin \theta} \frac{\partial}{\partial \phi} v_\phi \right)$  is non-linear, I cannot use  $\frac{\partial}{\partial \phi} \bar{v}_\phi = 0$ . I have to compute  $\frac{v_\phi}{r \sin \theta} \frac{\partial}{\partial \phi} v_\phi$  at every location and get an average over  $\phi$  to get the axisymmetric component. Therefore, 1888 the axisymmetric  $\phi$  component of the inertial term is:

$$\overline{[(\vec{v} \cdot \nabla) \vec{v}]}_\phi = \left[ \bar{v}_r \frac{\partial}{\partial r} \bar{v}_\phi + \frac{\bar{v}_\theta}{r} \frac{\partial}{\partial \theta} \bar{v}_\phi + \overline{\frac{v_\phi}{r \sin \theta} \frac{\partial}{\partial \phi} v_\phi} + \frac{\bar{v}_\phi \bar{v}_r}{r} + \frac{\bar{v}_\phi \bar{v}_\theta}{r} \cot \theta \right] \hat{\phi} \quad (\text{C.37})$$

1890 where bar denotes the axisymmetric component.

## 1891 C.4 Viscous Force

1892 In our model the fluid is incompressible  $\nabla \cdot \vec{v} = 0$ . We can simplify the computation of 1893  $\nabla^2 \vec{v}$  by using the following vector identity:

$$\nabla \times (\nabla \times \vec{v}) = \nabla(\nabla \cdot \vec{v}) - \nabla^2 \vec{v} \quad (\text{C.38})$$

$$\therefore \nabla^2 \vec{v} = -\nabla \times (\nabla \times \vec{v}) \quad (\text{C.39})$$

$$\nabla \times \vec{v} = \begin{vmatrix} \frac{1}{r^2 \sin \theta} \hat{r} & \frac{1}{r \sin \theta} \hat{\theta} & \frac{1}{r} \hat{\phi} \\ \frac{\partial}{\partial r} & \frac{\partial}{\partial \theta} & \frac{\partial}{\partial \phi} \\ v_r & r v_\theta & r \sin \theta v_\phi \end{vmatrix}$$

$$= \hat{r} \left( \frac{1}{r \sin \theta} \left[ \frac{\partial (\sin \theta v_\phi)}{\partial \theta} - \frac{\partial v_\theta}{\partial \phi} \right] \right) - \hat{\theta} \left( \frac{1}{r} \left[ \frac{\partial (r v_\phi)}{\partial r} - \frac{1}{\sin \theta} \frac{\partial v_r}{\partial \phi} \right] \right) + \hat{\phi} \left( \frac{1}{r} \left[ \frac{\partial (r v_\theta)}{\partial r} - \frac{\partial v_r}{\partial \theta} \right] \right)$$

$$\nabla \times (\nabla \times \vec{v}) = \begin{vmatrix} \frac{1}{r^2 \sin \theta} \hat{r} & \frac{1}{r \sin \theta} \hat{\theta} & \frac{1}{r} \hat{\phi} \\ \frac{\partial}{\partial r} & \frac{\partial}{\partial \theta} & \frac{\partial}{\partial \phi} \\ \frac{1}{r \sin \theta} \left[ \frac{\partial (\sin \theta v_\phi)}{\partial \theta} - \frac{\partial v_\theta}{\partial \phi} \right] & \left[ \frac{\partial (r v_\phi)}{\partial r} - \frac{1}{\sin \theta} \frac{\partial v_r}{\partial \phi} \right] & \sin \theta \left[ \frac{\partial (r v_\theta)}{\partial r} - \frac{\partial v_r}{\partial \theta} \right] \end{vmatrix}$$

<sup>1894</sup> The total  $r, \theta$  and  $\phi$  component of the viscous terms are:

$$\begin{aligned} [\nabla^2 \vec{v}]_r &= -[\nabla \times (\nabla \times \vec{v})]_r \\ &= -\frac{1}{r^2 \sin \theta} \left\{ \cos \theta \left[ r \frac{\partial v_\theta}{\partial r} + v_\theta - \frac{\partial v_r}{\partial \theta} \right] + \sin \theta \left[ r \frac{\partial^2 v_\theta}{\partial \theta \partial r} + \frac{\partial v_\theta}{\partial \theta} - \frac{\partial^2 v_r}{\partial \theta^2} \right] \right. \\ &\quad \left. + \left( \left[ r \frac{\partial^2 v_\phi}{\partial \phi \partial r} + \frac{\partial v_\phi}{\partial \phi} - \frac{1}{\sin \theta} \frac{\partial^2 v_r}{\partial \phi^2} \right] \right) \hat{r} \right\} \hat{r} \end{aligned} \quad (\text{C.40})$$

$$\begin{aligned} [\nabla^2 \vec{v}]_\theta &= -[\nabla \times (\nabla \times \vec{v})]_\theta \\ &= \frac{1}{r \sin \theta} \left\{ \sin \theta \left[ \frac{\partial v_\theta}{\partial r} + r \frac{\partial^2 v_\theta}{\partial r^2} + \frac{\partial v_\theta}{\partial r} - \frac{\partial^2 v_r}{\partial r \partial \theta} \right] \right. \\ &\quad \left. - \frac{1}{r \sin \theta} \left[ \cos \theta \frac{\partial v_\phi}{\partial \phi} + \sin \theta \frac{\partial^2 v_\phi}{\partial \phi \partial \theta} - \frac{\partial^2 v_\theta}{\partial \phi^2} \right] \right\} \hat{\theta} \end{aligned} \quad (\text{C.41})$$

$$\begin{aligned} [\nabla^2 \vec{v}]_\phi &= -[\nabla \times (\nabla \times \vec{v})]_\phi \\ &= \left[ \frac{\partial^2}{\partial r^2} v_\phi + \frac{1}{r} \left( 2 \frac{\partial}{\partial r} v_\phi - \frac{1}{\sin \theta} \frac{\partial}{\partial r} \frac{\partial}{\partial \phi} v_r \right) \right. \\ &\quad \left. + \frac{1}{r^2} \left( - \frac{v_\phi}{\sin^2 \theta} + \cot \theta \frac{\partial}{\partial \theta} v_\phi + \frac{\partial^2}{\partial \theta^2} v_\phi - \frac{1}{\sin \theta} \frac{\partial}{\partial \theta} \frac{\partial}{\partial \phi} v_\theta \right) \right] \hat{\phi} \end{aligned} \quad (\text{C.42})$$

<sup>1895</sup> Therefore, the axisymmetric  $\phi$  component of the viscous term is:

$$[\nabla^2 \vec{v}]_\phi = \left[ \frac{\partial^2}{\partial r^2} v_\phi + \frac{1}{r} \left( 2 \frac{\partial}{\partial r} v_\phi \right) + \frac{1}{r^2} \left( - \frac{v_\phi}{\sin^2 \theta} + \cot \theta \frac{\partial}{\partial \theta} v_\phi + \frac{\partial^2}{\partial \theta^2} v_\phi \right) \right] \hat{\phi} \quad (\text{C.43})$$

## <sup>1896</sup> C.5 Dynamo Generation Term

<sup>1897</sup> Magnetic Induction Equation:

$$\frac{\partial}{\partial t} \vec{B} = \underbrace{\nabla \times (\vec{v} \times \vec{B})}_{\text{Generation=Creation+Advection}} + \eta \underbrace{\nabla^2 \vec{B}}_{\text{Diffusion}} \quad (\text{C.44})$$

$$\nabla \times (\vec{v} \times \vec{B}) = \begin{vmatrix} \frac{1}{r^2 \sin \theta} \hat{r} & \frac{1}{r \sin \theta} \hat{\theta} & \frac{1}{r} \hat{\phi} \\ \frac{\partial}{\partial r} & \frac{\partial}{\partial \theta} & \frac{\partial}{\partial \phi} \\ (\vec{v} \times \vec{B})_r & r(\vec{v} \times \vec{B})_\theta & r \sin \theta (\vec{v} \times \vec{B})_\phi \end{vmatrix}$$

$$(\nabla \times (\vec{v} \times \vec{B}))_r = \frac{1}{r \sin \theta} \left[ \frac{\partial}{\partial \theta} (\sin \theta (\vec{v} \times \vec{B})_\phi) - \frac{\partial}{\partial \phi} (\vec{v} \times \vec{B})_\theta \right] \quad (C.45)$$

$$(\nabla \times (\vec{v} \times \vec{B}))_\theta = \frac{1}{r} \left[ \frac{1}{\sin \theta} \frac{\partial}{\partial \phi} (\vec{v} \times \vec{B})_r - \frac{\partial}{\partial r} (r(\vec{v} \times \vec{B})_\phi) \right] \quad (C.46)$$

$$(\nabla \times (\vec{v} \times \vec{B}))_\phi = \frac{1}{r} \left[ \frac{\partial}{\partial r} r(\vec{v} \times \vec{B})_\theta - \frac{\partial}{\partial \theta} (\vec{v} \times \vec{B})_r \right] \quad (C.47)$$

$$\begin{aligned} \therefore (\nabla \times (\vec{v} \times \vec{B}))_r &= \left( B_r \frac{\partial}{\partial r} v_r - v_r \frac{\partial}{\partial r} B_r \right) + \frac{1}{r} \left( B_\theta \frac{\partial}{\partial \theta} v_r - v_\theta \frac{\partial}{\partial \theta} B_r \right) \\ &\quad + \frac{1}{r \sin \theta} \left( B_\phi \frac{\partial}{\partial \phi} v_r - v_\phi \frac{\partial}{\partial \phi} B_r \right) \end{aligned} \quad (C.48)$$

$$\begin{aligned} (\nabla \times (\vec{v} \times \vec{B}))_\theta &= \frac{1}{r \sin \theta} \left( v_\theta \frac{\partial}{\partial \phi} B_\phi + B_\phi \frac{\partial}{\partial \phi} v_\theta - v_\phi \frac{\partial}{\partial \phi} B_\theta - B_\theta \frac{\partial}{\partial \phi} v_\phi \right) \\ &\quad - \left( v_r \frac{\partial}{\partial r} B_\theta + B_\theta \frac{\partial}{\partial r} v_r - v_\theta \frac{\partial}{\partial r} B_r - B_r \frac{\partial}{\partial r} v_\theta \right) \\ &\quad - \frac{1}{r} \left( v_r B_\theta - v_\theta B_r \right) \end{aligned} \quad (C.49)$$

$$\begin{aligned} (\nabla \times (\vec{v} \times \vec{B}))_\phi &= \frac{1}{r} \left( v_\phi B_r - v_r B_\phi - B_\phi \frac{\partial}{\partial \theta} v_\theta - v_\theta \frac{\partial}{\partial \theta} B_\phi + B_\theta \frac{\partial}{\partial \theta} v_\phi + v_\phi \frac{\partial}{\partial \theta} B_\theta \right) \\ &\quad + B_r \frac{\partial}{\partial r} v_\phi + v_\phi \frac{\partial}{\partial r} B_r - B_\phi \frac{\partial}{\partial r} v_r - v_r \frac{\partial}{\partial r} B_\phi \end{aligned} \quad (C.50)$$

## C.6 Dynamo Creation Term

1898

$$\begin{aligned}
 \nabla \times (\vec{v} \times \vec{B}) &= (\vec{B} \cdot \nabla) \vec{v} - (\vec{v} \cdot \nabla) \vec{B} + \vec{v} \underbrace{(\nabla \cdot \vec{B})}_{=0} - \vec{B} \underbrace{(\nabla \cdot \vec{v})}_{=0} \\
 &= \underbrace{(\vec{B} \cdot \nabla) \vec{v}}_{\text{Creation}} - \underbrace{(\vec{v} \cdot \nabla) \vec{B}}_{\text{Advection}}
 \end{aligned} \tag{C.51}$$

1899 where, the creation term is:

$$\begin{aligned}
 (\vec{B} \cdot \nabla) \vec{v} &= \underbrace{(\vec{B}_T \cdot \nabla) \vec{v}_P}_{\text{Creates } \vec{B}_P} + \underbrace{(\vec{B}_P \cdot \nabla) \vec{v}_P + (\vec{B}_P \cdot \nabla) \vec{v}_T^{Naxi} + (\vec{B}_T \cdot \nabla) \vec{v}_T^{Naxi}}_{\alpha \text{ effect}} \\
 &\quad + \underbrace{(\vec{B}_P \cdot \nabla) \vec{v}_T^{Axi} + (\vec{B}_T \cdot \nabla) \vec{v}_T^{Axi}}_{\omega \text{ effect}}
 \end{aligned} \tag{C.52}$$

$$\vec{B} \cdot \nabla = B_r \frac{\partial}{\partial r} + \frac{B_\theta}{r} \frac{\partial}{\partial \theta} + \frac{B_\phi}{r \sin \theta} \frac{\partial}{\partial \phi} \tag{C.53}$$

$$\vec{v} = v_r \hat{r} + v_\theta \hat{\theta} + v_\phi \hat{\phi} \tag{C.54}$$

$$\begin{aligned}
 (\vec{B} \cdot \nabla) \vec{v} &= B_r \frac{\partial}{\partial r} v_r \hat{r} + \frac{B_\theta}{r} \frac{\partial}{\partial \theta} v_r \hat{r} + \frac{B_\phi}{r \sin \theta} \frac{\partial}{\partial \phi} v_r \hat{r} \\
 &\quad + B_r \frac{\partial}{\partial r} v_\theta \hat{\theta} + \frac{B_\theta}{r} \frac{\partial}{\partial \theta} v_\theta \hat{\theta} + \frac{B_\phi}{r \sin \theta} \frac{\partial}{\partial \phi} v_\theta \hat{\theta} \\
 &\quad + B_r \frac{\partial}{\partial r} v_\phi \hat{\phi} + \frac{B_\theta}{r} \frac{\partial}{\partial \theta} v_\phi \hat{\phi} + \frac{B_\phi}{r \sin \theta} \frac{\partial}{\partial \phi} v_\phi \hat{\phi} \\
 &= B_r \left( \hat{r} \frac{\partial}{\partial r} v_r + v_r \frac{\partial}{\partial \hat{r}} \right) + \frac{B_\theta}{r} \left( \hat{r} \frac{\partial}{\partial \theta} v_r + v_r \frac{\partial}{\partial \hat{\theta}} \right) + \frac{B_\phi}{r \sin \theta} \left( \hat{r} \frac{\partial}{\partial \phi} v_r + v_r \frac{\partial}{\partial \hat{\phi}} \right) \\
 &\quad + B_r \left( \hat{\theta} \frac{\partial}{\partial r} v_\theta + v_\theta \frac{\partial}{\partial \hat{r}} \right) + \frac{B_\theta}{r} \left( \hat{\theta} \frac{\partial}{\partial \theta} v_\theta + v_\theta \frac{\partial}{\partial \hat{\theta}} \right) + \frac{B_\phi}{r \sin \theta} \left( \hat{\theta} \frac{\partial}{\partial \phi} v_\theta + v_\theta \frac{\partial}{\partial \hat{\phi}} \right) \\
 &\quad + B_r \left( \hat{\phi} \frac{\partial}{\partial r} v_\phi + v_\phi \frac{\partial}{\partial \hat{r}} \right) + \frac{B_\theta}{r} \left( \hat{\phi} \frac{\partial}{\partial \theta} v_\phi + v_\phi \frac{\partial}{\partial \hat{\theta}} \right) + \frac{B_\phi}{r \sin \theta} \left( \hat{\phi} \frac{\partial}{\partial \phi} v_\phi + v_\phi \frac{\partial}{\partial \hat{\phi}} \right) \\
 &\quad + v_\phi \frac{\partial}{\partial \phi} \hat{\phi}
 \end{aligned} \tag{C.55}$$

1900 Using the derivatives of the unit vectors as shown in appendix E, in the above equation,

<sub>1901</sub> we get:

$$\begin{aligned} \therefore (\vec{B} \cdot \nabla) \vec{v} = & B_r \left( \hat{r} \frac{\partial}{\partial r} v_r \right) + \frac{B_\theta}{r} \left( \hat{r} \frac{\partial}{\partial \theta} v_r + v_r \hat{\theta} \right) + \frac{B_\phi}{r \sin \theta} \left( \hat{r} \frac{\partial}{\partial \phi} v_r + v_r \sin \theta \hat{\phi} \right) \\ & + B_r \left( \hat{\theta} \frac{\partial}{\partial r} v_\theta \right) + \frac{B_\theta}{r} \left( \hat{\theta} \frac{\partial}{\partial \theta} v_\theta - v_\theta \hat{r} \right) + \frac{B_\phi}{r \sin \theta} \left( \hat{\theta} \frac{\partial}{\partial \phi} v_\theta + v_\theta \cos \theta \hat{\phi} \right) \\ & + B_r \left( \hat{\phi} \frac{\partial}{\partial r} v_\phi \right) + \frac{B_\theta}{r} \left( \hat{\phi} \frac{\partial}{\partial \theta} v_\phi \right) + \frac{B_\phi}{r \sin \theta} \left( \hat{\phi} \frac{\partial}{\partial \phi} v_\phi - v_\phi \sin \theta \hat{r} \right. \\ & \left. - v_\phi \cos \theta \hat{\theta} \right) \end{aligned} \quad (\text{C.57})$$

<sub>1902</sub> Separating into  $(\hat{r}, \hat{\theta}, \hat{\phi})$  components we get,

$$\begin{aligned} (\vec{B} \cdot \nabla) \vec{v} = & \left[ B_r \frac{\partial}{\partial r} v_r + \frac{B_\theta}{r} \frac{\partial}{\partial \theta} v_r + \frac{B_\phi}{r \sin \theta} \frac{\partial}{\partial \phi} v_r - \frac{B_\theta}{r} \frac{\partial}{\partial \theta} v_\theta - \frac{B_\theta v_\theta}{r} - \frac{B_\phi v_\phi}{r} \right] \hat{r} \\ & + \left[ B_r \frac{\partial}{\partial r} v_\theta + \frac{B_\theta}{r} \frac{\partial}{\partial \theta} v_\theta + \frac{B_\phi}{r \sin \theta} \frac{\partial}{\partial \phi} v_\theta + \frac{B_\theta v_r}{r} - \frac{B_\phi v_\phi \cos \theta}{r \sin \theta} \right] \hat{\theta} \\ & + \left[ B_r \frac{\partial}{\partial r} v_\phi + \frac{B_\theta}{r} \frac{\partial}{\partial \theta} v_\phi + \frac{B_\phi}{r \sin \theta} \frac{\partial}{\partial \phi} v_\phi + \frac{B_\phi v_r}{r} + \frac{B_\phi v_\theta \cos \theta}{r \sin \theta} \right] \hat{\phi} \end{aligned} \quad (\text{C.58})$$

<sup>1903</sup> **Appendix D**

<sup>1904</sup> **Benchmark**

<sup>1905</sup> **Christensen's Non-Dimensional Equations:**

$$E_c \left( \frac{\partial}{\partial t} \mathbf{v} + \mathbf{v} \cdot \nabla \mathbf{v} - \nabla^2 \mathbf{v} \right) + 2\hat{\mathbf{z}} \times \mathbf{v} = -\nabla P + Ra_c \frac{\mathbf{r}}{r_o} T + \frac{1}{P_m} (\nabla \times \mathbf{B}) \times \mathbf{B} \quad (\text{D.1})$$

$$\frac{\partial}{\partial t} \mathbf{B} = \nabla \times (\mathbf{v} \times \mathbf{B}) + \frac{1}{P_m} \nabla^2 \mathbf{B} \quad (\text{D.2})$$

$$\frac{\partial}{\partial t} T + \mathbf{v} \cdot \nabla T = \frac{1}{P_r} \nabla^2 T \quad (\text{D.3})$$

$$\nabla \cdot \mathbf{v} = 0 \quad (\text{D.4})$$

$$\nabla \cdot \mathbf{B} = 0 \quad (\text{D.5})$$

<sup>1906</sup> **Kuang Bloxham's Non-Dimensional Equations:**

$$Ro \left( \frac{\partial}{\partial t} \mathbf{v} + \mathbf{v} \cdot \nabla \mathbf{v} \right) + \hat{\mathbf{z}} \times \mathbf{v} = -\nabla P + Ra \Theta \mathbf{r} + (\nabla \times \mathbf{B}) \times \mathbf{B} + E \nabla^2 \mathbf{v} \quad (\text{D.6})$$

$$\frac{\partial}{\partial t} \mathbf{B} = \nabla \times (\mathbf{v} \times \mathbf{B}) + \nabla^2 \mathbf{B} \quad (\text{D.7})$$

$$\frac{\partial}{\partial t} \Theta + \mathbf{v} \cdot \nabla (T_0 + \Theta) = q_k \nabla^2 \Theta \quad (\text{D.8})$$

$$\nabla \cdot \mathbf{v} = 0 \quad (\text{D.9})$$

$$\nabla \cdot \mathbf{B} = 0 \quad (\text{D.10})$$

## D.1 Non-dimensionalization and Conversion of Control Parameters

The non-dimensionalization comparison and the conversion of input and output control parameters are presented in Tables D.1, D.2 and D.3 respectively.

Scales	Christensen	Kuang Bloxham	Conversion
length	$D$	$r_o$	$\bar{r} = \bar{r}_c \frac{D}{r_o} = \bar{r}_c (1 - r_{io})$
time	$\frac{D^2}{\nu}$	$\frac{r_o^2}{\eta}$	$\bar{t} = \bar{t}_c \frac{(1 - r_{io})^2}{Pm}$
velocity	$\frac{\nu}{D}$	$\frac{\eta}{r_o}$	$\bar{\mathbf{v}} = \bar{\mathbf{v}}_c \frac{Pm}{(1 - r_{io})}$
temperature (for fixed $\Delta T$ BC)	$\Delta T$	$h_T r_o$	$\bar{T} = \bar{T}_c r_{io} (1 - r_{io})$
magnetic field	$(\rho \mu \eta \Omega)^{1/2}$	$(2\rho \mu \eta \Omega)^{1/2}$	$\bar{\mathbf{B}} = \bar{\mathbf{B}}_c \frac{1}{\sqrt{2}}$
pressure	$\rho \eta \Omega$	$2\rho \eta \Omega$	$\bar{P} = \bar{P}_c \frac{1}{2}$

Table D.1: Non-Dimensionalization (bar denotes non-dimensional quantity)

## D.2 Computing Energy Density in the Kuang-Bloxham Model

Magnetic Energy Density can be computed as follows:

$$BE = \frac{1}{V_s} \int_{V_s} |\mathbf{B}|^2 dV \quad (\text{D.11})$$

Input Parameters	Christensen	Kuang Bloxham	Conversion
Prandtl	$Pr_c = \frac{\nu}{\kappa}$	$Pr = \frac{\nu}{\kappa}$	$Pr = Pr_c$
Magnetic Prandtl	$Pm_c = \frac{\nu}{\eta}$	-	-
Roberts	-	$q_k = \frac{\kappa}{\eta}$	$q_k = \frac{Pm_c}{Pr}$
Ekman	$E_c = \frac{\nu}{\Omega D^2}$	$E = \frac{\nu}{2\Omega r_o^2}$	$E = \frac{1}{2}(1 - r_{io})^2 E_c$
Magnetic Rossby	-	$Ro = \frac{\eta}{2\Omega r_o^2} = \frac{E}{q_k Pr}$	$Ro = \frac{1}{2Pm_c}(1 - r_{io})^2 E_c$
Modified Rayleigh (for fixed $\Delta T$ BC)	$Ra_c = \frac{\alpha g_o \Delta TD}{\nu \Omega}$	$Ra = \frac{\alpha g_o h_T r_o^2}{2\Omega \eta}$	$Ra = \frac{Pm_c}{2r_{io}(1 - r_{io})^2} Ra_c$

Table D.2: Input Control Parameters Conversion

<sup>1914</sup> where,

$$dV = r^2 \sin \theta \ dr \ d\theta \ d\phi \quad (\text{D.12})$$

$$V_s = \frac{4}{3}\pi(r_o^3 - r_i^3) = \frac{4}{3}\pi(1 - r_{io}^3) \text{ (non-dimensional)} \quad (\text{D.13})$$

$$\therefore BE = \frac{3}{4\pi(1 - r_{io}^3)} \int_{r_{io}}^1 \int_0^\pi \int_0^{2\pi} |\mathbf{B}(r, \theta, \phi)|^2 r^2 \sin \theta \ dr \ d\theta \ d\phi \quad (\text{D.14})$$

<sup>1915</sup> Note: The radial grid points are not equally spaced hence we have to take into account  
<sup>1916</sup> the different intervals.

Output Parameters	Christensen	Kuang Bloxham
Magnetic Energy	$BE_c = \frac{1}{E_c P_m} \frac{1}{2V_s} \int_{V_s} \mathbf{B}_c^2 dV$ $\therefore \mathbf{B}_c = \sqrt{2}\mathbf{B}$ $= \frac{1}{E_c P_m} 2 BE$ $= \frac{(1-r_{io})^2}{EP_m} BE$	$BE = \frac{1}{2V_s} \int_{V_s} \mathbf{B}^2 dV$ $\therefore \mathbf{B} = \frac{1}{\sqrt{2}} \mathbf{B}_c$ $= E_c P_m BE_c$ $= \frac{EP_m}{(1-r_{io})^2} BE_c$
Kinetic Energy	$KE_c = \frac{1}{2V_s} \int_{V_s} \mathbf{v}_c^2 dV$ $\therefore \mathbf{v}_c = \mathbf{v} \left( \frac{1-r_{io}}{P_m} \right)$ $= \left( \frac{1-r_{io}}{P_m} \right)^2 KE$	$KE = \frac{1}{2V_s} \int_{V_s} \mathbf{v}^2 dV$ $\therefore \mathbf{v} = \mathbf{v}_c \left( \frac{P_m}{1-r_{io}} \right)$ $= \left( \frac{P_m}{1-r_{io}} \right)^2 KE_c$

Table D.3: Output Control Parameters Conversion ( $V_s$  is the volume of the spherical shell)

$$r(i) = \frac{1}{2}(1 - r_{io}) \cos \left( \frac{(N_r - i)\pi}{N_r} \right) + \frac{1}{2}(1 + r_{io}) \quad (D.15)$$

$$\text{Let, } x(i) = \frac{(N_r - i)\pi}{N_r} \quad (D.16)$$

$$\therefore r(i) = \frac{1}{2}(1 - r_{io}) \cos x(i) + \frac{1}{2}(1 + r_{io}) \quad (D.17)$$

$$\frac{dr}{dx} = \frac{1}{2}(1 - r_{io})(-\sin x(i)) \quad (D.18)$$

$$\therefore dr(i) = -\frac{1}{2}(1 - r_{io}) \sin \left( \frac{(N_r - i)\pi}{N_r} \right) dx \quad (D.19)$$

$$\text{Let, } g(i) = -\frac{1}{2}(1 - r_{io}) \sin \left( \frac{(N_r - i)\pi}{N_r} \right) \quad (D.20)$$

$$\Delta x = \frac{(N_r - (i+1))\pi}{N_r} - \frac{(N_r - i)\pi}{N_r} \quad (D.21)$$

$$\therefore \Delta x = -\frac{\pi}{N_r} \quad (D.22)$$

$$\therefore \Delta r = g(i) \Delta x \quad (D.23)$$

$$\therefore BE = \frac{3}{4\pi(1-r_{io}^3)} \sum_{r_{io}}^1 \sum_0^\pi \sum_0^{2\pi} |\mathbf{B}(r, \theta, \phi)|^2 r^2 \sin \theta g(i) \Delta x \Delta \theta \Delta \phi \quad (\text{D.24})$$

<sup>1917</sup> where,

$$\Delta x = -\frac{\pi}{N_r}, \quad \Delta \theta = \frac{\pi}{N_\theta}, \quad \Delta \phi = \frac{2\pi}{N_\phi} \quad (\text{D.25})$$

$$\therefore \frac{1}{V_s} \Delta x \Delta \theta \Delta \phi = \frac{3}{4\pi(1-r_{io}^3)} \frac{(-\pi)(\pi) 2\pi}{N_r N_\theta N_\phi} = -\frac{3\pi^2}{2(1-r_{io}^3)} \frac{1}{N_r N_\theta N_\phi} \quad (\text{D.26})$$

$$\therefore BE = -\frac{3\pi^2}{2(1-r_{io}^3)} \frac{1}{N_r N_\theta N_\phi} \sum_{r_{io}}^1 \sum_0^\pi \sum_0^{2\pi} |\mathbf{B}(r, \theta, \phi)|^2 r^2 \sin \theta g(i) \quad (\text{D.27})$$

$$\text{Similarly, } KE = -\frac{3\pi^2}{2(1-r_{io}^3)} \frac{1}{N_r N_\theta N_\phi} \sum_{r_{io}}^1 \sum_0^\pi \sum_0^{2\pi} |\mathbf{v}(r, \theta, \phi)|^2 r^2 \sin \theta g(i) \quad (\text{D.28})$$

### <sup>1918</sup> D.3 Conversion of Christensen's Initial Magnetic &

#### <sup>1919</sup> Temperature Field to Kuang-Bloxham

##### <sup>1920</sup> D.3.1 Initial Magnetic Field

<sup>1921</sup> In Christensen 2001, the initial magnetic field for a conducting inner core dynamo model  
<sup>1922</sup> for  $0 \leq r \leq r_o$ :

$$(\mathbf{B}_r)_c = 5 \frac{4r_{oc} - 3r_c}{3 + r_{oc}} \cos \theta \quad (\text{D.29})$$

$$(\mathbf{B}_\theta)_c = 5 \frac{9r_c - 8r_{oc}}{2r_{oc} + 6} \sin \theta \quad (\text{D.30})$$

$$(\mathbf{B}_\phi)_c = 5 \sin \left( \pi \frac{r_c}{r_{oc}} \right) \sin 2\theta \quad (\text{D.31})$$

<sub>1923</sub> This corresponds to a dipolar ( $l = 1$  and  $m = 0$ ) poloidal field created by current density  
<sub>1924</sub> in the  $\phi$  direction.

<sub>1925</sub>

<sub>1926</sub> By converting Christensen's non-dimensionalization to Kuang-Bloxham's non-  
<sub>1927</sub> dimensionalization using:

$$r_c = \frac{r}{1 - r_{io}} , \quad r_{o_c} = \frac{1}{1 - r_{io}} \quad (\because r_o = 1) \quad \text{and} \quad \mathbf{B} = \mathbf{B}_c \frac{1}{\sqrt{2}} \quad (\text{D.32})$$

<sub>1928</sub> we get:

$$\mathbf{B}_r = \frac{5}{\sqrt{2}} \frac{4 - 3r}{4 - 3r_{io}} \cos \theta \quad (\text{D.33})$$

$$\mathbf{B}_\theta = \frac{5}{\sqrt{2}} \frac{9r - 8}{8 - 6r_{io}} \sin \theta \quad (\text{D.34})$$

$$\mathbf{B}_\phi = \frac{5}{\sqrt{2}} \sin(\pi r) \sin 2\theta \quad (\text{D.35})$$

<sub>1929</sub> In the Kuang-Bloxham dynamo model, we use:

$$\mathbf{B}_r = -\frac{\hat{L}}{r^2} P \quad (\text{D.36})$$

$$\mathbf{B}_\theta = \frac{1}{r \sin \theta} \left[ \sin \theta \frac{\partial}{\partial \theta} \frac{\partial}{\partial r} P + \frac{\partial}{\partial \phi} T \right] \quad (\text{D.37})$$

$$\mathbf{B}_\phi = \frac{1}{r \sin \theta} \left[ \frac{\partial}{\partial \phi} \frac{\partial}{\partial r} P - \sin \theta \frac{\partial}{\partial \theta} T \right] \quad (\text{D.38})$$

<sub>1930</sub> Separated into toroidal ( $\mathbf{B}_T$ ) and poloidal ( $\mathbf{B}_P$ ) fields,

$$\mathbf{B}_T = \frac{1}{r \sin \theta} \frac{\partial}{\partial \phi} T \hat{\theta} - \frac{1}{r} \frac{\partial}{\partial \theta} T \hat{\phi} \quad (\text{D.39})$$

$$\mathbf{B}_P = -\frac{\hat{L}}{r^2} P \hat{r} + \frac{1}{r} \frac{\partial}{\partial \theta} \frac{\partial}{\partial r} P \hat{\theta} + \frac{1}{r \sin \theta} \frac{\partial}{\partial \phi} \frac{\partial}{\partial r} P \hat{\phi} \quad (\text{D.40})$$

<sub>1931</sub> In spherical system we can expand the toroidal ( $T$ ) and poloidal ( $P$ ) scalars in spherical

<sup>1932</sup> harmonics:

$$T(r, \theta, \phi) = \sum_{l=0}^{\infty} \left[ w_l^0(r) Y_l^0(\theta, \phi) + \sum_{m=1}^l \left( w_l^m(r) Y_l^m(\theta, \phi) + w_l^{m*}(r) Y_l^{m*}(\theta, \phi) \right) \right] \quad (\text{D.41})$$

$$P(r, \theta, \phi) = \sum_{l=0}^{\infty} \left[ v_l^0(r) Y_l^0(\theta, \phi) + \sum_{m=1}^l \left( v_l^m(r) Y_l^m(\theta, \phi) + v_l^{m*}(r) Y_l^{m*}(\theta, \phi) \right) \right] \quad (\text{D.42})$$

<sup>1933</sup> where,  $m = 0$  coefficients have zero imaginary components and,

$$Y_l^m(\theta, \phi) = P_l^m(\theta) e^{im\phi} \quad (\text{D.43})$$

$$\hat{L} Y_l^m = -l(l+1) Y_l^m \quad (\text{D.44})$$

$$v_l^m(r) = a_l^m(r) + i b_l^m(r) \quad (\text{D.45})$$

$$w_l^m(r) = c_l^m(r) + i d_l^m(r) \quad (\text{D.46})$$

<sup>1934</sup> Using [D.41](#) in [D.39](#) and using [D.42](#) in [D.40](#) we get the total toroidal and poloidal fields,

$$\begin{aligned} \mathbf{B}_T &= -\frac{2}{r} \sum_{l,m} \left\{ \left( \frac{m}{\sin \theta} \left[ c_l^m(r) \sin(m\phi) + d_l^m(r) \cos(m\phi) \right] P_l^m(\theta) \right) \hat{\theta} \right. \\ &\quad \left. + \left( \left[ c_l^m(r) \cos(m\phi) - d_l^m(r) \sin(m\phi) \right] \frac{dP_l^m(\theta)}{d\theta} \right) \hat{\phi} \right\} \end{aligned} \quad (\text{D.47})$$

$$\begin{aligned} \mathbf{B}_P &= \frac{2}{r} \sum_{l,m} \left\{ \left( \frac{l(l+1)}{r} \left[ a_l^m(r) \cos(m\phi) - b_l^m(r) \sin(m\phi) \right] \right) \hat{r} \right. \\ &\quad \left. + \left( \frac{da_l^m(r)}{dr} \cos(m\phi) - \frac{db_l^m(r)}{dr} \sin(m\phi) \frac{dP_l^m(\theta)}{d\theta} \right) \hat{\theta} \right. \\ &\quad \left. - \left( \frac{m}{\sin \theta} \left[ \frac{da_l^m(r)}{dr} \sin(m\phi) + \frac{db_l^m(r)}{dr} \cos(m\phi) \right] P_l^m(\theta) \right) \hat{\phi} \right\} \end{aligned} \quad (\text{D.48})$$

<sup>1935</sup>  $\therefore$  The axisymmetric toroidal and poloidal fields are (by setting  $m=0$  and imaginary

<sup>1936</sup> components = 0 in eq [D.47](#) and [D.48](#)),

$$\bar{\mathbf{B}}_T = -\frac{1}{r} \sum_l \left( c_l^0(r) \frac{dP_l^0(\theta)}{d\theta} \right) \hat{\phi} \quad (\text{D.49})$$

$$\bar{\mathbf{B}}_P = \frac{1}{r} \sum_l \left\{ \left( \frac{l(l+1)}{r} a_l^0(r) \right) \hat{r} + \left( \frac{da_l^0(r)}{dr} \frac{dP_l^0(\theta)}{d\theta} \right) \hat{\theta} \right\} \quad (\text{D.50})$$

<sup>1937</sup> In the Kuang-Bloxham model, the magnetic field is stored as:

$$\text{Toroidal Magnetic Field : } coj_l^m = [c_l^m(r), d_l^m(r)] \quad (\text{D.51})$$

$$\text{Poloidal Magnetic Field : } cob_l^m = [a_l^m(r), b_l^m(r)] \quad (\text{D.52})$$

### <sup>1938</sup> Axisymmetric Poloidal Magnetic Field

$$\mathbf{B}_P = \mathbf{B}_r + \mathbf{B}_\theta = -\frac{\hat{L}}{r^2} P = \frac{1}{r} \sum_l \left\{ \left( \frac{l(l+1)}{r} a_l^0(r) \right) \hat{r} + \left( \frac{da_l^0(r)}{dr} \frac{dP_l^0(\theta)}{d\theta} \right) \hat{\theta} \right\} \quad (\text{D.53})$$

<sup>1939</sup> We know that the poloidal magnetic field is the axisymmetric dipole component hence  
<sup>1940</sup> its an  $l = 1$  and  $m = 0$  term. So equation [D.33](#) = equation [D.50](#) (excluding the  $2^{nd}$  term  
<sup>1941</sup> on RHS).

$$\mathbf{B}_r = \frac{1}{r} \sum_l \left( \frac{l(l+1)}{r} a_l^0(r) \right) \hat{r} = \frac{2}{r^2} (cob_1^0) Y_1^0(\theta, \phi) \quad (\text{D.54})$$

$$Y_1^0 = \frac{1}{2} \sqrt{\frac{3}{\pi}} \cos \theta \quad (\text{D.55})$$

$$\therefore \mathbf{B}_r = \frac{2}{r^2} (cob_1^0) \frac{1}{2} \sqrt{\frac{3}{\pi}} \cos \theta \quad (\text{D.56})$$

$$\therefore \frac{5}{\sqrt{2}} \frac{4-3r}{4-3r_{io}} \cos \theta = \frac{2}{r^2} (cob_1^0) \frac{1}{2} \sqrt{\frac{3}{\pi}} \cos \theta \quad (\text{D.57})$$

$$\therefore cob_1^0 = 5 \sqrt{\frac{\pi}{6}} \frac{4-3r}{4-3r_{io}} r^2 = 5 \sqrt{\frac{\pi}{6}} \frac{4r^2 - 3r^3}{4-3r_{io}} \quad (\text{D.58})$$

$$\frac{d}{dr} cob_1^0 = 5 \sqrt{\frac{\pi}{6}} \frac{8r - 9r^2}{4-3r_{io}} \quad (\text{D.59})$$

<sup>1942</sup> Another way to check the derivative of  $cob_1^0$  is by equating equation D.33 with equation  
<sup>1943</sup> D.50 (excluding the 1<sup>st</sup> term on RHS).

$$\mathbf{B}_\theta = \frac{1}{r} \sum_l \left( \frac{da_l^0(r)}{dr} \frac{dP_l^0(\theta)}{d\theta} \right) \hat{\theta} = \frac{1}{r} \frac{d}{dr} (cob_1^0) \frac{d}{dr} Y_1^0(\theta, \phi) \quad (\text{D.60})$$

$$\frac{d}{dr} Y_1^0 = -\frac{1}{2} \sqrt{\frac{3}{\pi}} \sin \theta \quad (\text{D.61})$$

$$\therefore \mathbf{B}_\theta = -\frac{1}{r} \frac{d}{dr} (cob_1^0) \frac{1}{2} \sqrt{\frac{3}{\pi}} \sin \theta \quad (\text{D.62})$$

$$\frac{5}{\sqrt{2}} \frac{9r - 8}{8 - 6r_{io}} \sin \theta = -\frac{1}{r} \frac{d}{dr} (cob_1^0) \frac{1}{2} \sqrt{\frac{3}{\pi}} \sin \theta \quad (\text{D.63})$$

$$\therefore \frac{d}{dr} cob_1^0 = 5 \sqrt{\frac{\pi}{6}} \frac{8r - 9r^2}{4 - 3r_{io}} \quad (\text{D.64})$$

#### <sup>1944</sup> Axisymmetric Toroidal Magnetic Field

<sup>1945</sup> We know that the toroidal magnetic field is the axisymmetric quadrupole component  
<sup>1946</sup> hence its an  $l = 2$  and  $m = 0$  term. So equation D.35 = equation D.49.

$$\mathbf{B}_\phi = -\frac{1}{r} \sum_l \left( c_l^0(r) \frac{dP_l^0(\theta)}{d\theta} \right) \hat{\phi} = -\frac{1}{r} (coj_2^0) \frac{dY_2^0(\theta, \phi)}{d\theta} \quad (\text{D.65})$$

$$\frac{dY_2^0(\theta, \phi)}{d\theta} = \frac{d}{d\theta} \left( \frac{1}{4} \sqrt{\frac{5}{\pi}} (3 \cos^2 \theta - 1) \right) = -\frac{3}{2} \sqrt{\frac{5}{\pi}} \sin \theta \cos \theta \quad (\text{D.66})$$

$$\therefore \mathbf{B}_\phi = \frac{1}{r} (coj_2^0) \frac{3}{2} \sqrt{\frac{5}{\pi}} \sin \theta \cos \theta \quad (\text{D.67})$$

$$\therefore \frac{5}{\sqrt{2}} \sin(\pi r) \sin 2\theta = \frac{1}{r} (coj_2^0) \frac{3}{2} \sqrt{\frac{5}{\pi}} \sin \theta \cos \theta \quad (\text{D.68})$$

$$\therefore \frac{5}{\sqrt{2}} \sin(\pi r) 2 \sin \theta \cos \theta = \frac{1}{r} (coj_2^0) \frac{3}{2} \sqrt{\frac{5}{\pi}} \sin \theta \cos \theta \quad (\text{D.69})$$

$$\therefore coj_2^0 = \frac{20}{3} \sqrt{\frac{\pi}{10}} r \sin(\pi r) \quad (\text{D.70})$$

$$\therefore \frac{d}{dr} coj_2^0 = \frac{20}{3} \sqrt{\frac{\pi}{10}} \left[ \sin(\pi r) + \pi r \cos(\pi r) \right] \quad (\text{D.71})$$

### 1947 D.3.2 Initial Velocity Field

1948 The initial velocity field is set to zero.

### 1949 D.3.3 Initial Temperature Field

#### 1950 Conductive State

$$T_c = \Delta T \left( \frac{r_o r_i}{r D} - \frac{r_i}{D} \right) \quad (D.72)$$

$$T = r_o h_T \left[ \frac{r_i^2}{r r_o} \left( 1 - \frac{\epsilon}{3} \frac{r_i}{r_o} \right) - \frac{\epsilon}{6} \left( \frac{r}{r_o} \right)^2 \right] + \tilde{T}_0 \quad (D.73)$$

1951 For benchmarking, equation D.72 should be equal to equation D.73 (i.e.  $T_c = T$ ). Therefore, after setting  $\epsilon = 0$  ( $\epsilon$  is internal heating rate coefficient) in equation D.73, we get:

$$T = h_T \frac{r_i^2}{r} + \tilde{T}_0 \quad (D.74)$$

1953 Comparing equation D.74 with equation D.72, we get:

$$h_T \frac{r_i^2}{r} = \Delta T \frac{r_o r_i}{r D} \implies h_T = \frac{r_o \Delta T}{r_i D} \implies h_T = \frac{\Delta T}{r_{io} D} \quad (D.75)$$

$$\tilde{T}_0 = -\Delta T \frac{r_i}{D} \quad (D.76)$$

#### 1954 Conductive state and 4<sup>th</sup> order and 4<sup>th</sup> degree temperature perturbation

$$T_c = \frac{r_{o_c} r_{i_c}}{r_c} - r_{i_c} + \frac{21}{\sqrt{17920\pi}} f_c(r_c) \sin^4 \theta \cos 4\phi \quad (D.77)$$

$$\text{Conductive state: } (T_c)_{cond} = \frac{r_{o_c} r_{i_c}}{r_c} - r_{i_c} \quad (D.78)$$

$$\text{Temperature perturbation: } (\Theta_c)_4^4 = \frac{21}{\sqrt{17920\pi}} f_c(r_c) \sin^4 \theta \cos 4\phi \quad (D.79)$$

<sup>1955</sup> where:

$$f_c(r_c) = (1 - 3x_c^2 + 3x_c^4 - x_c^6) \quad (\text{D.80})$$

$$x_c = 2r_c - r_{i_c} - r_{o_c} \quad (\text{D.81})$$

<sup>1956</sup> In the Kuang-Bloxham model,

<sup>1957</sup>

<sup>1958</sup> By converting Christensen's non-dimensionalization to Kuang-Bloxham's non-  
<sup>1959</sup> dimensionalization using:

$$r_c = \frac{r}{1 - r_{io}}, \quad r_{i_c} = \frac{r_{io}}{1 - r_{io}} \quad (\because r_i = r_{io}), \quad r_{o_c} = \frac{1}{1 - r_{io}} \quad (\because r_o = 1) \quad (\text{D.82})$$

<sup>1960</sup> we get:

$$\text{Conductive state: } T_{cond} = \frac{r_{io}}{1 - r_{io}} \left( \frac{1}{r} - 1 \right) \quad (\text{D.83})$$

$$\text{Derivative of Conductive state: } \frac{d}{dr} T_{cond} = -\frac{r_{io}}{1 - r_{io}} \left( \frac{1}{r^2} \right) \quad (\text{D.84})$$

$$\text{Temperature perturbation: } (\Theta)_4^4 = \frac{21}{\sqrt{17920\pi}} f(r) \sin^4 \theta \cos 4\phi \quad (\text{D.85})$$

<sup>1961</sup> where:

$$f(r) = (1 - 3x^2 + 3x^4 - x^6) \quad (\text{D.86})$$

$$x = \frac{1}{1 - r_{io}} (2r - r_{io} - 1) \quad (\text{D.87})$$

<sup>1962</sup> Since Temperature is a scalar we don't use toroidal-poloidal decomposition. We expand  
<sup>1963</sup> the temperature perturbation directly as:

$$\Theta = \sum_{lm} \frac{1}{r} \left[ T_l^m(r) Y_l^m(\theta, \phi) + T_l^{m*}(r) Y_l^{m*}(\theta, \phi) \right] \quad (\text{D.88})$$

<sup>1964</sup> let  $T_l^m(r) = g_l^m(r) + i h_l^m(r)$

$$\Theta = \frac{2}{r} \sum_{l,m} \left[ g_l^m(r) \cos(m\phi) - h_l^m(r) \sin(m\phi) \right] P_l^m(\theta) \quad (\text{D.89})$$

$$\therefore (\Theta)_4^4 = \frac{2}{r} (\cot_4^4) Y_4^4(\theta, \phi) \quad (\text{D.90})$$

$$Y_4^4(\theta, \phi) = \frac{3}{16} \sqrt{\frac{35}{2\pi}} \cos 4\phi \sin^4 \theta \quad (\text{D.91})$$

$$(\Theta)_4^4 = \frac{2}{r} (\cot_4^4) \frac{3}{16} \sqrt{\frac{35}{2\pi}} \cos 4\phi \sin^4 \theta \quad (\text{D.92})$$

$$\frac{21}{\sqrt{17920\pi}} f(r) \sin^4 \theta \cos 4\phi = \frac{2}{r} (\cot_4^4) \frac{3}{16} \sqrt{\frac{35}{2\pi}} \cos 4\phi \sin^4 \theta \quad (\text{D.93})$$

$$(\cot_4^4) = \frac{r}{2} \frac{16}{3} \sqrt{\frac{2\pi}{35}} \frac{21}{\sqrt{17920\pi}} f(r) \quad (\text{D.94})$$

$$\therefore (\cot_4^4) = \frac{8}{3} \sqrt{\frac{2\pi}{35}} \frac{21}{\sqrt{17920\pi}} r f(r) \quad (\text{D.95})$$

$$\therefore \frac{d}{dr} (\cot_4^4) = \frac{8}{3} \sqrt{\frac{2\pi}{35}} \frac{21}{\sqrt{17920\pi}} \left[ r f'(r) + f(r) \right] \quad (\text{D.96})$$

<sup>1965</sup> where:

$$f'(r) = \frac{2}{1 - r_{io}} \left( -6x + 12x^3 - 6x^5 \right) \quad (\text{D.97})$$

$$x = \frac{1}{1 - r_{io}} \left( 2r - r_{io} - 1 \right) \quad (\text{D.98})$$

1966

## Appendix E

1967

## Coordinate Transformation

1968

### E.1 Spherical to Cartesian

$$x = R \sin \theta \cos \phi \quad (\text{E.1})$$

$$y = R \sin \theta \sin \phi \quad (\text{E.2})$$

$$z = R \cos \theta \quad (\text{E.3})$$

$$\text{Let, } \vec{P} = P_r \hat{e}_r + P_\theta \hat{e}_\theta + P_\phi \hat{e}_\phi \quad (\text{E.4})$$

1969 We know that:

$$\hat{r} = x \hat{e}_x + y \hat{e}_y + z \hat{e}_z \quad (\text{E.5})$$

$$= R \sin \theta \cos \phi \hat{e}_x + R \sin \theta \sin \phi \hat{e}_y + R \cos \theta \hat{e}_z \quad (\text{E.6})$$

1970 where  $(\hat{e}_r, \hat{e}_\theta, \hat{e}_\phi)$  and  $(\hat{e}_x, \hat{e}_y, \hat{e}_z)$  are unit vectors parallel to coordinate lines. By definition,

Girija Dharmaraj (2009)

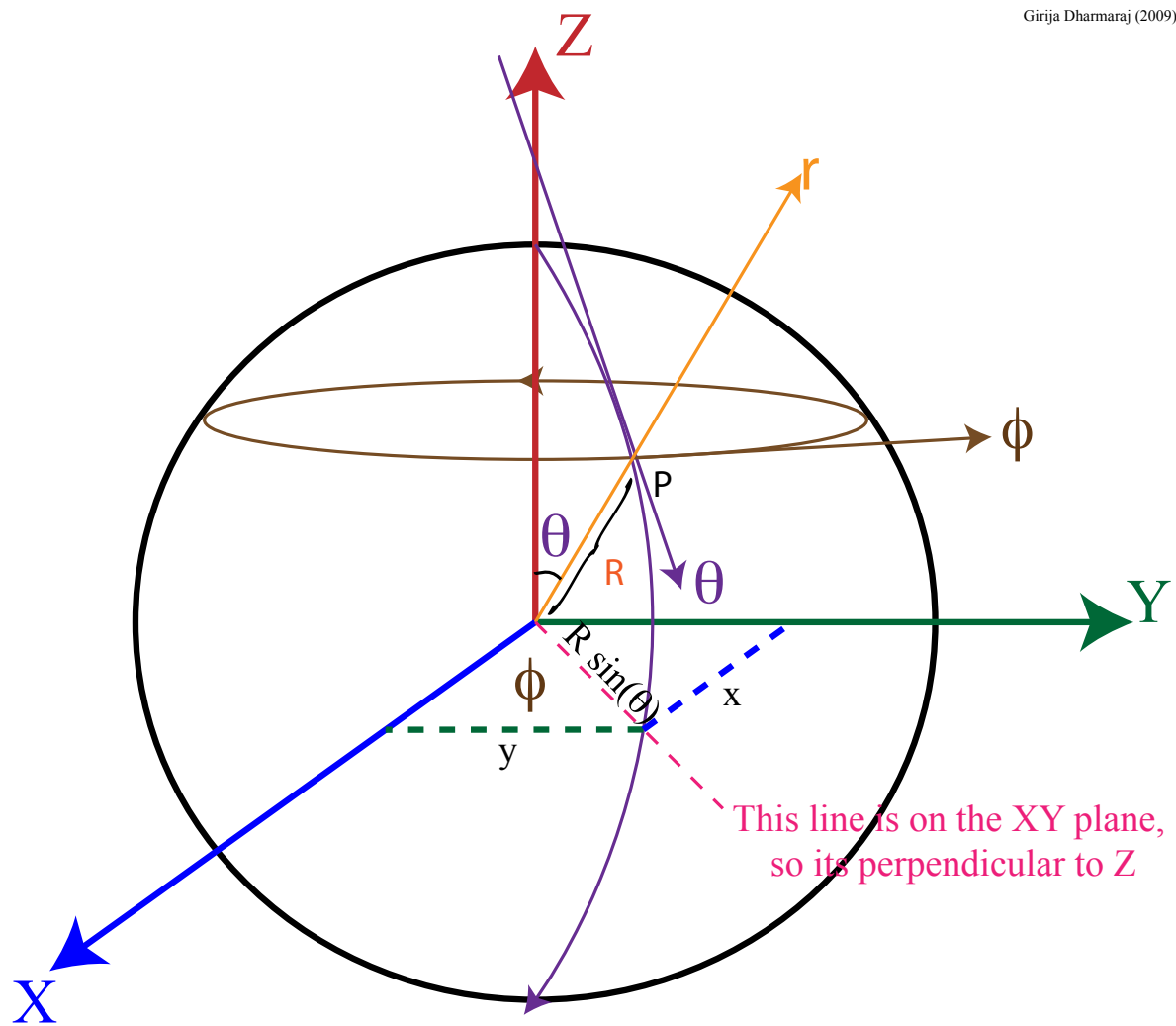


Figure E.1: Spherical Polar Coordinates

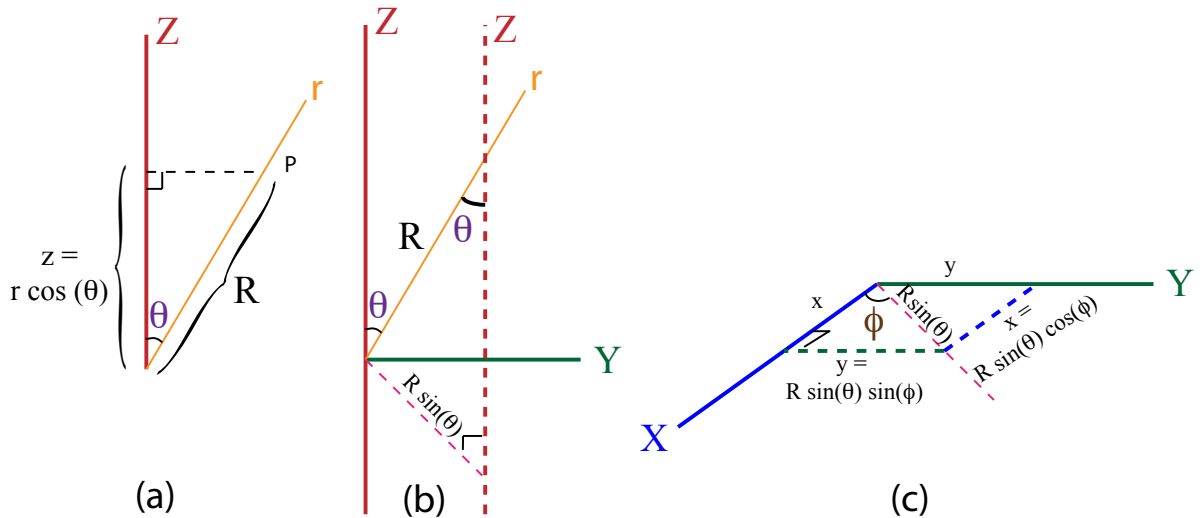


Figure E.2: Spherical to Cartesian Coordinates

<sup>1971</sup> we know that:

$$\hat{e}_r = \frac{1}{\left| \frac{\partial \vec{r}}{\partial R} \right|} \frac{\partial \vec{r}}{\partial R} \quad (E.7)$$

$$\hat{e}_\theta = \frac{1}{\left| \frac{\partial \vec{r}}{\partial \theta} \right|} \frac{\partial \vec{r}}{\partial \theta} \quad (E.8)$$

$$\hat{e}_\phi = \frac{1}{\left| \frac{\partial \vec{r}}{\partial \phi} \right|} \frac{\partial \vec{r}}{\partial \phi} \quad (E.9)$$

$$\frac{\partial \vec{r}}{\partial R} = \sin \theta \cos \phi \hat{e}_x + \sin \theta \sin \phi \hat{e}_y + \cos \theta \hat{e}_z \quad (E.10)$$

$$\left| \frac{\partial \vec{r}}{\partial R} \right| = \sqrt{\sin^2 \theta \cos^2 \phi + \sin^2 \theta \sin^2 \phi + \cos^2 \theta} \quad (E.11)$$

$$= \sqrt{\sin^2 \theta (\cos^2 \phi + \sin^2 \phi) + \cos^2 \theta} \quad (E.12)$$

$$= 1 \quad (E.13)$$

$$\frac{\partial \vec{r}}{\partial \theta} = R \cos \theta \cos \phi \hat{e}_x + R \cos \theta \sin \phi \hat{e}_y - R \sin \theta \hat{e}_z \quad (\text{E.14})$$

$$\left| \frac{\partial \vec{r}}{\partial \theta} \right| = \sqrt{R^2(\cos^2 \theta \cos^2 \phi + \cos^2 \theta \sin^2 \phi + \sin^2 \theta)} \quad (\text{E.15})$$

$$= \sqrt{R^2(\cos^2 \theta(\cos^2 \phi + \sin^2 \phi) + \sin^2 \theta)} \quad (\text{E.16})$$

$$= R \quad (\text{E.17})$$

$$\frac{\partial \vec{r}}{\partial \phi} = -R \sin \theta \sin \phi \hat{e}_x + R \sin \theta \cos \phi \hat{e}_y \quad (\text{E.18})$$

$$\left| \frac{\partial \vec{r}}{\partial \phi} \right| = \sqrt{R^2(\sin^2 \theta \sin^2 \phi + \sin^2 \theta \cos^2 \phi)} \quad (\text{E.19})$$

$$= \sqrt{R^2 \sin^2 \theta(\sin^2 \phi + \cos^2 \phi)} \quad (\text{E.20})$$

$$= R \sin \theta \quad (\text{E.21})$$

$$\therefore \hat{e}_r = \sin \theta \cos \phi \hat{e}_x + \sin \theta \sin \phi \hat{e}_y + \cos \theta \hat{e}_z \quad (\text{E.22})$$

$$\therefore \hat{e}_\theta = \cos \theta \cos \phi \hat{e}_x + \cos \theta \sin \phi \hat{e}_y - \sin \theta \hat{e}_z \quad (\text{E.23})$$

$$\therefore \hat{e}_\phi = -\sin \phi \hat{e}_x + \cos \phi \hat{e}_y \quad (\text{E.24})$$

$$\begin{bmatrix} \hat{e}_r \\ \hat{e}_\theta \\ \hat{e}_\phi \end{bmatrix} = \begin{bmatrix} \sin \theta \cos \phi & \sin \theta \sin \phi & \cos \theta \\ \cos \theta \cos \phi & \cos \theta \sin \phi & -\sin \theta \\ -\sin \phi & \cos \phi & 0 \end{bmatrix} \begin{bmatrix} \hat{e}_x \\ \hat{e}_y \\ \hat{e}_z \end{bmatrix}$$

<sup>1972</sup> Interestingly cartesian to spherical coordinate transformation is just a transpose of the

<sup>1973</sup> sin and cos terms (as its just projection),

$$\begin{bmatrix} \hat{e}_x \\ \hat{e}_y \\ \hat{e}_z \end{bmatrix} = \begin{bmatrix} \sin \theta \cos \phi & \cos \theta \cos \phi & -\sin \phi \\ \sin \theta \sin \phi & \cos \theta \sin \phi & \cos \phi \\ \cos \theta & -\sin \theta & 0 \end{bmatrix} \begin{bmatrix} \hat{e}_r \\ \hat{e}_\theta \\ \hat{e}_\phi \end{bmatrix}$$

<sup>1974</sup> **E.2 Derivative of unit vectors in spherical coordinates**

1975

$$\frac{\partial}{\partial r} \hat{\mathbf{r}} = 0 \quad (E.25)$$

$$\begin{aligned} \frac{\partial}{\partial \theta} \hat{\mathbf{r}} &= \cos \theta \cos \phi \hat{e}_x + \cos \theta \sin \phi \hat{e}_y - \sin \theta \hat{e}_z \\ &= \hat{\theta} \end{aligned} \quad (E.26)$$

$$\begin{aligned} \frac{\partial}{\partial \phi} \hat{\mathbf{r}} &= -\sin \theta \sin \phi \hat{e}_x + \sin \theta \cos \phi \hat{e}_y \\ &= \sin \theta \hat{\phi} \end{aligned} \quad (E.27)$$

$$\begin{aligned} \frac{\partial}{\partial r} \hat{\theta} &= 0 \\ \frac{\partial}{\partial \theta} \hat{\theta} &= -\sin \theta \cos \phi \hat{e}_x - \sin \theta \sin \phi \hat{e}_y - \cos \theta \hat{e}_z \\ &= -\hat{\mathbf{r}} \end{aligned} \quad (E.28)$$

$$\begin{aligned} \frac{\partial}{\partial \phi} \hat{\theta} &= -\cos \theta \sin \phi \hat{e}_x + \cos \theta \cos \phi \hat{e}_y \\ &= \cos \theta \hat{\phi} \end{aligned} \quad (E.29)$$

$$\frac{\partial}{\partial r} \hat{\phi} = 0 \quad (E.30)$$

$$\frac{\partial}{\partial \theta} \hat{\phi} = 0 \quad (E.31)$$

$$\begin{aligned} \frac{\partial}{\partial \phi} \hat{\phi} &= -\cos \phi \hat{e}_x - \sin \phi \hat{e}_y \\ &= -\sin \theta \hat{\mathbf{r}} - \cos \theta \hat{\theta} \end{aligned} \quad (E.32)$$

<sub>1976</sub> Since,

$$\begin{aligned}
 -\sin \theta \hat{\mathbf{r}} - \cos \theta \hat{\theta} &= -\sin^2 \theta \cos \phi \hat{e}_x - \sin^2 \theta \sin \phi \hat{e}_y - \sin \theta \cos \theta \hat{\mathbf{z}} \\
 &\quad - \cos^2 \theta \cos \phi \hat{e}_x - \cos^2 \theta \sin \phi \hat{e}_y + \cos \theta \sin \theta \hat{\mathbf{z}} \\
 &= -\cos \phi \hat{e}_x (\sin^2 \theta + \cos^2 \theta) - \sin \phi \hat{e}_y (\sin^2 \theta + \cos^2 \theta) \\
 &= -\cos \phi \hat{e}_x - \sin \phi \hat{e}_y
 \end{aligned} \tag{E.33}$$

<sup>1977</sup> **Appendix F**

<sup>1978</sup> **Tables**

Table F.1: Results of Dynamo Models for Hyperdiffusivity

Model	$l_0$	$Ra$	$\frac{Ra}{Ra_C}$	$E_B$	$E_k$	$\frac{E_{BP}}{E_{BT}}$	$\frac{E_{Bx}^{N_Axi}}{E_{BP}}$	$\frac{E_{Tx}^{N_Axi}}{E_{BT}}$	$\frac{E_{kP}^{N_Axi}}{E_{kP}}$	$\frac{E_{kT}^{N_Axi}}{E_{kT}}$	$f_{Dip}$	$Ro$	$Ro_l$	$Nu$	$M_{LC}$	$M_\alpha$	$M_\omega$	$\delta_{TIC}$	$\delta_{EIC}$
$E = 6.00e-05$ , $Ro_M = 2.00e-05$ and $q_k = 1$																			
FFSF-01	0	1.00e+04	34.97	1.5e+00	2.4e+05	3.8e-01	2.5e-01	2.8e-01	9.9e-01	4.1e-01	9.1e-01	9.8e-03	1.1e-02	2.55	0.16	0.32	0.49	7.4e-02	0.0e+00
FFSF-02	10	1.00e+04	34.97	1.9e+00	2.2e+05	7.2e-01	4.5e-01	6.1e-01	9.7e-01	5.8e-01	9.5e-01	9.4e-03	2.1e-02	3.24	0.31	0.40	0.22	7.4e-02	0.0e+00
FFSF-03	20	1.00e+04	34.97	3.5e+00	1.5e+05	8.7e-01	4.1e-01	4.6e-01	9.7e-01	6.6e-01	9.4e-01	7.9e-03	2.5e-02	3.40	0.42	0.32	0.21	7.7e-02	0.0e+00
FFSF-04	30	1.00e+04	34.97	3.8e+00	1.5e+05	8.0e-01	4.0e-01	4.4e-01	9.7e-01	6.4e-01	9.2e-01	7.7e-03	2.6e-02	3.37	0.46	0.19	0.33	7.8e-02	0.0e+00
FFSF-05	40	1.00e+04	34.97	3.9e+00	1.5e+05	8.0e-01	4.0e-01	4.3e-01	9.7e-01	6.2e-01	9.5e-01	7.8e-03	2.6e-02	3.38	0.46	0.24	0.24	7.2e-02	0.0e+00
FFSF-06	50	1.00e+04	34.97	3.7e+00	1.2e+05	1.2e+00	3.3e-01	4.6e-01	9.7e-01	6.6e-01	9.4e-01	7.0e-03	2.6e-02	3.47	0.47	0.23	0.32	7.2e-02	0.0e+00
FFNS-01	0	7.50e+03	31.12	1.1e-02	8.7e+04	4.8e-01	3.0e-01	2.9e-01	9.8e-01	5.7e-01	9.5e-01	5.9e-03	7.5e-03	2.67	-0.00	0.32	0.48	8.4e-02	3.0e-02
FFNS-02	10	7.50e+03	31.12	3.3e+00	8.8e+04	8.4e-01	3.1e-01	4.0e-01	9.6e-01	5.4e-01	9.9e-01	5.9e-03	1.2e-02	3.21	0.39	0.17	0.46	8.1e-02	3.0e-02
FFNS-03	20	7.50e+03	31.12	4.0e+00	6.5e+04	7.3e-01	3.7e-01	4.1e-01	9.6e-01	7.2e-01	9.2e-01	5.1e-03	1.4e-02	3.41	0.49	0.31	0.41	8.0e-02	2.7e-02
FFNS-04	30	7.50e+03	31.12	2.9e+00	6.6e+04	9.1e-01	3.8e-01	5.0e-01	9.7e-01	8.1e-01	8.4e-01	5.1e-03	1.6e-02	3.54	0.42	0.36	0.28	8.1e-02	3.0e-02
FFNS-05	40	7.50e+03	31.12	2.5e+00	7.2e+04	8.0e-01	3.9e-01	4.6e-01	9.7e-01	7.3e-01	9.5e-01	5.4e-03	1.7e-02	3.43	0.38	0.36	0.34	8.2e-02	2.8e-02
FFNS-06	50	7.50e+03	31.12	2.9e+00	6.6e+04	9.0e-01	3.6e-01	5.0e-01	9.7e-01	7.6e-01	9.1e-01	5.1e-03	1.7e-02	3.54	0.45	0.34	0.31	8.2e-02	2.4e-02
FTSF-01	0	3.00e+03	8.70	1.1e+00	7.3e+04	3.7e-01	1.3e-01	2.0e-01	1.0e+00	7.4e-01	1.0e+00	5.4e-03	9.4e-03	2.13	0.38	0.45	0.14	6.2e-02	0.0e+00
FTSF-02	10	3.00e+03	8.70	2.1e+00	1.4e+05	9.0e-01	3.8e-01	5.9e-01	9.8e-01	7.9e-01	9.9e-01	7.5e-03	2.1e-02	3.21	0.30	0.36	0.18	5.8e-02	0.0e+00
FTSF-03	20	3.00e+03	8.70	2.4e+00	1.4e+05	1.3e+00	3.5e-01	6.1e-01	9.9e-01	8.7e-01	1.0e+00	7.4e-03	3.1e-02	3.56	0.29	0.34	0.24	5.6e-02	0.0e+00
FTSF-04	30	3.00e+03	8.70	2.5e+00	1.3e+05	1.5e+00	3.4e-01	6.2e-01	9.9e-01	8.4e-01	1.0e+00	7.1e-03	3.4e-02	3.57	0.35	0.35	0.31	6.0e-02	0.0e+00
FTSF-05	40	3.00e+03	8.70	2.6e+00	1.2e+05	1.5e+00	3.2e-01	6.4e-01	9.9e-01	8.3e-01	1.0e+00	7.0e-03	3.3e-02	3.60	0.38	0.34	0.28	5.8e-02	0.0e+00
FTSF-06	50	3.00e+03	8.70	2.9e+00	1.1e+05	1.5e+00	3.0e-01	5.9e-01	9.9e-01	8.0e-01	1.0e+00	6.7e-03	3.2e-02	3.51	0.40	0.22	0.34	6.2e-02	0.0e+00
FTNS-01	0	3.00e+03	10.83	2.3e+00	5.3e+04	9.6e-01	1.1e-01	1.6e-01	9.9e-01	6.9e-01	1.0e+00	4.6e-03	7.3e-03	2.45	0.36	0.42	0.33	8.2e-02	3.7e-02
FTNS-02	10	3.00e+03	10.83	3.7e+00	1.0e+05	1.3e+00	2.5e-01	4.8e-01	9.7e-01	6.6e-01	1.0e+00	6.4e-03	1.6e-02	3.44	0.40	0.31	0.32	6.6e-02	3.0e-02
FTNS-03	20	3.00e+03	10.83	4.8e+00	8.0e+04	1.6e+00	2.8e-01	5.9e-01	9.7e-01	7.8e-01	1.0e+00	5.7e-03	2.0e-02	3.76	0.47	0.38	0.35	6.4e-02	3.2e-02
FTNS-04	30	3.00e+03	10.83	4.9e+00	7.7e+04	1.5e+00	2.9e-01	5.6e-01	9.7e-01	8.0e-01	9.9e-01	5.5e-03	2.1e-02	3.70	0.48	0.32	0.37	6.5e-02	3.2e-02
FTNS-05	40	3.00e+03	10.83	4.7e+00	7.9e+04	1.5e+00	3.0e-01	5.5e-01	9.6e-01	7.5e-01	9.9e-01	5.6e-03	2.1e-02	3.71	0.45	0.30	0.38	6.5e-02	3.0e-02
FTNS-06	50	3.00e+03	10.83	4.2e+00	8.4e+04	1.6e+00	3.3e-01	6.0e-01	9.7e-01	7.7e-01	1.0e+00	5.8e-03	2.3e-02	3.87	0.46	0.38	0.33	6.4e-02	2.4e-02

Table F.2: **Results of Dynamo Models.** The boundary conditions are applied at both the inner and outer core boundaries. For definition of the symbols please refer to the nomenclature.

Model	$Ra$	$\frac{Ra}{Ra_C}$	$E_B$	$E_k$	$\frac{E_{B_P}}{E_{B_T}}$	$\frac{E_{B_P}^{N\text{Axi}}}{E_{B_P}}$	$\frac{E_{B_T}^{N\text{Axi}}}{E_{B_T}}$	$\frac{E_{k_P}^{N\text{Axi}}}{E_{k_P}}$	$\frac{E_{k_T}^{N\text{Axi}}}{E_{k_T}}$	$f_{Dip}$	$Ro$	$Ro_l$	$Nu$	$M_{LC}$	$M_\alpha$	$M_\omega$	$\delta_{T_{IC}}$	$\delta_{E_{IC}}$
<i>E = 2.00e-05 , Ro<sub>M</sub> = 2.00e-05 and q<sub>k</sub> = 1</i>																		
FFSF-01	2.50e+03	6.98	2.6e-01	3.2e+05	3.5e-01	4.9e-01	5.0e-01	9.9e-01	7.2e-02	4.0e-01	1.1e-02	9.3e-03	1.62	0.17	0.39	0.41	0.0e+00	0.0e+00
FFSF-02	5.00e+03	13.97	6.4e-01	3.8e+05	4.0e-01	6.7e-01	6.2e-01	9.8e-01	1.5e-01	4.3e-01	1.2e-02	1.6e-02	2.06	0.24	0.44	0.34	0.0e+00	0.0e+00
FFSF-03	5.00e+03	13.97	1.7e+00	8.6e+04	8.4e-01	3.3e-01	5.0e-01	9.8e-01	7.6e-01	9.6e-01	5.9e-03	2.3e-02	2.40	0.38	0.32	0.16	0.0e+00	0.0e+00
FFSF-04	7.50e+03	20.95	2.4e+00	2.3e+05	9.7e-01	3.4e-01	5.0e-01	9.8e-01	3.7e-01	9.7e-01	9.6e-03	2.5e-02	2.81	0.39	0.30	0.28	0.0e+00	0.0e+00
FFSF-05	1.00e+04	27.93	3.9e+00	2.3e+05	9.5e-01	3.7e-01	4.9e-01	9.7e-01	5.0e-01	9.6e-01	9.6e-03	3.3e-02	3.22	0.46	0.22	0.29	0.0e+00	0.0e+00
FFSF-06	1.25e+04	34.92	4.9e+00	3.0e+05	7.6e-01	4.2e-01	5.0e-01	9.7e-01	5.3e-01	9.2e-01	1.1e-02	3.7e-02	3.64	0.41	0.24	0.34	0.0e+00	0.0e+00
FFSF-07	1.50e+04	41.90	5.9e+00	2.4e+05	8.6e-01	4.2e-01	5.3e-01	9.7e-01	7.4e-01	9.1e-01	9.9e-03	4.3e-02	4.01	0.44	0.30	0.26	0.0e+00	0.0e+00
FFNS-01	2.50e+03	9.03	7.5e-01	3.6e+04	1.0e+00	2.0e-01	4.3e-01	9.9e-01	7.8e-01	1.0e+00	3.8e-03	1.3e-02	1.96	0.32	0.33	0.21	0.0e+00	1.8e-02
FFNS-02	5.00e+03	18.05	2.9e+00	6.3e+04	7.9e-01	3.1e-01	3.9e-01	9.8e-01	7.3e-01	9.3e-01	5.0e-03	1.6e-02	2.73	0.42	0.37	0.22	0.0e+00	1.8e-02
FFNS-03	7.50e+03	27.08	5.0e+00	8.3e+04	8.5e-01	3.4e-01	4.3e-01	9.6e-01	7.4e-01	8.7e-01	5.8e-03	2.0e-02	3.39	0.49	0.27	0.27	0.0e+00	1.8e-02
FFNS-04	1.00e+04	36.10	6.3e+00	1.0e+05	8.8e-01	3.4e-01	4.5e-01	9.7e-01	7.8e-01	8.6e-01	6.5e-03	2.4e-02	3.84	0.49	0.27	0.35	0.0e+00	1.8e-02
FFNS-05	1.25e+04	45.13	6.9e+00	1.3e+05	8.9e-01	3.8e-01	4.9e-01	9.6e-01	8.1e-01	8.5e-01	7.2e-03	2.8e-02	4.23	0.48	0.34	0.27	0.0e+00	1.8e-02
FFNS-06	1.50e+04	54.15	6.8e+00	1.6e+05	8.7e-01	4.0e-01	5.1e-01	9.7e-01	8.1e-01	8.7e-01	8.0e-03	3.2e-02	4.58	0.48	0.40	0.23	0.0e+00	1.8e-02
FTSF-01	1.25e+03	2.71	8.1e-01	3.7e+04	1.1e+00	1.5e-01	4.3e-01	1.0e+00	7.9e-01	1.0e+00	3.8e-03	1.6e-02	1.91	0.36	0.33	0.23	6.5e-02	0.0e+00
FTSF-02	1.50e+03	3.25	1.1e+00	5.2e+04	1.1e+00	2.1e-01	4.6e-01	9.9e-01	8.2e-01	1.0e+00	4.6e-03	2.0e-02	2.13	0.28	0.32	0.10	6.0e-02	0.0e+00
FTSF-03	1.75e+03	3.79	1.4e+00	6.9e+04	1.0e+00	2.6e-01	4.6e-01	9.9e-01	8.1e-01	1.0e+00	5.2e-03	2.3e-02	2.30	0.34	0.36	0.12	6.7e-02	0.0e+00
FTSF-04	2.00e+03	4.33	1.7e+00	8.9e+04	9.2e-01	3.4e-01	5.0e-01	9.9e-01	8.3e-01	1.0e+00	5.9e-03	2.6e-02	2.51	0.30	0.41	0.13	7.0e-02	0.0e+00
FTSF-05	2.25e+03	4.87	1.8e+00	1.0e+05	1.1e+00	3.4e-01	5.5e-01	9.9e-01	8.6e-01	1.0e+00	6.3e-03	3.1e-02	2.69	0.32	0.38	0.20	5.8e-02	0.0e+00
FTSF-06	2.50e+03	5.41	2.2e+00	1.2e+05	9.9e-01	3.7e-01	5.7e-01	9.9e-01	8.5e-01	1.0e+00	7.0e-03	3.3e-02	2.90	0.32	0.40	0.23	6.1e-02	0.0e+00
FTSF-07	5.00e+03	10.82	6.2e+00	3.7e+05	1.4e+00	3.9e-01	7.1e-01	9.7e-01	8.6e-01	1.0e+00	1.2e-02	7.0e-02	4.94	0.34	0.39	0.28	5.2e-02	0.0e+00
FTSF-08	7.50e+03	16.23	1.0e+01	7.5e+05	1.3e+00	4.6e-01	7.6e-01	9.6e-01	8.3e-01	1.0e+00	1.7e-02	9.8e-02	6.75	0.31	0.39	0.27	4.6e-02	0.0e+00
FTSF-09	1.00e+04	21.65	7.1e+00	2.7e+06	6.9e-01	9.2e-01	8.8e-01	9.3e-01	4.1e-01	2.3e-01	3.3e-02	1.2e-01	7.59	0.09	0.56	0.19	4.5e-02	0.0e+00
FTSF-10	1.25e+04	27.06	9.6e+00	4.1e+06	6.9e-01	9.2e-01	8.7e-01	9.1e-01	3.8e-01	2.6e-01	4.0e-02	1.4e-01	8.71	0.08	0.48	0.26	3.8e-02	0.0e+00
FTSF-11	1.50e+04	32.47	1.3e+01	5.4e+06	6.8e-01	9.1e-01	8.7e-01	9.0e-01	3.8e-01	2.7e-01	4.6e-02	1.5e-01	9.82	0.09	0.52	0.21	3.6e-02	0.0e+00
FTNS-01	1.25e+03	3.46	9.9e-01	3.2e+04	1.4e+00	1.6e-01	4.4e-01	1.0e+00	8.8e-01	1.0e+00	3.5e-03	1.5e-02	2.07	0.29	0.39	0.16	7.3e-02	1.8e-02
FTNS-02	1.50e+03	4.16	2.8e+00	4.3e+04	1.8e+00	1.9e-01	5.3e-01	9.7e-01	8.2e-01	1.0e+00	4.1e-03	2.1e-02	2.89	0.32	0.55	0.18	5.3e-02	4.0e-03
FTNS-03	1.75e+03	4.85	2.9e+00	4.1e+04	1.8e+00	1.8e-01	5.0e-01	9.8e-01	8.2e-01	1.0e+00	4.1e-03	1.9e-02	2.64	0.41	0.27	0.38	6.8e-02	1.2e-02
FTNS-04	1.75e+03	4.85	2.2e+00	4.8e+04	1.4e+00	1.9e-01	4.3e-01	9.9e-01	8.4e-01	1.0e+00	4.4e-03	1.8e-02	2.48	0.43	0.25	0.41	7.5e-02	1.9e-02
FTNS-05	2.00e+03	5.54	2.6e+00	5.7e+04	1.6e+00	2.0e-01	4.9e-01	9.9e-01	8.3e-01	1.0e+00	4.8e-03	2.1e-02	2.72	0.48	0.26	0.39	6.0e-02	2.0e-02
FTNS-06	2.25e+03	6.23	3.7e+00	6.5e+04	1.8e+00	2.2e-01	5.5e-01	9.7e-01	8.2e-01	1.0e+00	5.1e-03	2.6e-02	3.05	0.46	0.21	0.42	7.0e-02	1.1e-02

Continued on next page

Table F.2 -- Continued from previous page

Model	$Ra$	$\frac{Ra}{Ra_C}$	$E_B$	$E_k$	$\frac{E_{B_P}}{E_{B_T}}$	$\frac{E_{N_Axi}^{B_P}}{E_{B_P}}$	$\frac{E_{N_Axi}^{B_T}}{E_{B_T}}$	$\frac{E_{N_Axi}^{k_P}}{E_{k_P}}$	$\frac{E_{N_Axi}^{k_T}}{E_{k_T}}$	$f_{Dip}$	$Ro$	$Ro_l$	$Nu$	$M_{LC}$	$M_\alpha$	$M_\omega$	$\delta_{T_{IC}}$	$\delta_{E_{IC}}$
FTNS-07	2.25e+03	6.23	2.9e+00	7.3e+04	1.8e+00	2.3e-01	5.6e-01	9.9e-01	8.4e-01	1.0e+00	5.4e-03	2.6e-02	3.04	0.43	0.31	0.31	6.3e-02	1.9e-02
FTNS-08	2.50e+03	6.93	3.7e+00	7.8e+04	1.9e+00	2.4e-01	6.1e-01	9.9e-01	8.5e-01	1.0e+00	5.6e-03	2.9e-02	3.22	0.45	0.23	0.40	6.3e-02	2.2e-02
FTNS-09	2.50e+03	6.93	3.3e+00	8.5e+04	1.6e+00	2.6e-01	5.9e-01	9.9e-01	8.5e-01	1.0e+00	5.8e-03	2.8e-02	3.27	0.47	0.30	0.35	6.2e-02	2.5e-02
FTNS-10	5.00e+03	13.85	5.9e+00	2.9e+05	1.3e+00	4.3e-01	6.6e-01	9.7e-01	7.7e-01	9.9e-01	1.1e-02	5.9e-02	5.18	0.32	0.45	0.25	5.6e-02	1.8e-02
FTNS-11	5.00e+03	13.85	7.3e+00	2.8e+05	1.5e+00	3.9e-01	6.7e-01	9.7e-01	7.9e-01	1.0e+00	1.1e-02	5.1e-02	5.22	0.42	0.41	0.26	5.4e-02	1.9e-02
FTNS-12	7.50e+03	20.78	9.6e+00	5.6e+05	1.3e+00	4.9e-01	7.3e-01	9.6e-01	7.8e-01	9.2e-01	1.5e-02	7.5e-02	6.94	0.33	0.51	0.21	4.6e-02	1.8e-02
FTNS-13	1.00e+04	27.70	5.7e+00	1.8e+06	7.7e-01	9.1e-01	8.9e-01	9.4e-01	4.9e-01	1.9e-01	2.7e-02	1.1e-01	8.45	-0.00	0.51	0.21	4.1e-02	1.6e-02
FTNS-14	1.25e+04	34.63	7.5e+00	2.6e+06	7.6e-01	9.2e-01	8.9e-01	9.2e-01	4.7e-01	1.5e-01	3.2e-02	1.4e-01	9.37	-0.02	0.38	0.26	3.9e-02	3.7e-02
FTNS-15	1.25e+04	34.63	7.5e+00	2.6e+06	7.5e-01	9.2e-01	8.9e-01	9.2e-01	4.6e-01	1.9e-01	3.2e-02	1.3e-01	9.33	0.02	0.50	0.20	3.8e-02	1.7e-02
FTNS-16	1.50e+04	41.55	9.8e+00	3.4e+06	7.5e-01	9.2e-01	8.9e-01	9.1e-01	4.4e-01	9.5e-02	3.7e-02	1.5e-01	10.21	-0.01	0.46	0.21	3.5e-02	1.6e-02

$E = 6.00e-05$ ,  $Ro_M = 2.00e-05$  and  $q_k = 1$

FFSF-08	3.50e+03	12.24	8.4e-01	5.6e+04	7.6e-01	3.0e-01	4.6e-01	9.9e-01	7.5e-01	9.9e-01	4.7e-03	1.4e-02	2.18	0.33	0.30	0.17	0.0e+00	0.0e+00
FFSF-09	5.00e+03	17.48	1.4e+00	7.1e+04	1.0e+00	3.0e-01	4.9e-01	9.9e-01	7.3e-01	1.0e+00	5.3e-03	1.8e-02	2.54	0.36	0.26	0.22	0.0e+00	0.0e+00
FFSF-10	5.00e+03	17.48	2.2e-01	1.2e+05	4.3e-01	7.8e-01	8.1e-01	9.9e-01	3.9e-01	3.7e-01	6.9e-03	1.7e-02	2.29	0.12	0.66	0.16	0.0e+00	0.0e+00
FFSF-11	6.00e+03	20.98	1.9e+00	8.4e+04	9.7e-01	3.3e-01	4.5e-01	9.8e-01	6.7e-01	9.7e-01	5.8e-03	1.9e-02	2.70	0.41	0.21	0.22	0.0e+00	0.0e+00
FFSF-12	6.00e+03	20.98	2.9e-01	1.8e+05	4.5e-01	5.6e-01	6.2e-01	9.8e-01	3.3e-01	2.9e-01	8.5e-03	1.9e-02	2.51	0.14	0.46	0.31	0.0e+00	0.0e+00
FFSF-13	7.50e+03	26.22	3.1e+00	1.1e+05	8.2e-01	3.6e-01	4.0e-01	9.8e-01	6.3e-01	9.4e-01	6.6e-03	2.2e-02	2.98	0.45	0.29	0.20	0.0e+00	0.0e+00
FFSF-14	7.50e+03	26.22	3.5e-01	2.2e+05	4.6e-01	7.4e-01	8.0e-01	9.8e-01	3.3e-01	2.9e-01	9.3e-03	2.3e-02	2.67	0.13	0.51	0.29	0.0e+00	0.0e+00
FFSF-15	1.00e+04	34.97	4.0e+00	1.4e+05	8.1e-01	4.1e-01	4.8e-01	9.8e-01	6.7e-01	9.4e-01	7.5e-03	2.6e-02	3.46	0.49	0.29	0.17	0.0e+00	0.0e+00
FFSF-16	1.00e+04	34.97	3.6e-01	3.2e+05	4.2e-01	8.7e-01	8.8e-01	9.5e-01	3.0e-01	2.2e-01	1.1e-02	2.8e-02	2.93	0.11	0.57	0.26	0.0e+00	0.0e+00
FFSF-17	1.25e+04	43.71	4.2e+00	1.9e+05	9.2e-01	4.2e-01	5.0e-01	9.7e-01	6.8e-01	9.6e-01	8.6e-03	3.3e-02	3.83	0.42	0.34	0.27	0.0e+00	0.0e+00
FFSF-18	1.50e+04	52.45	6.0e+00	2.1e+05	8.0e-01	4.5e-01	4.8e-01	9.7e-01	6.9e-01	9.0e-01	9.2e-03	3.3e-02	4.15	0.49	0.30	0.22	0.0e+00	0.0e+00
FFSF-19	1.50e+04	52.45	7.3e-01	5.4e+05	4.8e-01	7.3e-01	6.3e-01	9.3e-01	2.9e-01	4.1e-01	1.5e-02	3.8e-02	3.57	0.12	0.49	0.33	0.0e+00	0.0e+00
FFSF-20	2.00e+04	69.93	7.6e+00	2.6e+05	8.4e-01	4.8e-01	5.3e-01	9.7e-01	7.4e-01	8.7e-01	1.0e-02	4.0e-02	4.80	0.50	0.33	0.26	0.0e+00	0.0e+00
FFSF-21	2.50e+04	87.41	8.1e+00	3.2e+05	8.8e-01	5.0e-01	5.8e-01	9.7e-01	7.7e-01	8.4e-01	1.1e-02	4.6e-02	5.36	0.45	0.39	0.23	0.0e+00	0.0e+00
FFSF-22	3.00e+04	104.90	8.1e+00	3.9e+05	8.7e-01	5.4e-01	6.4e-01	9.7e-01	8.0e-01	8.1e-01	1.2e-02	5.2e-02	5.85	0.45	0.45	0.19	0.0e+00	0.0e+00
FFSF-23	3.50e+04	122.38	9.1e+00	4.2e+05	9.1e-01	5.4e-01	6.5e-01	9.7e-01	8.4e-01	7.9e-01	1.3e-02	5.6e-02	6.32	0.41	0.51	0.16	0.0e+00	0.0e+00
FFSF-24	5.00e+04	174.83	9.9e+00	6.6e+05	9.0e-01	5.8e-01	6.9e-01	9.6e-01	7.9e-01	8.3e-01	1.6e-02	7.2e-02	7.32	0.36	0.58	0.15	0.0e+00	0.0e+00
FFSF-25	7.50e+04	262.24	1.0e+01	1.0e+06	9.1e-01	6.4e-01	7.5e-01	9.6e-01	7.9e-01	8.0e-01	2.0e-02	9.0e-02	8.60	0.31	0.57	0.17	0.0e+00	0.0e+00
FFSF-26	7.50e+04	262.24	3.8e+00	2.6e+06	5.9e-01	8.9e-01	8.2e-01	9.2e-01	3.3e-01	3.9e-01	3.2e-02	9.1e-02	8.07	0.12	0.52	0.25	0.0e+00	0.0e+00
FFSF-27	8.00e+04	279.72	9.9e+00	1.1e+06	8.9e-01	6.6e-01	7.7e-01	9.6e-01	7.9e-01	7.8e-01	2.1e-02	9.4e-02	8.85	0.31	0.58	0.15	0.0e+00	0.0e+00
FFSF-28	9.50e+04	332.17	4.7e+00	3.1e+06	6.1e-01	9.1e-01	8.5e-01	9.2e-01	3.4e-01	2.5e-01	3.5e-02	1.0e-01	8.99	0.11	0.60	0.21	0.0e+00	0.0e+00
FFNS-07	3.00e+03	12.45	5.3e-01	3.3e+04	8.7e-01	2.7e-01	3.9e-01	9.7e-01	7.2e-01	9.8e-01	3.6e-03	1.0e-02	2.27	0.25	0.38	0.29	0.0e+00	2.4e-02

Continued on next page

Table F.2 -- Continued from previous page

Model	$Ra$	$\frac{Ra}{Ra_C}$	$E_B$	$E_k$	$\frac{E_{B_P}}{E_{B_T}}$	$\frac{E_{N_Axi}}{E_{B_P}}$	$\frac{E_{N_Axi}}{E_{B_T}}$	$\frac{E_{N_Axi}}{E_{k_P}}$	$\frac{E_{N_Axi}}{E_{k_P}}$	$\frac{f_{Dip}}{E_{k_T}}$	$f_{Dip}$	$Ro$	$Ro_l$	$Nu$	$M_{LC}$	$M_\alpha$	$M_\omega$	$\delta_{T_{IC}}$	$\delta_{E_{IC}}$
FFNS-08	3.50e+03	14.52	1.4e+00	3.5e+04	8.7e-01	2.8e-01	3.2e-01	9.7e-01	6.8e-01	9.8e-01	3.8e-03	1.0e-02	2.48	0.34	0.14	0.51	0.0e+00	2.4e-02	
FFNS-09	5.00e+03	20.75	2.2e+00	4.7e+04	7.6e-01	3.4e-01	3.6e-01	9.7e-01	6.9e-01	9.3e-01	4.3e-03	1.2e-02	2.89	0.47	0.19	0.42	0.0e+00	2.4e-02	
FFNS-10	6.00e+03	24.90	2.7e+00	5.4e+04	8.7e-01	3.4e-01	4.2e-01	9.7e-01	7.3e-01	9.4e-01	4.6e-03	1.4e-02	3.15	0.42	0.33	0.31	0.0e+00	2.6e-02	
FFNS-11	7.50e+03	31.12	3.4e+00	6.2e+04	8.1e-01	3.9e-01	4.3e-01	9.7e-01	7.8e-01	8.5e-01	5.0e-03	1.6e-02	3.52	0.46	0.28	0.38	0.0e+00	2.9e-02	
FFNS-12	1.00e+04	41.49	4.4e+00	8.2e+04	8.2e-01	4.1e-01	4.9e-01	9.7e-01	7.7e-01	8.7e-01	5.7e-03	1.8e-02	3.94	0.49	0.28	0.40	0.0e+00	2.4e-02	
FFNS-13	1.25e+04	51.87	4.8e+00	9.6e+04	9.7e-01	4.4e-01	5.8e-01	9.7e-01	8.2e-01	7.9e-01	6.2e-03	2.2e-02	4.38	0.45	0.42	0.27	0.0e+00	2.8e-02	
FFNS-14	1.50e+04	62.24	4.8e+00	1.2e+05	8.7e-01	4.6e-01	5.5e-01	9.7e-01	7.9e-01	7.9e-01	7.0e-03	2.4e-02	4.57	0.46	0.44	0.23	0.0e+00	3.0e-02	
FFNS-15	2.00e+04	82.99	4.5e+00	1.6e+05	1.0e+00	5.0e-01	6.6e-01	9.7e-01	8.3e-01	7.9e-01	8.1e-03	3.0e-02	5.21	0.42	0.52	0.17	0.0e+00	2.9e-02	
FFNS-16	2.50e+04	103.73	5.1e+00	2.1e+05	1.0e+00	5.4e-01	6.6e-01	9.7e-01	7.7e-01	7.7e-01	9.1e-03	3.5e-02	5.59	0.39	0.45	0.23	0.0e+00	2.6e-02	
FFNS-17	3.00e+04	124.48	5.3e+00	2.5e+05	9.6e-01	5.7e-01	6.4e-01	9.6e-01	7.3e-01	8.1e-01	1.0e-02	3.8e-02	5.93	0.36	0.52	0.21	0.0e+00	2.5e-02	
FFNS-18	3.50e+04	145.23	5.5e+00	2.8e+05	1.0e+00	5.9e-01	6.9e-01	9.7e-01	8.0e-01	7.9e-01	1.1e-02	4.2e-02	6.29	0.34	0.50	0.22	0.0e+00	2.6e-02	
FFNS-19	5.00e+04	207.47	5.9e+00	3.9e+05	1.0e+00	6.2e-01	7.5e-01	9.7e-01	8.4e-01	7.3e-01	1.2e-02	5.2e-02	7.15	0.29	0.60	0.14	0.0e+00	2.7e-02	
FFNS-20	7.50e+04	311.20	5.9e+00	6.0e+05	1.0e+00	6.9e-01	8.1e-01	9.6e-01	8.0e-01	6.9e-01	1.5e-02	6.6e-02	8.18	0.22	0.66	0.14	0.0e+00	2.5e-02	
FFNS-21	8.00e+04	331.95	3.9e+00	7.7e+05	8.6e-01	7.8e-01	8.3e-01	9.6e-01	7.0e-01	6.1e-01	1.8e-02	7.1e-02	8.38	0.11	0.69	0.11	0.0e+00	2.4e-02	
FFNS-22	9.50e+04	394.19	4.6e+00	8.4e+05	9.6e-01	7.7e-01	8.7e-01	9.6e-01	7.8e-01	5.9e-01	1.8e-02	7.8e-02	8.86	0.13	0.69	0.11	0.0e+00	2.7e-02	
FTSF-12	1.50e+03	4.35	1.0e+00	4.0e+04	1.4e+00	2.0e-01	5.1e-01	1.0e+00	8.9e-01	1.0e+00	4.0e-03	1.6e-02	2.32	0.36	0.35	0.09	7.0e-02	0.0e+00	
FTSF-13	2.00e+03	5.80	1.6e+00	6.3e+04	1.4e+00	2.5e-01	5.3e-01	9.9e-01	8.6e-01	1.0e+00	5.0e-03	2.2e-02	2.74	0.34	0.25	0.26	6.3e-02	0.0e+00	
FTSF-14	2.50e+03	7.25	6.4e-01	2.1e+05	6.3e-01	6.4e-01	6.9e-01	9.9e-01	4.4e-01	6.7e-01	9.2e-03	2.5e-02	3.11	0.19	0.34	0.41	6.6e-02	0.0e+00	
FTSF-15	5.00e+03	14.49	4.6e+00	3.1e+05	1.3e+00	4.5e-01	7.1e-01	9.8e-01	8.3e-01	1.0e+00	1.1e-02	5.5e-02	5.06	0.36	0.41	0.27	5.3e-02	0.0e+00	
FTSF-16	7.50e+03	21.74	7.0e+00	6.2e+05	1.2e+00	5.4e-01	7.8e-01	9.7e-01	8.1e-01	9.6e-01	1.6e-02	7.8e-02	6.70	0.32	0.54	0.20	4.7e-02	0.0e+00	
FTSF-17	1.00e+04	28.99	3.8e+00	1.6e+06	8.3e-01	9.1e-01	9.1e-01	9.7e-01	5.4e-01	3.0e-01	2.5e-02	9.6e-02	8.00	0.11	0.57	0.21	4.4e-02	0.0e+00	
FTSF-18	1.25e+04	36.23	5.6e+00	2.2e+06	8.4e-01	9.3e-01	9.2e-01	9.6e-01	5.3e-01	2.3e-01	3.0e-02	1.1e-01	9.11	0.13	0.56	0.22	4.0e-02	0.0e+00	
FTSF-19	1.50e+04	43.48	7.6e+00	2.9e+06	8.3e-01	9.3e-01	9.2e-01	9.5e-01	5.3e-01	1.7e-01	3.4e-02	1.3e-01	10.09	0.12	0.58	0.21	3.8e-02	0.0e+00	
FTSF-20	2.00e+04	57.97	1.2e+01	4.8e+06	8.1e-01	9.4e-01	9.1e-01	9.3e-01	4.9e-01	1.6e-01	4.4e-02	1.5e-01	11.74	0.09	0.60	0.19	3.2e-02	0.0e+00	
FTSF-21	2.50e+04	72.46	1.6e+01	6.8e+06	7.9e-01	9.4e-01	9.1e-01	9.2e-01	4.7e-01	1.4e-01	5.2e-02	1.8e-01	13.16	0.10	0.58	0.19	3.1e-02	0.0e+00	
FTNS-17	1.00e+03	3.61	4.1e-01	1.6e+04	2.0e+00	1.2e-01	4.4e-01	1.0e+00	8.9e-01	1.0e+00	2.5e-03	9.2e-03	1.96	0.25	0.46	0.11	7.4e-02	2.6e-02	
FTNS-18	1.50e+03	5.42	3.5e+00	2.2e+04	1.7e+00	1.2e-01	3.2e-01	9.7e-01	7.5e-01	1.0e+00	3.0e-03	9.5e-03	2.45	0.48	0.15	0.52	7.7e-02	3.1e-02	
FTNS-19	2.00e+03	7.22	4.5e+00	3.5e+04	1.8e+00	1.9e-01	4.7e-01	9.7e-01	7.9e-01	1.0e+00	3.7e-03	1.3e-02	2.93	0.50	0.20	0.52	7.5e-02	3.2e-02	
FTNS-20	2.50e+03	9.03	4.6e+00	5.6e+04	1.7e+00	2.4e-01	5.5e-01	9.7e-01	8.1e-01	1.0e+00	4.7e-03	1.8e-02	3.38	0.50	0.27	0.42	7.4e-02	3.0e-02	
FTNS-21	3.00e+03	10.83	4.2e+00	8.0e+04	1.5e+00	3.0e-01	5.7e-01	9.7e-01	7.6e-01	1.0e+00	5.6e-03	2.2e-02	3.66	0.46	0.33	0.36	6.2e-02	3.1e-02	
FTNS-22	3.00e+03	10.83	5.4e+00	7.2e+04	1.4e+00	2.9e-01	5.3e-01	9.7e-01	7.8e-01	1.0e+00	5.4e-03	2.0e-02	3.61	0.48	0.33	0.35	6.6e-02	3.0e-02	
FTNS-23	3.50e+03	12.64	4.8e+00	1.1e+05	1.5e+00	3.3e-01	6.0e-01	9.6e-01	7.4e-01	9.9e-01	6.5e-03	2.5e-02	4.05	0.44	0.31	0.38	6.1e-02	1.2e-02	
FTNS-24	5.00e+03	18.05	6.6e+00	1.7e+05	1.3e+00	4.3e-01	6.8e-01	9.7e-01	8.2e-01	9.1e-01	8.3e-03	3.4e-02	5.05	0.47	0.39	0.32	5.8e-02	2.9e-02	
FTNS-25	6.00e+03	21.66	6.1e+00	2.6e+05	1.3e+00	4.8e-01	7.0e-01	9.7e-01	7.6e-01	8.8e-01	1.0e-02	4.2e-02	5.59	0.42	0.52	0.24	5.7e-02	2.8e-02	
FTNS-26	7.50e+03	27.08	5.6e+00	3.9e+05	1.2e+00	5.6e-01	7.6e-01	9.6e-01	7.4e-01	8.5e-01	1.2e-02	5.3e-02	6.36	0.33	0.57	0.19	4.8e-02	2.7e-02	

Continued on next page

Table F.2 -- Continued from previous page

Model	$Ra$	$\frac{Ra}{Ra_C}$	$E_B$	$E_k$	$\frac{E_{B_P}}{E_{B_T}}$	$\frac{E_{N_Axi}^P}{E_{B_P}}$	$\frac{E_{N_Axi}^T}{E_{B_T}}$	$\frac{E_{kP}^{N_Axi}}{E_{kP}}$	$\frac{E_{kT}^{N_Axi}}{E_{kT}}$	$f_{Dip}$	$Ro$	$Ro_l$	$Nu$	$M_{LC}$	$M_\alpha$	$M_\omega$	$\delta_{T_{IC}}$	$\delta_{E_{IC}}$
FTNS-27	1.00e+04	36.10	5.5e+00	6.3e+05	1.1e+00	6.5e-01	8.1e-01	9.6e-01	7.6e-01	7.6e-01	1.6e-02	6.9e-02	7.47	0.21	0.63	0.15	4.5e-02	2.6e-02
FTNS-28	1.25e+04	45.13	2.9e+00	1.1e+06	9.3e-01	9.1e-01	9.2e-01	9.6e-01	6.4e-01	2.1e-01	2.1e-02	9.1e-02	8.55	-0.08	0.63	0.17	3.9e-02	2.9e-02
FTNS-29	1.50e+04	54.15	4.2e+00	1.4e+06	9.4e-01	9.2e-01	9.2e-01	9.6e-01	6.5e-01	1.1e-01	2.4e-02	9.9e-02	9.16	-0.04	0.64	0.15	3.9e-02	2.9e-02
FTNS-30	1.50e+04	54.15	4.2e+00	1.4e+06	9.3e-01	9.2e-01	9.3e-01	9.6e-01	6.5e-01	1.5e-01	2.4e-02	1.0e-01	9.21	-0.04	0.60	0.18	3.7e-02	2.9e-02
FTNS-31	2.00e+04	72.20	6.9e+00	2.0e+06	9.3e-01	9.2e-01	9.2e-01	9.5e-01	6.4e-01	1.1e-01	2.8e-02	1.2e-01	10.21	-0.04	0.60	0.17	3.3e-02	2.9e-02
FTNS-32	2.50e+04	90.25	1.0e+01	2.4e+06	9.2e-01	9.2e-01	9.2e-01	9.5e-01	6.5e-01	1.4e-01	3.1e-02	1.3e-01	11.04	0.02	0.66	0.12	3.4e-02	3.0e-02
FTNS-33	3.00e+04	108.30	1.3e+01	3.3e+06	9.1e-01	9.3e-01	9.2e-01	9.4e-01	6.0e-01	9.9e-02	3.6e-02	1.4e-01	11.75	0.02	0.67	0.12	3.2e-02	3.3e-02
FTNS-34	3.50e+04	126.35	1.6e+01	3.9e+06	9.2e-01	9.3e-01	9.2e-01	9.4e-01	6.0e-01	1.2e-01	3.9e-02	1.5e-01	12.30	0.01	0.62	0.15	3.0e-02	3.3e-02
FTNS-35	4.00e+04	144.40	1.9e+01	4.5e+06	9.2e-01	9.3e-01	9.1e-01	9.4e-01	5.9e-01	1.0e-01	4.2e-02	1.6e-01	12.84	0.04	0.68	0.10	2.8e-02	3.4e-02
FTNS-36	5.00e+04	180.51	2.6e+01	5.9e+06	9.3e-01	9.3e-01	9.1e-01	9.3e-01	5.7e-01	1.2e-01	4.9e-02	1.8e-01	13.77	0.04	0.69	0.09	2.9e-02	4.2e-02

$E = 2.00e-04$ ,  $Ro_M = 1.00e-04$  and  $q_k = 1$

FFSF-29	7.50e+03	31.91	6.1e-01	2.6e+05	3.1e-01	6.3e-01	5.1e-01	9.3e-01	2.0e-01	2.6e-01	5.0e-02	6.9e-02	3.09	0.09	0.24	0.46	0.0e+00	0.0e+00
FFSF-30	1.00e+04	42.55	6.1e-01	3.2e+05	3.3e-01	6.2e-01	5.3e-01	8.9e-01	1.9e-01	3.0e-01	5.7e-02	8.5e-02	3.45	0.06	0.40	0.39	0.0e+00	0.0e+00
FFSF-31	1.25e+04	53.19	6.9e-01	7.3e+05	2.9e-01	7.6e-01	4.7e-01	8.4e-01	1.2e-01	3.6e-01	8.4e-02	1.1e-01	3.63	0.09	0.42	0.40	0.0e+00	0.0e+00
FFSF-32	1.50e+04	63.83	1.3e+00	5.6e+05	3.4e-01	7.4e-01	6.0e-01	8.7e-01	1.7e-01	2.5e-01	7.5e-02	1.1e-01	4.20	0.09	0.31	0.47	0.0e+00	0.0e+00
FFSF-33	2.00e+04	85.11	2.4e+00	1.7e+06	1.6e-01	8.2e-01	3.6e-01	7.3e-01	9.4e-02	2.4e-01	1.3e-01	1.6e-01	4.59	0.02	0.36	0.47	0.0e+00	0.0e+00
FFSF-34	3.00e+04	127.66	3.7e+00	1.6e+06	2.8e-01	8.2e-01	5.4e-01	7.6e-01	1.4e-01	4.3e-01	1.3e-01	1.9e-01	5.73	0.07	0.29	0.46	0.0e+00	0.0e+00
FFSF-35	4.00e+04	170.21	6.0e+00	2.5e+06	3.0e-01	8.1e-01	5.8e-01	6.9e-01	1.2e-01	6.1e-01	1.6e-01	2.4e-01	6.59	0.09	0.37	0.38	0.0e+00	0.0e+00
FFSF-36	5.00e+04	212.77	6.8e+00	3.3e+06	2.6e-01	8.6e-01	5.1e-01	6.4e-01	1.1e-01	2.2e-01	1.8e-01	2.7e-01	7.25	0.04	0.29	0.48	0.0e+00	0.0e+00
FFSF-37	6.00e+04	255.32	8.1e+00	3.4e+06	2.9e-01	8.6e-01	5.5e-01	6.8e-01	1.2e-01	2.2e-01	1.8e-01	2.8e-01	7.78	0.04	0.39	0.40	0.0e+00	0.0e+00
FFSF-38	7.00e+04	297.87	7.6e+00	5.2e+06	3.1e-01	8.7e-01	6.3e-01	6.1e-01	9.2e-02	2.4e-01	2.3e-01	3.2e-01	8.19	0.02	0.33	0.43	0.0e+00	0.0e+00
FFNS-23	5.00e+04	241.55	7.4e-01	3.4e+05	6.9e-01	8.1e-01	7.9e-01	8.9e-01	5.9e-01	4.9e-01	5.9e-02	1.6e-01	6.13	-0.02	0.48	0.30	0.0e+00	4.4e-02
FFNS-24	6.00e+04	289.86	3.9e-01	4.5e+05	7.1e-01	8.6e-01	8.4e-01	8.8e-01	5.5e-01	4.1e-01	6.7e-02	1.8e-01	6.43	-0.01	0.54	0.25	0.0e+00	4.4e-02
FFNS-25	7.00e+04	338.16	3.0e+00	5.2e+05	8.1e-01	8.9e-01	8.6e-01	9.0e-01	4.7e-01	1.7e-01	7.2e-02	1.8e-01	6.66	-0.02	0.65	0.15	0.0e+00	4.8e-02
FFNS-26	1.00e+05	483.09	2.5e+00	8.0e+05	7.8e-01	8.9e-01	8.4e-01	8.8e-01	4.9e-01	2.5e-01	8.9e-02	2.2e-01	7.25	-0.01	0.54	0.22	0.0e+00	4.4e-02
FFNS-27	1.50e+05	724.64	7.2e+00	1.3e+06	7.9e-01	9.2e-01	8.6e-01	8.6e-01	3.8e-01	1.6e-01	1.1e-01	2.4e-01	7.94	-0.02	0.55	0.20	0.0e+00	4.4e-02
FTSF-22	2.50e+03	9.19	3.9e+00	5.5e+04	1.4e+00	2.5e-01	5.0e-01	9.6e-01	7.6e-01	1.0e+00	2.3e-02	7.3e-02	3.24	0.32	0.21	0.47	7.2e-02	0.0e+00
FTSF-23	2.50e+03	9.19	6.6e-01	2.2e+05	4.5e-01	6.5e-01	5.8e-01	9.5e-01	1.8e-01	2.0e-01	4.7e-02	6.1e-02	2.85	0.01	0.22	0.56	7.0e-02	0.0e+00
FTSF-24	3.00e+03	11.03	1.3e+00	3.1e+05	4.6e-01	7.3e-01	6.4e-01	9.5e-01	1.9e-01	1.7e-01	5.5e-02	7.3e-02	3.42	0.09	0.29	0.49	6.7e-02	0.0e+00
FTSF-25	5.00e+03	18.38	2.6e+00	8.4e+05	4.2e-01	8.1e-01	7.2e-01	8.9e-01	1.5e-01	2.3e-01	9.1e-02	1.2e-01	4.65	0.03	0.35	0.43	6.1e-02	0.0e+00
FTSF-26	7.50e+03	27.57	5.5e+00	1.6e+06	4.2e-01	8.3e-01	7.0e-01	8.4e-01	1.5e-01	2.0e-01	1.3e-01	1.6e-01	5.91	0.03	0.37	0.42	5.1e-02	0.0e+00
FTSF-27	1.00e+04	36.76	6.3e+00	2.4e+06	4.3e-01	8.7e-01	7.3e-01	6.9e-01	1.4e-01	1.7e-01	1.6e-01	2.3e-01	7.02	0.02	0.32	0.45	4.7e-02	0.0e+00
FTSF-28	1.25e+04	45.96	6.0e+00	2.1e+06	6.7e-01	9.2e-01	8.6e-01	8.1e-01	2.6e-01	1.6e-01	3.1e-01	7.44	0.03	0.42	0.32	4.6e-02	0.0e+00	

Continued on next page

Table F.2 -- Continued from previous page

Model	$Ra$	$\frac{Ra}{Ra_C}$	$E_B$	$E_k$	$\frac{E_{B_P}}{E_{B_T}}$	$\frac{E_{N_Axi}^P}{E_{B_P}}$	$\frac{E_{N_Axi}^T}{E_{B_T}}$	$\frac{E_{kP}^{N_Axi}}{E_{kP}}$	$\frac{E_{kT}^{N_Axi}}{E_{kT}}$	$f_{Dip}$	$Ro$	$Ro_l$	$Nu$	$M_{LC}$	$M_\alpha$	$M_\omega$	$\delta_{T_{IC}}$	$\delta_{E_{IC}}$
FTSF-29	1.50e+04	55.15	8.5e+00	3.4e+06	5.6e-01	9.1e-01	8.1e-01	6.9e-01	1.8e-01	1.8e-01	1.8e-01	3.4e-01	8.20	0.01	0.30	0.44	3.9e-02	0.0e+00
FTSF-30	2.00e+04	73.53	1.4e+01	4.5e+06	6.2e-01	9.2e-01	8.4e-01	6.9e-01	2.1e-01	1.7e-01	2.1e-01	4.3e-01	9.37	0.02	0.40	0.33	3.7e-02	0.0e+00
FTNS-37	2.50e+03	10.73	9.9e-01	4.5e+04	1.1e+00	3.3e-01	4.7e-01	9.5e-01	6.7e-01	9.6e-01	2.1e-02	5.8e-02	3.15	0.04	0.34	0.46	7.8e-02	4.4e-02
FTNS-38	2.50e+03	10.73	1.3e+00	4.6e+04	1.1e+00	3.2e-01	4.6e-01	9.5e-01	6.6e-01	9.6e-01	2.1e-02	5.7e-02	3.21	0.04	0.27	0.48	7.3e-02	4.5e-02
FTNS-39	3.00e+03	12.88	1.4e+00	6.2e+04	1.1e+00	3.7e-01	5.1e-01	9.4e-01	6.2e-01	9.6e-01	2.5e-02	6.6e-02	3.48	0.06	0.27	0.43	7.2e-02	4.0e-02
FTNS-40	5.00e+03	21.46	2.8e-01	1.7e+05	6.7e-01	8.0e-01	5.5e-01	9.0e-01	5.0e-01	1.5e-01	4.1e-02	1.1e-01	4.33	-0.01	0.57	0.23	6.5e-02	4.0e-02
FTNS-41	5.00e+03	21.46	2.9e-01	1.7e+05	6.8e-01	7.5e-01	5.1e-01	9.0e-01	4.8e-01	2.4e-01	4.1e-02	1.1e-01	4.33	-0.01	0.53	0.25	7.2e-02	3.8e-02
FTNS-42	7.50e+03	32.19	8.8e-01	3.0e+05	8.4e-01	7.6e-01	6.1e-01	8.7e-01	4.4e-01	1.3e-01	5.4e-02	1.4e-01	5.06	-0.01	0.55	0.24	5.7e-02	4.0e-02
FTNS-43	7.50e+03	32.19	7.0e-01	3.0e+05	8.4e-01	7.8e-01	6.8e-01	8.7e-01	4.4e-01	1.4e-01	5.5e-02	1.4e-01	5.15	-0.01	0.55	0.23	5.5e-02	4.3e-02
FTNS-44	1.00e+04	42.92	1.1e+00	4.3e+05	8.9e-01	8.6e-01	8.1e-01	8.8e-01	4.7e-01	1.1e-01	6.5e-02	1.8e-01	5.91	-0.03	0.54	0.23	5.0e-02	4.6e-02
FTNS-45	1.00e+04	42.92	1.2e+00	4.3e+05	8.7e-01	8.8e-01	8.5e-01	8.8e-01	4.7e-01	1.6e-01	6.5e-02	1.8e-01	5.88	-0.04	0.52	0.27	5.2e-02	4.6e-02
FTNS-46	1.25e+04	53.65	2.6e+00	5.4e+05	8.8e-01	9.2e-01	8.9e-01	8.9e-01	4.5e-01	1.5e-01	7.3e-02	2.0e-01	6.36	-0.04	0.56	0.21	4.9e-02	5.7e-02
FTNS-47	1.25e+04	53.65	1.7e+00	5.9e+05	8.4e-01	9.0e-01	8.8e-01	8.6e-01	4.4e-01	9.8e-02	7.7e-02	2.1e-01	6.39	-0.02	0.53	0.21	4.7e-02	5.5e-02
FTNS-48	1.50e+04	64.38	3.8e+00	6.8e+05	8.8e-01	9.3e-01	8.9e-01	8.9e-01	4.4e-01	1.6e-01	8.3e-02	2.2e-01	6.81	-0.02	0.57	0.21	4.6e-02	5.6e-02
FTNS-49	1.50e+04	64.38	4.3e+00	6.8e+05	8.8e-01	9.2e-01	8.9e-01	8.8e-01	4.5e-01	1.6e-01	8.2e-02	2.2e-01	6.76	-0.04	0.57	0.21	4.5e-02	5.4e-02
FTNS-50	1.50e+04	64.38	4.2e+00	7.6e+05	8.4e-01	9.2e-01	8.8e-01	8.7e-01	4.0e-01	1.3e-01	8.7e-02	2.2e-01	6.73	-0.05	0.50	0.25	4.5e-02	7.2e-02
FTNS-51	2.00e+04	85.84	7.2e+00	1.0e+06	8.5e-01	9.2e-01	8.9e-01	8.7e-01	4.1e-01	1.2e-01	1.0e-01	2.5e-01	7.42	-0.06	0.52	0.22	4.4e-02	1.0e-01
FTNS-52	3.00e+04	128.76	1.6e+01	1.8e+06	8.3e-01	9.3e-01	8.7e-01	8.5e-01	3.4e-01	1.5e-01	1.4e-01	3.1e-01	8.37	-0.02	0.58	0.17	3.9e-02	6.2e-02
FTNS-53	4.00e+04	171.67	2.4e+01	3.1e+06	7.8e-01	9.3e-01	8.6e-01	8.3e-01	2.8e-01	1.4e-01	1.8e-01	3.6e-01	9.14	-0.02	0.55	0.16	3.6e-02	9.2e-02
FTNS-54	5.00e+04	214.59	2.9e+01	4.3e+06	7.7e-01	9.3e-01	8.4e-01	8.0e-01	2.6e-01	1.2e-01	2.1e-01	4.2e-01	9.83	-0.03	0.53	0.17	3.4e-02	1.1e-01

**Table F.3: Results of Convection Models.** The boundary conditions are applied at both the inner and outer core boundaries. For definition of the symbols please refer to the nomenclature.

Model	Ra	$\frac{Ra}{Ra_C}$	$E_k$	$\frac{E_{kP}^{N\Delta xi}}{E_{kT}^{N\Delta xi}}$	$\frac{E_{kT}^{N\Delta xi}}{E_{kP}^{N\Delta xi}}$	$Ro$	$Ro_l$	$Nu$	$\delta_{T_{IC}}$	$\delta_{E_{IC}}$	$\delta_{T_{OC}}$	$\delta_{E_{OC}}$
$E = 2.00e-05$ , $Ro_M = 2.00e-05$ and $q_k = 1$												
FFSF <sub>C</sub> -01	2.50e+03	6.98	3.4e+05	1.0e+00	4.1e-02	1.2e-02	1.1e-02	1.36	6.6e-02	0.0e+00	4.2e-03	0.0e+00
FFSF <sub>C</sub> -02	5.00e+03	13.97	2.0e+06	9.4e-01	2.0e-02	2.8e-02	2.3e-02	1.73	7.6e-02	0.0e+00	1.5e-03	0.0e+00
FFSF <sub>C</sub> -03	7.50e+03	20.95	4.4e+06	8.2e-01	1.3e-02	4.2e-02	3.4e-02	2.02	6.7e-02	0.0e+00	5.4e-03	0.0e+00
FFSF <sub>C</sub> -04	1.00e+04	27.93	7.6e+06	7.8e-01	1.2e-02	5.5e-02	4.6e-02	2.31	6.2e-02	0.0e+00	7.4e-04	0.0e+00
FFSF <sub>C</sub> -05	1.25e+04	34.92	1.4e+07	7.1e-01	8.3e-03	7.4e-02	6.1e-02	2.60	6.2e-02	0.0e+00	0.0e+00	0.0e+00
FFSF <sub>C</sub> -06	1.50e+04	41.90	2.1e+07	6.6e-01	7.2e-03	9.1e-02	7.6e-02	2.89	5.9e-02	0.0e+00	2.4e-04	0.0e+00
FFNS <sub>C</sub> -01	2.50e+03	9.03	4.4e+04	9.9e-01	5.6e-01	4.2e-03	1.7e-02	1.75	9.4e-02	1.4e-01	0.0e+00	5.5e-01
FFNS <sub>C</sub> -02	5.00e+03	18.05	1.3e+05	9.8e-01	5.4e-01	7.1e-03	2.7e-02	2.40	7.5e-02	1.8e-02	0.0e+00	5.5e-01
FFNS <sub>C</sub> -03	7.50e+03	27.08	2.2e+05	9.5e-01	4.2e-01	9.5e-03	3.5e-02	2.79	6.0e-02	1.3e-02	0.0e+00	5.5e-01
FFNS <sub>C</sub> -04	1.00e+04	36.10	3.3e+05	9.4e-01	3.4e-01	1.2e-02	4.0e-02	3.13	5.6e-02	1.3e-02	0.0e+00	5.5e-01
FFNS <sub>C</sub> -05	1.25e+04	45.13	5.1e+05	9.2e-01	2.7e-01	1.4e-02	4.4e-02	3.39	5.3e-02	1.3e-02	0.0e+00	5.5e-01
FFNS <sub>C</sub> -06	1.50e+04	54.15	7.0e+05	9.2e-01	2.3e-01	1.7e-02	4.8e-02	3.69	5.1e-02	1.3e-02	0.0e+00	5.5e-01
FTSF <sub>C</sub> -01	2.50e+03	5.41	1.1e+06	9.9e-01	2.3e-02	2.1e-02	1.7e-02	1.54	3.8e-02	0.0e+00	0.0e+00	0.0e+00
FTSF <sub>C</sub> -02	5.00e+03	10.82	8.8e+06	6.9e-01	1.0e-02	5.9e-02	4.9e-02	2.45	4.6e-02	0.0e+00	1.8e-01	0.0e+00
FTSF <sub>C</sub> -03	7.50e+03	16.23	2.1e+07	1.6e-01	1.2e-02	9.1e-02	1.3e-01	6.50	3.3e-02	0.0e+00	1.5e-01	0.0e+00
FTSF <sub>C</sub> -04	1.00e+04	21.65	3.5e+07	1.5e-01	1.1e-02	1.2e-01	1.7e-01	7.73	3.3e-02	0.0e+00	1.4e-01	0.0e+00
FTSF <sub>C</sub> -05	1.25e+04	27.06	5.2e+07	1.1e-01	9.6e-03	1.4e-01	2.3e-01	9.62	2.9e-02	0.0e+00	1.2e-01	0.0e+00
FTSF <sub>C</sub> -06	1.50e+04	32.47	7.6e+07	1.0e-01	8.9e-03	1.7e-01	2.6e-01	10.54	2.6e-02	0.0e+00	1.2e-01	0.0e+00
FTNS <sub>C</sub> -01	2.50e+03	6.93	1.7e+05	9.7e-01	4.8e-01	8.3e-03	3.9e-02	2.90	6.0e-02	5.6e-02	1.5e-01	5.6e-01
FTNS <sub>C</sub> -02	5.00e+03	13.85	7.7e+05	8.9e-01	2.8e-01	1.8e-02	6.6e-02	4.08	4.9e-02	1.3e-02	1.3e-01	5.5e-01
FTNS <sub>C</sub> -03	7.50e+03	20.78	2.0e+06	8.3e-01	2.3e-01	2.8e-02	1.0e-01	5.62	3.9e-02	1.3e-02	9.9e-02	5.5e-01
FTNS <sub>C</sub> -04	1.00e+04	27.70	4.1e+06	7.9e-01	1.7e-01	4.1e-02	1.4e-01	7.13	3.1e-02	1.3e-02	8.4e-02	5.5e-01
FTNS <sub>C</sub> -05	1.25e+04	34.63	7.5e+06	7.1e-01	1.4e-01	5.5e-02	1.8e-01	8.75	2.8e-02	1.6e-02	7.6e-02	5.5e-01
FTNS <sub>C</sub> -06	1.50e+04	41.55	1.2e+07	6.5e-01	1.1e-01	6.9e-02	2.2e-01	9.54	2.9e-02	1.8e-02	7.1e-02	5.5e-01
$E = 6.00e-05$ , $Ro_M = 2.00e-05$ and $q_k = 1$												
FFSF <sub>C</sub> -07	2.50e+03	8.74	8.0e+04	1.0e+00	2.7e-01	5.6e-03	1.0e-02	1.74	9.5e-02	0.0e+00	0.0e+00	0.0e+00
FFSF <sub>C</sub> -08	5.00e+03	17.48	3.0e+05	9.8e-01	1.6e-01	1.1e-02	1.5e-02	2.23	8.6e-02	0.0e+00	1.5e-03	0.0e+00
FFSF <sub>C</sub> -09	7.50e+03	26.22	5.7e+05	9.6e-01	1.3e-01	1.5e-02	2.1e-02	2.59	8.2e-02	0.0e+00	0.0e+00	0.0e+00
FFSF <sub>C</sub> -10	1.00e+04	34.97	7.1e+05	9.0e-01	1.2e-01	1.7e-02	2.7e-02	2.86	7.4e-02	0.0e+00	0.0e+00	0.0e+00
FFSF <sub>C</sub> -11	1.25e+04	43.71	1.1e+06	9.3e-01	1.0e-01	2.1e-02	2.8e-02	3.34	8.0e-02	0.0e+00	0.0e+00	0.0e+00
FFSF <sub>C</sub> -12	1.50e+04	52.45	1.4e+06	9.0e-01	1.0e-01	2.4e-02	3.5e-02	3.42	6.7e-02	0.0e+00	0.0e+00	0.0e+00
FFSF <sub>C</sub> -13	2.00e+04	69.93	2.6e+06	8.9e-01	8.0e-02	3.2e-02	4.3e-02	3.96	6.4e-02	0.0e+00	0.0e+00	0.0e+00
FFSF <sub>C</sub> -14	2.50e+04	87.41	4.9e+06	9.0e-01	5.9e-02	4.4e-02	5.5e-02	4.37	5.9e-02	0.0e+00	0.0e+00	0.0e+00
FFSF <sub>C</sub> -15	3.00e+04	104.90	1.1e+07	7.8e-01	3.4e-02	6.5e-02	7.5e-02	4.49	5.5e-02	0.0e+00	0.0e+00	0.0e+00
FFSF <sub>C</sub> -16	3.50e+04	122.38	1.5e+07	7.5e-01	2.9e-02	7.6e-02	8.6e-02	4.83	5.3e-02	0.0e+00	0.0e+00	0.0e+00
FFSF <sub>C</sub> -17	5.00e+04	174.83	3.2e+07	6.7e-01	2.0e-02	1.1e-01	1.2e-01	5.61	4.5e-02	0.0e+00	0.0e+00	0.0e+00
FFSF <sub>C</sub> -18	7.50e+04	262.24	7.1e+07	5.2e-01	1.3e-02	1.7e-01	1.7e-01	7.03	3.7e-02	0.0e+00	7.4e-03	0.0e+00
FFSF <sub>C</sub> -19	8.00e+04	279.72	8.1e+07	4.9e-01	1.3e-02	1.8e-01	1.9e-01	7.33	3.6e-02	0.0e+00	2.9e-03	0.0e+00
FFSF <sub>C</sub> -20	9.50e+04	332.17	1.1e+08	4.5e-01	1.1e-02	2.1e-01	2.1e-01	8.11	3.3e-02	0.0e+00	6.1e-03	0.0e+00
FFNS <sub>C</sub> -07	2.50e+03	10.37	2.8e+04	9.9e-01	7.4e-01	3.4e-03	9.8e-03	2.03	1.0e-01	3.0e-02	0.0e+00	5.7e-01
FFNS <sub>C</sub> -08	5.00e+03	20.75	7.2e+04	9.6e-01	6.1e-01	5.4e-03	1.6e-02	2.75	8.2e-02	2.4e-02	0.0e+00	5.7e-01
FFNS <sub>C</sub> -09	7.50e+03	31.12	1.3e+05	9.3e-01	5.0e-01	7.1e-03	2.0e-02	3.22	6.9e-02	2.2e-02	0.0e+00	5.7e-01
FFNS <sub>C</sub> -10	1.00e+04	41.49	2.0e+05	9.4e-01	3.8e-01	8.9e-03	2.3e-02	3.58	6.3e-02	2.1e-02	0.0e+00	5.7e-01
FFNS <sub>C</sub> -11	1.25e+04	51.87	2.7e+05	9.4e-01	3.5e-01	1.0e-02	2.6e-02	3.90	5.8e-02	1.9e-02	0.0e+00	5.7e-01

*Continued on next page*

Table F.3 -- Continued from previous page

Model	$Ra$	$\frac{Ra}{Ra_C}$	$E_k$	$\frac{E_{kP}^{N_Axi}}{E_{kP}}$	$\frac{E_{kT}^{N_Axi}}{E_{kT}}$	$Ro$	$Ro_l$	$Nu$	$\delta_{T_{IC}}$	$\delta_{E_{IC}}$	$\delta_{T_{OC}}$	$\delta_{E_{OC}}$
FFNS <sub>C</sub> -12	1.50e+04	62.24	3.4e+05	9.4e-01	3.2e-01	1.2e-02	2.8e-02	4.19	5.3e-02	1.8e-02	6.1e-05	5.7e-01
FFNS <sub>C</sub> -13	2.00e+04	82.99	4.4e+05	9.4e-01	3.3e-01	1.3e-02	3.3e-02	4.82	5.3e-02	1.9e-02	0.0e+00	5.7e-01
FFNS <sub>C</sub> -14	2.50e+04	103.73	5.9e+05	9.4e-01	3.1e-01	1.5e-02	3.7e-02	5.20	5.0e-02	1.9e-02	0.0e+00	5.7e-01
FFNS <sub>C</sub> -15	3.00e+04	124.48	7.5e+05	9.4e-01	2.9e-01	1.7e-02	4.1e-02	5.58	4.8e-02	1.8e-02	0.0e+00	5.7e-01
FFNS <sub>C</sub> -16	3.50e+04	145.23	8.6e+05	9.4e-01	3.0e-01	1.8e-02	4.4e-02	5.96	4.6e-02	1.9e-02	0.0e+00	5.7e-01
FFNS <sub>C</sub> -17	5.00e+04	207.47	1.3e+06	9.4e-01	2.7e-01	2.3e-02	5.4e-02	6.75	4.2e-02	1.9e-02	0.0e+00	5.7e-01
FFNS <sub>C</sub> -18	7.50e+04	311.20	1.7e+06	9.3e-01	3.2e-01	2.6e-02	7.1e-02	7.87	3.9e-02	2.2e-02	0.0e+00	5.7e-01
FFNS <sub>C</sub> -19	8.00e+04	331.95	1.9e+06	9.3e-01	3.1e-01	2.7e-02	7.2e-02	8.01	3.9e-02	1.9e-02	0.0e+00	5.7e-01
FFNS <sub>C</sub> -20	9.50e+04	394.19	2.0e+06	9.3e-01	3.5e-01	2.8e-02	8.1e-02	8.50	3.8e-02	2.1e-02	0.0e+00	5.7e-01
FTSF <sub>C</sub> -07	2.50e+03	7.25	4.5e+05	9.9e-01	1.2e-01	1.3e-02	1.7e-02	2.42	6.0e-02	0.0e+00	1.8e-01	0.0e+00
FTSF <sub>C</sub> -08	5.00e+03	14.49	3.2e+06	9.6e-01	5.5e-02	3.6e-02	3.5e-02	3.81	5.5e-02	0.0e+00	1.5e-01	0.0e+00
FTSF <sub>C</sub> -09	7.50e+03	21.74	6.5e+06	8.9e-01	4.9e-02	5.1e-02	5.4e-02	4.87	5.2e-02	0.0e+00	1.3e-01	0.0e+00
FTSF <sub>C</sub> -10	1.00e+04	28.99	1.5e+07	8.7e-01	3.7e-02	7.6e-02	7.6e-02	5.96	4.7e-02	0.0e+00	1.1e-01	0.0e+00
FTSF <sub>C</sub> -11	1.25e+04	36.23	2.9e+07	7.7e-01	2.8e-02	1.1e-01	1.0e-01	7.25	3.9e-02	0.0e+00	1.1e-01	0.0e+00
FTSF <sub>C</sub> -12	1.50e+04	43.48	4.4e+07	5.4e-01	2.4e-02	1.3e-01	1.4e-01	8.91	3.2e-02	0.0e+00	9.6e-02	0.0e+00
FTSF <sub>C</sub> -13	2.00e+04	57.97	6.2e+07	3.1e-01	2.3e-02	1.6e-01	2.1e-01	11.41	3.1e-02	0.0e+00	8.4e-02	0.0e+00
FTSF <sub>C</sub> -14	2.50e+04	72.46	8.9e+07	3.0e-01	2.1e-02	1.9e-01	2.4e-01	12.48	2.9e-02	0.0e+00	7.2e-02	0.0e+00
FTSF <sub>C</sub> -15	3.00e+04	86.96	1.1e+08	3.2e-01	2.3e-02	2.1e-01	2.8e-01	13.47	2.5e-02	0.0e+00	6.6e-02	0.0e+00
FTSF <sub>C</sub> -16	3.50e+04	101.45	1.3e+08	2.8e-01	2.2e-02	2.3e-01	3.2e-01	14.73	2.5e-02	0.0e+00	5.7e-02	0.0e+00
FTNS <sub>C</sub> -07	2.50e+03	9.03	1.1e+05	9.8e-01	7.1e-01	6.6e-03	2.7e-02	3.49	6.5e-02	2.5e-02	7.8e-02	5.8e-01
FTNS <sub>C</sub> -08	5.00e+03	18.05	4.2e+05	9.5e-01	4.1e-01	1.3e-02	4.1e-02	4.65	5.5e-02	2.3e-02	6.0e-02	5.7e-01
FTNS <sub>C</sub> -09	7.50e+03	27.08	9.4e+05	9.5e-01	3.3e-01	1.9e-02	5.6e-02	5.94	4.7e-02	2.2e-02	5.2e-02	5.7e-01
FTNS <sub>C</sub> -10	1.00e+04	36.10	1.4e+06	9.4e-01	3.6e-01	2.4e-02	7.6e-02	7.29	4.2e-02	2.2e-02	4.6e-02	5.7e-01
FTNS <sub>C</sub> -11	1.25e+04	45.13	2.0e+06	9.3e-01	3.4e-01	2.8e-02	9.0e-02	8.09	3.9e-02	2.4e-02	4.0e-02	5.7e-01
FTNS <sub>C</sub> -12	1.50e+04	54.15	2.4e+06	9.2e-01	3.9e-01	3.1e-02	1.1e-01	8.98	3.8e-02	2.4e-02	3.9e-02	5.7e-01
FTNS <sub>C</sub> -13	2.00e+04	72.20	4.0e+06	9.0e-01	3.3e-01	4.0e-02	1.4e-01	10.09	3.2e-02	2.6e-02	3.4e-02	5.7e-01
FTNS <sub>C</sub> -14	2.50e+04	90.25	6.6e+06	8.8e-01	2.6e-01	5.1e-02	1.6e-01	10.89	3.1e-02	2.5e-02	3.2e-02	5.7e-01
FTNS <sub>C</sub> -15	3.00e+04	108.30	1.0e+07	8.7e-01	2.1e-01	6.3e-02	1.8e-01	11.63	2.9e-02	2.4e-02	3.1e-02	5.7e-01
FTNS <sub>C</sub> -16	3.50e+04	126.35	1.4e+07	8.5e-01	1.7e-01	7.6e-02	2.0e-01	12.21	2.7e-02	2.8e-02	3.2e-02	5.7e-01

$E = 2.00 \times 10^{-4}$ ,  $Ro_M = 1.00 \times 10^{-4}$  and  $q_k = 1$

FFSF <sub>C</sub> -21	2.50e+03	10.64	1.1e+05	9.6e-01	8.9e-01	3.2e-02	1.5e-01	1.17	9.2e-03	0.0e+00	2.3e-02	0.0e+00
FFSF <sub>C</sub> -22	5.00e+03	21.28	2.1e+05	9.5e-01	1.4e-01	4.6e-02	5.3e-02	2.42	9.5e-02	0.0e+00	0.0e+00	0.0e+00
FFSF <sub>C</sub> -23	7.50e+03	31.91	3.7e+05	8.9e-01	1.2e-01	6.1e-02	7.3e-02	2.78	8.3e-02	0.0e+00	0.0e+00	0.0e+00
FFSF <sub>C</sub> -24	1.00e+04	42.55	6.3e+05	8.6e-01	1.0e-01	8.0e-02	9.2e-02	3.17	7.3e-02	0.0e+00	0.0e+00	0.0e+00
FFSF <sub>C</sub> -25	1.25e+04	53.19	1.1e+06	8.1e-01	7.9e-02	1.1e-01	1.3e-01	3.81	6.3e-02	0.0e+00	0.0e+00	0.0e+00
FFSF <sub>C</sub> -26	1.50e+04	63.83	1.8e+06	7.0e-01	6.0e-02	1.3e-01	1.6e-01	4.13	6.0e-02	0.0e+00	0.0e+00	0.0e+00
FFNS <sub>C</sub> -21	2.50e+03	12.08	1.7e+04	9.6e-01	6.2e-01	1.3e-02	2.6e-02	2.20	1.1e-01	4.5e-02	1.3e-03	6.0e-01
FFNS <sub>C</sub> -22	5.00e+03	24.15	3.8e+04	9.3e-01	5.6e-01	2.0e-02	4.2e-02	2.91	7.6e-02	3.7e-02	0.0e+00	6.0e-01
FFNS <sub>C</sub> -23	7.50e+03	36.23	5.8e+04	9.2e-01	5.5e-01	2.4e-02	5.5e-02	3.39	8.3e-02	4.4e-02	4.3e-04	6.0e-01
FFNS <sub>C</sub> -24	1.00e+04	48.31	7.4e+04	9.3e-01	6.1e-01	2.7e-02	6.6e-02	3.77	5.5e-02	4.4e-02	1.2e-04	6.0e-01
FFNS <sub>C</sub> -25	1.25e+04	60.39	9.0e+04	9.4e-01	6.7e-01	3.0e-02	7.4e-02	4.13	6.1e-02	4.3e-02	5.3e-04	6.0e-01
FFNS <sub>C</sub> -26	1.50e+04	72.46	1.1e+05	9.2e-01	6.3e-01	3.3e-02	8.2e-02	4.35	7.1e-02	4.5e-02	1.2e-04	6.0e-01
FTSF <sub>C</sub> -17	2.50e+03	9.19	3.8e+05	9.5e-01	9.5e-02	6.1e-02	5.9e-02	2.53	6.9e-02	0.0e+00	1.4e-01	0.0e+00
FTSF <sub>C</sub> -18	5.00e+03	18.38	2.3e+06	8.3e-01	4.8e-02	1.5e-01	1.2e-01	3.90	5.5e-02	0.0e+00	1.0e-01	0.0e+00
FTSF <sub>C</sub> -19	7.50e+03	27.57	2.9e+06	3.6e-01	5.8e-02	1.7e-01	2.4e-01	5.98	4.7e-02	0.0e+00	7.4e-02	0.0e+00
FTSF <sub>C</sub> -20	1.00e+04	36.76	4.3e+06	3.3e-01	6.6e-02	2.1e-01	3.1e-01	7.16	4.1e-02	0.0e+00	6.8e-02	0.0e+00
FTSF <sub>C</sub> -21	1.25e+04	45.96	6.0e+06	3.2e-01	6.9e-02	2.5e-01	3.8e-01	7.94	4.1e-02	0.0e+00	6.4e-02	0.0e+00
FTSF <sub>C</sub> -22	1.50e+04	55.15	6.8e+06	3.7e-01	8.5e-02	2.6e-01	4.5e-01	8.58	3.9e-02	0.0e+00	6.0e-02	0.0e+00
FTNS <sub>C</sub> -17	2.50e+03	10.73	5.3e+04	9.5e-01	5.7e-01	2.3e-02	6.2e-02	3.14	7.6e-02	4.5e-02	6.9e-02	6.0e-01
FTNS <sub>C</sub> -18	5.00e+03	21.46	1.7e+05	9.0e-01	5.1e-01	4.1e-02	1.1e-01	4.48	6.3e-02	3.9e-02	5.4e-02	6.0e-01
FTNS <sub>C</sub> -19	7.50e+03	32.19	3.1e+05	8.8e-01	4.7e-01	5.6e-02	1.5e-01	5.36	5.5e-02	4.5e-02	5.1e-02	6.0e-01

Continued on next page

Table F.3 -- *Continued from previous page*

Model	$Ra$	$\frac{Ra}{Ra_C}$	$E_k$	$\frac{E_{kP}^{N\text{Ax}i}}{E_{kP}}$	$\frac{E_{kT}^{N\text{Ax}i}}{E_{kT}}$	$Ro$	$Ro_l$	$Nu$	$\delta_{T_{IC}}$	$\delta_{E_{IC}}$	$\delta_{T_{OC}}$	$\delta_{E_{OC}}$
FTNS <sub>C</sub> -20	1.00e+04	42.92	5.1e+05	8.5e-01	4.0e-01	7.1e-02	1.9e-01	5.96	4.9e-02	4.5e-02	4.7e-02	6.0e-01
FTNS <sub>C</sub> -21	1.25e+04	53.65	7.6e+05	8.1e-01	3.4e-01	8.7e-02	2.2e-01	6.35	4.7e-02	4.5e-02	4.7e-02	6.0e-01
FTNS <sub>C</sub> -22	1.50e+04	64.38	1.1e+06	7.8e-01	3.0e-01	1.0e-01	2.5e-01	6.76	4.6e-02	4.5e-02	4.6e-02	6.0e-01

<sup>1982</sup>

## Appendix G

<sup>1983</sup>

## Power-Law Implications

<sup>1984</sup> The following are from Olson 2007, treatise of geophysics Ch8: Pg6 unless stated.

<sup>1985</sup>

Table G.1: Known physical properties

Property	Notation	Value	Units
CMB radius	$r_o$	3.48 e6	m
inner core radius	$r_i$	1.22 e6	m
inner to outer core radius ratio	$r_{io} = r_i/r_o$		
outer core shell thickness	$D = r_o - r_i$		m
angular velocity of rotation	$\Omega$	7.292 e-5	rad/s
CMB gravity	$g_o$	10.68	$m/s^2$
core density	$\rho$	1.09 e4	$kg/m^{-3}$
permeability of free space	$\mu_0$	$4 \pi 1e-7$	H/m

Table G.2: Thermodynamic and transport properties

Property	Notation	Value	Units
CMB temperature	$T_{CMB}$	4000	K
ICB temperature	$T_{ICB}$	5500	K
specific heat	$C_p$	850	J/kgK
thermal expansivity	$\alpha_T$	1.4 e-5	$K^{-1}$
thermal conductivity	$k$	45	W/m K
thermal conductivity (Pozzo, 2012)	$k$	110 (90 - 130)	W/m K
thermal diffusivity	$\kappa = \frac{k}{\rho C_p}$		$m^2/s$
kinematic viscosity of outer core	$\nu$	1 e-5	$m^2/s$
magnetic diffusivity	$\eta$	1.5	$m^2/s$
adiabatic heat flux at CMB (Pozzo, 2012)	$Q$	15.5 (15 - 16)	TW
adiabatic temp gradient at CMB	$(\frac{dT}{dr})_{CMB}$	3 e-4	K/m
adiabatic temp gradient at CMB (Pozzo)	$(\frac{dT}{dr})_{CMB} = \frac{Q}{4\pi r_o^2 k}$		K/m
adiabatic temperature gradient velocity	$h_T = (\frac{dT}{dr})_{CMB}/(r_{io}^2)$	0.5	K/m
			$mm/s^2$

<sub>1986</sub> Non-dimensional number estimates for Earth:

<sub>1987</sub>

<sub>1988</sub> Input Control Parameters

$$Ra = \frac{\alpha_T g_o h_T r_o^2}{2\Omega\eta} = 6.2359 e10 \quad (G.1)$$

$$E = \frac{\nu}{2\Omega r_o^2} = 5.6619 e - 15 \quad (G.2)$$

$$Ro_M = \frac{\eta}{2\Omega r_o^2} = 8.4929 e - 10 \quad (G.3)$$

$$q_k = \frac{\kappa}{\eta} = 7.9151 e - 06 \quad (G.4)$$

$$Pr = \frac{\nu}{\kappa} = 0.8423 \quad (G.5)$$

$$Pm = \frac{\nu}{\eta} = 6.6667 e - 06 \quad (G.6)$$

<sub>1989</sub> Input Control Parameters

$$Re_M = \frac{vr_o}{\eta} = 1.1035 e3 \quad (G.7)$$

$$Re = \frac{vr_o}{\nu} = 1.6553 e8 \quad (G.8)$$

$$Ro = \frac{v}{2\Omega r_o} = 9.3719 e - 7 \quad (G.9)$$

<sub>1990</sub> Rayleigh number estimates for Earth:

$$Ra_{Critical} \approx 10.1E^{-1/3} = 5.6667 e5 \quad (G.10)$$

$$Ra_{FT} = \frac{\alpha_T g_o (T_{ICB} - T_{CMB}) r_o}{2\Omega\eta r_{io}(1 - r_{io})} = 6.2359 e10 \quad (G.11)$$

$$\frac{Ra_{FT}}{Ra_{Critical}} \approx 1.1004 e5 \quad (G.12)$$

$$Ra_{Conventional} = \frac{\alpha_T g_o (T_{ICB} - T_{CMB}) D^3}{\kappa\nu} = 8.6771 e28 \quad (G.13)$$

$$Ra_Q^* = \frac{\alpha_T g_o Q}{4\pi r_o r_i \rho C_p \Omega^3 D^2} = 2.3674 e - 12 \quad (G.14)$$

<sup>1991</sup> From our scaling law studies we obtained:

$$Nu_{FF} \text{ Dipolar} = 0.013 Ra_{FT}^{0.71} = 6.0024 e5 \quad (\text{G.15})$$

$$Nu_{FT} \text{ Dipolar} = 0.020 Ra_{FT}^{0.65} = 2.0783 e5 \quad (\text{G.16})$$

$$Nu_{FT} \text{ Multipolar} = 0.380 Ra_{FT}^{0.34} = 1.7785 e3 \quad (\text{G.17})$$

<sup>1992</sup> We know that:

$$Nu = \frac{\left(\frac{dT}{dr}\right)_{CMB}}{\frac{r_{io}\Delta T}{D}} \quad (\text{G.18})$$

$$Q_{Convective} = Q_{Total} - Q_{Conductive} \quad (\text{G.19})$$

<sup>1993</sup> From Braginsky and Roberts (1995), we know that  $Q_{Conductive} \approx 5.2$  TW. Christensen  
<sup>1994</sup> (2006) uses a value of  $Q_{Convective} = 2$  TW and estimates a superadiabatic temperature  
<sup>1995</sup> contrast ( $\Delta T$ ) of 0.001 K. From Pozzo (2012), we have a new estimate of  $Q_{Total} \approx 15 - 16$   
<sup>1996</sup> TW, so new  $Q_{Convective} \approx 10$  TW. Using this the superadiabatic temperature contrast  
<sup>1997</sup> from the inner core boundary to the outer core boundary is:  $\Delta T \approx 0.01$  K for us. The  
<sup>1998</sup> adiabatic heat flux estimate can be obtained by:

$$F = 4\pi r_o^2 k \left(\frac{dT}{dr}\right)_{CMB} \quad (\text{G.20})$$

<sup>1999</sup> From our scaling law studies we also obtained:

$$Ro_{FF} \text{ Dipolar} = 0.83 Ra_Q^{*0.4} \quad (\text{G.21})$$

$$Ro_{FT} \text{ Dipolar} = 0.89 Ra_Q^{*0.41} \quad (\text{G.22})$$

$$Ro_{FT} \text{ Multipolar} = 0.33 Ra_Q^{*0.24} \quad (\text{G.23})$$

<sup>2000</sup> The flow velocities can be estimated using:

$$Ro = \frac{v}{\Omega D} \quad (G.24)$$

$$v = Ro\Omega D \quad (G.25)$$

<sup>2001</sup> Therefore, the adiabatic heat flux out of the CMB and the flow velocities in the outer core can be estimated as:

Table G.3: Scaling Laws Implications. The multipolar values are mentioned for reference and does not apply to Earth.

Regime	Adiabatic heat flux at CMB Units: TW	Flow Velocity Units: mm/s
Earth	15 - 16 (Pozzo, 2012)	0.5 (Bloxham, 1991)
Fixed Flux	Dipolar	15.6
Fixed Temperature	Dipolar	5.4
Fixed Temperature	Multipolar	0.05
		88.2

<sup>2002</sup>

2003 **Rossby numer**

2004

2005 Christensen (2006) estimates Rossby number ( $Ro^c$ ) as:

$$Ro^c = \frac{u_D}{\Omega D} \quad (\text{G.26})$$

2006 where, the subscript D means dimensional.

2007

2008 They define their characteristic  $u_D$  as:

$$u_D = \left[ \frac{1}{V_D} \int \mathbf{v}_D \cdot \mathbf{v}_D \, dV_D \right]^{1/2} \quad (\text{G.27})$$

$$\therefore Ro^c = \frac{\left[ \frac{1}{V_D} \int \mathbf{v}_D \cdot \mathbf{v}_D \, dV_D \right]^{1/2}}{\Omega D} \quad (\text{G.28})$$

2009 Let us non-dimensionalize  $\mathbf{v}_D$  and  $V_D$  using:

$$\mathbf{v}_D = \mathbf{v}_N^c \Omega D \quad (\text{G.29})$$

$$V_D = V_N D^3 \quad (\text{G.30})$$

2010 Using these we get,

$$Ro^c = \frac{\left[ \frac{1}{V_N D^3} \int \mathbf{v}_N^c \Omega D \cdot \mathbf{v}_N^c \Omega D \, dV_N \, D^3 \right]^{1/2}}{\Omega D} \quad (\text{G.31})$$

$$= \left[ \frac{1}{V_N} \int \mathbf{v}_N^c \cdot \mathbf{v}_N^c \, dV_N \right]^{1/2} \quad (\text{G.32})$$

2011 Also,

$$E_{k,N}^c = \frac{1}{2} \int \mathbf{v}_N^c \cdot \mathbf{v}_N^c \, dV_N \quad (\text{G.33})$$

<sup>2012</sup> Therefore,

$$Ro^c = \left( \frac{2E_{k,N}^c}{V_N} \right)^{\frac{1}{2}} \quad (\text{G.34})$$

<sup>2013</sup> Now, let us estimate the Kuang-Bloxham  $Ro^c$  the same way as above but using our  
<sup>2014</sup> non-dimensionalization as follows:

$$\mathbf{v}_D = \mathbf{v}_N^k \frac{\eta}{r_o} \quad (\text{G.35})$$

$$V_D = V_N r_o^3 \quad (\text{G.36})$$

<sup>2015</sup> Therefore,

$$\therefore Ro^c = \frac{\left[ \frac{1}{V_N r_o^3} \int \mathbf{v}_N^k \frac{\eta}{r_o} \cdot \mathbf{v}_N^k \frac{\eta}{r_o} dV_N r_o^3 \right]^{1/2}}{\Omega D} \quad (\text{G.37})$$

<sup>2016</sup> Using:  $D = r_o(1 - r_{io})$ , we get:

$$Ro^c = \frac{\eta}{\Omega r_o^2 (1 - r_{io})} \left[ \frac{1}{V_N} \int \mathbf{v}_N^k \cdot \mathbf{v}_N^k dV_N \right]^{1/2} \quad (\text{G.38})$$

<sup>2017</sup> Using:

$$Ro_M^k = \frac{\eta}{2\Omega r_o^2} \quad (\text{G.39})$$

$$E_{k,N}^k = \int \mathbf{v}_N^k \cdot \mathbf{v}_N^k dV_N \quad (\text{G.40})$$

<sup>2018</sup> We get,

$$Ro^c = (E_{k,N}^k)^{1/2} \frac{2 Ro_M^k}{(1 - r_{io})(V_N)^{1/2}} \quad (\text{G.41})$$

<sup>2019</sup> Using  $r_i = 12/35$ ,  $r_o = 35/35$  and  $V_N = (4/3)\pi(r_o^3 - r_i^3)$

$$\frac{2}{(1 - r_{io})\sqrt{V_N}} = 1.518 \quad (\text{G.42})$$

<sup>2020</sup> Therefore,

$$Ro^c = 1.518 Ro_M^k (E_{k,N}^k)^{1/2} \quad (\text{G.43})$$

## <sup>2021</sup> Lorentz number

<sup>2022</sup>

<sup>2023</sup> Christensen (2006) gives the relationship between the Elsasser number and the Lorentz number ( $Lo$ ) as:

$$\Lambda = Lo^2 Pm E^{-1} \quad (\text{G.44})$$

$$Lo = \sqrt{\Lambda E Pm^{-1}} \quad (\text{G.45})$$

<sup>2025</sup> Using:

$$\Lambda = \frac{B^2}{\rho \mu \eta \Omega} \quad (\text{G.46})$$

$$E = \frac{\nu}{\Omega D^2} \quad (\text{G.47})$$

$$Pm = \frac{\nu}{\eta} \quad (\text{G.48})$$

<sup>2026</sup> We get,

$$Lo = \sqrt{\frac{B^2}{\rho \mu \eta \Omega} \frac{\nu}{\Omega D^2} \frac{\eta}{\nu}} \quad (\text{G.49})$$

$$= \sqrt{\frac{B_D^2}{\rho \mu \Omega^2 D^2}} \quad (\text{G.50})$$

<sup>2027</sup> where, the subscript D means dimensional.

2028

<sup>2029</sup> They define their characteristic  $B_D$  as:

$$B_D = \left[ \frac{1}{V_D} \int \mathbf{B}_D \cdot \mathbf{B}_D dV_D \right]^{1/2} \quad (\text{G.51})$$

$$\therefore Lo = \sqrt{\frac{\frac{1}{V_D} \int \mathbf{B}_D \cdot \mathbf{B}_D dV_D}{\rho \mu \Omega^2 D^2}} \quad (\text{G.52})$$

<sup>2030</sup> Let us non-dimensionalize  $\mathbf{B}_D$  and  $V_D$  using:

$$\mathbf{B}_D = \mathbf{B}_N^c \sqrt{\rho \mu} \Omega D \quad (\text{G.53})$$

$$V_D = V_N D^3 \quad (\text{G.54})$$

<sup>2031</sup> Using these we get,

$$Lo = \sqrt{\frac{\frac{1}{V_N D^3} \int \mathbf{B}_N^c \sqrt{\rho \mu} \Omega D \cdot \mathbf{B}_N^c \sqrt{\rho \mu} \Omega D dV_N D^3}{\rho \mu \Omega^2 D^2}} \quad (\text{G.55})$$

$$= \left[ \frac{1}{V_N} \int \mathbf{B}_N^c \cdot \mathbf{B}_N^c dV_N \right]^{1/2} \quad (\text{G.56})$$

<sup>2032</sup> Also,

$$E_{B,N}^c = \frac{1}{2} \int \mathbf{B}_N^c \cdot \mathbf{B}_N^c dV_N \quad (\text{G.57})$$

<sup>2033</sup> Therefore,

$$Lo = \left( \frac{2E_{B,N}^c}{V_N} \right)^{\frac{1}{2}} \quad (\text{G.58})$$

<sup>2034</sup> Now, let us estimate the Kuang-Bloxham  $Lo$  the same way as above but using our non-

<sup>2035</sup> dimensionalization as follows:

$$\mathbf{B}_D = \mathbf{B}_N^k \sqrt{2\rho\mu\Omega\eta} \quad (G.59)$$

$$V_D = V_N r_o^3 \quad (G.60)$$

<sup>2036</sup> Therefore,

$$\therefore Lo = \sqrt{\frac{\frac{1}{V_N r_o^3} \int \mathbf{B}_N^k \sqrt{2\rho\mu\Omega\eta} \cdot \mathbf{B}_N^k \sqrt{2\rho\mu\Omega\eta} dV_N r_o^3}{\rho\mu \Omega^2 D^2}} \quad (G.61)$$

<sup>2037</sup> Using:  $D = r_o(1 - r_{io})$ , we get:

$$Lo = \left[ \frac{2\eta}{\Omega r_o^2 (1 - r_{io})^2} \frac{1}{V_N} \int \mathbf{B}_N^k \cdot \mathbf{B}_N^k dV_N \right]^{1/2} \quad (G.62)$$

$$= \frac{2}{(1 - r_{io})} \left[ \frac{\eta}{2\Omega r_o^2} \frac{1}{V_N} \int \mathbf{B}_N^k \cdot \mathbf{B}_N^k dV_N \right]^{1/2} \quad (G.63)$$

<sup>2038</sup> Using:

$$Ro_M^k = \frac{\eta}{2\Omega r_o^2} \quad (G.64)$$

$$E_{B,N}^k = \int \mathbf{B}_N^k \cdot \mathbf{B}_N^k dV_N \quad (G.65)$$

<sup>2039</sup> We get,

$$Lo = (E_{B,N}^k)^{1/2} \frac{2(Ro_M^k)^{1/2}}{(1 - r_{io})(V_N)^{1/2}} \quad (G.66)$$

<sup>2040</sup> Using  $r_i = 12/35$ ,  $r_o = 35/35$  and  $V_N = (4/3)\pi(r_o^3 - r_i^3)$

$$\frac{2}{(1 - r_{io})\sqrt{V_N}} = 1.518 \quad (G.67)$$

<sup>2041</sup> Therefore,

$$Lo = 1.518 (Ro_M^k)^{1/2} (E_{B,N}^k)^{1/2} \quad (G.68)$$

## <sup>2042</sup> Ohmic Dissipation

<sup>2043</sup>

<sup>2044</sup> Fraction of Ohmic Dissipation:

$$f_{ohm} = \frac{D_\eta}{P} \quad (G.69)$$

<sup>2045</sup> Rate of Ohmic Dissipation (notice this is non-dimensional):

$$D_\eta = E_\eta \int (\nabla \times \mathbf{B})^2 dV \quad (G.70)$$

<sup>2046</sup> Power generated by buoyancy forces:

$$P = 2\pi r_{io} \frac{1 + r_{io}}{1 - r_{io}} Ra_Q^* \approx 7.01 Ra_Q^* \quad (G.71)$$

<sup>2047</sup> Since  $D_\eta$  is non-dimentional, we will convert their non-dimensionalization to theirs:

$$\mathbf{B}_D^c = \mathbf{B}_N^c \sqrt{\rho\mu} \Omega D \quad (G.72)$$

$$\mathbf{B}_D^k = \mathbf{B}_N^k \sqrt{2\rho\mu\Omega\eta} \quad (G.73)$$

$$\therefore \mathbf{B}_D^c = \mathbf{B}_D^k \quad (G.74)$$

$$\mathbf{B}_N^c = \mathbf{B}_N^k \sqrt{2\rho\mu\Omega\eta} \frac{1}{\sqrt{\rho\mu} \Omega D} \quad (G.75)$$

$$= \mathbf{B}_N^k \frac{\sqrt{2\eta}}{\sqrt{\Omega} D} \quad (G.76)$$

$$= \mathbf{B}_N^k \left( \frac{4}{(1 - r_{io})^2} \frac{\eta}{2\Omega r_o^2} \right)^{1/2} \quad (G.77)$$

$$\therefore \mathbf{B}_N^c = \mathbf{B}_N^k \frac{2}{(1 - r_{io})} Ro_M^{1/2} \quad (G.78)$$

<sup>2048</sup> Using the Kuang-Bloxham non-dimensionalization and:

$$E_\eta^c = Ro_M^k \frac{2}{(1 - r_{io})^2} \quad (G.79)$$

<sup>2049</sup> We get,

$$D_\eta^k = Ro_M^k \frac{2}{(1 - r_{io})^2} \int (\nabla \times \mathbf{B}_N^k \frac{2}{(1 - r_{io})} Ro_M^{1/2})^2 dV_N \quad (G.80)$$

$$= Ro_M^k \frac{2}{(1 - r_{io})^2} \frac{4}{(1 - r_{io})^2} Ro_M \int (\nabla \times \mathbf{B}_N^k)^2 dV_N \quad (G.81)$$

$$= Ro_M^k \frac{8}{(1 - r_{io})^4} \int (\nabla \times \mathbf{B}_N^k)^2 dV_N \quad (G.82)$$

<sup>2050</sup> Also,

$$P^k = 6.6989 Ra_Q^* \quad (G.83)$$

<sup>2051</sup> Magnetic Dissipation Time:

$$\tau_{diss} = \frac{E_B}{D_\eta} \quad (G.84)$$

<sup>2052</sup> Magnetic Energy:

$$E_B^c = \frac{1}{2} \int \mathbf{B}_D \cdot \mathbf{B}_D dV \quad (G.85)$$

$$\therefore \mathbf{B}_N^c = \mathbf{B}_N^k \frac{2}{(1 - r_{io})^2} \sqrt{Ro_M} \quad (G.86)$$

$$\therefore E_B^c = \frac{1}{2} \int \mathbf{B}_N^k \frac{2}{(1 - r_{io})^2} \sqrt{Ro_M} \cdot \mathbf{B}_N^k \frac{2}{(1 - r_{io})^2} \sqrt{Ro_M} dV \quad (G.87)$$

$$= \frac{2 Ro_M}{(1 - r_{io})^4} r_o^3 E_B^k \quad (G.88)$$

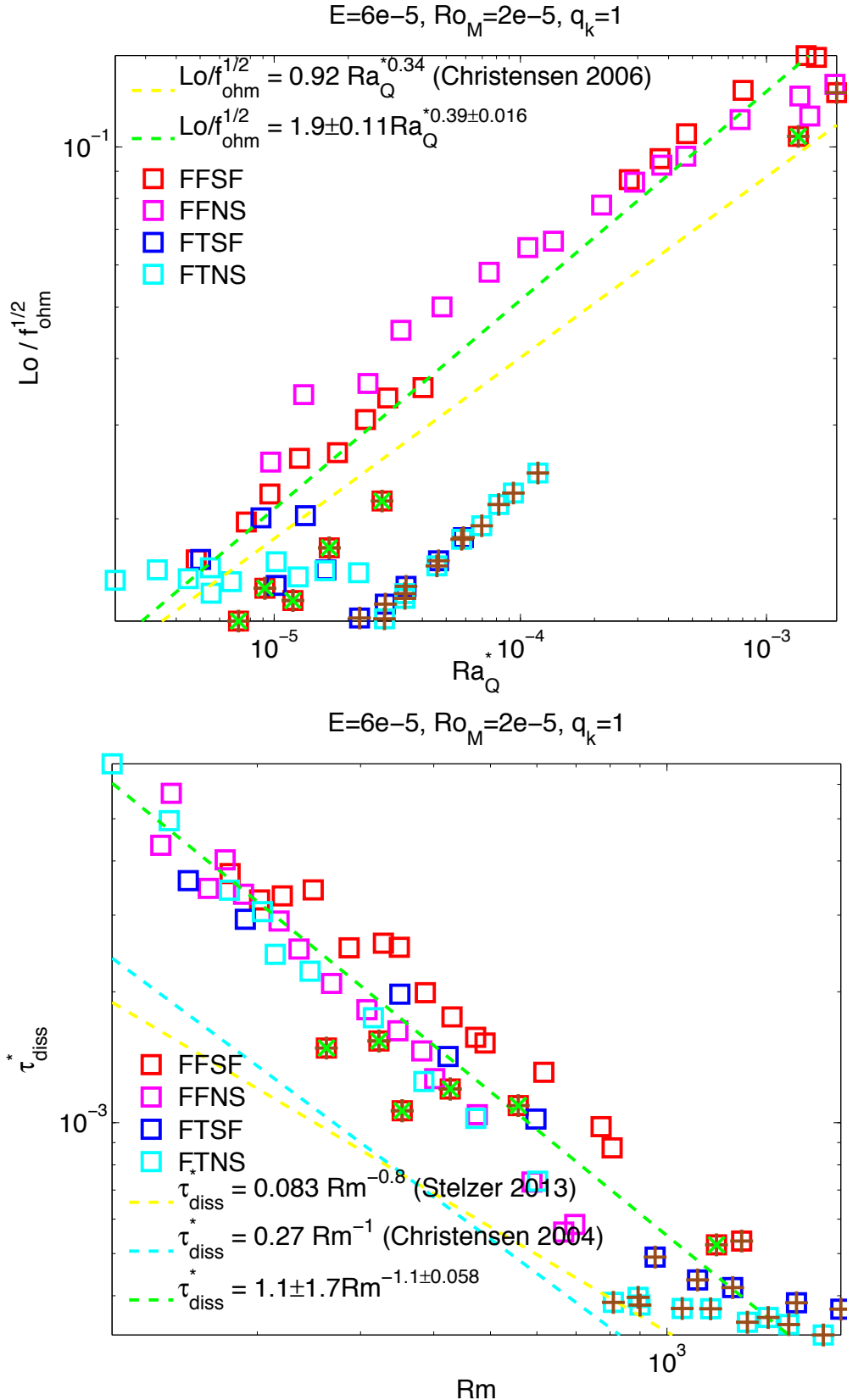


Figure G.1: Our estimates for Earth: Ohmic Dissipation ( $D_\eta$ ) = 0.4 - 1 TW and Magnetic Dissipation Time ( $\tau_\eta$ ) = 20.3 yrs. (top)  $Lo/f_{\text{ohm}}^{1/2}$  vs  $Ra_Q^*$ . (bottom)  $\tau_{\text{diss}}^*$  vs  $Rm$ .

<sup>2053</sup> Magnetic diffusion time (this is dimensional):

$$\tau_{\eta D}^c = \frac{D^2}{\eta} \quad (G.89)$$

<sup>2054</sup> Christensen's non-dimensionalization:

$$\tau_D^c = \tau_N^c \frac{1}{\Omega} \quad (G.90)$$

<sup>2055</sup> Using this:

$$\tau_{\eta N}^c = \Omega \frac{D^2}{\eta} = \frac{\Omega r_o^2 (1 - r_{io})^2}{\eta} \quad (G.91)$$

$$= \frac{(1 - r_{io})^2}{2 R o_M} \quad (G.92)$$

<sup>2056</sup> Normalized magnetic dissipation time:

$$\tau_{diss}^* = \frac{\tau_{diss}}{\tau_\eta} \quad (G.93)$$

<sup>2057</sup> Magnetic Reynolds number:

$$Rm = \frac{\mathbf{v}_D}{\eta D} \quad (G.94)$$

$$Rm^c = \frac{\left[ \frac{1}{V_D} \int \mathbf{v}_D \cdot \mathbf{v}_D dV_D \right]^{1/2}}{\eta D} \quad (G.95)$$

$$Rm^k = \frac{\left[ \frac{1}{V_N r_o^3} \int \mathbf{v}_N^k \frac{\eta}{r_o} \cdot \mathbf{v}_N^k \frac{\eta}{r_o} dV_D r_o^3 \right]^{1/2}}{\eta D} \quad (G.96)$$

$$= \frac{1}{r_o^2 (1 - r_{io})} \frac{1}{\sqrt{V_N}} (E_k^k)^{1/2} \quad (G.97)$$

<sup>2058</sup> Our Power law:

$$\frac{Lo}{f_{ohm}^{1/2}} = 1.9 \pm 0.12 Ra_Q^{0.39 \pm 0.016} \quad (G.98)$$

$$\tau_{diss}^* = 1.1 \pm 1.7 Rm^{-1.1 \pm 0.058} \quad (G.99)$$

$$\text{Ohmic dissipation: } D_\eta = \frac{E_B Rm^{1.1}}{1.1 \tau_\eta} \quad (G.100)$$

$$\text{For Earth: } E_B = 2.8 - 6.2e20 J, \quad Rm = 2300 \quad (G.101)$$

$$\text{Our estimate: } D_\eta = 0.4 - 0.8 \text{ TW}, \quad \tau_\eta = 23.8 \text{ yrs} \quad (G.102)$$

<sup>2059</sup> In all the above scaling  $Nu > 2$ ,  $f_{Dip} > 0.35$ .

Table G.4: Scaling Laws Implications. The multipolar values are mentioned for reference and does not apply to Earth.

	Scaling Law	Ohmic Dissipation Time Units: TW	Magnetic Dissipation Time Units: yrs
Christensen (2004)	$\tau_{diss}^* = 0.27 Rm^{-1}$	0.2 - 0.5	42
Stelzer (2013)	$\tau_{diss}^* = 0.83 Rm^{-0.8}$	0.5 - 1	18.2
Stelzer (2013)	$\tau_{diss}^* = 0.33 Rm^{-0.89} Pm^{0.1} E_k^{0.09}$	3.4 - 8.4	2.3
This work	$\tau_{diss}^* = 1.1 \pm 1.7 Rm^{-1.1 \pm 0.058}$	0.4 - 0.8	23.8

2060

# Bibliography

- 2061 M.H. Acuña, J.E. Connerney, N.F. Ness, R.P. Lin, D. Mitchell, and et. al. Global dis-  
2062 tribution of crustal magnetization discovered by the Mars Global Surveyor MAG/ER  
2063 experiment. *Science*, 284:790–793, 1999.
- 2064 J. Aubert. Steady zonal flows in spherical shell dynamos. *Journal of Fluid Mechanics*,  
2065 542:53 – 67, 2005.
- 2066 J. Aubert, S. Labrosse, and C. Poitou. Modelling the palaeo-evolution of the geodynamo.  
2067 *Geophysical Journal International*, 179:1414 – 1428, 2009.
- 2068 J. Aurnou, D. Brito, and P. Olson. Anomalous rotation of the inner core and the toroidal  
2069 magnetic field. *Journal of Geophysical Research*, 103(B5):9721–9738, 1998.
- 2070 J. Aurnou, S. Andreadis, Zhu L.X., and P. Olson. Experiments on convection in Earth’s  
2071 core tangent cylinder. *Earth and Planetary Science Letters*, 212:119 – 134, 2003.
- 2072 B.M. Boubnov and S. Golitsyn. Temperature and velocity field regimes of convective  
2073 motions in a rotating plane fluid layer. *Journal of Fluid Mechanics*, 219:215 – 239,  
2074 1990.
- 2075 B.A. Buffett and J. Bloxham. Energetics of numerical geodynamo models. *Geophysical  
2076 Journal International*, 149:211 – 224, 2002.
- 2077 E. Bullard and H. Gellman. Homogeneous Dynamos and Terrestrial Magnetism. *Royal  
2078 Society of London Philosophical Transactions Series A*, 247:213 – 278, 1954.

- 2079 F.H. Busse and R.D. Simitev. Toroidal flux oscillations as possible cause of geomagnetic  
2080 excursions and reversals. *Physics of the Earth and Planetary Interiors*, 168:237 – 243,  
2081 2008.
- 2082 F.H. Busse, G. Eike, and A. Tilgner. On convection driven dynamos in rotating spherical  
2083 shells. *Studia Geophysica et Geodaetica*, 42(3):211 – 223, 1998.
- 2084 U. R. Christensen and J. Aubert. Scaling properties of convection-driven dynamos in  
2085 rotating spherical shells and application to planetary magnetic fields. *Geophysical  
2086 Journal International*, 166:97 – 114, 2006.
- 2087 U.R. Christensen. Dynamo scaling laws and applications to the planets. *Space Science  
2088 Reviews*, 152((1-4)):565 – 590, 2010.
- 2089 U.R. Christensen and P. Olson. A dynamo model interpretation of geomagnetic field  
2090 structures. *Geophysical Research Letters*, 25(10):1565 – 1568, 1998.
- 2091 U.R. Christensen and A. Tilgner. Power requirement of the geodynamo from ohmic losses  
2092 in numerical and laboratory dynamos. *Nature*, 429(6988):169 – 171, 2004.
- 2093 U.R. Christensen and J. Wicht. Numerical dynamo simulations, core dynamics. *Treatise  
2094 on Geophysics*, 8(08):249, 2007.
- 2095 U.R. Christensen, P. Olson, and G.A. Glatzmaier. Numerical modelling of the geody-  
2096 namo: a systematic parameter study. *Geophysical Journal International*, 138:393 –  
2097 409, 1999.
- 2098 U.R. Christensen, J. Aubert, P. Cardin, E. Dormy, Gibbons S., G.A. Glatzmaier,  
2099 E. Grote, Y. Honkura, C. Jones, M. Kono, M. Matsushima, A. Sakuraba, F. Taka-  
2100 hashi, A. Tilgner, J. Wicht, and K. Zhang. A Numerical Dynamo Benchmark. *Physics  
2101 of the Earth and Planetary Interiors*, 128:25 – 34, 2001.

- 2102 U.R. Christensen, V. Holzwarth, and A. Reiners. Energy flux determines magnetic field  
2103 strength of planets and stars. *Nature*, 457:167 – 169, 2009.
- 2104 T.G. Cowling. The magnetic field of sunspots. *Monthly Notices of the Royal Astronomical  
2105 Society*, 94:39–48, 1933.
- 2106 G. Dharmaraj and S. Stanley. Effect of inner core conductivity on planetary dynamo  
2107 models. *Physics of the Earth and Planetary Interiors*, 212-213:1–9, 2012. doi: <http://dx.doi.org/10.1016/j.pepi.2012.09.003>.
- 2109 E. Dormy and J. le Mouël. Geomagnetism and the dynamo: where do we stand? *Comptes  
2110 Rendus Physique*, 9:711 – 720, 2008.
- 2111 E. Dormy, J-P. Valet, and V. Courtillot. Numerical models of the geodynamo and  
2112 observational constraints. *G-Cubed Geochemistry, Geophysics, Geosystems*, 1(10):1037,  
2113 2000.
- 2114 A.M. Dziewonski and D.L. Anderson. Preliminary reference Earth model. *Physics of the  
2115 Earth and Planetary Interiors*, 25:297–356, 1981.
- 2116 T. Gastine, L. Duarte, and J. Wicht. Dipolar versus multipolar dynamos: the influence  
2117 of the background density stratification. *Astronomy and Astrophysics*, 546:A19:1–13,  
2118 2012.
- 2119 G.A. Glatzmaier and P.H. Roberts. A three-dimensional self-consistent computer simu-  
2120 lation of a geomagnetic field reversal. *Nature*, 377:203 – 209, 1995a.
- 2121 G.A. Glatzmaier and P.H. Roberts. A three-dimensional convective dynamo solution  
2122 with rotating and finitely conducting inner core and mantle. *Physics of the Earth and  
2123 Planetary Interiors*, 91:63 – 75, 1995b.
- 2124 G.A. Glatzmaier and P.H. Roberts. An anelastic evolutionary geodynamo simulation  
2125 driven by compositional and thermal convection. *Physica D*, 97:81 – 94, 1996.

- 2126 E. Grote, F. H. Busse, and A. Tilgner. Effects of hyperdiffusivities on dynamo simulations.
- 2127 *Geophysical Research Letters*, 27:2001 – 2004, 2000.
- 2128 E. Grote, F.H. Busse, and A. Tilgner. Regular and chaotic spherical dynamos. *Physics*  
2129 *of the Earth and Planetary Interiors*, 117:259–272, 2000.
- 2130 D. Gubbins. The distinction between geomagnetic excursions and reversals. *Geophysical*  
2131 *Journal International*, 137:F1 – F3, 1999.
- 2132 N.G. Hogg and H.M. Stommel. The Heton, an Elementary Interaction Between Discrete  
2133 Baroclinic Geostrophic Vortices, and Its Implications Concerning Eddy Heat-Flow.  
2134 *Proceedings of the Royal Society of London. Series A, Mathematical and Physical Sci-*  
2135 *ences*, 397(1812):1 – 20, 1985.
- 2136 R. Hollerbach. Imposing a magnetic field across a non-axisymmetric shear-layer in a  
2137 rotating spherical-shell. *Physics of Fluids*, 6:2540 – 2544, 1994.
- 2138 R. Hollerbach and C.A. Jones. Influence of the Earth’s inner core on geomagnetic fluc-  
2139 tuations and reversals. *Nature*, 365:541 – 543, 1993.
- 2140 R. Hollerbach, C.F. Barenghi, and C.A. Jones. Taylor’s constraint in a spherical alpha-  
2141 omega dynamo. *Geophysical and Astrophysical Fluid Dynamics*, 67:3 – 25, 1991.
- 2142 K. Hori, J. Wicht, and U.R. Christensen. The effect of thermal boundary conditions on  
2143 dynamos driven by internal heating. *Physics of the Earth and Planetary Interiors*, 182:  
2144 85 – 97, 2010. doi: 10.1016/j.pepi.2010.06.011.
- 2145 K. Hori, J. Wicht, and U.R. Christensen. The influence of thermo-compositional bound-  
2146 ary conditions on convection and dynamos in a rotating spherical shell. *Physics of the*  
2147 *Earth and Planetary Interiors*, 196, 2012.
- 2148 N. Ishihara and S. Kida. Dynamo mechanism in a rotating spherical shell: competition

- 2149      between magnetic field and convection vortices. *Journal of Fluid Mechanics*, 465:1–32,  
2150      2002.
- 2151      W. Jiang and W. Kuang. An MPI-based MoSST core dynamics model. *Physics of the*  
2152      *Earth and Planetary Interiors*, 170(1-2):46 – 51, 2008.
- 2153      S. Johnsen and K.J. Lohmann. The physics and neurobiology of magnetoreception.  
2154      *Nature reviews. Neuroscience*, 6:703–712, 2005.
- 2155      A. Kageyama and T. Sato. Dipole field generation by an mhd dynamo. *Plasma Physics*  
2156      *and Controlled Fusion*, 39(5A):A83 – A91, 1997.
- 2157      A. Kageyama, T. Sato, K. Watanabe, R. Horiuchi, T. Hayashi, Y. Todo, T. H. Watanabe,  
2158      and H. Takamaru. Computer simulation of a magnetohydrodynamic dynamo 2. *Physics*  
2159      *Plasma*, pages 1421 – 1431, 1994.
- 2160      R. Kerr. Are we ready for the next solar maximum? no way, say scientists. *Science News*  
2161      *Focus*, 324:1640 – 1641, 2009.
- 2162      E.M. King, S. Stellmach, N. Noir, U. Hansen, and J.M. Aurnou. Boundary layer  
2163      control of rotating convection systems. *Nature*, 457:301 – 304, 2009. doi: doi:  
2164      10.1038/nature07647.
- 2165      E.M. King, K.M. Soderlund, U.R. Christensen, J. Wicht, and J.M. Aurnou. Convective  
2166      heat transfer in planetary dynamo models. *G-Cubed Geochemistry, Geophysics,*  
2167      *Geosystems*, 11:Q06016, 2010. doi: doi:10.1029/2010GC003053.
- 2168      H. Kitauchi and K. Shigeo. Intensification of magnetic field by concentrate-and-stretch  
2169      of magnetic flux lines, year = 1998, journal = Physics of Fluids, volume = 10, number  
2170      = 2, pages = 457 - 468.
- 2171      W. Kuang. Force balances and convective state in the earth's core. *Physics of the Earth*  
2172      *and Planetary Interiors*, 116:65 – 79, 1999.

- 2173 W. Kuang and J. Bloxham. An earth-like numerical dynamo model. *Letters to Nature*,  
2174 389:371, 1997.
- 2175 W. Kuang and J. Bloxham. Numerical modeling of magnetohydrodynamic convection in  
2176 a rapidly rotating spherical shell: Weak and strong field dynamo action. *Journal of*  
2177 *Computational Physics*, 1999.
- 2178 C. Kutzner and U.R. Christensen. Effects of driving mechanisms in geodynamo models.  
2179 *Geophysical Research Letters*, 27:29 – 32, 2000.
- 2180 C. Kutzner and U.R. Christensen. From stable dipolar towards reversing numerical  
2181 dynamos. *Physics of the Earth and Planetary Interiors*, 131:29 – 45, 2002.
- 2182 L.D. Landau and E.M. Lifshitz. Fluid mechanics. *Pergamon Elmsford, New York*, 1981.
- 2183 M. Landeau and J. Aubert. Equatorially asymmetric convection inducing a hemispher-  
2184 ical magnetic field in rotating spheres and implications for the past martian dynamo.  
2185 *Physics of the Earth and Planetary Interiors*, 185: 3-4:61–73, 2011.
- 2186 C.G. Langereis, M.J. Dekkers, G.J. de Lange, and P.J.M. van Santvoort. Magnetostratig-  
2187 raphy and astronomical calibration of the last 1.1 Myr from an eastern Mediterranean  
2188 piston core and dating of short events in the Brunhes. *Geophysical Journal Interna-*  
2189 *tional*, 129:75 – 94, 1997.
- 2190 J. Larmor. How could a rotating body such as the sun become a magnet? *Report of the*  
2191 *British Association for the Advancement of Science*, 87th Meeting:159 – 160, 1919.
- 2192 R.T. Merrill, M.W. McElhinny, and P.L. McFadden. Magnetic Field of the Earth: Pale-  
2193 omagnetism, the Core, and the Deep Mantle. *International Geophysics Series*, 63:31  
2194 – 32, 1996.
- 2195 T. Miyagoshi, A. Kageyama, and T. Sato. Zonal flow formation in the earths core.  
2196 *Nature*, 463:793 – 796, 2010. doi: doi:10.1038/nature08754.

- 2197 T. Miyagoshi, A. Kageyama, and T. Sato. Formation of sheet plumes, current coils,  
2198 and helical magnetic fields in a spherical magnetohydrodynamic dynamo. *Physics of  
2199 Plasmas*, 18:072901, 2011. doi: doi:10.1063/1.3603822.
- 2200 P. Olson and J. Aurnou. A polar vortex in the Earth's core. *Nature*, 402:170 – 173, 1999.
- 2201 P. Olson and U. Christensen. Dipole moment scaling for convection-driven planetary  
2202 dynamos. *Earth and Planetary Science Letters*, 250:561 – 571, 2006.
- 2203 P. Olson, U. Christensen, and G. A. Glatzmaier. Numerical modeling of the geodynamo:  
2204 Mechanisms of field generation and equilibration. *Journal of Geophysical Research*,  
2205 104:10383 – 10404, 1999.
- 2206 I. Proudman. The almost-rigid rotation of viscous fluid between concentric spheres.  
2207 *Journal of Fluid Mechanics*, 1:5:505 – 516, 1956.
- 2208 J. Proudman. On the motions of solids in a liquid possessing vorticity. *Proc. R. Soc.  
2209 London, A*, 92:418 – 424, 1916.
- 2210 A.P. Roberts. Geomagnetic excursions: Knowns and unknowns. *Geophysical Research  
2211 Letters*, 35, 2008.
- 2212 P.H. Roberts and G.A. Glatzmaier. Geodynamo theory and simulations. *Reviews of  
2213 Modern Physics*, 72(4):1081 – 1123, 2000.
- 2214 P.H. Roberts and G.A. Glatzmaier. The Geodynamo, Past, Present and Future. *Geo-  
2215 physical and Astrophysical Fluid Dynamics*, 94:47 – 84, 2001.
- 2216 A. Sakuraba and M. Kono. Effects of the inner core on the numerical solution of the  
2217 magnetohydrodynamic dynamo. *Physics of the Earth and Planetary Interiors*, 111:105  
2218 – 121, 1999.

- 2219 A. Sakuraba and P.H. Roberts. Generation of a strong magnetic field using uniform  
2220 heat flux at the surface of the core. *Nature Geoscience*, 2:802–805, 2009. doi: doi:  
2221 10.1038/ngeo643.
- 2222 Y. Sasaki, S. Takehiro, K. Kuramoto, and Y. Hayashi. Weak-field dynamo emerging in  
2223 a rotating spherical shell with stress-free top and no-slip bottom boundaries. *Physics*  
2224 *of the Earth and Planetary Interiors*, 188: 3-4:203–213, 2011.
- 2225 M. Schrinner, L. Petitdemange, and E. Dormy. Dipole collapse and dynamo waves in  
2226 global direct numerical simulations. 2012.
- 2227 Z. Selzer and A. Jackson. Extracting scaling laws from numerical dynamo models. *Geo-*  
2228 *physical Journal International*, 2013.
- 2229 R.D. Simitev and F.H. Busse. Prandtl number dependence of convection driven dynamos  
2230 in rotating spherical fluid shells. *Journal of Fluid Mechanics*, 532:365–388, 2005.
- 2231 R.D. Simitev and F.H. Busse. Bistability and hysteresis of dipolar dynamos generated by  
2232 turbulent convection in rotating spherical shells. *Europhysics Letters*, 85:19001–p1–p5,  
2233 2009.
- 2234 R.D. Simitev and F.H. Busse. Bistable attractors in a model of convection-driven spher-  
2235 ical dynamos. *Physica Scripta*, 2012.
- 2236 K.M. Soderlund, E.M. King, and J.M. Aurnou. The influence of magnetic fields in  
2237 planetary dynamo models. *Earth and Planetary Science Letters*, 333, 2012.
- 2238 J Sonke and J.L. Kenneth. The physics and neurobiology of magnetoreception. *Nature*  
2239 *Reviews*, 6:703 – 712, 2005.
- 2240 B. Sreenivasan and C.A. Jones. Structure and dynamics of the polar vortex in the earth’s  
2241 core. *Geophysical Research Letters*, 32:L20301, 2005.

- 2242 B. Sreenivasan and C.A. Jones. Azimuthal winds, convection and dynamo action in the  
2243 polar regions of planetary cores. *Geophysical and Astrophysical Fluid Dynamics*, 100:  
2244 319 – 339, 2006a.
- 2245 B. Sreenivasan and C.A. Jones. The role of inertia in the evolution of spherical dynamos.  
2246 *Geophysical Journal International*, 164:467 – 476, 2006b.
- 2247 S. Stanley. *So Many Dynamos: A study of planetary magnetic field morphologies*. PhD  
2248 thesis, Harvard University, 2004.
- 2249 S. Stanley and J. Bloxham. Convective-region geometry as the cause of Uranus' and  
2250 Neptune's unusual magnetic fields. *Nature*, 428:151 – 153, 2004.
- 2251 S. Stanley and J. Bloxham. Numerical dynamo models of Uranus and Neptunes magnetic  
2252 fields. *Icarus*, 184:556 – 572, 2006.
- 2253 S. Stanley and G. Glatzmaier. Dynamo models for planets other than earth. *Space  
2254 Science Reviews*, 152:617–649, 2009.
- 2255 S. Stanley, L. Elkins-Tanton, M.T. Zuber, and E.M. Parmentier. Mars' paleomagnetic  
2256 field as the result of a single-hemisphere dynamo. *Science*, 321:1822–1825, 2008.
- 2257 S.V. Starchenko and C.A. Jones. Typical velocities and magnetic field strengths in plan-  
2258 etary interiors. *Icarus*, 157:151 – 153, 2002.
- 2259 D.J. Stevenson. Turbulent thermal convection in the presence of rotation and a magnetic  
2260 field: a heuristic theory. *Geophysical and Astrophysical Fluid Dynamics*, 12:139 – 169,  
2261 1979.
- 2262 D.J. Stevenson. Planetary magnetic fields. *Earth and Planetary Science Letters*, 208:1 –  
2263 11, 2003.
- 2264 D.J. Stevenson. Nondynamo Theories, In Encyclopedia of Geomagnetism and Paleomag-  
2265 netism. *New York: Springer*, pages 704–706, 2007.

- 2266 I. Sumita and P. Olson. Laboratory experiments on high rayleigh number thermal con-  
2267 vection in a rapidly rotating hemispherical shell. *Physics of the Earth and Planetary*  
2268 *Interiors*, 117:153 – 170, 2000.
- 2269 P.J. Tackley. Dynamics and evolution of the deep mantle resulting from thermal, chem-  
2270 ical, phase and melting effects. *Earth-Science Reviews*, 110:1–25, 2012.
- 2271 F. Takahashi, M. Matsushima, and Y. Honkura. Simulations of a quasi-taylor state  
2272 geomagnetic field including polarity reversals on the earth simulator. *Science*, 309:459  
2273 – 461, 2005.
- 2274 F. Takahashi, M. Matsushima, and Y. Honkura. Scale variability in convection-driven  
2275 mhd dynamos at low ekman number. *Physics of the Earth and Planetary Interiors*,  
2276 167:168 – 178, 2008.
- 2277 John A. Tarduno, Rory D. Cottrell, Francis Nimmo, Julianna Hopkins, Julia Voronov,  
2278 Austen Erickson, Eric Blackman, Edward R.D. Scott, and Robert McKinley. Evidence  
2279 for a dynamo in the main group pallasite parent body. *Science*, 338(6109):939–942,  
2280 2012. doi: 10.1126/science.1223932.
- 2281 G. I. Taylor. Motion of solids in fluids when the flow is not irrotational. *Proc. R. Soc.*  
2282 *London, A*, 93:99 – 113, 1917.
- 2283 A. Tilgner. Treatise on Geophysics, Chapter 8.07: Rotational Dynamics of the Core.  
2284 *Elsevier*, 8:207–243, 2007.
- 2285 R.C. Weber, P-Y. Lin, E.J. Garnero, Q. Williams, and P. Lognonné. Seismic Detection  
2286 of the Lunar Core. *Science Reports*, 331:309 – 312, 2011.
- 2287 J. Wicht. Inner-core conductivity in numerical dynamo simulations. *Physics of the Earth*  
2288 *and Planetary Interiors*, 132:281 – 302, 2002.

- 2289 J. Wicht and A. Tilgner. Theory and modeling of planetary dynamos. *Space Science  
Reviews*, 152:501 – 542, 2010.
- 2291 D.U. Wise, M.P. Golombek, and G.E. McGill. Tectonic evolution of mars. *Journal of  
Geophysical Research*, 84-B14:7934 – 7939, 1979.
- 2293 R.K. Yadav, T. Gastine, and U.R. Christensen. Scaling laws in spherical shell dynamos  
2294 with free-slip boundaries. *Icarus*, 225:185 – 193, 2013.
- 2295 K. Zhang and C.A. Jones. The effect of hyperviscosity on geodynamo models. *Geophysical  
Research Letters*, 24:2869 – 2872, 1997.
- 2297 K. Zhang, C.A. Jones, and G.R. Sarson. The dynamical effect of hyperviscosity on  
2298 numerical geodynamo models. *Studia Geophysica et Geodaetica*, 42:247 – 253, 1998.